Modeling of dynamically loaded hydrodynamic bearings at low Sommerfeld numbers

Thomsen, Kim; Klit, Peder; Vølund, Anders; Santos, Ilmar

Publication date:
2012

Document Version
Publisher's PDF, also known as Version of record

Modeling of dynamically loaded hydrodynamic bearings at low Sommerfeld numbers

PhD Thesis

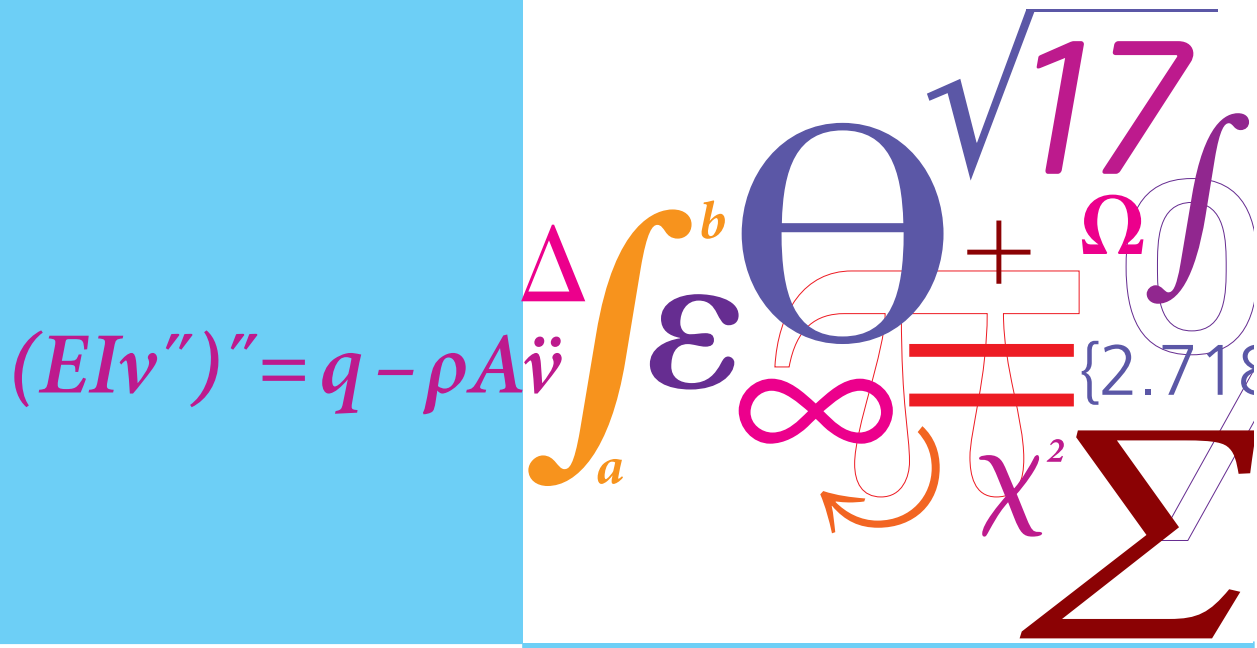

Kim Thomsen
DCAMM Special Repport No. S144
March 2012

DTU Mechanical Engineering
Department of Mechanical Engineering

Modeling of dynamically loaded hydrodynamic bearings at low Sommerfeld numbers

Kim Thomsen

Siemens Wind Power
&
Department of Mechanical Engineering
Technical University of Denmark

Modeling of dynamically loaded hydrodynamic bearings at low Sommerfeld numbers
March 2012

Supervisors:
Peder Klit
Professor
Technical University of Denmark

Anders Vølund
Senior Research Engineer, M.Sc., Ph.D.
MAN B&W

Ilmar Ferreira Santos
Associate Professor Dr.-Tech.
Technical University of Denmark

ISBN 978-87-90416-84-3
DCAMM Special Report No. 5144

Preface

This thesis is submitted as partial fulfillment of the requirements for awarding the Danish Ph.D. degree. The work has been carried out from February 2009 to March 2012 at Siemens Wind Power in cooperation with the Technical University of Denmark and with financial support from the Danish Agency for Science, Technology and Innovation.

I wish to express my gratitude to Siemens Wind Power for initiating and supporting my work on this exiting research project. I would also like to express my deepest thanks to my advisors Professor Peder Klit, Senior Research Engineer Anders Vølund and Associate Professor Dr.-Tech. Ilmar Ferreira Santos for support, inspiration and guidance throughout my research.

I also wish to thank Director of Research at CNRS Michel Fillon for his hospitality and guidance during my stay at University of Poitiers.

At Siemens Wind Power I thank my colleagues Bo Pedersen, Pierre-Antoine Guerenbourg, Klaus Kjølhede, Daniel Meldgaard and Akhilesh Shukla for the numerous discussions on numerical approaches and practical aspects of tribology as well as invaluable guidance on the use of Ansys.

Siemens Wind Power
Brande, March 2012

Kim Thomsen

Abstract

Current state of the art within the wind industry dictates the use of conventional rolling element bearings for main bearings. As wind turbine generators increase in size and output, so does the size of the main bearings and accordingly also the cost and potential risk of failure modes.

The cost and failure risk of rolling element bearings do, however, grow exponentially with the size. Therefore hydrodynamic bearings can prove to be a competitive alternative to the current practice of rolling element bearings and ultimately help reducing the cost and carbon footprint of renewable energy generation.

The challenging main bearing operation conditions in a wind turbine pose a demanding development task for the design of a hydrodynamic bearing. In general these conditions include operation at low Reynolds numbers with frequent start and stop at high loads as well as difficult operating conditions dictated by environment and other wind turbine components.

In this work a numerical multiphysics bearing model is developed in order to allow for accurate performance prediction of hydrodynamic bearings subjected to the challenging conditions that exist in modern wind turbines. This requires the coupling of several different theoretical fields:

- fluid film forces
- heat transfer
- thermoviscous effects
- dynamic response
- deformation of structure and components
- angular misalignment
- wear

The multiphysics bearing model is applied for various bearing types in order to study the bearings, their hydrodynamic performance and related phenomena:

- a new wear model is proposed which can, with only moderate efforts, be implemented into existing EHD models.
- it is discovered that radial tilting pad bearings can exhibit discontinuity effects when subjected high dynamic loads.

- the influence of compliant liners on the dynamic response of journal bearings subjected to dynamic loads is studied using a soft EHD model.
- the influence of the geometrical design parameters of a radial flexure pad is studied as well as the effect of a compliant liner using an EHD model.
- an innovative radial flexure journal bearing designed for operation at heavy angular misalignment is presented. Its hydrodynamic behavior, as well as the effect of a compliant liner, is studied using a TEHD model.
- the EHD model is extended to cover 5 degrees of freedom and is applied for a novel compact moment-carrying hydrodynamic bearing.

Abstrakt

Nuværende state-of-the-art indenfor vindmølleindustrien dikterer brugen af konventionelle rulningslejer for hovedlejer. I takt med at vindmøllerne stiger i størrelse og effekt stiger også størrelsen af lejerne og således også kostprisen og den mulige risiko for skader.

Kostprisen og risikoen for skader for rulningslejer stiger dog eksponentielt med størrelsen. Derfor kan hydrodynamiske glidelejer vise sig at være et konkurrencedygtigt alternativ til den nuværende praksis med rulningslejer og ultimativt bidrage til at reducere udgiften og klimapåvirkningen for vedvarende energiproduktion.

De udfordrende driftsbetingelser for hovedlejerne i en vindmølle udgør en krævende udviklingsopgave for designet af et hydrodynamisk glideleje. Generelt indebærer driftsbetingelserne drift ved lave Reynolds værdier med jævnlige start-stop cykler ved høje laster såvel som vanskelige betingelser dikteret af omgivelserne og de øvrige vindmølle komponenter.

I dette værk udvikles en multifysisk lejemodel der muliggør præcis forudsigelse af et hydrodynamisk glidelejes drift når det udsættes for de udfordrende driftsbetingelser som eksisterer i moderne vindmøller. Dette kræver kobling af adskillige forskellige teoretiske felter:

- smørrefilmens kræfter
- varmeledning
- termoviskose effekter
- dynamisk respons
- deformation af struktur
- vinkelskævhed
- slid

Den udviklede multifysiske lejemodel anvendes på adskillige lejetyper for at studere lejerne og deres hydrodynamiske drift samt relaterede fænomener:

- en ny slidmodel opstilles som kan, med moderat indsats, implementeres i eksisterende EHD modeller.
- det afsløres at radiale vippeskolejer kan udvise diskontinuitets-fænomener når de udsættes for meget dynamiske laster.

- indflydelsen af komplianse linere på den dynamiske respons af radiale glidelejer udsat for dynamiske laster studeres ved brug af en soft EHD model.
- de geometriske designparametre for et radial-fleks-vippeskoleje studeres sammen med påvirkning af kompliante linere ved brug af en EHD model.
- et innovativt radial-fleks-glideleje udviklet for drift ved stor vinkelskævhed præsenteres. Dets hydrodynamiske drift, og indflydelsen af en kompliant liner, studeres ved brug af en TEHD model.
- EHD modellen udvides til at dække 5 frihedsgrader og anvendes på et nyskabende, kompakt, momentbærende hydrodynamisk glideleje.

Contents

List of Figures

List of Tables

Nomenclature

$\mathbf{A}$	Integration matrix	$[m^2]$
$\mathbf{H}$	Fluidity matrix	$[m^3/(Pas)]$
$\mathbf{K}$	Force stiffness matrix	$[N/m]$
$\mathbf{J}$	Jacobian matrix	$[m^3/(Pas)]$
$\mathbf{L}$	Pressure compliance matrix	$[m/Pa]$
$\mathbf{M}$	Mass matrix	$[kg]$
A	Element area	$[m^2]$
A_J	Journal cross sectional area	$[m^2]$
E	Modulus of elasticity	$[N/m^2]$
F	Force	$[N]$
F	Bearing reaction force	$[N]$
G	External moments on bearing	$[Nm]$
L	Journal width	$[m]$
M	Moment	$[Nm]$
P	Power	$[J/s]$
R	Radius	$[m]$
Re	Reynolds number	$[-]$
S	Residual	$[m^3/s]$
So	Sommerfeld number	$[-]$
T	Temperature	$[C]$
T_J	Journal temperature	$[C]$
T_m	Lubricant mean temperature	$[C]$
V	Fluidity vector	$[m^3/s]$
W	External force on bearing	$[N]$
b	Element coefficient	$[m]$
c	Element coefficient	$[m]$
c_p	Specific heat capacity of lubricant	$[J/kg/K]$
d	Deformation vector	$[m]$
e	Error	varies
f	Functional	$[m^3/s]$

h	Lubricant film thickness	[m]
h_0	Lubricant film thickness in the undeformed state	[m]
k	Lubricant thermal conductivity	[W/m/K]
k_J	Journal thermal conductivity	[W/m/K]
n	Unit vector normal to bearing surface	[m]
p	Pressure	[Pa]
q	Lubricant flow rate	[m^3/s]
s	Lubricant shear rate	[s^{-1}]
t	Time	[s]
x, y, z	Linear coordinates, mesh	[m]
$\bar{x}, \bar{y}, \bar{z}$	Linear coordinates, system	[m]
α_J	Heat transfer coefficient between interface: Journal/oil	[$W/m^2/K$]
β	Coefficient of relaxation	[−]
θ	Angular coordinate	[rad]
λ	Film thickness vs. surface roughness ratio	[−]
Λ	Boundary length	[m]
μ	Lubricant viscosity	[Pas]
μ_m	Mean lubricant viscosity	[Pas]
ν	Poisson's ratio	[−]
ν	Kinematic viscosity	[m^2/s]
ρ	Lubricant density	[kg/m^3]
τ	Shear stress	[N/m^2]
χ	Linear coordinate for rotor position in stator	[m]
ψ	Angular coordinate for rotor position in stator	[rad]
ω	Rotational speed	[rad/s]
Ω	Area	[m^2]

Abbreviations

COF	Coefficient of friction
DOF	Degree(s) of freedom
EHD	Elastohydrodynamic
FDM	Finite difference method
FEM	Finite element method
FSAL	First-same-as-last
HD	Hydrodynamic
LMS	Least-mean-squares
PEEK	Polyetheretherketone
PTFE	Polytetrafluoroethylene
TEHD	Thermoelastohydrodynamic

THD Thermhydrodynamic

Chapter 1

Introduction

The understanding of hydrodynamic bearings began with Beauchamp Tower's discovery of the hydrodynamic lubrication effect in 1883 and Osborne Reynolds (1886) equation describing the hydrodynamic pressure build-up in the oil film. Since then the hydrodynamic bearing technology has proven its worth in numerous applications. The bearings are used extensively within the marine industry, for hydro power plants, steam turbines and combustion engines. Figure 1.1 shows various examples of conventional hydrodynamic bearings for a wide range of applications.

However, the wind industry has relied on rolling element bearings from the very first kW rated turbines to the latest state-of-the-art MW power plants. Thus the rolling element bearing technology has grown to be a well proven and trusted technology within the wind industry. Recent examples are the geared Siemens Wind Power 2.3 MW wind turbine [SWT-2.3-101] and the Siemens Wind Power 2.3 MW direct drive wind turbine [SWT-2.3-113] shown in figures 1.2(a) and 1.2(b) respectively.

The geared wind turbine uses two double row spherical bearings for supporting the 62 ton rotor. The bearing type is shown in figure 1.3 and supports both axial and radial loads. Furthermore it allows the rollers and cage to adjust to angular deflection along the bearing center line and hence avoid severe edge loading when the structure deforms due to external loading on the overhung rotor.

The direct drive wind turbine is built around a revolutionizing permanent magnet generator which enables the number of parts to be reduced with 50% compared to a traditional geared wind turbine. A double row tapered bearing of the type shown in figure 1.3 supports the rotor.

The increasing size of wind turbines and increasing trend towards offshore turbines puts high demands on bearing robustness and the ability to accurately predict bearing lifetime. As the size of bearings increases, so does the risk of potential failure modes. Classic ones being for example material flaws or contamination initiating local damages which then spread within the bearing, often with exponential growth rate.

The thin lubricant film and extreme pressures occurring in rolling element bearings, even when operating at normal operating conditions, make the bearings sensitive to deviations from design specifications. For idealized pure rolling an oil film of molecu-

Figure 1.1: Examples of hydrodynamic bearings. a: Thrust tilting pad bearing [Kingsbury] b: Radial tilting pad bearing [Kingsbury] c: Automotive plain bearing shells d: Thrust bearing with hydrostatic jacking for hydro power plant [Pioneer Motor Bearing] e: Stern tube bearing using polymer liner [Thordon Bearings] f: Bearings for 2800 kW ball mills [KEW Foundries].

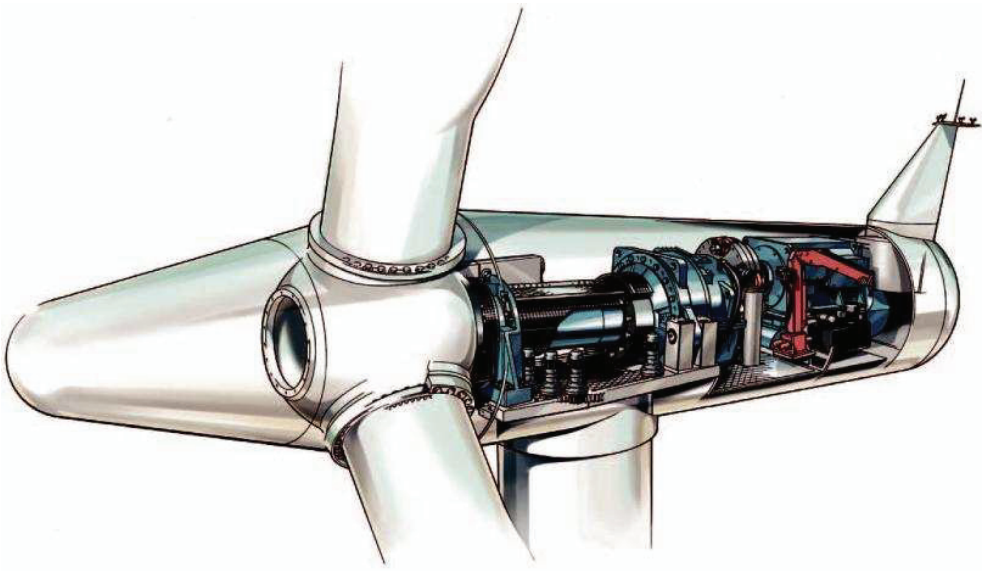

(a) Siemens Wind Power 2.3 MW geared wind turbine

(b) Siemens Wind Power 2.3 MW direct drive wind turbine

Figure 1.2: State of the art wind turbines

Figure 1.3: Double row spherical roller bearings (left) and double row tapered roller bearing (right) [NKE Bearings].

lar dimensions is sufficient to fully separate the roller and raceway [2]. However, when factors as sliding, contamination, lubrication, electrical currents, deformation, thermal expansion or corrosion is included it gets difficult to predict the bearing lifetime, especially for large bearings. Another aspect is the manufacturing of large bearings. There are only a relative few companies which supply these bearings which hinders a good procurement situation.

Hydrodynamic bearings operate at much thicker films and lower pressures compared to roller bearings. This reduces many of the failure modes known from rolling element bearings.

The general properties of a hydrodynamic bearing is listed below, compared to a rolling element bearing:

- overall more robust, when designed correctly for the application
- requires a minimum rotational speed for full film operation
- much higher friction at startup
- moderately higher friction at normal operation
- less sensitive to particles and contamination
- less sensitive to material failures, as bearing sizes grows this becomes more and more pronounced since bearing surface increases
- less strict requirements for manufacturing tolerances
- no wear or fatigue when operating at full film and steady state
- more potential suppliers and thus easier to procure
- no requirement for high grade steel and surface treatment
- lower stiffness

- higher damping

The most significant differences between the two bearing technologies are the high startup torque, when starting with load applied, and the requirement for a minimum sliding speed before a fully separating lubrication film is reached. The high friction at start-up can be eliminated using hybrid or hydrostatic bearings. This will then imply the addition of a high pressure lubrication system to the bearing application, which then adds complexity and possible failure modes. The focus of this work will be on hydrodynamic bearings. Assuming that the friction challenges can be solved, the hydrodynamic mode of operation looks very attractive compared to rolling element bearings. As bearings sizes grow, to suit larger wind turbines, this becomes more pronounced. Offshore wind turbines furthermore benefit from a more robust design since main bearing repairs are very costly due to offshore service crane costs and challenging conditions at sea.

This leads to the interesting question: Why are hydrodynamic bearings not yet adopted as main bearings by the wind industry?

Compared to typical applications, where hydrodynamic bearings are used, there are a number of challenging operating conditions related to wind turbine operation:

- gravitational load is high giving correspondingly high loads at start-up
- no direct control of external loads
- low sliding speeds
- frequent start and stop
- difficult operating conditions, for a hydrodynamic bearing, dictated by environment and other components

It is not uncommon to see hydrodynamic bearing applications operating under one or two of the listed items, but not all of them at one time. All items exist in a wind turbine and therefore increases the complexity of the design task.

In this work a numerical multiphysics bearing model has been developed in order to allow for accurate performance prediction of a hydrodynamic bearing subjected to conditions existing in modern wind turbines. This includes simulation of the following parameters:

- fluid film forces
- heat transfer
- thermoviscous effects
- dynamic response
- deformation of structure and components
- angular misalignment
- wear

When these are combined they comprise a thermoelastohydrodynamic (TEHD) model that can simulate the response for dynamic loads and estimate wear when operating at thin films. In this work the numerical models will be derived and applied on various bearing applications.

Ultimately the goal of this work is to reduce the carbon footprint of energy production through improvement of one of the central components in wind turbines. This is facilitated through the development of knowledge and know-how required to implement a hydrodynamic bearing solution in a wind turbine and thereby present a strong alternative to current state of the art.

Chapter 2

Hydrodynamic bearings

Hydrodynamic bearings rely on the pressure generated when two conditions for a sliding pair are met:

- the surfaces must move relative to each other
- the surfaces must form a converging oil film geometry

In a conventional journal bearing, such as the ones shown in figure 1.1c, e and f, the converging geometry is formed when the journal center location is non-concentric in the bearing. The journal rotation drags oil into the wedge and generates pressure which then separates the sliding pair.

The generated pressure is a function of numerous geometrical and operational parameters. For a journal bearing the dimensionless Sommerfeld number So (2.1) states the relationship between the primary parameters:

$$So = \frac{\mu\omega}{p}\left(\frac{R}{c_r}\right)^2 \tag{2.1}$$

For example halving the radial clearance will result in a quadruplicating of the pressure and so on. Early studies often depicted results as functions of the Sommerfeld number since one figure can show the influence of all five variables [3]. This approach does, however, neglect many important non-linear interrelated phenomena such as thermo-viscous and elasticity effects and influences of more complex geometries.

2.1 Tilting pad bearings

Since A.G.M. Michells discovery of the tilting pad bearing it has been widely adopted for both thrust and radial bearing applications. The pivoted pad bearing allows the angular position of the pad to adjust according to the operating conditions. Ideally the pivot ensures that the pad operates with constant ratio between oil film thickness at leading and trailing edge of the pad [4]. Thereby the pivoted pad operates better over

a much broader range of operation conditions compared to a fixed geometry pad like the tapered thrust pad with a flat land. Figure 1.1a, b and d shows typical examples of radial and thrust tilting pad bearings. Figure 1.1a shows several interesting features worth noticing:

- a leading edge groove supplies lubricant directly at the leading edge allowing the bearing to run without submersion into an oil bath thereby reducing parasitic losses.
- an offset pivot point positioned roughly 65% from leading edge.
- a load equalization system using mechanical lever arms.
- a two-half design allowing the bearing to be split and mounted radially.

The location of the pivot has significant influence on the hydrodynamic performance of the tilting pad bearing. For bi-directional operation a central location, i.e. 50 % from leading edge, is the preferred choice. But for uni-directional operation locations from 60 to 80 % have been reported as optimum choice. It is important to consider thermo-hydrodynamics when searching for the optimum pivot location, since the lubricant flow into the bearing is increased rapidly, and hence also the cooling, when moving the pivot towards the trailing edge [5]. From this it is evident that the optimum pivot location depends on the specific bearing application.

Large tilting pad bearings cannot make use of the conventional rocker pivot contact, as shown in figure 1.1a, since the stresses on the contact zone will be excessive. Figure 2.1 shows examples of alternative pivot mechanisms: cylindrical line contact support, flexure pivots, fluid pivots and spring beds. All alternative solutions either increase resistance towards angular adjustment or increase complexity. Some designs does however give additional advantages, for example the required pad stiffness is reduced significantly for the spring bed supported pad since it is supported under the full pad length and deformations due to bending are reduced.

Niclas and Wygant [6] study tilting pads with cylindrical line contacts, spherical point contacts and ball-in-socket designs for high load applications. The pivot designs are compared and design guidelines given for high load applications.

Kim and Kim [7] show that the frictional resistance in the pivot can have a high influence on bearing performance and that the resistance is increased significantly for bearings using ball-in-socket pivot mechanisms.

Tilting pad thrust bearings always comprises several individual pads, more than 10 pads is not unusual. This will inevitably result in some difference in pad height due to assembly and manufacturing tolerances of the complete bearing system. When this is combined with general operational misalignment due to elastic and thermal distortion equal load sharing cannot be expected without a equalizing system. Load equalization can be achieved through mechanical systems using levers, hydraulics or elasticity. Alternatively the bearings are designed without equalization system, this usually results in lower load capacity corresponding to the accuracy of the assembled bearing.

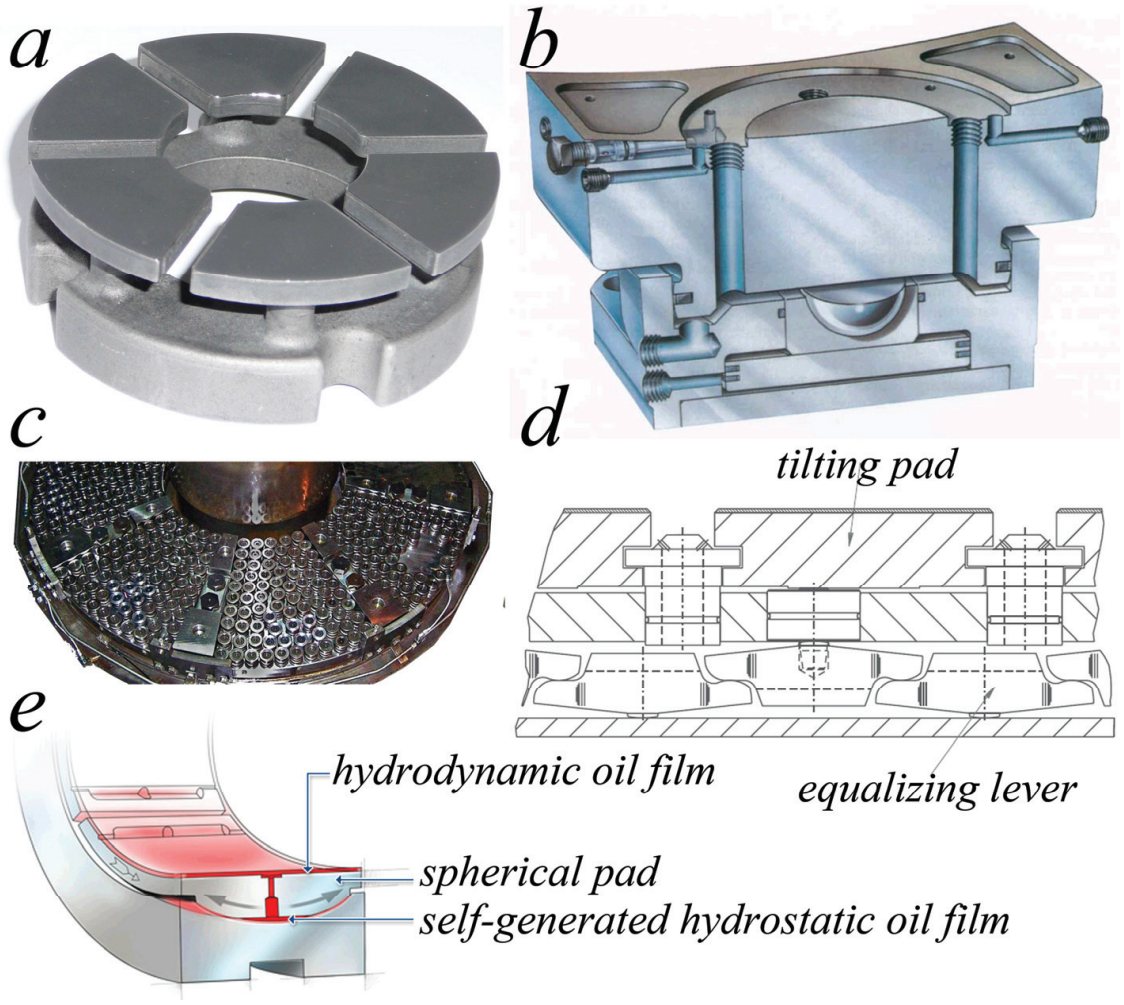

Figure 2.1: Alternative pivot mechanisms. a: Flexure bearing for small pump application [Grundfos]. b: Advanced hydrostatic tilting pad using ball-in-socket pivot mechanism and hydraulic load equalization for large ball mill [SKF]. c: Spring bed support for hydro power plant. d: Mechanical equalization using lever arms [Waukesha Bearings]. e: Fluid pivot using self-generated hydrostatic film [Pioneer Motor Bearing].

Flexible rotors operating at high rotational speeds are often supported in tilting pad journal bearings due to their stabilizing effect compared to other bearing types with fixed geometry. The tilting pads ensure that the cross-coupling coefficients in the stiffness and damping matrices of the bearing are small compared to the direct coefficients. For applications where high shaft misalignments are unavoidable, radial tilting pad bearings can also be the preferred choice over plain journal bearings due to low sensitivity to this issue.

Thomsen and Klit [8], appendix A, has shown that large radial tilting pad bearings seeing highly dynamically loads during slow rotation can show instabilities when the squeeze term dominates the right-hand side of Reynolds equation and the pad circumferential extent is large. The work also discusses calculation of angular moment equilibrium and how it correlates with angular position.

Hargreaves and Fillon [9] studied fluttering and spragging and describes how an instability at one pad can cause the neighboring pads to reach instabilities when the journal changes position due to the decreased pressure at some pads.

Gardner [10] studies flutter experimentally and successfully provokes flutter conditions, which is shown to develop at low oil flow rates for unloaded tilting pads. Flutter reveals as clicking sounds and can eventually cause fatigue damages.

Adams and Payandeh [11] describe how unloaded pads can show self-excited vibrations if a pad's operating pivot clearance is larger than the concentric bearing clearance. Preloading is shown to reduce instabilities and it is also found that smaller pads are less prone to self-excited vibrations.

A topic not covered in this work is thermal crowning of the tilting pads. Since the subject is of high importance for highly loaded tilting pad bearings it deserves a brief notice.

The viscous dissipation in the lubricant heats the sliding surfaces and the heat flux induces a thermal gradient through the pad resulting in differential thermal expansion. This is known as thermal crowning. Ettles [12] has studied the size effects when scaling up bearings and reports that the effect of thermal crowning increases with bearing size. He mentions insulation, cooling and elaborate pad support systems as methods to reduce thermal crowning. Heinrichson [13] has studied thrust pads and uses a flat plate approximation for calculation of thermal crowning and finds good correlation with experimental results. Glavatskih [5] describes how elasticity can be used to counteract thermal crowning if the deformation is concave. He also refers to efficient oil supply decreasing hot oil carry over and high pad thermal conductivity as means of reducing thermal crowning effect.

2.2 Flexure bearings

The term flexure bearing is used for bearings for which important parts of their tribological characteristics are achieved through structural flexibility. One family

of the flexure bearings are the flexure pad bearings, in which the pivot mechanism from conventional pads is replaced with a flexible structure that allows the bearing to adapt to the load and operating conditions. Hereby pivot contact related failure modes are eliminated and load capacity is not restricted by the force that can be transfered through the pivot contact. The flexure bearing combines the simplicity and sturdiness of a fixed geometry bearing with the adaptable nature of the pivoted pad. From a manufacturing viewpoint the flexure bearing can also be advantageous because the number of parts is reduced and the tolerance chain is shorter. Figure 2.1a shows an example of a mass-produced flexure bearing for a small pump application using process-medium, in this case water, as lubricant. The stiffness of the a flexure pad design eliminates the risk of pad flutter that otherwise can be encountered on the unloaded pads when using traditional tilting pad bearings. The flexure pad bearing is, however, more sensitive to the initial alignment as it takes a minimum pad load to elastically deform the pad and align it to the sliding pair if not perfectly aligned at assembly.

In [14], appendix C, a flexure thrust pad is studied. The main geometrical dimensions of a radial flexure pad are varied and the affect on pad performance is analyzed and it is shown that flexure pads can be an attractive alternative to pivoted pads.

A flexure bearing does not necessarily need to use pads, i.e., a radial or a thrust pad bearing. Traditional journal bearings can also take advantage of flexibility. It can be used to increase tolerance to misalignment for traditional journal bearings significantly as shown in [15], appendix D. Here it is shown that the flexure journal can operate safely at much higher journal misalignments compared to a traditional stiff bearing design.

2.3 Compliant liners

The study of compliant liners have seen increasing interest in the recent years. Due to the polymer liners' low brake away friction and good wear properties the liners have very good operational characteristics when operating in the mixed lubrication regime. When this is combined with the compliant nature of the polymer bearings it also mean that they are less sensible to imperfections in the bearing surface geometry. This is particularly interesting for large bearings.

The polymers does, however, also give the engineers new challenges in the form of creep, the Achilles heel of polymers when applied to bearing applications. For example PTFE will creep even at low temperatures and it is therefore not suitable for highly loaded applications in its pure form. In order to decrease creep to an acceptable level, the polymers are often reinforced with glass or carbon fibers.

The fiber reinforcement furthermore has the advantage of increasing the wear resistance of the polymer provided that there is a strong adhesion between the fibers and the polymer base material [4]. The fibers can, however, increase the wear of the sliding partner.

The low thermal conductivity of polymers must also be taken into account when introducing polymer liners in hydrodynamic bearings as it will reduce the heat flux between bearing and lubricant. This can be a disadvantage giving higher lubricant temperatures. However, it can also be an advantage since it will reduce thermal crowning for pads using polymer liners.

PTFE and PEEK composites are popular choices for bearing applications. The polymer composition and fillers have major influence on its mechanical and tribological properties and this may be used to engineer the best compromise among the required material properties.

The polymer technology has been implemented for diverse bearing applications. Examples from the industry are water hydraulic pumps, thrust bearings for hydro power plants and propulsion shaft and stern tube bearings used in marine applications. Cases from the industry [16] show that it is possible to up-rate existing machinery when replacing the existing metal alloy faced bearings with polymer liners. The uprating can either be used to decrease the bearing size and thereby reduce loss or to simply use the same bearings to carry a higher load and hereby increase the load density of the machinery.

Local pressures up to 35 MPa are common for bearings in large combustion engines using babbitted liners and typical industry design guidelines state around 4 MPa as maximum specific pressure for babbitted bearings. Ettles [12] reports specific loads up to 5.5 MPa and down to 3.3 MPa for large thrust bearings. 3.5 MPa is reported by Nicholas [17] for heavily loaded radial tilting pad bearings.

When using polymer lined pads the specific pressure can be increased and thereby increase the potential load density of the bearing. Specific loads of up to 11 MPa are reported as safe operational loads for large thrust bearings in hydro power plants [18].

When using polymer lined bearings it is furthermore possible to design hydrodynamic bearing systems, which would traditionally need jack-up systems, without jack-up. This is because of the polymers' low brake away friction and good wear properties when operating in the mixed lubrication region. When considering to start-up a bearing at high load without a jacking system it is important to consider that the static friction increases over time due to increase in adhesion. The static friction can more than double over time, having the highest gradient just after contact and standstill is initiated. The adhesion increases with smoothness of the sliding pair and therefore start-up frictional moment can increase as the surfaces smoothen and conform during running-in [19].

The better operational characteristics at thin films make it possible to use alternative lubricants, in some cases even water, or to use thinner oil in order to reduce power loss.

The influence of the liner stiffness on the dynamic response of a highly dynamically loaded journal bearing is studied in [20], appendix B. Three configurations with different liner stiffnesses are evaluated on the parameters that are traditionally used

to evaluate hydrodynamic bearing designs: dynamic response, maximum pressure, minimum film thickness, wear, power loss and temperature response. The primary findings are that the maximum pressures are reduced significantly and this comes at the expense of slightly higher eccentricity ratios during operation.

The radial flexure pad study [14], appendix C, also includes the influence of a compliant liner and its stiffness on the hydrodynamic performance of the pad. It is found that the liner clearly reduces peak pressures giving a flatter pressure profile. The concave deformation contribution of the polymer liner reduces the lubricant flow into the pad because the film thickness is reduced at the edges of the pad. There is no clear trend in the polymer liner effect on either power loss or lubricant film thickness. Another conclusion is that very compliant liners must be avoided. If liner deformation is excessive its concave contribution will exceed the convex contribution from the pad body and thus pad performance decreases drastically. Thicknesses of 2 mm are generally performing well.

The effect of compliant liners is a part of the work [15] appendix D. Here it is found that the compliant liner shows a remarkably increase in hydrodynamic performance when applied to a conventional stiff journal bearing. It increases the hydrodynamic performance at normal operating conditions with perfect alignment and also at significant misalignment. The positive influence is however not observed for the studied flexure journal bearing.

Chapter 3

General bearing design limits

In this chapter the general limits of operation for a hydrodynamic bearing will be explained briefly:

- thin lubricant film limit
- liner temperature&pressure limit
- lubricant temperature limit
- instability limit
- mechanical strength limit
- thermal expansion limit

Figure 3.1 shows three of the limits for a tilting pad bearing as function of shaft speed and load. When considering all bearing operational conditions the picture inevitable becomes more complex. In the following sections the limits will be discussed individually.

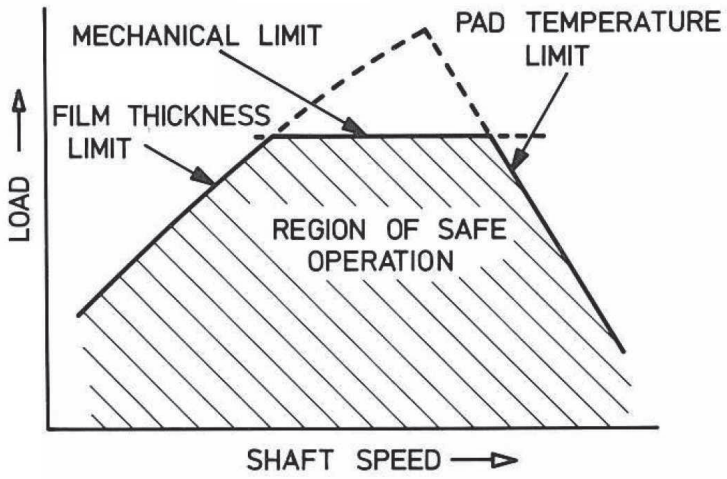

Figure 3.1: Limits of safe operation for tilting pad bearings [1]

3.1 Thin lubricant film limit

The lubrication regime in a hydrodynamic bearing can be divided into three categories: boundary, mixed and hydrodynamic lubrication. The three lubrication regimes are shown in figure 3.2. In order for a hydrodynamic bearing to function properly the lubricant film must ensure full separation of the bearing surfaces and thus primarily operate in the hydrodynamic regime.

- During boundary lubrication there is no lubricating film separating the sliding pair and there is significant asperity contact resulting in high friction and wear. In this zone the physical and chemical composition of the sliding pair&lubricant interaction determines the friction and wear properties. The term *lubricity* is used to describe the friction and wear properties of a sliding pair&lubricant and can be improved by the use of boundary lubricants/additives. Lubricant viscosity is not an influential parameter in this lubrication regime [21].
- In mixed lubrication some asperity contact occurs and the tribological properties are governed by a combination of boundary and hydrodynamic lubrication.
- At full hydrodynamic film there is no asperity contact and the tribological properties can be described using Reynolds equation.

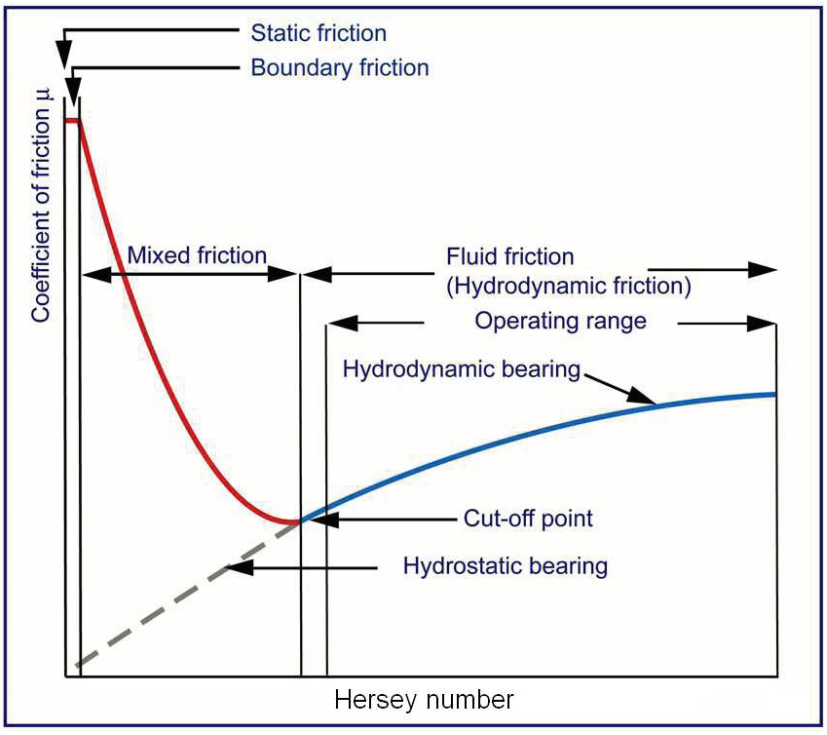

Figure 3.2: Typical Stribeck curve showing typical conditions from start-up to normal hydrodynamic operation. Hersey number: $\mu\omega/p$

From an efficiency viewpoint a hydrodynamic bearing must operate near the cut-off point, in the full film film regime, of figure 3.2. In this case power loss is minimal and no wear occurs. However, in order to ensure safe operation of the bearing some safety margin must be added. The lambda ratio, which specifies the ratio between the lubricant film thickness and the effective surface roughness, is used for this purpose. It is generally accepted that the lubricant zone can be characterized as fully hydrodynamic if $\lambda > 5$. Mixed lubrication occurs in the interval $1 < \lambda < 5$ and finally boundary lubrication is present when $\lambda < 1$. When factors such as contamination of lubricant, misalignment, surface finish and general build quality are controlled very well, one can reduce the λ value required for safe operation.

$$\lambda = \frac{h}{\sqrt{R_{q_a}^2 + R_{q_b}^2}} \tag{3.1}$$

Jacobson [2] has explained how λ values down to 0.05 can still fully separate two surfaces in extreme cases. This is possible if the slopes of the surface roughness peaks are in the range of 10^{-3} to 10^{-4} and they then act as small inclined sliders. Hereby a pressure will build up and elastically deform the peak leaving a thin lubricant film to separate the surfaces. Cann et al. [22] report the same findings and conclude that the traditional use of the λ-ratio cannot determine the lubrication regime.

Xiaobin and Khonsari [23] has studied the transition zone from mixed to full hydrodynamic film experimentally for a small journal bearing. The Stribeck curve is established for a series of different configurations of load and lubricant temperature. To give an example, full hydrodynamic lubrication is achieved at a sliding speed of 0.2 m/s at a specific load of 1.1 MPa using SAE 5W30 at 40 °C.

3.2 Liner temperature&pressure limit

The mechanical properties of the liner compose a design limit for hydrodynamic bearings. The absolute maximum temperature of a babbitt liner is defined by its melting point. However, the mechanical strength is reduced significantly at these high temperatures and therefore the temperature limit is well below the melting point. The liner will creep when exposed to high pressure at elevated temperature. As an example for a specific alloy creep begins at 190 °C for a pressure of 1.4 MPa and at 127 °C for a pressure of 7 MPa [24]. For comparison, the yield limit for typical babbitt materials at 120 °C is 20-30 MPa [25]. Typical allowable liner temperatures for babbitt alloys are 120-200 °C [26]. The choice of babbitt alloy is a compromise between strength, ductility, ability to embed particles, behavior at mixed lubrication and temperature dependence.

Typical maximum temperatures for polymer composites, based on PTFE or PEEK, are 170 to 200 °C [25]. The creep, pressure and temperature correlation for polymers applied to bearing applications is not well described in the literature and it is difficult to give design guidelines on this.

3.3 Lubricant temperature limit

Mineral oils will rapidly oxidize if exposed to high temperatures. The lubricant degradation is a function of time of exposure and, most important, temperature since oxidation increases exponentially with temperature. Mineral oils typically oxidize excessively at temperatures above 75-80 °C [27] whereas some synthetic oils can withstand temperatures higher than 300 °C [4].

3.4 Instability limit

Lightly loaded journal bearings operating at high speeds are in danger of whirl and whip phenomena. This is due to the high cross coupling coefficients of journal bearings. For rotor-bearing-systems deemed in the danger-zone of instability a stability analysis must be performed. A widely used analytical criterion for simplified analysis is that of Routh-Hurwitz.

Tilting pad bearings and non-circular bearings like the lemon bore bearings display significantly reduced cross couping coefficients and are thus less prone to instability phenomena.

3.5 Mechanical strength limit

For moderately sized tilting pad bearings the load capacity of a conventional pivot mechanism is in the same order of magnitude as the load capacity of the oil film. Since the pivot load capacity is limited by the allowable Hertzian contact stress and that the pivot mechanism cannot be scaled up without loosing its tilting ability, large tilting pad bearings must use alternative tilting mechanisms. These are then a compromise since they often introduce resistance towards angular rotation which again reduces pad performance.

3.6 Thermal expansion limit

Radial bearings, and in less degree also thrust bearings, can seize if the clearance is consumed by difference in thermal expansion. The clearance can be increased to reduce the risk of thermal seizure, however, this will also impact the overall bearing properties since the clearance is an important design parameter. Generally a higher clearance implies:

- lower minimum film thickness
- lower stiffness and dampening coefficients
- higher flow rate
- lower viscous loss

- lower lubricant temperature

Tilting pad bearings are furthermore exposed to thermal crowning, due to differential thermal expansion, which changes pad geometry and effectively reduces the load carrying area of the pad.

Chapter 4

Wear

One of the most important failure modes for hydrodynamic bearings is wear of the bearing liner, especially for machines operating at low Reynolds numbers or machines subjected to frequent start and stop cycles. For hydrodynamic bearings the typical wear phenomena can be divided into two groups: abrasive and adhesive wear respectively. Sometimes fatigue, corrosive and chemical failure modes are also categorized as wear. These will, however, not be addressed in this work.

Generally bearing grade polymers display much improved wear properties compared to the conventional babbitt alloys.

Simmons et al. [16] give references to laboratory work and applications from hydro power plants, where exceptional low wear rates are observed using polymers, compared to babbitt. The same conclusion is drawn by McCarthy and Glavatskih [28] who study the wear and friction behavior of PTFE and babbitt at thin lubricating films.

For bearings, where the sliding pair consists of a polymer sliding against a steel surface, it is common practice to use hardened steel. This is in order to avoid abrasion of the steel surface which subsequently then continuously abrades the polymer sliding partner. Some studies has used a hardness of 700 Vickers giving good results [4],[29].

The roughness of the sliding partner for polymer bearing applications is generally required to be as low as possible, in order to reduce wear. However, it is shown that some polymers during dry sliding exhibit least wear at a specific surface roughness. For Ultra-High Molecular Weight Polyethylene a minimum amount of wear is observed at a roughness of Ra 0.2 μm [30].

4.1 Abrasive wear

Abrasive wear is one of the most dominant causes of failures in mechanical machines and causes the largest costs to industries, compared to other types of wear.

Plowing and cutting processes are both categorized as abrasive wear, where a hard particle or asperity is sliding over a surface and hereby causing damage.

For metals the primary resistance towards abrasion is hardness. Generally it is

stated that abrasive wear rate is inverse proportional to hardness. As a rule of thumb, the hardness of a surface must be at least 0.8 times the hardness of the abrasive particles or asperities in order to keep the wear rate on an acceptable level [4].

Polymers generally have increased resistance towards abrasive wear, despite their low hardness, compared to metals. Polymer surfaces tend to deform elastically instead of abrading. Furthermore, abrasion in metal to metal contacts often produce sharp particles whereas the particle or asperity will stay blunt, or at least not be sharpened, when metal is sliding against a polymer [4].

4.2 Adhesive wear

Adhesive wear is the results of micro-welds between a sliding pair when the load is so high, that contacting asperities deform and adhere to each other and thereby cause material transfer from one sliding partner to the other.

The terms galling, scuffing, scoring, or smearing are sometimes used for severe cases of adhesive wear although the terms are not strictly defined.

In general, most metals are prone to adhesive wear. Conventional babbitt alloys has improved resistance towards adhesion compared to other metals.

Most polymers adhere to other materials through van der Waals forces. Generally this form of adhesion is not strong enough for asperities to be torn off the contact and will thus not cause damage [4].

Lubricants can, through composition and additives, be designed to 'contaminate' the surfaces of the sliding pair and thereby not allow the creation of strong bonds between them and thus avoid adhesive wear.

4.3 Prediction of wear

Since wear is one of the most important failure modes for hydrodynamic bearings it is of high interest to be able to predict the wear rate reliably. It is however very difficult to quantify the expected wear with good accuracy. The λ-ratio defined in equation (3.1) can be used with reasonable confidence to evaluate if a bearing operates within the full film regime of lubrication, and thus not subjected to wear (assuming no or low contamination levels).

Back in 1961 Archard [31] suggested that the wear volume is proportional to the real contact area times the sliding distance. If we assume this simple postulate is true, it is still a demanding task to implement it in a hydrodynamic bearing simulation tool. Using the traditional form of Reynolds equation contact newer occurs because, as the minimum film thickness approaches zero the pressure, and thus the load carrying capacity, goes towards infinity.

Basically the problem of wear modeling can be broken into three steps:

- determination of the oil film pressure at thin films including surface roughness, elasticity and preferably also lubricant piezo-viscous and thermo-viscous effects
- determination of contact area and force
- determination of wear rate as a function of the properties of the contact zone

Patir and Cheng [32][33] suggest an average flow model which includes the effects of surface roughness in the pressure field using a stochastic roughness profile and hereby extends the validity of Reynolds equation to very thin films. The work of Patir and Cheng is compared to modern deterministic models by Dobrica at al. [34] and is found to correctly anticipate the effects of surface roughness.

The contact pressure is usually derived from dividing the load carrying zone into two regions: one governed by Reynolds equation, where the surfaces are fully separated and one which is governed by contact mechanics, for example using Greenwood and Tripp's [35] model for asperity contact. When using conventional models the boundary between the regions must be determined. One criteria for transition from the film zone to the contact zone is based on the film thickness. Hu and Zhu [36] present a method where Reynolds equation can be applied to both the full film zone and the contact zone, and thus circumventing the problem of defining the boundary.

Experimental data is required in order to establish the relation between the wear rate and its influencing parameters. The primary factors are the contact pressure, sliding speed and material hardness. In this context it is also interesting to mention the term *lubricity* which is used to characterize the wear properties of a given sliding pair and lubricant.

Zhu et al. [37] present a numerical implementation for prediction of sliding wear of a deterministic surface operating in the mixed lubrication regime. They apply the model for a sliding contact and compare the results qualitatively finding good correlation.

The workshop presentation by Thomsen and Klit [38], appendix E, proposes a wear model based on film thickness only. A significant advantage of this approach is that it is relatively simple to introduce into existing EHL solvers and does not require additional computational capacity. The wear model is applied using a soft EHL model to predict the wear of a compliant liner under misaligned operation and the results are compared qualitatively to experimental results finding good correlation. Due to the simplicity of the model it can only be expected to give reliable results for simulation parameters close to that of the experimental setup, for which the wear coefficients are obtained. Especially with respect to material and lubricant properties. This is, however, an inherent attribute of all wear models.

Chapter 5

Fluid film forces

In this chapter the basis for the derivation of Reynolds equations is explained and it is shown how the equation is used for finding the fluid film forces through application of finite element theory. In parallel with the derivation of the finite element equations for Reynolds equation the corresponding models for the dynamic coefficients of the film are derived using Lund's principle of perturbation.

5.1 Reynolds equation

5.1.1 Assumptions

Reynolds equation can be derived from Navier-Stokes equation assuming that the pressure and viscous terms are much more dominant than the inertia and body force terms. The Reynolds number (Re), Frode number and Euler number are used to evaluate the significance of the various terms and can be used in combination to asses the validity of the assumption.

$$\text{Reynolds number} = \frac{\text{inertia}}{\text{viscous}} \tag{5.1}$$

$$\text{Frode number} = \frac{\text{inertia}}{\text{gravity}} \tag{5.2}$$

$$\text{Euler number} = \frac{\text{pressure}}{\text{inertia}} \tag{5.3}$$

Further necessary assumptions for this work are listed below and are addressed individually in the following paragraphs.

- lubricant is Newtonian.
- flow is laminar.
- lubricant film thickness is much smaller than all other dimensions.
- fluid is iso-viscous across film thickness.

- no slip at boundaries.
- surfaces are smooth compared to film thickness.
- incompressible lubricant

Assumption on Newtonian fluid

For a Newtonian fluid the viscosity μ is proportional with the shear stress τ over the shear rate s as shown in (5.4).

$$\mu = \frac{\tau}{s} \tag{5.4}$$

This assumption is generally deemed valid for all traditional lubricants. The viscosity, and consequently shear stress, can however be functions of other parameters such as pressure and temperature while maintaining its Newtonian properties.

Assumption on laminar flow

Reynolds equation is only valid for laminar flow. If Reynolds number (5.1) exceeds 2000 [39] there is possibility of turbulent flow and the premises of Reynolds equation change. For a journal bearing the flow can be assumed as inbetween parallel plates and Reynolds number is defined as in equation (5.5):

$$\mathrm{Re} = \frac{\rho \omega R c_r}{\mu} < 2000 \tag{5.5}$$

Assumption on lubricant film thickness

Reynolds equation assumes a film thickness much smaller than all other dimensions. For bearing applications this always holds true since the film thickness is in the order of μm while other dimensions are in the order of mm.

Assumption on iso-viscous lubricant across film thickness

This is a common assumption when analyzing hydrodynamic bearings in order to reduce the size of the computational problem. However, at high specific viscous dissipations in the lubricant film the temperature, and thus also the viscosity, will vary significantly across the lubricant film thickness. Dowson [40] has shown this already in the 1960's.

For wind turbine main bearing applications the rotational speed is low inducing low specific viscous dissipation and hence temperature gradients are correspondingly small.

Assumption on no slip at boundaries

For hydrodynamic bearing applications this will always hold true. In extreme cases with extremely high sliding speed and low film thickness slip may occur. For this to happen other assumptions are also violated and Reynolds equation will not give reliable results.

Assumption on smooth surfaces

The assumption of smooth surfaces can be assessed with the λ-value given in equation (3.1). As explained earlier, it is generally accepted that the lubricant zone can be characterized as fully hydrodynamic if $\lambda > 5$. At these λ-ratios the roughnesses has only negligible effect.

Assumption on incompressibility

For oil lubricated hydrodynamic bearings this assumption is deemed valid for all cases.

5.1.2 The reduced form of Reynolds equation

Equations (5.6), (5.7) and (5.8) shows the standard reduced forms of Reynolds equation presented in Cartesian, cylindrical and polar coordinate systems respectively. The left hand side represents the Poiseuille terms whereas the two right hand terms represent the Couette and squeeze terms.

$$\frac{\partial}{\partial z}\left(\frac{h^3}{\mu}\frac{\partial p}{\partial z}\right)+\frac{\partial}{\partial y}\left(\frac{h^3}{\mu}\frac{\partial p}{\partial y}\right)=6v\frac{\partial h}{\partial y}+12\frac{\partial h}{\partial t} \tag{5.6}$$

$$\frac{1}{R}\frac{\partial}{\partial \theta}\left(\frac{h^3}{\mu R}\frac{\partial p}{\partial \theta}\right)+\frac{\partial}{\partial z}\left(\frac{h^3}{\mu}\frac{\partial p}{\partial z}\right)=6\omega\frac{\partial h}{\partial \theta}+12\frac{\partial h}{\partial t} \tag{5.7}$$

$$\frac{1}{R}\frac{\partial}{\partial \theta}\left(\frac{h^3}{\mu R}\frac{\partial p}{\partial \theta}\right)+\frac{\partial}{\partial R}\left(\frac{h^3}{\mu}\frac{\partial p}{\partial R}\right)=6\omega\frac{\partial h}{\partial \theta}+12\frac{\partial h}{\partial t} \tag{5.8}$$

Figure 5.1(a) shows the coordinate system for a full journal bearing matching the cylindrical representation of Reynolds equation. The bar denotes system coordinates $(\bar{x}, \bar{y}, \bar{z})$ whereas (x, y, z) are mesh coordinates. $\bar{z}$ is coincident with z, this is also the case for θ where no bar notation is used.

Figure 5.1(b) shows the unwrapped mesh coordinate system, here shown with equidistant node layout. The x-coordinate represents the film thickness direction.

The basic film geometry for a full journal bearing, as illustrated in figure 5.1(a), is calculated using equation (5.9). In this form the film thickness is only a function of the journal's position in the bearing $(\bar{x}, \bar{y})$ and the radial clearance c_r. The equation can be modified to include misalignment, grooves or pockets for oil in- and outlet and other geometrical features.

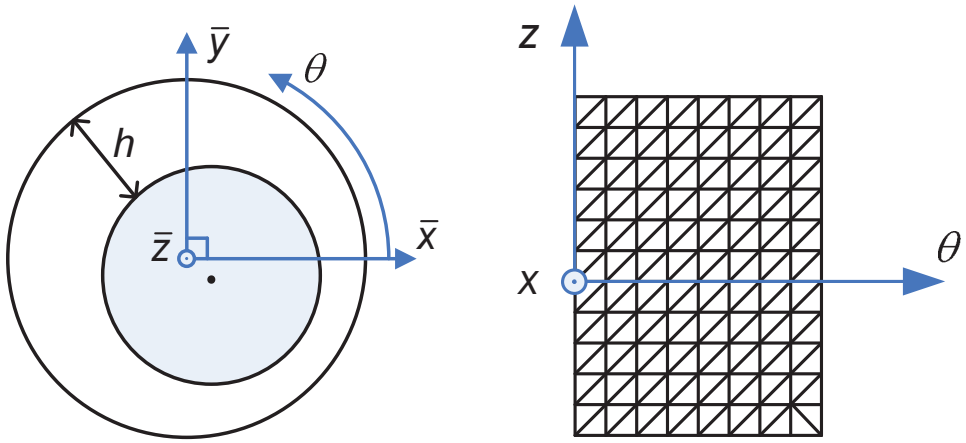

(a) System coordinates (b) Mesh coordinates

Figure 5.1: Coordinate systems for cylindrical representation

$$h = c_r - \bar{x}\cos(\theta) - \bar{y}\sin(\theta) \tag{5.9}$$

5.1.3 Viscous friction and flow

The lubricant velocity components v across the film thickness is expressed in equation (5.10) and (5.11). The tangential flow rate (5.10) includes contributions from Poiseuille and Couette flow whereas the axial side flow (5.11) only contains the Poiseuille flow.

$$v_\theta = \frac{(x-h)\,x}{2\mu R}\frac{\partial p}{\partial \theta} + \omega R\frac{x}{h} \tag{5.10}$$

$$v_z = \frac{(x-h)\,x}{2\mu}\frac{\partial p}{\partial z} \tag{5.11}$$

Figure 5.2 shows the fully developed Poiseuille and Couette velocity profiles as well as the combined velocity across the film thickness.

The lubricant volume flow rate q per unit width is calculated by integration of the lubricant velocity over the lubricant film height:

$$q'_\theta = \int_0^h (v_\theta)\,dx = -\frac{h^3}{12\mu R}\frac{\partial p}{\partial \theta} + \frac{\omega R}{2}h \tag{5.12}$$

$$q'_z = \int_0^h (v_z)\,dx = -\frac{h^3}{12\mu}\frac{\partial p}{\partial z} \tag{5.13}$$

The power loss P is derived multiplying the sliding speed ωR with the shear stress τ in sliding direction at the journal surface ($x = h$) integrated over the bearing

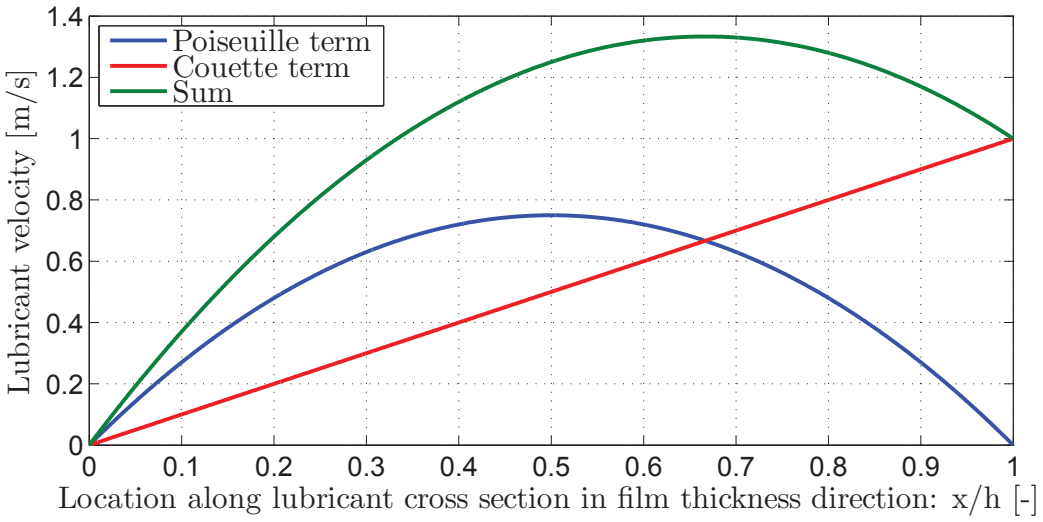

Figure 5.2: Velocity profiles along lubricant cross section (film height)

area Ω. From equation (5.4) we know that the shear stress in a Newtonian fluid is equal to the fluid viscosity times the shear rate where the later can be expressed using the derivative of (5.10). This is then combined into equation (5.14) expressing the viscous power loss in a journal bearing.

$$\begin{aligned} P &= \omega R \int_{\Omega} \left(\tau_{x\theta}\left(x=h\right)\right) d\Omega \\ &= \omega R \int_{\Omega} \left(\mu \frac{\partial v_{\theta}\left(x=h\right)}{\partial x}\right) d\Omega \\ &= \omega R \int_{\Omega} \left(\frac{h}{2R}\frac{\partial p}{\partial \theta} + \frac{\mu \omega R}{h}\right) d\Omega \end{aligned} \tag{5.14}$$

5.2 Dynamic coefficients

In this section it is shown how Lund's principle of infinitesimally small perturbation [41] is used for finding the linearized dynamic coefficients.

The dynamic coefficients can be used for stability analysis. A simplified approach is the Routh-Hurwitz criterion of stability. If this simplified approach indicates an unstable condition, and hence a large journal orbit, the dynamic forces cannot be assumed proportional to the displacements. In this case the dynamic coefficients cannot be assumed linear and one must perform an integration in time in order to find the dynamic response of the bearing and finally evaluate if the resulting orbit violates a specified critical threshold. This limit is also referred to as *limit-cycle*.

An alternative method for calculating the dynamic coefficients is to perform finite perturbations to the journal position and velocity, this is however associated with

extra computational efforts since perturbation is required in all dimensions and its derivatives in time. Furthermore, since the problem is not linear, the magnitude of perturbation will influence the accuracy of the solution. Qiu and Tieu [42] has studied this subject and finds that the method of finite perturbation converges to that of infinitesimally small perturbation if the perturbation magnitude is sufficiently small. They also give guidelines on how to select perturbation amplitudes.

For this work the thermo- and elastohydrodynamic effects are assumed constant at the state of perturbation. This implies that the oil film characteristics account for the most significant parts of the stiffness and damping properties of the bearing. Kuznetsov and Glavatskih [43] have included the elasticity of a compliant liner in the calculation of the dynamic coefficients. They have, however, not compared their method with the traditional assumption of constant thermo- and elastohydrodynamic conditions at the state of perturbation.

As explained, the equations for calculating the dynamic coefficients are derived using Lund's principle of infinitesimally small perturbation. Reynolds equation (5.7) and the expression for the film thickness (5.9) are perturbed with respect to journal center position and velocity using equation (5.15).

$$\begin{aligned} \bar{x} &= \bar{x}_0 + \Delta\bar{x} \\ \bar{y} &= \bar{y}_0 + \Delta\bar{y} \\ \dot{\bar{x}} &= \dot{\bar{x}}_0 + \Delta\dot{\bar{x}} \\ \dot{\bar{y}} &= \dot{\bar{y}}_0 + \Delta\dot{\bar{y}} \\ \Delta\bar{x}, \Delta\bar{y}, \Delta\dot{\bar{x}}, \Delta\dot{\bar{y}} &\ll 1 \end{aligned} \tag{5.15}$$

The solution for p at this perturbed condition around the known solution p_0 can then be approximated using a Taylor expansion if the derivatives of the pressure with respect to the perturbation dimensions are known:

$$\begin{aligned} p =& p_0 + \Delta\bar{x}\frac{\partial p}{\partial \bar{x}} + \Delta\bar{y}\frac{\partial p}{\partial \bar{y}} + \Delta\dot{\bar{x}}\frac{\partial p}{\partial \dot{\bar{x}}} + \Delta\dot{\bar{y}}\frac{\partial p}{\partial \dot{\bar{y}}} \\ &+ \frac{\Delta\bar{x}^2}{2!}\frac{\partial^2 p}{\partial \bar{x}^2} + \frac{\Delta\bar{y}^2}{2!}\frac{\partial^2 p}{\partial \bar{y}^2} + \frac{\Delta\dot{\bar{x}}^2}{2!}\frac{\partial^2 p}{\partial \dot{\bar{x}}^2} + \frac{\Delta\dot{\bar{y}}^2}{2!}\frac{\partial^2 p}{\partial \dot{\bar{y}}^2} + ... \end{aligned} \tag{5.16}$$

Assuming that the perturbations are small only the first order terms are significant giving equation (5.17) when using the notation $\partial p/\partial i = p_i$ for the derivatives of the pressure. The linearization of the dynamic coefficients originates from the neglection of higher order terms of the perturbation.

$$p = p_0 + \Delta\bar{x}p_{\bar{x}} + \Delta\bar{y}p_{\bar{y}} + \Delta\dot{\bar{x}}p_{\dot{\bar{x}}} + \Delta\dot{\bar{y}}p_{\dot{\bar{y}}} \tag{5.17}$$

The perturbed expression of the film thickness and its derivatives, equations (5.18) to (5.20), are inserted into Reynolds equation (5.7) giving equation (5.21). The derivative of h_0 is not expanded in order to allow for alternative expressions for the initial film thickness, e.g. a lemon bore geometry or similar.

$$h = \underbrace{c_r - \bar{x}\cos(\theta) - \bar{y}\sin(\theta)}_{h_0} - \Delta\bar{x}\cos(\theta) - \Delta\bar{y}\sin(\theta) \tag{5.18}$$

$$\frac{\partial h}{\partial \theta} = \frac{\partial h_0}{\partial \theta} + \Delta\bar{x}\sin(\theta) - \Delta\bar{y}\cos(\theta) \tag{5.19}$$

$$\frac{\partial h}{\partial t} = -\left(\dot{\bar{x}}_0 + \Delta\dot{\bar{x}}\right)\cos(\theta) - \left(\dot{\bar{y}}_0 + \Delta\dot{\bar{y}}\right)\sin(\theta) \tag{5.20}$$

$$\begin{aligned}\frac{1}{R}\frac{\partial}{\partial\theta}\left(\frac{h_0^3}{\mu R}\frac{\partial p}{\partial\theta}\right) + \frac{\partial}{\partial z}\left(\frac{h_0^3}{\mu}\frac{\partial p}{\partial z}\right) = 6\omega\left[\frac{\partial h_0}{\partial\theta} + \Delta\bar{x}\sin(\theta) - \Delta\bar{x}\cos(\theta)\right] \\ -12\left[\left(\dot{\bar{x}}_0 + \Delta\dot{\bar{x}}\right)\cos(\theta) + \left(\dot{\bar{y}}_0 + \Delta\dot{\bar{y}}\right)\sin(\theta)\right]\end{aligned} \tag{5.21}$$

Equation (5.17) is then inserted into (5.21) and the equation is separated with respect to the perturbations and keeping only the first order perturbation terms:

$$\begin{aligned}&\frac{1}{R}\frac{\partial}{\partial\theta}\left(\frac{h_0^3}{\mu R}\frac{\partial p_i}{\partial\theta}\right) + \frac{\partial}{\partial z}\left(\frac{h_0^3}{\mu}\frac{\partial p_i}{\partial z}\right) = \\ &\begin{cases} 6\omega\frac{\partial h_0}{\partial\theta} - 12\left[\dot{\bar{x}}_0\cos(\theta) + \dot{\bar{y}}_0\sin(\theta)\right] & , p_i = p_0 \\ \frac{1}{R}\frac{\partial}{\partial\theta}\left(\frac{3h_0^2\cos(\theta)}{\mu R}\frac{\partial p_0}{\partial\theta}\right) + \frac{\partial}{\partial z}\left(\frac{3h_0^2\cos(\theta)}{\mu}\frac{\partial p_0}{\partial z}\right) + 6\omega\sin(\theta) & , p_i = p_{\bar{x}} \\ \frac{1}{R}\frac{\partial}{\partial\theta}\left(\frac{3h_0^2\sin(\theta)}{\mu R}\frac{\partial p_0}{\partial\theta}\right) + \frac{\partial}{\partial z}\left(\frac{3h_0^2\sin(\theta)}{\mu}\frac{\partial p_0}{\partial z}\right) - 6\omega\cos(\theta) & , p_i = p_{\bar{y}} \\ -12\cos(\theta) & , p_i = p_{\dot{\bar{x}}} \\ -12\sin(\theta) & , p_i = p_{\dot{\bar{y}}} \end{cases}\end{aligned} \tag{5.22}$$

Equation (5.22) is used to solve for the pressure distribution p_0 and its derivatives with respect to the perturbation dimensions. Finally the resulting oil film force components and dynamic coefficients are found through integration using equation (5.23) to (5.27).

$$\begin{Bmatrix} F_{\bar{x}} \\ F_{\bar{y}} \end{Bmatrix} = R\int_{-L/2}^{+L/2}\int_0^{2\pi} p_0 \begin{Bmatrix} \cos(\theta) \\ \sin(\theta) \end{Bmatrix} d\theta dz \tag{5.23}$$

$$\mathbf{K} = \begin{bmatrix} k_{\bar{x}\bar{x}} & k_{\bar{x}\bar{y}} \\ k_{\bar{y}\bar{x}} & k_{\bar{y}\bar{y}} \end{bmatrix} \tag{5.24}$$

$$\begin{aligned}\begin{Bmatrix} k_{\bar{x}\bar{x}} \\ k_{\bar{y}\bar{x}} \end{Bmatrix} &= R\int_{-L/2}^{+L/2}\int_0^{2\pi} p_x \begin{Bmatrix} \cos(\theta) \\ \sin(\theta) \end{Bmatrix} d\theta dz \\ \begin{Bmatrix} k_{\bar{x}\bar{y}} \\ k_{\bar{y}\bar{y}} \end{Bmatrix} &= R\int_{-L/2}^{+L/2}\int_0^{2\pi} p_y \begin{Bmatrix} \cos(\theta) \\ \sin(\theta) \end{Bmatrix} d\theta dz\end{aligned} \tag{5.25}$$

$$\mathbf{D} = \begin{bmatrix} d_{\bar{x}\bar{x}} & d_{\bar{x}\bar{y}} \\ d_{\bar{y}\bar{x}} & d_{\bar{y}\bar{y}} \end{bmatrix} \tag{5.26}$$

$$\begin{aligned} \begin{Bmatrix} d_{\bar{x}\bar{x}} \\ d_{\bar{y}\bar{x}} \end{Bmatrix} &= R\int_{-L/2}^{+L/2}\int_{0}^{2\pi} p_{\dot{x}} \begin{Bmatrix} \cos(\theta) \\ \sin(\theta) \end{Bmatrix} d\theta dz \\ \begin{Bmatrix} d_{\bar{x}\bar{y}} \\ d_{\bar{y}\bar{y}} \end{Bmatrix} &= R\int_{-L/2}^{+L/2}\int_{0}^{2\pi} p_{\dot{y}} \begin{Bmatrix} \cos(\theta) \\ \sin(\theta) \end{Bmatrix} d\theta dz \end{aligned} \tag{5.27}$$

Ultimately the force equilibrium equation can be assembled where W is the external load to be counterbalanced by the oil film forces and inertia as shown in (5.28).

$$\begin{Bmatrix} W_{\bar{x}} \\ W_{\bar{y}} \end{Bmatrix} + \begin{Bmatrix} F_{\bar{x}} \\ F_{\bar{y}} \end{Bmatrix} = \begin{Bmatrix} W_{\bar{x}} \\ W_{\bar{y}} \end{Bmatrix} + \mathbf{K}\begin{Bmatrix} \bar{x} \\ \bar{y} \end{Bmatrix} + \mathbf{D}\begin{Bmatrix} \dot{\bar{x}} \\ \dot{\bar{y}} \end{Bmatrix} + \mathbf{M}\begin{Bmatrix} \ddot{\bar{x}} \\ \ddot{\bar{y}} \end{Bmatrix} = \begin{Bmatrix} 0 \\ 0 \end{Bmatrix} \tag{5.28}$$

For this work accelerations are assumed negligible and hence the mass term cancels out.

5.3 Finite element formulation

In this chapter the derivation of the finite elements equations matching Reynolds equation and the corresponding perturbed equations (5.22) is explained.

5.3.1 Variational principle

The variational approach, also used by Booker and Huebner [44], is used to derive the element equations equivalent to equations (5.22). Functionals F_i (5.29) corresponding to the equations must be found so that they extremize the equations for which a solution is searched for (5.22). This is ensured when the Euler-Lagrange equation (5.30) is satisfied. Equation (5.31) can then be used to to solve for the stationary nodal values.

$$I_i = \int_A F_i d\Omega \quad , \quad i = 0, \bar{x}, \bar{y}, \dot{\bar{x}}, \dot{\bar{y}} \tag{5.29}$$

$$\frac{\partial F}{\partial p_i} - \frac{\partial}{\partial \theta}\left(\frac{\partial F}{\partial \frac{\partial p_i}{\partial \theta}}\right) - \frac{\partial}{\partial z}\left(\frac{\partial F}{\partial \frac{\partial p_i}{\partial z}}\right) = 0 \quad , \quad i = 0, \bar{x}, \bar{y}, \dot{\bar{x}}, \dot{\bar{y}} \tag{5.30}$$

$$\begin{aligned} \frac{\partial I_i}{\partial p_{i_j}} &= \int_\Omega \frac{\partial F_i}{\partial p_{i_j}} d\Omega = 0 \quad , \quad i = 0, \bar{x}, \bar{y}, \dot{\bar{x}}, \dot{\bar{y}} \\ &j \text{ indicates the nodal number of the element.} \end{aligned} \tag{5.31}$$

The functionals (5.32) satisfying the Euler-Lagrange equation are found using educated guesses together with trial'n'error.

$$F_i = \frac{h^3}{2\mu}\left(\left(\frac{1}{R}\frac{\partial p_i}{\partial \theta}\right)^2 + \left(\frac{\partial p_i}{\partial z}\right)^2\right)$$

$$\begin{cases} -\left(6\omega h_0 - 12\dot{\bar{x}}_0 \sin(\theta) + 12\dot{\bar{y}}_0 \cos(\theta)\right)\frac{\partial p_0}{\partial \theta} & , p_i = p_0 \\ +\left(-\frac{3h_0^2\cos(\theta)}{\mu R^2}\frac{\partial p_0}{\partial \theta} + 6\omega\cos(\theta)\right)\frac{\partial p_{\bar{x}}}{\partial \theta} - \frac{3h_0^2\cos(\theta)}{\mu}\frac{\partial p_0}{\partial z}\frac{\partial p_{\bar{x}}}{\partial z} & , p_i = p_{\bar{x}} \\ +\left(-\frac{3h_0^2\sin(\theta)}{\mu R^2}\frac{\partial p_0}{\partial \theta} + 6\omega\sin(\theta)\right)\frac{\partial p_{\bar{y}}}{\partial \theta} - \frac{3h_0^2\sin(\theta)}{\mu}\frac{\partial p_0}{\partial z}\frac{\partial p_{\bar{y}}}{\partial z} & , p_i = p_{\bar{y}} \\ +12\sin(\theta)\frac{\partial p_{\dot{\bar{x}}}}{\partial \theta} & , p_i = p_{\dot{\bar{x}}} \\ -12\cos(\theta)\frac{\partial p_{\dot{\bar{y}}}}{\partial \theta} & , p_i = p_{\dot{\bar{y}}} \end{cases} \tag{5.32}$$

(5.32) are then inserted into (5.31) giving the element equations for a single element prior to inserting interpolation functions. A set of equations are constructed for every node j in the element:

$$\int_\Omega \frac{\partial F_i}{\partial p_{i_j}} d\Omega = 0 = \int_\Omega \left[\frac{h_0^3}{\mu}\left(\frac{1}{R^2}\frac{\partial p_i}{\partial \theta}\frac{\partial}{\partial \theta}\left(\frac{\partial p_i}{\partial p_{i_j}}\right) + \frac{\partial p_i}{\partial z}\frac{\partial}{\partial z}\left(\frac{\partial p_i}{\partial p_{i_j}}\right)\right)\right.$$

$$\begin{cases} -\left(6\omega h_0 - 12\dot{x}_0\sin(\theta) + 12\dot{y}_0\cos(\theta)\right)\frac{\partial}{\partial \theta}\left(\frac{\partial p_0}{\partial p_{0_j}}\right)\Big] d\Omega & , p_i = p_0 \\ +\left(-\frac{3h_0^2\cos(\theta)}{\mu R^2}\frac{\partial p_0}{\partial \theta} + 6\omega\cos(\theta)\right)\frac{\partial}{\partial \theta}\left(\frac{\partial p_{\bar{x}}}{\partial p_{\bar{x}_j}}\right) - \frac{3h_0^2\cos(\theta)}{\mu}\frac{\partial p_0}{\partial z}\frac{\partial}{\partial z}\left(\frac{\partial p_{\bar{x}}}{\partial p_{\bar{x}_j}}\right)\Big] d\Omega & , p_i = p_{\bar{x}} \\ +\left(-\frac{3h_0^2\sin(\theta)}{\mu R^2}\frac{\partial p_0}{\partial \theta} + 6\omega\sin(\theta)\right)\frac{\partial}{\partial \theta}\left(\frac{\partial p_{\bar{y}}}{\partial p_{\bar{y}_j}}\right) - \frac{3h_0^2\sin(\theta)}{\mu}\frac{\partial p_0}{\partial z}\frac{\partial}{\partial z}\left(\frac{\partial p_{\bar{y}}}{\partial p_{\bar{y}_j}}\right)\Big] d\Omega & , p_i = p_{\bar{y}} \\ +12\sin(\theta)\frac{\partial}{\partial \theta}\left(\frac{\partial p_{\dot{\bar{x}}}}{\partial p_{\dot{\bar{x}}_j}}\right)\Big] d\Omega & , p_i = p_{\dot{\bar{x}}} \\ -12\cos(\theta)\frac{\partial}{\partial \theta}\left(\frac{\partial p_{\dot{\bar{y}}}}{\partial p_{\dot{\bar{y}}_j}}\right)\Big] d\Omega & , p_i = p_{\dot{\bar{y}}} \end{cases} \tag{5.33}$$

5.3.2 Interpolation functions

Three-node triangular elements are used for the element formulation along with linear interpolation functions N. Using the interpolation functions any field variable ϕ inside an element can be evaluated at any point in the element using equation (5.34) where m represents the respective node numbers:

$$\phi = \sum_{m=1}^{3} N_m \phi_m \tag{5.34}$$

The linear interpolation functions, derived in [45], and their derivatives, using natural coordinates, are shown in equation (5.35) and (5.36):

$$N_j = \frac{1}{2A}\left(a_j + b_j R\theta + c_j z\right) \tag{5.35}$$

$$\begin{aligned}\frac{\partial N_j}{\partial \theta} &= \frac{R}{2A} b_j \\ \frac{\partial N_j}{\partial z} &= \frac{1}{2A} c_j\end{aligned} \tag{5.36}$$

A characteristic of the interpolation function is that the sum at any point inside the element is 1:

$$\sum_{m=1}^{3} N_m = 1 \tag{5.37}$$

The calculation of the element area A and definition of the coefficients a, b, and c is shown in equation (5.38) and (5.39).

$$A = \frac{R}{2} \begin{vmatrix} 1 & \theta_1 & z_1 \\ 1 & \theta_2 & z_2 \\ 1 & \theta_3 & z_3 \end{vmatrix} \tag{5.38}$$

$$\begin{array}{lll} a_1 = R\left(\theta_2 z_3 - \theta_3 z_2\right) & b_1 = z_2 - z_3 & c_1 = R\left(\theta_3 - \theta_2\right) \\ a_2 = R\left(\theta_3 z_1 - \theta_1 z_3\right) & b_2 = z_3 - z_1 & c_2 = R\left(\theta_1 - \theta_3\right) \\ a_3 = R\left(\theta_1 z_2 - \theta_2 z_1\right) & b_3 = z_1 - z_2 & c_3 = R\left(\theta_2 - \theta_1\right) \end{array} \tag{5.39}$$

Equation (5.34) is then used to calculate the derivatives of a field variable ϕ:

$$\begin{aligned}\frac{\partial \phi}{\partial \theta} &= \sum_{m=1}^{3} \frac{\partial \phi}{\partial N_m} \frac{\partial N_m}{\partial \theta} = \sum_{m=1}^{3} \phi_m \frac{\partial N_m}{\partial \theta} \\ \frac{\partial \phi}{\partial z} &= \sum_{m=1}^{3} \frac{\partial \phi}{\partial N_m} \frac{\partial N_m}{\partial z} = \sum_{m=1}^{3} \phi_m \frac{\partial N_m}{\partial z}\end{aligned} \tag{5.40}$$

When introducing the interpolation functions into the functionals (5.33) the following expressions are also needed:

$$\begin{aligned}\frac{\partial}{\partial \theta}\left(\frac{\partial \phi}{\partial \phi_j}\right) &= \frac{\partial N_j}{\partial \theta} \\ \frac{\partial}{\partial z}\left(\frac{\partial \phi}{\partial \phi_j}\right) &= \frac{\partial N_j}{\partial z}\end{aligned} \tag{5.41}$$

5.3.3 Derivation of element equations

In order to find the element equations (5.40) and (5.41) are inserted into (5.33):

$$\frac{\partial I_i}{\partial p_{i_j}} = \int_\Omega \frac{\partial F_i}{\partial p_{i_j}} d\Omega = \int_\Omega \left[\frac{h_0^3}{\mu} \left(\frac{1}{R^2} \sum_{m=1}^{3} \left(p_{i_m} \frac{\partial N_m}{\partial \theta} \right) \frac{\partial N_j}{\partial \theta} + \sum_{m=1}^{3} \left(p_{i_m} \frac{\partial N_m}{\partial z} \right) \frac{\partial N_j}{\partial z} \right) \right.$$

$$\begin{cases} \left. - \left(6\omega h_0 - 12\dot{\bar{x}}_0 \sin\theta + 12\dot{\bar{y}}_0 \cos\theta\right) \frac{\partial N_j}{\partial \theta} \right] d\Omega & p_i = p_0 \\ \left(-\frac{3h_0^2 \cos\theta}{\mu R^2} \sum_{m=1}^{3} \left(p_{0_m} \frac{\partial N_m}{\partial \theta} \right) + 6\omega \cos\theta \right) \frac{\partial N_j}{\partial \theta} - \frac{3h_0^2 \cos\theta}{\mu} \sum_{m=1}^{3} \left(p_{0_m} \frac{\partial N_m}{\partial z} \right) \frac{\partial N_j}{\partial z} \Bigg] d\Omega & p_i = p_{\bar{x}} \\ \left(-\frac{3h_0^2 \sin\theta}{\mu R^2} \sum_{m=1}^{3} \left(p_{0_m} \frac{\partial N_m}{\partial \theta} \right) + 6\omega \sin\theta \right) \frac{\partial N_j}{\partial \theta} - \frac{3h_0^2 \sin\theta}{\mu} \sum_{m=1}^{3} \left(p_{0_m} \frac{\partial N_m}{\partial z} \right) \frac{\partial N_j}{\partial z} \Bigg] d\Omega & p_i = p_{\bar{y}} \\ \left. 12 \sin\theta \frac{\partial N_j}{\partial \theta} \right] d\Omega & p_i = p_{\dot{\bar{x}}} \\ \left. -12 \cos\theta \frac{\partial N_j}{\partial \theta} \right] d\Omega & p_i = p_{\dot{\bar{y}}} \end{cases}$$

and j=1,2,3 (5.42)

The interpolation functions (5.35) and their derivatives (5.36) are inserted into (5.42) and the system of equations is set up for for all nodes j giving equations (5.43) to (5.49). For simplicity the equations are shown before integration over the element is performed.

$$\underset{3\times3}{\left[\mathbf{H}_{i_{jk}}\right]} \underset{3\times1}{\left\{p_{i_j}\right\}} = \underset{3\times1}{\left\{V_{i_j}\right\}}$$

where

$i = 0, \bar{x}, \bar{y}, \dot{\bar{x}}, \dot{\bar{y}}$

$j = 1, 2, 3$

$k = 1, 2, 3$ (5.43)

$$\left[\mathbf{H}_{i_{jk}}\right] = \int_\Omega \left[\frac{h_0^3}{4\mu A^2} \left(b_j b_k + c_j c_k \right) \right] d\Omega \tag{5.44}$$

It is seen from equation (5.44) that the fluidity matrix $\mathbf{H}$ is symmetric. This can be used with advantage by assembling only the upper triangular part of $\mathbf{H}$ when solving equation (5.43) and hereby reduce memory requirements and increase performance of the solver.

$$\left\{V_{0_j}\right\} = \int_\Omega \left\{ \frac{3Rb_j}{A} \left(\omega h_0 - 2\dot{\bar{x}}_0 \sin(\theta) + 2\dot{\bar{y}}_0 \cos(\theta) \right) \right\} d\Omega \tag{5.45}$$

$$\begin{aligned} \left\{V_{x_j}\right\} = \int_\Omega \Bigg\{ & \left(\frac{3h_0^2 \cos(\theta)}{\mu R^2} \sum_{m=1}^{3} \left(p_{0_m} \frac{R}{2A} b_m \right) - 6\omega \cos(\theta) \right) \frac{R}{2A} b_j \\ & + \frac{3h_0^2 \cos(\theta)}{\mu} \sum_{m=1}^{3} \left(p_{0_m} \frac{1}{2A} c_m \right) \frac{1}{2A} c_j \Bigg\} d\Omega \end{aligned} \tag{5.46}$$

$$\begin{aligned}\left\{V_{y_j}\right\} = \int_\Omega \Bigg\{ &\left(\frac{3h_0^2 \sin(\theta)}{\mu R^2} \sum_{m=1}^{3} \left(p_{0_m} \frac{R}{2A} b_m \right) - 6\omega \sin(\theta) \right) \frac{R}{2A} b_j \\ &+ \frac{3h_0^2 \sin(\theta)}{\mu} \sum_{m=1}^{3} \left(p_{0_m} \frac{1}{2A} c_m \right) \frac{1}{2A} c_j \Bigg\} d\Omega \end{aligned} \tag{5.47}$$

$$\left\{V_{\dot{x}_j}\right\} = \int_\Omega \left\{ -12 \sin(\theta) \frac{R}{2A} b_j \right\} d\Omega \tag{5.48}$$

$$\left\{V_{\dot{y}_j}\right\} = \int_\Omega \left\{ 12 \cos(\theta) \frac{R}{2A} b_j \right\} d\Omega \tag{5.49}$$

5.3.4 Integration of field variables

Integration over the element is performed using Gauss integration. Three-node triangular elements have only one Gauss point and thus the integration of a single field variable over the element area presented by equation (5.50) is straight forward:

$$\int_\Omega \phi d\Omega = \frac{A}{3} \sum_{m=1}^{3} \phi_m \tag{5.50}$$

For terms including products of field variables equation (5.51) presents a convenient method:

$$\int_\Omega N_1^\alpha N_2^\beta N_3^\gamma d\Omega = \frac{\alpha!\beta!\gamma!}{(\alpha+\beta+\gamma+2)!} 2A \tag{5.51}$$

Equation (5.51) is used to integrate ϕ^2 over the element area. This is done by expanding the sums and products of the interpolation functions and finally applying (5.51) for integration:

$$\begin{aligned}\int_\Omega \phi^2 d\Omega &= \int_\Omega \left(\sum_{m=1}^{3} \phi_m N_m \right)^2 d\Omega \\ &= \int_\Omega \left(2N_1N_2\phi_1\phi_2 + 2N_1N_3\phi_1\phi_3 + 2N_2N_3\phi_2\phi_3 \right. \\ &\quad \left. + N_1^2\phi_1^2 + N_2^2\phi_2^2 + N_3^2\phi_3^2 \right) d\Omega \\ &= \frac{A}{12} \left(\left(\sum_{m=1}^{3} \phi_m \right)^2 + \sum_{m=1}^{3} \phi_m^2 \right)\end{aligned} \tag{5.52}$$

Same procedure is applied for ϕ^3 and $\phi^2\psi$ giving equations (5.53) and (5.54)

$$\int_\Omega \phi^3 d\Omega = \frac{A}{10}\left(\left(\sum_{m=1}^{3}\phi_m\right)\left(\sum_{m=1}^{3}\phi_m^2\right) + \prod_{m=1}^{3}\phi_m\right) \tag{5.53}$$

$$\begin{aligned}\int_\Omega \phi^2\psi d\Omega =& \frac{A}{30}\left(\left(\sum_{m=1}^{3}\phi_m\right)^2\left(\sum_{m=1}^{3}\psi_m\right) + \left(2\sum_{m=1}^{3}\phi_m^2\psi_m\right)\right. \\ &\left. - (\phi_1\phi_2\psi_3 + \phi_1\phi_3\psi_2 + \phi_2\phi_3\psi_1)\right)\end{aligned} \tag{5.54}$$

5.4 Temperature-viscosity relation

The Walther and McCoull [46] expression (5.55) is used to describe the temperature and viscosity correlation. Please note the special units used for this expression.

$$\log\log(\nu + a) = b - n\log(T) \tag{5.55}$$

ν is kinematic viscosity in mm^2/s
T is temperature in K
$a = 0.7$ when ν>2 mm^2/s
b, n constants of the lubricant

The relation between kinematic and dynamic viscosity is defined as shown in (5.56):

$$\mu = \nu\rho \tag{5.56}$$

The term *viscosity index* is also used to state the viscosity-temperature dependency of a fluid. In qualitatively terms a lubricant's viscosity-temperature dependency decreases with increasing viscosity index. Generally synthetic oils have higher viscosity index compared to mineral based oils [47].

5.5 Pressure-viscosity relation

Oil possesses a piezo-viscous property where the viscosity changes with pressure. It does however only start to have an influence when pressures reach that of rolling element bearings, i.e. in the GPa range. At extreme pressures the viscosity can reach values where an oil film can be maintained even in a non-conformal contact zone at high forces, such as in a rolling element bearing. When included in elasto-hydrodynamics the lubrication regime is said to shift from soft EHD to hard EHD because the roller and raceway, in the case of a rolling element bearing, will now see pressures where the oil pressure reaches levels where deformation of the contact bodies is significant.

One approach for including the piezo-viscous effect is that of Barus [48] shown in (5.57), where ξ is a pressure-viscosity coefficient:

$$\ln\left(\frac{\mu}{\mu_0}\right) = \xi p \tag{5.57}$$

Although the Barus formula, which excels in its simplicity, is extensively used it is not considered very accurate. The work of Roelands [49] is considered a much better approximation. Roelands furthermore suggests an expression which includes both the pressure- and temperature effects.

For this work viscosity is considered to vary with temperature only. All other fluid properties are considered constant.

5.6 Boundary conditions and cavitation

The general boundary condition for all nodes located at the edges of the bearing, and thus separating the bearing area from the ambient environment, is a pressure of zero. Pressures below this levels is referred to as negative pressures, although the absolute pressures are naturally positive.

Cavitation occurs due to the lubricant's inability to endure pressures below the ambient one. Cavitation can take place in one or more of the following phenomena:

- air coming from the external environment may enter the bearing at the boundary nodes due to lower pressure in the bearing lubricant. Hereby pressure is equalized.
- lubricant pressure is below the vapour pressure of either the lubricant or gases dissolved in it. The lubricant or gases then vaporize and thereby equalizes pressure to that of the vapour pressure.

The iterative procedure shown in figure 5.3 is used to define the cavitated region. In each iteration the Reynolds equation (5.7) is solved to solve for the pressure p. Nodes with negative pressures are identified and a pressure value of zero is enforced on the regions with the lowest pressure. This procedure is repeated until no nodes exhibit negative pressures and no nodes continuously changes back and forth between cavitated and non-cavitated state.

It is possible, especially when the cavitation algorithm is coupled with elasto- or thermohydrodynamics, that a number of nodes continuously change back and forth from cavitated to non-cavitated status. To account for this a counter n_j is introduced. It keeps track of the number of times n every node j has changed cavitation status. If the number of occurrences passes 10 the node will have its status permanently set to cavitated until the calling function is converged.

The algorithm uses a fixed mesh and this gives a slightly non-conservative result because the cavitated region is underestimated. The error depends on the size of the

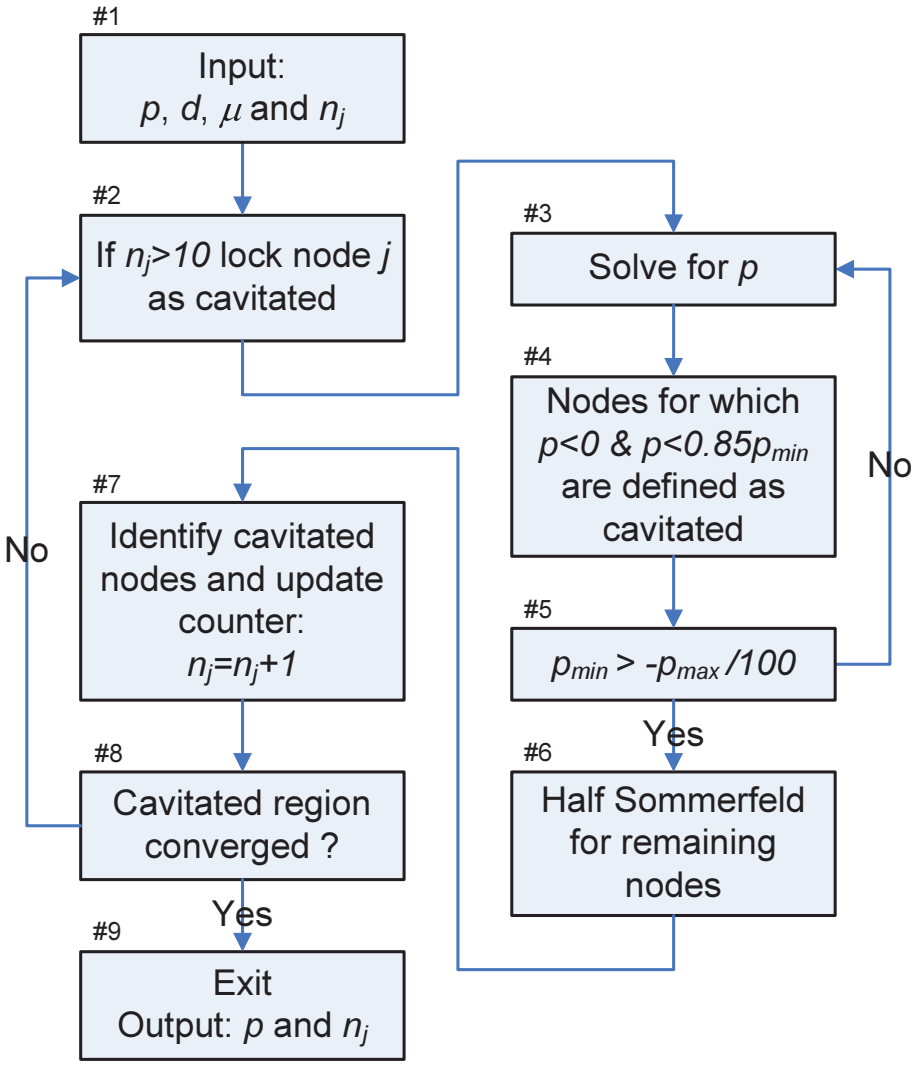

Figure 5.3: Algorithm for defining cavitated region

elements and the maximum error (in area) is the sum of areas for all elements which have at least 1 but not all nodes in the cavitated region. Adaptive meshes can be implemented to eliminate this error.

Linear three-node triangular elements are used and thus Reynolds boundary condition, for which the pressure gradient is zero at the onset of cavitation, cannot be fulfilled.

An important comment regarding the described algorithm is that it does not ensure mass-equilibrium. Hereby the algorithm can underestimate the cavitated region of the bearing. Care needs to be taken for highly dynamically loaded bearings in which the journal rapidly changes direction and also bearing designs without axial oil supply grooves. Kumar and Booker [50] suggest a cavitation algorithm which ensures mass conservation.

Chapter 6

Elasticity

As briefly mentioned earlier in this work, the elasticity of the bearing and journal can have a significant impact on the tribological properties of a hydrodynamic bearing. This is for example evident from the work of Garnier et al. [51] who analyze the hydrodynamic bearings of a four cylinder automotive engine. It is concluded that the modern light weight engines deform excessively under operation. This requires the use of elastohydrodynamic models in order to reliably predict bearing performance.

Desbordes et al. [52] compare the response of a dynamically loaded radial tilting-pad bearing using different stiffness approaches. They find a significant difference when assuming the pads as infinity stiff, compared to using a full 3-dimensional elastic model.

McIvor and Fenner [53][54] have studied elastohydrodynamics and done an extensive work on the implementation of Newthon-Raphson methods which allows for rapid computational convergence when coupling elasticity and hydrodynamics.

In the following sections two different approaches for implementing elasticity in the oil film calculations are described. The first approach uses an analytical expression to include the effects of a compliant liner whereas the second method derives the Newton-Raphson method allowing the full elasticity of bearings and surrounding structure to be implemented.

The work presented in appendix B relies on the analytical approach and studies the influence of compliant liners for highly dynamically loaded bearings while the work presented in appendix C and D are based on the full elastic model.

6.1 Modeling compliant liner using column model

The column model shown in equation (6.1) can be used for bearings with compliant liners. Only the liner is modeled and the supporting structure is regarded as infinity stiff. The model is adequate for representing bearings with polymer liners operating at moderate loads where the supporting structure does not deform significantly under the lubricant pressure. Even though the structure is typically many times stiffer

compared to the compliant liner its elasticity often cannot be disregarded. This is shown by Thomsen and Klit [15], appendix D, who show that a solid steel bearing housing, that would traditionally be regarded as infinitely stiff, deforms up to 10 μm at a specific load of 5 MPa and misaligned operation.

Due to the thin compliant liner a local pressure does not affect other parts of the bearing liner, and especially not when using the column model since neighboring nodes are completely de-coupled. However, for the supporting structure, the elasticity is typically coupled much stronger and local pressures will affect the deformations of other sections of the bearing.

Convergence can be difficult to achieve with the column model because deformation of neighboring nodes is only indirectly coupled through Reynolds equation. This can lead to high pressure gradients which are prone to give non-converging iterations. A fine mesh in high-pressure regions reduces instabilities in the iteration procedure.

$$d = Lp = \frac{(1+\nu)(1-2\nu)}{1-\nu}\frac{t}{E}p \tag{6.1}$$

In [55] references are made to comparisons with finite element models that confirms the accuracy of the equation.

6.2 Under-relaxation method

An under-relaxation method can be used to implement the compliance of the bearing structure and liner using strong under-relaxation as shown in equation (6.2). Especially when using the column model it is necessary to apply under-relaxation because of the very non-linear coupling between the oil film forces and the liner compliance.

d_l is the deformation at the l'th iteration and is added to the undeformed film thickness h_0 to give the film thickness at the l'th iteration.

$$\begin{aligned} d_l &= \alpha L p_l + (1-\alpha)\, d_{l-1} \\ h_l &= h_0 + d_l \end{aligned} \tag{6.2}$$

The iteration loop is repeated until convergence is achieved. A convergence criteria is shown in equation (6.3).

$$\frac{|Lp_l - d_{l-1}|}{|Lp_l|} < 10^{-4} \tag{6.3}$$

The under-relaxation method slows down the rate of advance by using linear interpolation between the two solutions d_{k-1} and Lp_k. The optimum value of the under-relaxation factor α depends on the EHD problem. Values from 0.001 to 0.1 have been used with success. When the iteration process is converging the under-relaxation factor can be increased in order to speed up the rate of convergence.

The advantage of using the under-relaxation method for coupling elasticity with hydrodynamics is its simplicity whereas the disadvantage is slow convergence and even the risk of no convergence.

6.3 Full elastic model

In this work an industrial state-of-the-art finite element program, in this case Ansys, is used when including the full elasticity of a bearing structure. A link is created so that Ansys can be called from the developed simulation tool in order to export the stiffness matrix. If the Ansys structural model is parametric the simulation tool can make successive calls to Ansys, varying the geometry for each call, and hereby perform a geometrical parameter study as done for the work [14], appendix C.

Since the fluid film forces are only acting on the bearing surfaces it is advantageous to condense the stiffness matrix into a superelement before exporting it. The method of exporting and reading the stiffness matrix is verified by modeling geometries than can be compared to analytical results using elementary beam theory.

6.4 Force and pressure formulation

The exported superelement stiffness matrix $\mathbf{K}$ correlates forces F with deformations d. However, when coupling elasticity with lubricant pressure it is advantageous to convert the force stiffness matrix to pressure compliance matrix $\mathbf{L}$. This is done using the integration matrix $\mathbf{A}$ as shown in equation (6.4). Hence the deformations can be calculated directly using $\mathbf{L}$ and p.

$$\begin{aligned} &[\mathbf{K}]\{d\} = \{F\} \Leftrightarrow \\ &\{d\} = [\mathbf{K}]^{-1}\{F\} = [\mathbf{K}]^{-1}[\mathbf{A}]\{p\} = [\mathbf{L}]\{p\} \end{aligned} \tag{6.4}$$

The element integration matrix for the three-node triangular element using one Gauss point is shown in equation (6.5) where $\mathbf{1}$ is the unit matrix, consisting of all 1s, and A is the element area. (6.5) is then assembled into the full system integration matrix.

$$[\mathbf{A}] = A\frac{1}{9}[\mathbf{1}]_{3\text{x}3} \tag{6.5}$$

6.5 Newton-Raphson method

The Newton-Raphson method is a very robust scheme for coupling elasticity with the hydrodynamic forces. It is derived using a Taylor expansion around the solution $f(p)$ with respect to p giving equation (6.6).

$$f\left(p+\Delta p\right)=f\left(p\right)+\Delta p\frac{\partial f\left(p\right)}{\partial p}+\frac{\Delta p^{2}}{2!}\frac{\partial^{2}f\left(p\right)}{\partial p^{2}}+\frac{\Delta p^{3}}{3!}\frac{\partial^{3}f\left(p\right)}{\partial p^{3}}+...+\frac{\Delta p^{n}}{n!}\frac{\partial^{n}f\left(p\right)}{\partial p^{n}} \quad (6.6)$$

Derivatives of orders higher than one are neglected giving equation (6.7).

$$\begin{aligned}&\Delta p\frac{\partial f\left(p\right)}{\partial p}=f\left(p+\Delta p\right)-f\left(p\right)\\&\text{where }\frac{\Delta p^{n}}{n!}\frac{\partial^{n}f\left(p\right)}{\partial p^{n}}\ll\Delta p\frac{\partial f\left(p\right)}{\partial p}\text{ for }n>1\end{aligned} \quad (6.7)$$

The functionals $f(p)$ and $f(p+\Delta p)$ are the usual Reynolds equation (5.7) where the later is perturbed with respect to the pressure. The two functionals are shown in equations (6.8) and (6.9). h_0 is the oil film thickness for the undeformed structure.

$$\begin{aligned}&f\left(p\right)=\frac{1}{R}\frac{\partial}{\partial\theta}\left(\frac{h^{3}}{\mu R}\frac{\partial p}{\partial\theta}\right)+\frac{\partial}{\partial z}\left(\frac{h^{3}}{\mu}\frac{\partial p}{\partial z}\right)-6\omega\frac{\partial h}{\partial\theta}-12\frac{\partial h}{\partial t}\\&\text{where }h=h_{0}+\mathbf{L}p\end{aligned} \quad (6.8)$$

$$\begin{aligned}&f\left(p+\Delta p\right)=\frac{1}{R}\frac{\partial}{\partial\theta}\left(\frac{h^{3}}{\mu R}\frac{\partial\left(p+\Delta p\right)}{\partial\theta}\right)+\frac{\partial}{\partial z}\left(\frac{h^{3}}{\mu}\frac{\partial\left(p+\Delta p\right)}{\partial z}\right)-6\omega\frac{\partial h}{\partial\theta}-12\frac{\partial h}{\partial t}\\&\text{where }h=h_{0}+\mathbf{L}\left(p+\Delta p\right)\end{aligned} \quad (6.9)$$

h^3 from equation (6.9) is reformulated and terms including $\mathbf{L}\Delta p$ in powers of 2 or higher are neglected:

$$\begin{aligned}&h^{3}=\left(h_{0}+\mathbf{L}\left(p+\Delta p\right)\right)^{3}=\left(h_{0}+\mathbf{L}p\right)^{3}+3\mathbf{L}\Delta p(h_{0}+\mathbf{L}p)^{2}\\&\text{and }\left(\mathbf{L}\Delta p\right)^{n}\ll h_{0}\,\text{for}\,n>1\end{aligned} \quad (6.10)$$

Equations (6.8), (6.9) and (6.10) are put together and simplifies to (6.11).

$$\begin{aligned}\Delta p\frac{\partial f\left(p\right)}{\partial p}=&f\left(p+\Delta p\right)-f\left(p\right)\\=&\frac{1}{R}\frac{\partial}{\partial\theta}\left(\frac{3h^{2}\mathbf{L}\Delta p}{\mu R}\frac{\partial p}{\partial\theta}\right)+\frac{\partial}{\partial z}\left(\frac{3h^{2}\mathbf{L}\Delta p}{\mu}\frac{\partial p}{\partial z}\right)\\&+\frac{1}{R}\frac{\partial}{\partial\theta}\left(\frac{h^{3}}{\mu R}\frac{\partial\Delta p}{\partial\theta}\right)+\frac{\partial}{\partial z}\left(\frac{h^{3}}{\mu}\frac{\partial\Delta p}{\partial z}\right)\\&-6\omega\frac{\partial\mathbf{L}\Delta p}{\partial\theta}-12\frac{\partial\mathbf{L}\Delta p}{\partial t}\\\text{where }h=&h_{0}+\mathbf{L}p\end{aligned} \quad (6.11)$$

Equation (6.11) can then be used to solve for Δp using (6.12) where S is the residual from equation (5.43) when assembled over all elements.

$$\left[\frac{\partial f\left(p\right)}{\partial p}\right]\left\{\Delta p\right\} = \left[\mathbf{J}\right]\left\{\Delta p\right\} = \left\{S\right\} = \left[\mathbf{H}\right]\left\{p\right\} - \left\{V\right\} \tag{6.12}$$

The final solution for the pressure p and the corresponding state of deformation d is found by solving equation (6.12) multiple times through an iterative procedure until the convergence criterion stated in (6.13) is fulfilled. In each iteration l the pressure is updated using (6.14) which, when the solution is converging, will find successively better approximations to the true solutions of p and the corresponding deformation.

$$\frac{|\Delta p|}{|p|} < 10^{-4} \tag{6.13}$$

$$p_l = p_{l-1} + \Delta p \tag{6.14}$$

The algorithm used to implement the Newton-Raphson scheme is presented in section 6.5.2 page 48.

6.5.1 Finite element formulation

The finite element technique is used to solve for Δp using equation (6.12). The Jacobian matrix of (6.12) consists of six terms corresponding to the right hand terms of equation (6.11):

$$\left[\mathbf{J}\right] = \left[\mathbf{J}\right]_I + \left[\mathbf{J}\right]_{II} + \left[\mathbf{J}\right]_{III} + \left[\mathbf{J}\right]_{IV} + \left[\mathbf{J}\right]_V + \left[\mathbf{J}\right]_{VI} \tag{6.15}$$

The derivation of the element equations is shown in the following paragraphs.

First term

The first term of equation (6.11) is expanded and the derivative of p of second order is neglected:

$$\begin{aligned}\frac{1}{R}\frac{\partial}{\partial\theta}\left(\frac{3h^2\mathbf{L}\Delta p}{\mu R}\frac{\partial p}{\partial\theta}\right) =& \frac{1}{R}\frac{\partial}{\partial\theta}\left(\frac{3h^2\mathbf{L}\Delta p}{\mu R}\right)\frac{\partial p}{\partial\theta} + \frac{3h^2\mathbf{L}\Delta p}{\mu R^2}\underbrace{\frac{\partial^2 p}{\partial\theta^2}}_{\ll\frac{\partial p}{\partial\theta}} \\ =& \frac{6h\mathbf{L}\Delta p}{\mu R^2}\frac{\partial h}{\partial\theta}\frac{\partial p}{\partial\theta} + \frac{3h^2}{\mu R^2}\mathbf{L}\frac{\partial\Delta p}{\partial\theta}\frac{\partial p}{\partial\theta}\end{aligned} \tag{6.16}$$

Equation (6.16) is put into integral form according to the Galerkin principle. For each element an equation is set up for all nodes j:

$$\int_\Omega \left(\frac{6h}{\mu R^2} \frac{\partial h}{\partial \theta} \frac{\partial p}{\partial \theta} \mathbf{L} \Delta p N_j \right) d\Omega + \int_\Omega \left(\frac{3h^2}{\mu R^2} \frac{\partial p}{\partial \theta} \mathbf{L} \frac{\partial \Delta p}{\partial \theta} N_j \right) d\Omega \tag{6.17}$$

The field variable Δp and its derivatives are expressed using interpolation functions (5.34) and (5.40). Furthermore the field variables h, p, μ and its derivatives are integrated using a single Gauss point. Therefore they can be moved out of the integration bracket and be treated as constants with their respective values at the element centroid.

$$\frac{6h}{\mu R^2} \frac{\partial h}{\partial \theta} \frac{\partial p}{\partial \theta} \int_\Omega \left(\mathbf{L} \sum_{m=1}^{3} (\Delta p_m N_m) N_j \right) d\Omega + \frac{3h^2}{\mu R^2} \frac{\partial p}{\partial \theta} \int_\Omega \left(\mathbf{L} \sum_{m=1}^{3} \left(\Delta p_m \frac{\partial N_m}{\partial \theta} \right) N_j \right) d\Omega \tag{6.18}$$

The interpolation functions (5.36) are then inserted into (6.18) and integration is performed using (5.51). The resulting formula is put into matrix form (6.19) and shown in (6.20), where $\mathbf{I}$ is the identity matrix and $\mathbf{1}$ is the unit matrix.

$$[\mathbf{J}_{jk}]_I \{\Delta p_j\} \tag{6.19}$$

$$[\mathbf{J}_{jk}]_I = \frac{Ah}{2\mu R^2} \frac{\partial h}{\partial \theta} \frac{\partial p}{\partial \theta} \mathbf{L} ([\mathbf{1}] + [\mathbf{I}]) + \frac{h^2}{2\mu R} \frac{\partial p}{\partial \theta} \mathbf{L} b_k \tag{6.20}$$

Note that since $\mathbf{L}$ is a full matrix of size $n \times n$, $\mathbf{J}_I$ becomes $3 \times n$ when using 3 DOF elements.

Second term

The second term of equation (6.11) is derived using the same procedure as for the first term. The contribution to the Jacobian matrix is shown in equation (6.21).

$$[\mathbf{J}_{jk}]_{II} = \frac{Ah}{2\mu} \frac{\partial h}{\partial z} \frac{\partial p}{\partial z} \mathbf{L} ([\mathbf{1}] + [\mathbf{I}]) + \frac{h^2}{2\mu} \frac{\partial p}{\partial z} L c_k \tag{6.21}$$

Third term

The third term of equation (6.11) is shown in equation (6.22) and expanded.

$$\frac{1}{R} \frac{\partial}{\partial \theta} \left(\frac{h^3}{\mu R} \frac{\partial \Delta p}{\partial \theta} \right) = \frac{h^3}{\mu R^2} \frac{\partial^2 \Delta p}{\partial \theta^2} + \frac{1}{\mu R^2} \frac{\partial h^3}{\partial \theta} \frac{\partial \Delta p}{\partial \theta} \tag{6.22}$$

Equation (6.22) is put into integral form and for each element an equation is set up for all nodes j. As for the first term, the field variables h, μ and its derivatives can be moved out of the integration bracket because they are integrated using a single Gauss point.

$$\frac{h^3}{\mu R^2} \int_\Omega \left(\frac{\partial^2 \Delta p}{\partial \theta^2} N_j \right) d\Omega + \frac{1}{\mu R^2} \frac{\partial h^3}{\partial \theta} \int_\Omega \left(\frac{\partial \Delta p}{\partial \theta} N_j \right) d\Omega \tag{6.23}$$

Integration by parts is used to reduce the order of the first term in equation (6.23) giving (6.24). The first term of (6.24) cancels itself at all interior nodes of the solution domain. For the nodes located on the boundary the term brings in the possibility of specifying the pressure gradient, and hence the flow, as a boundary condition. However, since I wish to solve for Δp, I do not need to specify the gradient. The gradient is overwritten when specifying Δp at boundary nodes and therefore the term is removed from equation (6.24).

$$\frac{h^3}{\mu R^2}\left(\underbrace{\left[\frac{\partial \Delta p}{\partial \theta}N_j\right]_\Omega}_{\text{cancels out}} - \int_\Omega \left(\frac{\partial \Delta p}{\partial \theta}\frac{\partial N_j}{\partial \theta}\right)d\Omega\right) + \frac{1}{\mu R^2}\frac{\partial h^3}{\partial \theta}\int_\Omega \left(\frac{\partial \Delta p}{\partial \theta}N_j\right)d\Omega \tag{6.24}$$

The interpolation functions (5.36) and (5.40) are introduced in equation (6.24) giving (6.25):

$$-\frac{h^3}{\mu R^2}\int_\Omega \left(\sum_{m=1}^{3}\left(\Delta p_m \frac{R}{2A}b_m\right)\frac{R}{2A}b_j\right)d\Omega + \frac{1}{\mu R^2}\frac{\partial h^3}{\partial \theta}\int_\Omega \left(\sum_{m=1}^{3}\left(\Delta p_m \frac{R}{2A}b_m\right)N_j\right)d\Omega \tag{6.25}$$

Equation (6.25) is integrated giving (6.26):

$$-\frac{h^3}{4A\mu}\sum_{m=1}^{3}(\Delta p_m b_m)b_j + \frac{1}{6\mu R}\frac{\partial h^3}{\partial \theta}\sum_{m=1}^{3}(\Delta p_m b_m) \tag{6.26}$$

Finally the equation is put into matrix form stating the element equations:

$$[\mathbf{J}_{jk}]_{III} = -\frac{h^3}{4A\mu}b_j b_k + \frac{1}{6\mu R}\frac{\partial h^3}{\partial \theta}b_k \tag{6.27}$$

Fourth term

The fourth term of equation (6.11) is derived using the same procedure as for the third term. The contribution to the Jacobian matrix is shown in equation (6.28).

$$[\mathbf{J}_{jk}]_{IV} = -\frac{h^3}{4A\mu}c_j c_k + \frac{1}{6\mu}\frac{\partial h^3}{\partial z}c_k \tag{6.28}$$

Fifth term

The fifth term of equation (6.11) is shown in (6.29). It originates from the Couette term of equation (5.7).

$$-6\omega\frac{\partial \mathbf{L}\Delta p}{\partial \theta} \tag{6.29}$$

The term is put into integral form using the Galerkin principle:

$$-6\omega \int_{\Omega} \left(\frac{\partial \mathbf{L}\Delta p}{\partial \theta} N_j \right) d\Omega \tag{6.30}$$

Interpolation functions are introduced giving equation (6.31):

$$-6\omega \int_{\Omega} \left(\sum_{m=1}^{3} \left(\mathbf{L}\Delta p_m \frac{R}{2A} b_m \right) N_j \right) d\Omega \tag{6.31}$$

Integration is performed producing equation (6.32):

$$-R\omega\mathbf{L} \sum_{m=1}^{3} (\Delta p_m b_m) \tag{6.32}$$

The resulting set of equations is put into matrix form (6.19) and shown in (6.33):

$$[\mathbf{J}_{jk}]_V = -R\omega\mathbf{L}b_k \tag{6.33}$$

Sixth term

The sixth term of equation (6.11) is shown in (6.34). It originates from the squeeze term of equation (5.7). Since Δp is not time dependent the term cannot be expressed and the contribution to the overall Jacobian matrix is set to 0 as stated in equation (6.35).

$$-12\frac{\partial \mathbf{L}\Delta p}{\partial t} \tag{6.34}$$

$$[\mathbf{J}_{jk}]_{VI} = 0 \tag{6.35}$$

6.5.2 Numerical implementation

The Newton-Raphson method is implemented using the algorithm shown in figure 6.1. The Newton-Raphson method does not account for cavitation and thus any cavitated region must be specified before initializing the Newton-Raphson scheme. The scheme can be initiated with both pressure and deformation set to 0. If another solution is available, e.g. from integration in time domain or in connection with coupling with the energy equation, it can be used with great advantage to achieve a rapid convergence.

The pressure p is updated using equation (6.14) and the convergence of the Newton-Raphson (figure 6.1 #5) method is checked using (6.13). The handling of cavitation (figure 6.1 #2) is described in section 5.6 page 38. n_j is a counter used in the cavitation algorithm that needs initialization here.

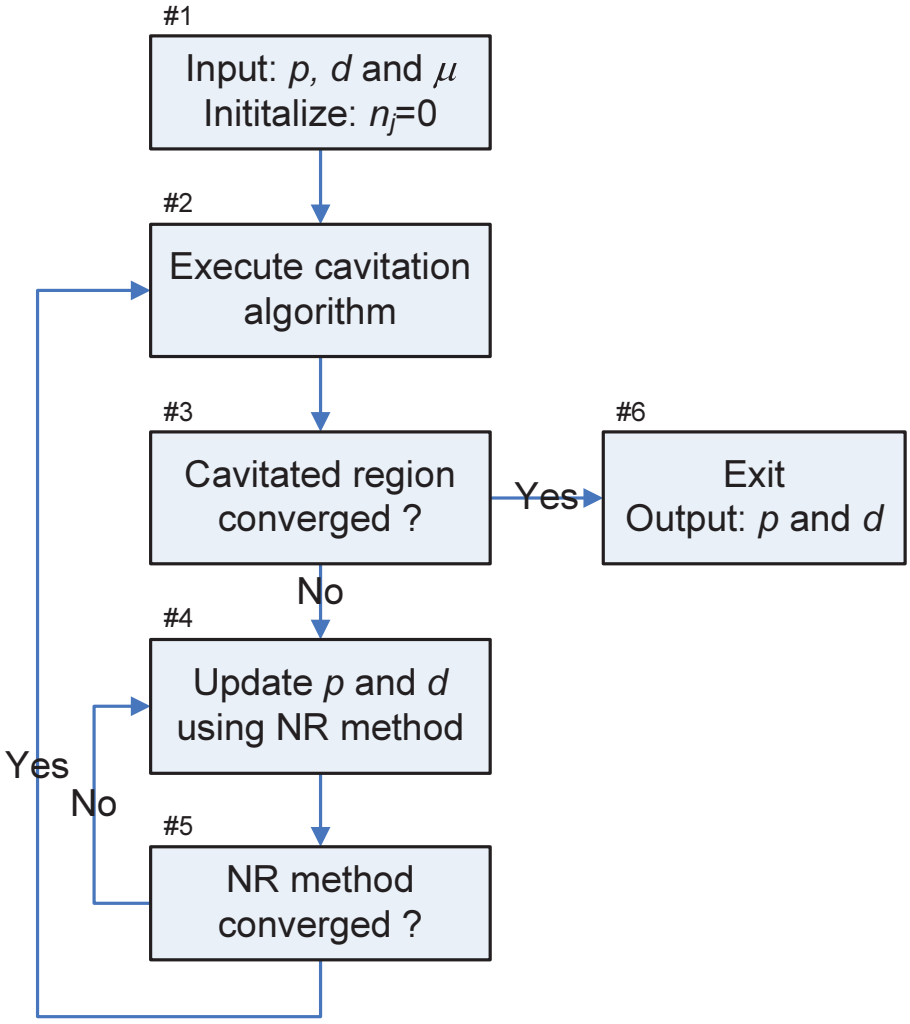

Figure 6.1: Algorithm for integrating cavitation algorithm with Newton-Raphson method

Chapter 7

Thermal modeling

In this chapter it is shown how the energy equation is used to determine the heat flux in lubricant, journal and bearing using the finite difference technique.

Since the cavitation algorithm applied in this work does not ensure mass conservation, energy balance cannot be assured in the cavitated region either. Van Ostayen and van Beek [56] uses a mass-conserving cavitation algorithm that enables accurate prediction of energy flow in the cavitated regions.

It is important to consider the thermal effects when performing hydrodynamic bearing studies. Dowsen et al. [40][57] revealed this already in the 1960's. In order to model the thermohydrodynamics better than the isothermal and adiabatic approaches they propose a model which includes the heat transfer from lubricant to bearing using heat transfer coefficients and compare the results with experimental findings. Good agreement is found when comparing experimental findings with theoretical results.

Klit [58] has studied the energy-balance in journal bearings and showed that thermo-viscous effects have significant influence on bearing performance. Bearing- and journal-temperature have great impact on the temperature distribution in the lubricant which is also shown to vary strongly across the film thickness. The majority of the dissipated heat is carried from bearing through convection.

Glavatskih et al. [47] study the influence of lubricant viscosity and viscosity index on thrust bearing performance experimentally and compare with simulations using a TEHD model. Interestingly it is found that bearing efficiency can be increased without sacrificing bearing safety by substituting a mineral oil with a thinner synthetic oil having a higher viscosity index. The viscous shear is reduced while maintaining the same lubricant film thickness.

When not using full CFD simulations to solve the flow conditions, as done by Piotr for a fully flooded bearing [25], it is difficult to predict, with sufficient accuracy, the mixing of hot and cold oil at the oil inlet system. This is an issue for all types of bearings ranging from conventional full journal bearings to pad bearings being fully flooded or fitted with leading edge grooves or spray bars. It is important to know the mixing parameters due to the high temperature-dependency of lubricant viscosity and hence load carrying capacity. Heshmat and Pinkus [59] have studied

the topic experimentally and propose empirical relations for a wide range of operating conditions and bearing sizes covering both thrust and journal bearings.

Ettles [60] has performed a similar experimental study on 14 different thrust bearing assemblies and reports that 60 to 80 %, depending on sliding speed and bearing type, of hot oil is carried over to the next pad.

Using a THD model Roy [61] has performed a parametric study in order to determine the influence of the lubrication groove position in a conventional journal bearing. The optimum groove location and size is found to depend heavily on bearing operational parameters.

Other interesting studies are that of Fillon, Frene et al. [62],[63],[64] which treat dynamic thermo-hydrodynamic behavior of thrust bearings both theoretically and experimentally. Different thermo-hydrodynamic models are compared and dynamic responses are studied. It is shown that isothermal assumptions are not very accurate and that thermoelastic deformations can lead to significant changes in bearing performance.

7.1 Energy equation

The differential equation shown in equation (7.1), also called the energy equation, describes the energy balance of convection, conduction and dissipation. For this work four different thermo-models will be derived:

- isothermal assumption, i.e. constant lubricant temperature
- adiabatic assumption, i.e. no energy transfer from lubricant
- energy transfer using radial temperature gradient
- energy transfer using heat transfer coefficients

The most basic method of hydrodynamic bearing analysis assumes isothermal conditions in the lubricant. Since the lubricant temperature is regarded as constant, regardless of bearing conditions, the energy equation is not required for this modeling approach.

The adiabatic assumption is a special case of using heat transfer coefficients, where the coefficients are set to zero and thus not allowing heat transfer to and from lubricant.

Two sections are dedicated to the description of the two remaining models: *7.1.1 Conduction using radial temperature gradient* and *7.1.2 Conduction using heat transfer coefficients*.

The energy equation (7.1) is shown in its cylindrical form, which is suited for journal bearings. The corresponding coordinate system is shown in figure 5.1(b) page 28.

A number of assumptions are made in order to reduce the complexity of the problem:

- steady state conditions are assumed when solving for the temperature
- heat conduction is only included in radial direction
- viscous dissipation terms assume large velocity gradients in radial direction compared to other directions
- lubricant velocity component in radial direction is negligible
- convection terms assume a mean lubricant temperature across the lubricant thickness

Conduction is only included in radial direction since convection dominates the energy transfer in circumferential and axial direction. The viscous dissipation term assumes a thin lubricant film giving large velocity gradients in radial direction compared to other dimensions.

$$\rho c_p \left(\frac{1}{R}\frac{\partial}{\partial\theta}\left(v_\theta T\right) + \frac{\partial}{\partial z}\left(v_z T\right) + \frac{\partial}{\partial x}\left(v_x T\right) \right) = k\frac{\partial^2 T}{\partial x^2} + \mu\left(\left(\frac{\partial v_\theta}{\partial x}\right)^2 + \left(\frac{\partial v_z}{\partial x}\right)^2 \right) \tag{7.1}$$

In the following sections the finite difference equations for implementing the energy equation in the TEHD bearing model will be derived.

Equation (7.2) shows the left-hand-side of equation (7.1) after integration over the lubricant film thickness h. The velocity gradients cancel out when using the continuity equation shown in equation (7.3) and the velocity component in radial direction is assumed much smaller than in the other dimensions and is therefore negligible.

$$\begin{aligned} LHS =& \rho c_p \int_0^h \left(\frac{1}{R}\frac{\partial}{\partial\theta}\left(v_\theta T\right) + \frac{\partial}{\partial z}\left(v_z T\right) + \frac{\partial}{\partial x}\left(v_x T\right) \right) dx \\ =& \rho c_p \left(\frac{1}{R}\int_0^h \left(\underbrace{\frac{\partial v_\theta}{\partial\theta}}_{\text{cancels}} T + v_\theta \frac{\partial T}{\partial\theta} \right) dx + \int_0^h \left(\underbrace{\frac{\partial v_z}{\partial z}}_{\text{cancels}} T + v_z \frac{\partial T}{\partial z} \right) dx \right. \\ & \left. + \int_0^h \left(\underbrace{\frac{\partial v_x}{\partial x}}_{\text{cancels}} T + \underbrace{v_x}_{\substack{\ll v_\theta \\ \ll v_z}} \frac{\partial T}{\partial x} \right) dx \right) \\ =& \rho c_p \left(\frac{1}{R}\int_0^h \left(v_\theta \frac{\partial T}{\partial\theta} \right) dx + \int_0^h \left(v_z \frac{\partial T}{\partial z} \right) dx \right) \end{aligned} \tag{7.2}$$

$$\frac{1}{R}\frac{\partial v_\theta}{\partial\theta} + \frac{\partial v_z}{\partial z} + \frac{\partial v_x}{\partial x} = 0 \tag{7.3}$$

In equation (7.4) the temperature T from (7.2), for the convection terms, is expressed using the mean temperature T_m over the lubricant film thickness and hence

the temperature derivatives are constant across the film thickness and can be moved outside the integrals.

The integration of the fluid velocity components in (7.2) equals the flow per unit width and can be replaced by equations (5.12) and (5.13) as also shown in (7.4).

$$\begin{aligned} LHS =& \rho c \left(\frac{1}{R} \frac{\partial T_m}{\partial \theta} \int_0^h v_\theta dx + \frac{\partial T_m}{\partial z} \int_0^h v_z dx \right) \\ =& \rho c \left(\frac{1}{R} \frac{\partial T_m}{\partial \theta} q'_\theta + \frac{\partial T_m}{\partial z} q'_z \right) \end{aligned} \tag{7.4}$$

Equation (7.5) shows the right-hand-side of the energy equation (7.1) when integrated across the lubricant film thickness h.

$$RHS = \int_0^h \left(k \frac{\partial^2 T}{\partial x^2} + \mu \left(\left(\frac{\partial v_\theta}{\partial x} \right)^2 + \left(\frac{\partial v_z}{\partial x} \right)^2 \right) \right) dx \tag{7.5}$$

The expressions for the fluid velocities (5.10) and (5.11) are inserted and differentiation of these are applied. Furthermore a mean viscosity μ_m, corresponding to the mean temperature, is employed. Finally integration of the expression leads to equation (7.6).

$$RHS = \left[k \frac{\partial T}{\partial x} \right]_{x=0}^{x=h} + \frac{\mu_m \omega^2 R^2}{h} + \frac{h^3}{12 \mu_m} \left(\frac{1}{R^2} \left(\frac{\partial p}{\partial \theta} \right)^2 + \left(\frac{\partial p}{\partial z} \right)^2 \right) \tag{7.6}$$

Equation (7.4) and (7.6) are put together giving the final form of the energy equation as shown in equation (7.7). The left hand side represents the convection term whereas the right hand side represents the conduction, viscous dissipation due to Couette flow and viscous dissipation due to Poiseuille flow respectively.

However, before numerical implementation is possible, the conductive term needs further attention. The sections 7.1.1 and 7.1.2 are dedicated to this.

$$\begin{aligned} \rho c \left(\frac{1}{R} \frac{\partial T_m}{\partial \theta} q'_\theta + \frac{\partial T_m}{\partial z} q'_z \right) = & \left[k \frac{\partial T}{\partial x} \right]_{x=0}^{x=h} + \frac{\mu_m \omega^2 R^2}{h} \\ & + \frac{h^3}{12 \mu_m} \left(\frac{1}{R^2} \left(\frac{\partial p}{\partial \theta} \right)^2 + \left(\frac{\partial p}{\partial z} \right)^2 \right) \end{aligned} \tag{7.7}$$

7.1.1 Conduction using radial temperature gradient

In this section it is explained how conduction from lubricant to journal is calculated assuming a parabolic temperature profile across the film thickness. The method resembles the approach originally developed by Klit [58].

In this work emphasis is put on compliant polymer liners, of which a side effect is their highly insulating properties. Therefore the bearing surface is treated as adiabatic only allowing conduction through the journal.

The conduction is calculated using the temperature gradient of a parabolic temperature profile and the thermal conductivity of the lubricant. For the derivation, using this approach, two assumptions are made:

- the temperature gradients for the convection terms are set to 0
- pure Couette flow is assumed
- a polymer material is used for the bearing liner giving adiabatic conditions on this side

In order to derive an expression for the temperature variation across the lubricant film thickness the energy equation (7.1) is used. Equivalent to the steps from (7.1) to (7.5) integration, this time indefinite, is performed on both sides and again the continuity equation (7.3) is employed.

Furthermore the temperature gradients in circumferential and axial direction are set to 0 as shown in equation (7.8). These gradients are small compared to the radial temperature gradient. Therefore we can can, with good approximation, neglect the convective terms when evaluating the radial heat transfer. This only leaves the constant of integration on the left-hand-side which is moved to the right-hand-side giving (7.9).

$$\frac{\partial T}{\partial \theta} = \frac{\partial T}{\partial z} = 0 \tag{7.8}$$

$$0 = k\frac{\partial T}{\partial x} + \mu_m \int \left(\left(\frac{\partial v_\theta}{\partial x} \right)^2 + \left(\frac{\partial v_z}{\partial x} \right)^2 \right) dx + C_1 \tag{7.9}$$

Pure Couette flow is assumed giving the expressions for the velocity components shown in (7.10).

$$\begin{aligned} v_\theta &= \omega R \frac{x}{h} \\ v_z &= 0 \end{aligned} \tag{7.10}$$

Equations (7.10) are then inserted into (7.9) giving (7.11):

$$0 = k\frac{\partial T}{\partial x} + \frac{\mu_m \omega^2 R^2 x}{h^2} + C_1 \tag{7.11}$$

Equation (7.11) is integrated again giving (7.12):

$$0 = kT + \frac{\mu_m \omega^2 R^2 x^2}{2h^2} + C_1 x + C_2 \tag{7.12}$$

The constants of integration are determined using the boundary conditions at $x = 0$ and $x = h$ corresponding to the bearing surfaces at the bearing and journal.

For a polymer material the radial temperature gradient is very small, corresponding to good insulating properties. As a result the gradient is set to 0 as shown in equation (7.13) stating the boundary conditions for the bearing:

$$\begin{aligned} &x = 0 \\ &\frac{\partial T}{\partial x} = 0 \end{aligned} \tag{7.13}$$

For the journal a fixed temperature T_J is chosen as boundary condition. This is believed to be a good assumption since the journal rotational speed is typically at a magnitude that gives a very small local transient temperature fluctuation at the journal surface during rotation. The journal boundary conditions are shown in equation (7.14):

$$\begin{aligned} &x = h \\ &T = T_J \end{aligned} \tag{7.14}$$

The constants of integration are then identified using (7.12), (7.13) and (7.14):

$$\begin{aligned} C_1 &= 0 \\ C_2 &= -kT_J - \frac{1}{2}\mu_m \omega^2 R^2 \end{aligned} \tag{7.15}$$

The constants are inserted into (7.16) expressing temperature as a function of x:

$$T = \frac{\mu_m \omega^2 R^2}{2k}\left(1 - \frac{x^2}{h^2}\right) + T_J \tag{7.16}$$

The final form of the energy equation (7.7) is expressed using the mean temperature. Therefore the mean value of (7.16) is found through integration as shown in (7.17). The expression is rearranged to allow for substitution into (7.16) giving (7.18).

$$\begin{aligned} T_m = \frac{1}{h}\int_0^h T dx = \frac{\mu_m R^2 \omega^2}{3k} + T_J \Leftrightarrow \\ \frac{\mu_m \omega^2 R^2}{2k} = \frac{3}{2}\left(T_m - T_J\right) \end{aligned} \tag{7.17}$$

Equation (7.18) shows the parabolic temperature variation across the lubricant film thickness with the given assumptions.

$$\mathrm{T} = \frac{3}{2}\left(T_m - T_J\right)\left(1 - \frac{x^2}{h^2}\right) + T_J \tag{7.18}$$

Figure 7.1 shows an example of a local temperature distribution for a journal temperature of 50 ° C and a lubricant mean temperature of 60 ° C. This gives a maximum temperature of 65 ° C at the polymer lined bearing surface. The temperature gradient at the journal surface is negative leading to a negative conductive term corresponding to cooling of the lubricant.

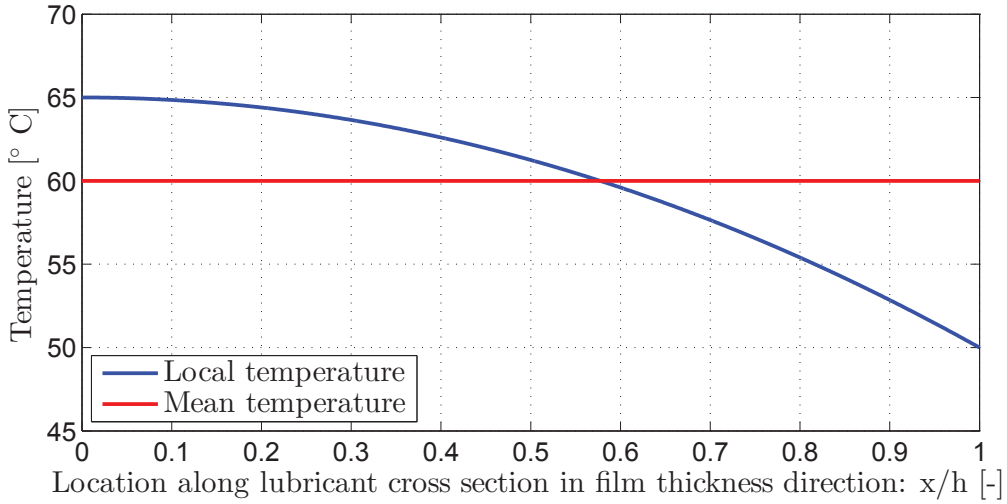

Figure 7.1: Parabolic temperature distribution along lubricant cross section (film height)

The approach used to derive the temperature profile given in (7.18) has a questionable element. The assumption on the temperature gradients stated in (7.8) basically induces that the viscous dissipation is equal to the conduction through the journal surface when the pressure gradients are zero. This aspect does not originate in a real physical condition and is as such difficult to justify. It may however give a better representation of the thermal conditions than an adiabatic model. Another aspect of the derivation of (7.18) is that pure Couette flow is assumed. The Poiseuille terms can also be included, this does however not lead to as elegant a solution as for the pure Couette assumption.

Calculation of mass and energy balance

In this section is is shown how the mass and energy balance is checked for the thermo-model using the radial temperature gradient for calculating the conduction. A control volume, as shown in figure 7.2, is moved along the oil-filled bearing clearance and for every location the mass and energy balance is checked. This approach will show if

the assumptions give valid results obeying the rules of mass and energy conservation. Since the cavitation algorithm applied in this work does not ensure mass conservation, energy balance cannot be assured in the cavitated region either.

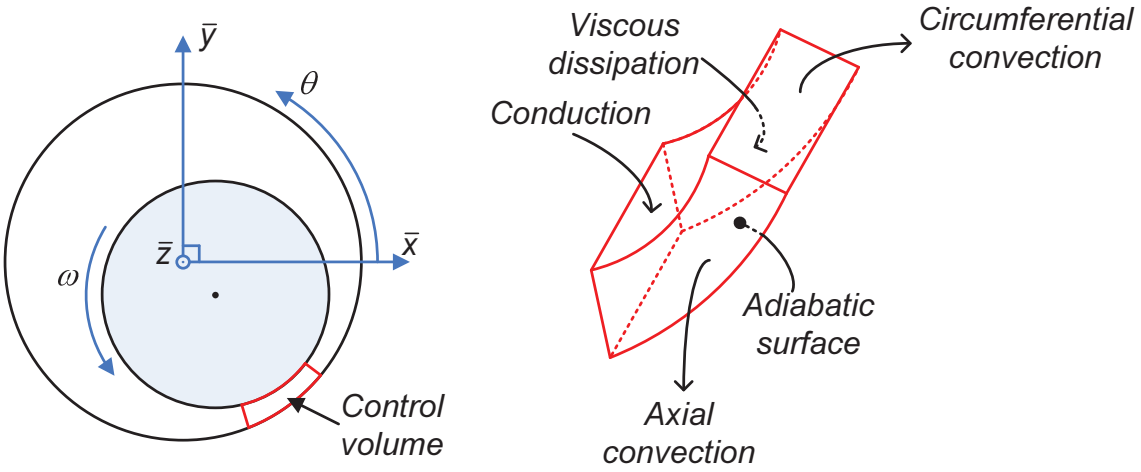

Figure 7.2: Control volume for energy and mass balance

For checking the mass balance, equations (5.12) and (5.13) are used.

Convection of energy through axial flow per unit length is calculated using (7.18) inserted into (5.11) as shown in (7.19). The equation states the energy flux through a cross section over the lubricant thickness in circumferential direction as illustrated in figure 7.2. Sign is according to the cylindrical coordinate system.

$$\begin{aligned} P'_{Axial} &= \rho c_p \int_0^h (v_z T) dx \\ &= -\frac{1}{240\mu_m} \rho \mathrm{c} \frac{\partial p}{\partial z} h^3 \left(21 T_m - T_J\right) \end{aligned} \tag{7.19}$$

Energy convection through circumferential flow per unit width is calculated using (5.10) and (7.18) as expressed in (7.20). The equation states the energy flux through a cross section over the lubricant thickness in radial direction. Sign is according to the cylindrical coordinate system.

$$\begin{aligned} P'_{Circumferential} &= \rho c_p \int_0^h (v_\theta T) dx \\ &= \frac{1}{8} \rho \mathrm{c} \omega R h \left(3 T_m + T_J\right) - \frac{1}{240\mu_m R} \rho \mathrm{c} \frac{\partial p}{\partial \theta} h^3 \left(21 T_m - T_J\right) \end{aligned} \tag{7.20}$$

Energy conduction through the journal is calculated using the temperature gradient derived from (7.18) at $x = h$ as expressed in (7.21). A positive value denotes flux into the control volume.

$$\begin{aligned} P_{Conduction} &= \int_{\Omega} \left(k \frac{\partial T}{\partial x}_{x=h} \right) d\Omega \\ &= \int_{\Omega} \left(\frac{3k}{h} \left(T_J - T_m \right) \right) d\Omega \end{aligned} \tag{7.21}$$

The viscous dissipation in the lubricant is calculated using (5.14).
Finally the energy balance can be expressed using (7.22) where e is the error:

$$\int P'_{Axial} d\Lambda + \int P'_{Circumferential} d\Lambda + P_{Conduction} + P_{Viscousdissipation} = e \tag{7.22}$$

7.1.2 Conduction using heat transfer coefficients

An alternative approach to the method based on the radial temperature gradient and thermal conductivity of the lubricant is to use the temperature difference of lubricant and solid coupled with the heat transfer coefficient of the interface according to Newton's law of cooling: "The rate of heat loss of a body is proportional to the difference in temperatures between the body and its surroundings" [65]. Basically this approach requires only one assumption:

- Newton's law of cooling is assumed valid using a mean lubricant temperature T_m across the lubricant thickness

Applying this method the conduction term of equation (7.7) is replaced with the terms using heat transfer coefficients as shown in (7.23). The ratio heat loss to temperature difference is called the heat transfer coefficient α.

The transfer of energy from solid to lubricant is also known as convective heat transfer, however, the term conduction will be used in this work. As previously T_J denotes the temperature of the journal and T_B the temperature of the bearing. α_J and α_B are the heat transfer coefficients of the corresponding interfaces.

$$\left[k \frac{\partial T}{\partial x} \right]_{x=0}^{x=h} = \alpha_J \left(T_J - T_m \right) + \alpha_B \left(T_B - T_m \right) \tag{7.23}$$

When inserted into the energy equation (7.7) it becomes:

$$\begin{aligned} \rho c \left(\frac{1}{R} \frac{\partial T_m}{\partial \theta} q'_{\theta} + \frac{\partial T_m}{\partial z} q'_{z} \right) =& \alpha_J \left(T_J - T_m \right) + \alpha_B \left(T_B - T_m \right) \\ &+ \frac{\mu_m \omega^2 R^2}{h} + \frac{h^3}{12 \mu_m} \left(\frac{1}{R^2} \left(\frac{\partial p}{\partial \theta} \right)^2 + \left(\frac{\partial p}{\partial z} \right)^2 \right) \end{aligned} \tag{7.24}$$

Using this method the questionable nature of the method derived in section 7.1.1 is avoided, where the viscous dissipation equals the conduction through the journal surface when the pressure gradients are zero, but a new challenge rises: How to select proper heat transfer coefficients and corresponding boundary conditions. These problems of defining proper system parameters and boundary conditions can be reduced by increasing the system which is modeled. This will move the boundary conditions further away and also, in most cases, make it easier to identify true values for the system. The disadvantage is naturally that the modeling and computational task increases drastically.

Calculation of mass and energy balance

In this section is shown how the mass and energy balance is checked for the thermo-model using heat transfer coefficients for calculating the conduction. Again the control volume principle shown in figure 7.2 is used for the the control of mass and energy balance. For calculation of the former, equations (5.12) and (5.13) are used.

Convection through axial flow per unit length is calculated using (5.11) together with the mean temperature T_m which is constant across the lubricant film thickness.

$$\begin{aligned} P'_{Axial} &= \rho c_p \int_0^h (v_z T_m) dx \\ &= -\frac{1}{12\mu_m} \rho \mathrm{c}_p \frac{\partial p}{\partial z} h^3 T_m \end{aligned} \tag{7.25}$$

Similarly the convection through circumferential flow per unit width is calculated using (5.10) as stated in (7.26).

$$\begin{aligned} P'_{Circumferential} &= \rho c_p \int_0^h (v_\theta T_m) dx \\ &= \frac{1}{2} \rho \mathrm{c}_p \omega R h T_m - \frac{1}{12\mu_m R} \rho \mathrm{c}_p \frac{\partial p}{\partial \theta} h^3 T_m \end{aligned} \tag{7.26}$$

The conduction through the journal and bearing using heat transfer coefficients is calculated using (7.23) as stated in (7.27):

$$P_{Conduction} = \int_\Omega \left(\alpha_J \left(T_J - T_m \right) + \alpha_B \left(T_B - T_m \right) \right) d\Omega \tag{7.27}$$

The viscous dissipation in the lubricant is found using (5.14) and finally the energy balance is calculated using (7.22).

Heat transfer coefficients

In this work emphasis is put on polymer lined bearings. The heat transfer coefficient for the bearing α_B is then close to that of adiabatic conditions and therefore set to zero.

Jiji [66] states that the typical heat transfer coefficient for forced convection in liquids is stated to be in the range 50 to 20,000 W/m^2/°C

Using Baehr and Stephan's [67] approach, the heat transfer coefficient for internal forced laminar flow between between parallel plates can be approximated using (7.28) where the Nusselt number Nu is 7.5. The Nusselt number is the ratio of convective to conductive heat transfer through a surface.

$$\alpha = \frac{k\mathrm{Nu}}{2h} \tag{7.28}$$

Equation (7.28) gives a local heat transfer coefficient of 11,250 W/m^2/°C using a thermal conductivity of 0.15 W/m/°C, corresponding to that of conventional lubrication oil, and a film thickness of 50 μm.

This value is a gross overestimation when comparing to the work of Almquist et al. [68] who compare a THD model of a tilting pad thrust bearing with experiments and adjust model parameters to obtain good correlation between measurements and simulation results with emphasis on the thermal response. They achieve fairly good agreement using a coefficient of 1,000 W/m^2/°C.

7.2 Variable journal temperature

Both presented methods for calculating the conduction through the journal surface require the journal temperature to be defined. A model is developed for the axial energy conduction in the journal which allows the journal temperature to be defined at the bearing edges only. For this approach two assumptions are made:

- journal temperature is constant at any radial cross section
- journal temperature profile in axial direction is symmetric about bearing center

In order to maintain energy conservation the heat flux from oil film to the journal, $P_{Conduction}$, must be transfered axially in the journal, P_J, imposing a temperature gradient in the journal.

The axial journal temperature variation is determined assuming that the journal temperature is constant at any radial cross section, and thus independent of radial and circumferential coordinates R and θ. For simplicity the conduction from lubricant to journal is also assumed to be symmetric about the midsection of the bearing ($z = 0$) giving (7.29). Hereby the energy conduction through any section of the journal can be calculated using (7.30). The journal temperature is then defined at the bearing edges only ($z = \pm\frac{L}{2}$).

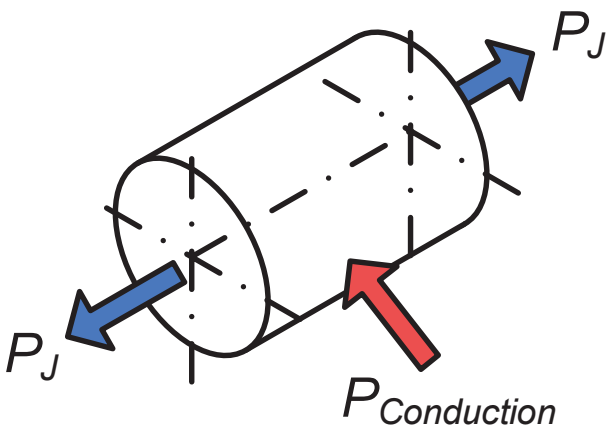

Figure 7.3: Heat flux in journal

$$P_J = \frac{P_{Conduction}}{2} \tag{7.29}$$

$$P_J = A_J k_J \frac{\partial T_J}{\partial z} \tag{7.30}$$

Given the assumption on symmetric conduction from lubricant to journal, the power through any cross section ($z = z_{cs}$) of the journal can be calculated using the conductive terms (7.21) and (7.27) as expressed in (7.31). The double prime indicates pr. unit area.

$$P_{J_{z=\pm z_{cs}}} = R \int_{-z_{cs}}^{+z_{cs}} \int_{-\pi}^{+\pi} \frac{P''_{Conduction}}{2} d\theta dz \tag{7.31}$$

Finally (7.30) and (7.31) are combined into (7.32) expressing the journal temperature gradient at any cross section of the journal:

$$\frac{\partial T_J}{\partial z}_{z=\pm z_{cs}} = \frac{R \int_{-z_{cs}}^{+z_{cs}} \int_{-\pi}^{+\pi} P''_{Conduction} d\theta dz}{2 A_J k_J} \tag{7.32}$$

Hereby the axial temperature profile can be found solving the boundary value problem described by the differential equation (7.32) knowing the temperature at $z = \pm\frac{L}{2}$.

Figure 7.4 shows an example of the axial temperature variation in a journal using a constant conduction from the lubricant. The impact of the variable journal temperature is that the journal is capable of transferring a higher heat flux at the edges of the journal which are closer connected to the boundary with no lubricant heat flux and thus a big heat sink and heat transfer capacity by convection and conduction.

Once the validity of the axial temperature profile is established through comparison with a full 3-dimensional thermal model or an experimental setup it is easy to

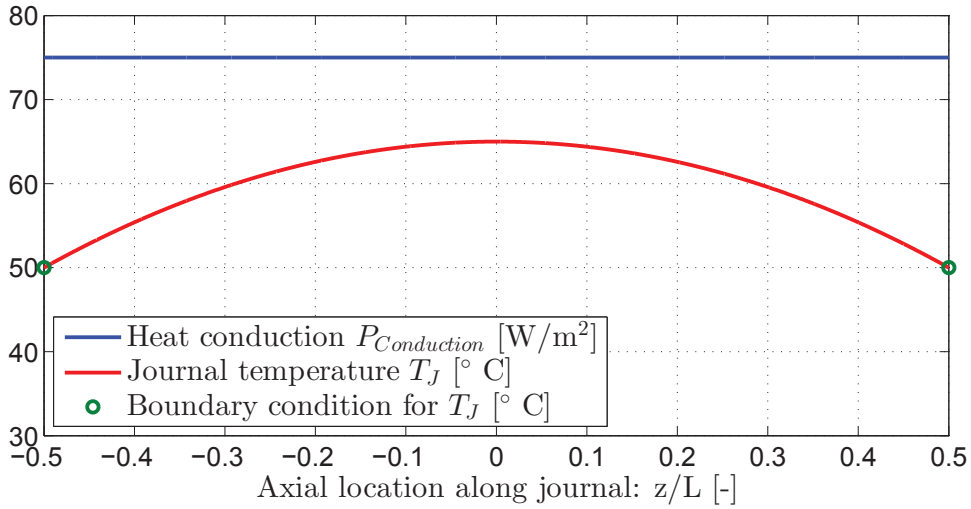

Figure 7.4: Example of variation of journal temperature at constant heat conduction through journal.

apply to various bearing applications since the temperature at the bearing edges is straightforward to measure accurately.

7.3 Boundary conditions

The lubricant temperature for all nodes located in the inlet grooves or on the groove boundary as well, as journal temperatures for all nodes on the journal edges, are defined and constant throughout an analysis.

The iterative procedure required to include a hot oil carry-over effect is not implemented. This corresponds to a very effective oil exchange at the lubrication grooves.

In order to compensate for the missing implementation of the hot oil carry-over effect, the lubricant inlet temperature is offset, typically +5 to +10 °C, compared to the actual lubricant supply temperature.

7.4 Finite difference formulation

The energy equations (7.7) and (7.24) are solved numerically using finite difference formulation where the temperature gradient at each individual node is approximated using the node value together with the neighboring nodes' values as illustrated in figure 7.5. $D\phi(x^*)_{centered}$ denotes the derivative of the field variable $\phi(x)$ at x^* using a centered approximation. Using this method the derivatives are removed from the energy equations and instead a linear system of equations is obtained. The pressure gradients will not be expressed using finite difference. Instead the FEM interpolation functions (5.40) are used for the gradients at the FDM node locations.

The finite element method can be applied for the energy equation although special attention is required since the convective term in the energy equation can cause instabilities when using FEM. This can be solved using upwind finite element techniques [69][70][71].

The thermo-model is coupled with the elastohydrodynamic model using direct substitution.

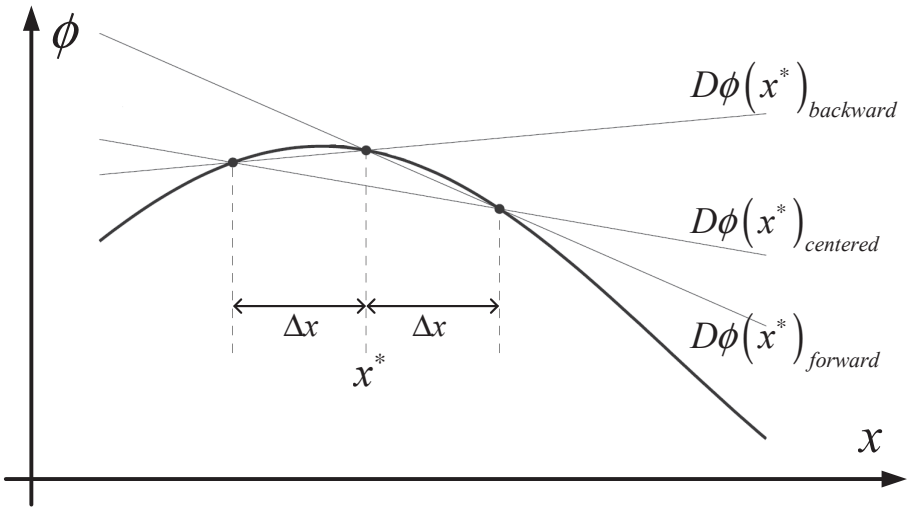

Figure 7.5: Finite difference approximations: Forward, backward and central approximations

The finite difference equations corresponding to the energy equations (7.7) and (7.24) are derived simultaneously including both of the two methods representing the conduction terms as shown in (7.33).

$$\begin{aligned}
&\rho c\left(\frac{1}{R}\frac{\partial T_m}{\partial \theta}q'_\theta + \frac{\partial T_m}{\partial z}q'_z\right) = \\
&\left[k\frac{\partial T}{\partial x}\right]_{x=0}^{x=h} + \alpha_J\left(T_J - T_m\right) + \alpha_B\left(T_B - T_m\right) \\
&+ \frac{\mu_m\omega^2R^2}{h} + \frac{h^3}{12\mu_m}\left(\frac{1}{R^2}\left(\frac{\partial p}{\partial \theta}\right)^2 + \left(\frac{\partial p}{\partial z}\right)^2\right)
\end{aligned} \tag{7.33}$$

The definite integral of (7.33) is calculated using the temperature profile (7.18) to calculate gradients at $x = 0$ and $x = h$ as shown in (7.34) and (7.35).

$$\frac{\partial T}{\partial x}_{x=0} = 0 \tag{7.34}$$

$$\frac{\partial T}{\partial x}_{x=h} = \frac{3\left(T_J - T_m\right)}{h} \tag{7.35}$$

(7.34) and (7.35) are substituted into (7.33) giving (7.36). The flow expressions q'_θ (5.12) and q'_z (5.13) are left out for simplicity.

$$\begin{aligned}&\rho c\left(\frac{1}{R}\frac{\partial T_m}{\partial\theta}q'_\theta+\frac{\partial T_m}{\partial z}q'_z\right)=\\&\frac{3k\left(T_J-T_m\right)}{h}+\alpha_J\left(T_J-T_m\right)+\alpha_B\left(T_B-T_m\right)\\&+\frac{\mu_m\omega^2R^2}{h}+\frac{h^3}{12\mu_m}\left(\frac{1}{R^2}\left(\frac{\partial p}{\partial\theta}\right)^2+\left(\frac{\partial p}{\partial z}\right)^2\right)\end{aligned}\tag{7.36}$$

7.4.1 Derivation of finite difference approximations

The centered finite difference approximation is derived using the two neighboring node values as illustrated in figure 7.5. The three node values are combined in a linear manner as shown in equation (7.37).

$$D\phi(x^*)_{centered}=a\phi\left(x^*\right)+b\phi\left(x^*+\Delta x\right)+c\phi\left(x^*-\Delta x\right)\tag{7.37}$$

The unknowns a, b and c are determined using the Taylor expansions of $\phi\left(x\right)$ around x^* shown in (7.38):

$$\begin{aligned}\phi\left(x^*+\Delta x\right)&=\phi\left(x^*\right)+\Delta x\frac{\partial\phi}{\partial x^*}+\frac{1}{2!}\Delta x^2\frac{\partial^2\phi}{\partial x^{*2}}+\frac{1}{3!}\Delta x^3\frac{\partial^3\phi}{\partial x^{*3}}+...\\\phi\left(x^*-\Delta x\right)&=\phi\left(x^*\right)-\Delta x\frac{\partial\phi}{\partial x^*}+\frac{1}{2!}\Delta x^2\frac{\partial^2\phi}{\partial x^{*2}}-\frac{1}{3!}\Delta x^3\frac{\partial^3\phi}{\partial x^{*3}}+...\end{aligned}\tag{7.38}$$

The Taylor expansions (7.38) are inserted into (7.37) giving (7.39). Since only three coefficients (a, b and c) are chosen for the approximation, terms of Δx^3 and higher cannot be included and hence the order of accuracy of the approximation is $O\left(\Delta x^2\right)$.

$$D\phi(x^*)_{centered}=\left(a+b+c\right)\phi\left(x^*\right)+\left(b-c\right)\Delta x\frac{\partial\phi}{\partial x^*}+\left(b+c\right)\frac{1}{2!}\Delta x^2\frac{\partial^2\phi}{\partial x^{*2}}+O\left(\Delta x^3\right)\tag{7.39}$$

In order for the approximation to be valid equation (7.40) must be satisfied. Using this requirement together with (7.39) allows for the establishment of the equations (7.41) which are then used to determine the coefficients a, b and c.

$$D\phi\left(x^*\right)=\frac{\partial\phi}{\partial x^*}\tag{7.40}$$

$$\begin{array}{lcl} a+b+c=0 & & a=0 \\ (b-c)\,\Delta x=1 & \Leftrightarrow & b=\frac{1}{2\Delta x} \\ (b+c)\,\frac{1}{2!}\Delta x^2=0 & & c=\frac{-1}{2\Delta x} \end{array} \tag{7.41}$$

Combining (7.41) and (7.39) gives the central finite difference approximation:

$$D\phi(x^*)_{centered}=\frac{\phi\,(x^*+\Delta x)-\phi\,(x^*-\Delta x)}{2\Delta x} \tag{7.42}$$

The same procedure is applied to achieve the forward and backward approximations shown in (7.43) and (7.44) obtaining the same order of accuracy as the centered approximation (7.42): $O\,(\Delta x^2)$.

$$D\phi(x^*)_{forward}=\frac{-\frac{3}{2}\phi\,(x^*)+2\phi\,(x^*+\Delta x)-\frac{1}{2}\phi\,(x^*+2\Delta x)}{\Delta x} \tag{7.43}$$

$$D\phi(x^*)_{backward}=\frac{\frac{3}{2}\phi\,(x^*)-2\phi\,(x^*-\Delta x)+\frac{1}{2}\phi\,(x^*-2\Delta x)}{\Delta x} \tag{7.44}$$

7.4.2 Finite difference equations

The finite difference approximations (7.42), (7.43) and (7.44) are used to create approximations of the derivatives of the lubricant temperature in axial and circumferential direction. These expressions are then substituted into the energy equation (7.36). The forward and backward approximations are applied for the boundary nodes which only have neighboring nodes to one side.

When the centered approximations are used in both the axial and circumferential direction the energy equation (7.36) is expressed as shown in (7.45) using the node values illustrated in figure 7.6.

$$\begin{aligned} &-T\,(\theta^*,z^*-\Delta z)\,\frac{1}{2}\frac{\rho c q'_z}{\Delta z}+T\,(\theta^*,z^*+\Delta z)\,\frac{1}{2}\frac{\rho c q'_z}{\Delta z} \\ &+T\,(\theta^*,z^*)\,\frac{\alpha_B h+\alpha_J h+3k}{h} \\ &-T\,(\theta^*-\Delta\theta,z^*)\,\frac{1}{2}\frac{\rho c q'_\theta}{\Delta\theta R}+T\,(\theta^*+\Delta\theta,z^*)\,\frac{1}{2}\frac{\rho c q'_\theta}{\Delta\theta R} \\ &=\alpha_J T_J+\alpha_B T_B+\frac{3kT_J}{h}+\frac{\mu\omega^2R^2}{h}+\frac{1}{12}\left(\frac{\partial p}{\partial\theta}\right)^2\frac{h^3}{\mu R^2}+\frac{1}{12}\left(\frac{\partial p}{\partial z}\right)^2\frac{h^3}{\mu} \end{aligned} \tag{7.45}$$

The same procedure is applied to obtain the remaining 8 combinations of forward/central/backward approximations in axial and circumferential direction.

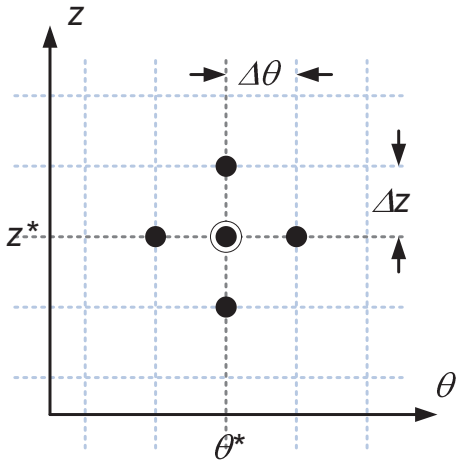

Figure 7.6: Node values used for finite difference center/centre approximation for energy equation

7.5 Conversion between FEM mesh and FDM mesh

When the finite element based hydrodynamic and elasticity equations are coupled with the finite difference based energy equations a conversion between the field variables is required due to the different mesh layouts. The FEM mesh originates from the finite element program used to set up the force-displacement correlation. The FEM mesh must therefore be expected to be arbitrary whereas the FDM mesh requires an equidistant node layout.

Mesh transformation: FEM to FDM

A transformation matrix is used to convert field variables from the FEM mesh to the FDM mesh. The element interpolation functions are used for this purpose using the procedure described in the following:

All coefficients of the element interpolation functions are found using (5.38) and (5.39). Then, for all elements, the natural coordinates N_j can be found for all FDM nodes using the nodal coordinates in equation (5.35). When all natural coordinates are known, the values are used to identify the FEM elements in which the individual FDM nodes reside. When an FDM node is inside or at the boundary of an FEM element all natural coordinates will be equal to or less than 1. If a natural coordinate equals 1 the FDM node is coincident with a FEM node and thus several FEM elements can be used for the interpolation. Since the FEM mesh has C_0 continuity it does not matter which of these elements is chosen for mesh transformation.

A transformation matrix $\mathbf{T}$ can then be established by assembly of the identified natural coordinates N_1 to N_3 for all FDM nodes. The method of assembly is shown in (7.46) for meshes comprised of m FEM nodes and n FDM nodes.

$$\phi_{FDM} = \mathbf{T}\phi_{FEM}$$

$$\underset{FDM\ n\times 1}{\begin{Bmatrix} \cdot \\ \phi \\ \cdot \\ \cdot \\ \cdot \end{Bmatrix}} = \underset{n\times m}{\begin{bmatrix} \cdot & \cdot & \cdot & \cdot & \cdot & \cdot \\ \cdot & N_1 & \cdot & \cdot & N_2 & N_3 \\ \cdot & \cdot & \cdot & \cdot & \cdot & \cdot \\ \cdot & \cdot & \cdot & \cdot & \cdot & \cdot \\ \cdot & \cdot & \cdot & \cdot & \cdot & \cdot \end{bmatrix}} \underset{FEM\ m\times 1}{\begin{Bmatrix} \cdot \\ \phi_1 \\ \cdot \\ \cdot \\ \phi_2 \\ \phi_3 \end{Bmatrix}} \tag{7.46}$$

Mesh transformation: FDM to FEM

When performing the reverse transformation, from FDM to FEM mesh, is it straight forward to apply double linear interpolation due to the equidistant properties of the FDM mesh.

7.6 Check of mass and energy balance

To evaluate the implementation of the models described in chapter 7, the energy- and mass-balance is checked. This is done for the two different methods of treating the conduction term.

A conventional full journal bearing is used for this purpose and the bearing parameters and operating conditions are shown in table 7.1.

Bearing radius	R	50	mm
Bearing length	L	50	mm
Radial clearance	$\mathrm{C_r}$	50	μm
Rotational speed	ω	1690	rpm
Journal position in x	χ_x	0	μm
Journal position in y	χ_y	$-0.8C_r$	μm
Journal velocity in x	$\dot{\chi}_x$	0	mm/s
Journal velocity in y	$\dot{\chi}_y$	0	mm/s
Lubricant grade ISO VG	-	32	-
Lubricant temperature at inlet	T_{Inlet}	50	$^\circ$ C
Journal temperature at brg.edge	T_J	55	$^\circ$ C
Lubricant thermal conductivity	k	0.13	W/m/°C
Journal thermal conductivity	k_J	40	W/m/°C
Heat transfer coefficient	α	1500	W/m^2/°C

Table 7.1: Bearing geometry and operating conditions

Due to the complications of mass- and energy-balance calculations at the lubrication grooves the bearing used for the verification purpose only has a single groove at $\theta = 0$. See figures 5.1(a) and 5.1(b) for coordinate system (page 28).

7.6.1 Conduction using temperature gradient

Using the temperature gradient model to predict conduction through the journal, the steady state solution is found for the bearing parameters listed in table 7.1. In the following pages the thermohydrodynamic behavior is examined through discussion of the solutions found for pressure, lubricant temperature, conduction and viscous dissipation. Finally the mass- and energy-balance analysis is shown.

Figure 7.7 shows the pressure distribution reaching a maximum pressure of 14.1 MPa giving a load carrying capacity of 19.6 kN. As expected the the pressure build-up zone is only covering the left section of the bearing, i.e. $0.5\pi < \theta < 1.5\pi$, due to cavitation in the region with divergent bearing clearance.

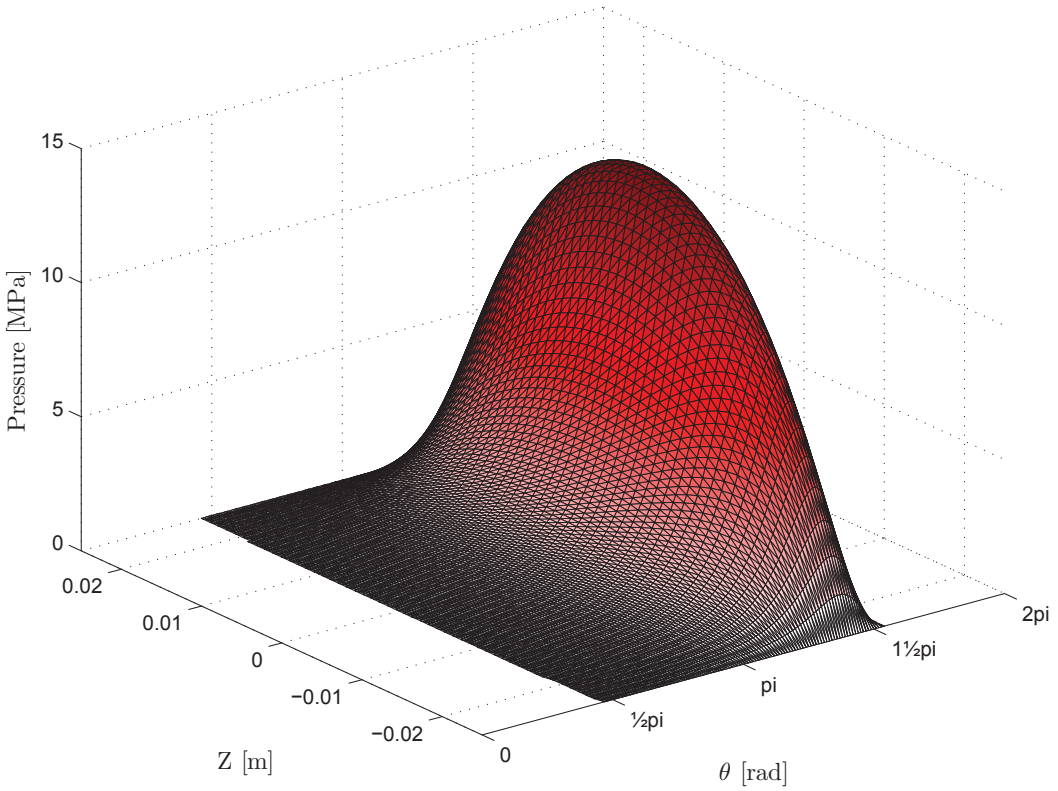

Figure 7.7: Pressure distribution. No mesh shown for cavitated nodes.

Figure 7.8 shows the mean temperature in the lubricant with a maximum mean value of 62.5 °C corresponding to a maximum lubricant temperature of 63.9 °C at the adiabatic surface ($x = 0$) according to equation (7.18).

As stated in table 7.1 the journal temperature is set to 55 °C at the bearing edges and is found to increase to a maximum value of 59.8 °C at the bearing center in a parabolic manner as illustrated in figure 7.4 page 63.

Interestingly the temperature gradient $\frac{\partial T_m}{\partial \theta}$ is zero in the cavitated region just after the pressure build-up ($1.5\pi < \theta < 2\pi$).

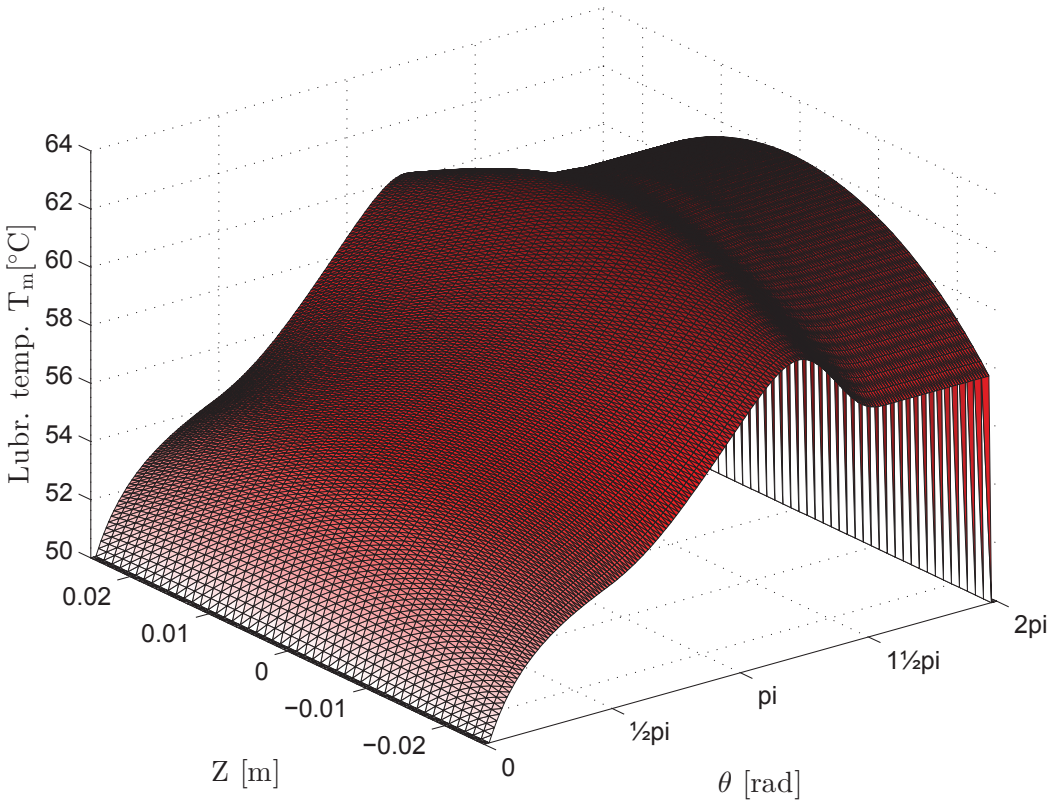

Figure 7.8: Local mean lubricant temperature. Averaging over lubricant film thickness as described in equation (7.17).

Figure 7.9 shows the local energy conduction though the journal surface. Just after the lubricant inlet groove, $\theta = 0$, the journal heats up the lubricant. At the pressure build-up zone, and also the following cavitated region, the viscous dissipation heats the lubricant to a level above that of the journal and hence the journal removes energy in this region.

From this it is evident that the journal transfers energy to and from the lubricant and hence smoothens the temperature spikes. In this case it furthermore has an overall cooling effect on the lubricant (evident from figure 7.12).

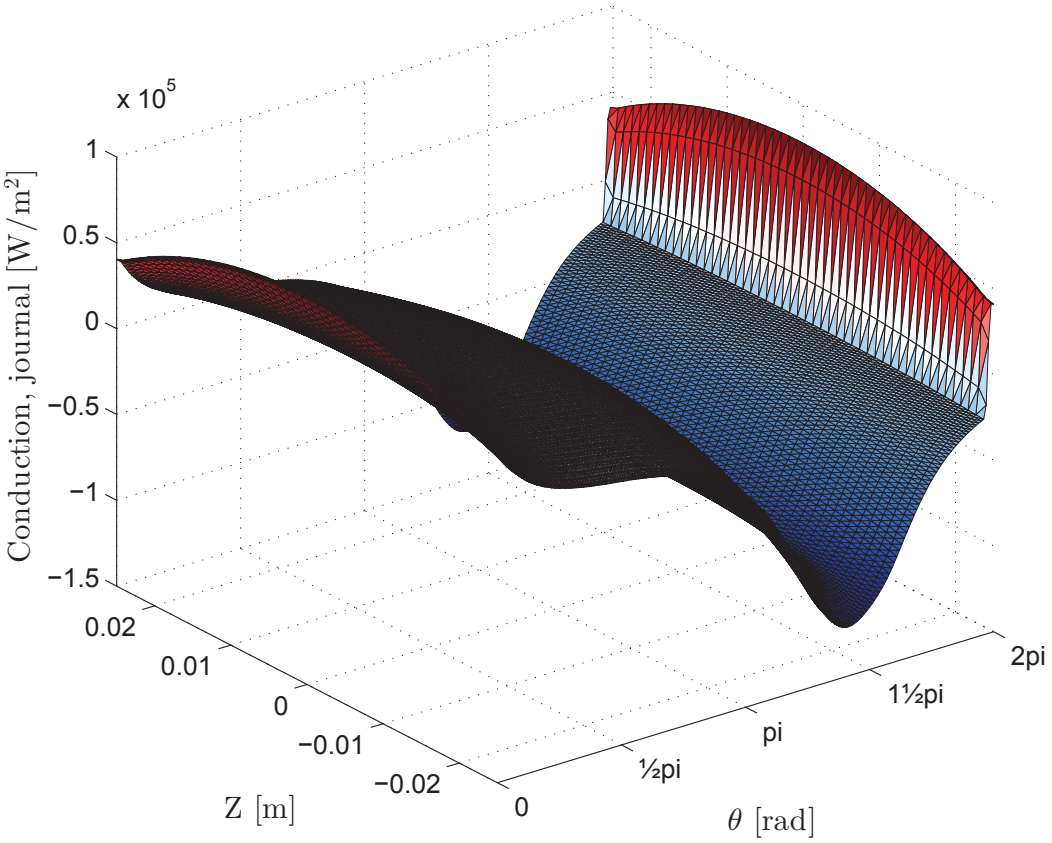

Figure 7.9: Local conduction through journal. Negative values (blue) imply cooling of the lubricant.

Figure 7.10 shows the local viscous dissipation pr. unit film height in the bearing. Interestingly the maximum specific dissipation occurs at the edges of the bearing. This is due to the high axial pressure gradient at this location imposing a high axial flow and thus also a correspondingly high shear rate dissipating energy into the lubricant. Furthermore, the lubricant temperature is also low at the edges, giving a correspondingly higher viscosity which again leads to higher viscous dissipation when exposed to shear.

Also worth noticing, the location with the maximum temperature (on figure 7.8) does not hold the highest viscous dissipation, on the contrary, there is actually a dip on viscous dissipation in this zone. This is because the Poiseuille flow counterbalances the Couette flow and hence reduces viscous shear due to reduced lubricant flow rate. The reduced flow rate also induces less lubricant exchange and this then results in high lubricant temperatures.

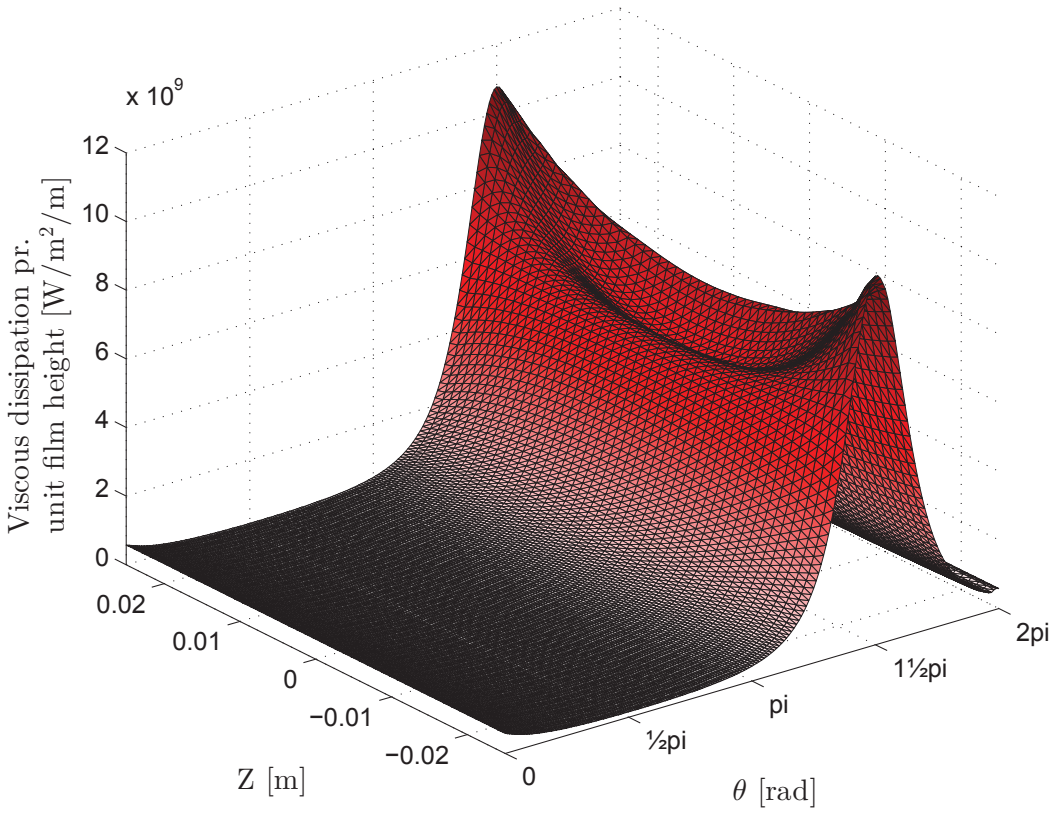

Figure 7.10: Local viscous dissipation per unit film height.

The mass- and energy-balance is checked using a control volume as illustrated in figure 7.2 page 58. The volume has a circumferential extent of 10 °. The volume is moved along the bearing clearance and for each location the error e is found and plotted in figure 7.11.

The error is calculated using equations (7.47) and (7.48), where the subscript Λ

denotes *through boundary*.

$$e_{\text{massbalance}} = \frac{\sum q_\Lambda}{\sum |q_\Lambda|} 100\% \tag{7.47}$$

$$e_{\text{energybalance}} = \frac{\sum P_\Lambda}{\sum |P_\Lambda|} 100\% \tag{7.48}$$

As expected figure 7.11 shows a significant error in energy-balance in the cavitated regions. This error is a consequence of the cavitation algorithm which does not ensure mass-balance in the cavitated regions. It is also seen that the error in energy-balance starts already at the zone with a high pressure gradient just before the cavitated region, near $\theta = 1.5\pi$.

Overall the mass-balance error is at a very low level, around 0.2 %, in the pressure build-up zone and the energy-balance error is within 1-5 %, in the major part, which is believed to be within acceptable accuracy.

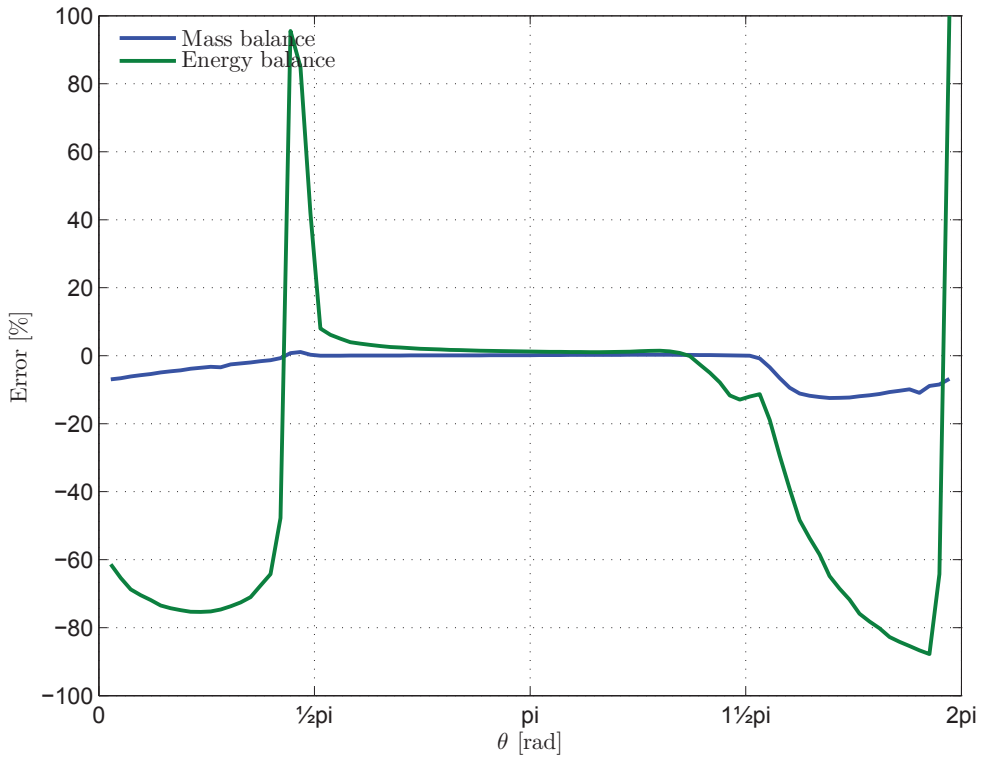

Figure 7.11: Mass and energy balance check.

Figure 7.12 breaks the energy flows into the individual contributers: viscous dissipation, axial convection, circumferential convection and conduction. Positive is defined as energy into the lubricant.

Interestingly, the viscous dissipation is almost entirely counterbalanced by the conduction. Thus the axial convection is counterbalanced by circumferential convection.

Ideally the sum should be 0 over the entire circumference if energy-balance was achieved.

The spikes are caused by jumps in the size of the control volume at locations when the mesh does not coincide nicely with the control volume.

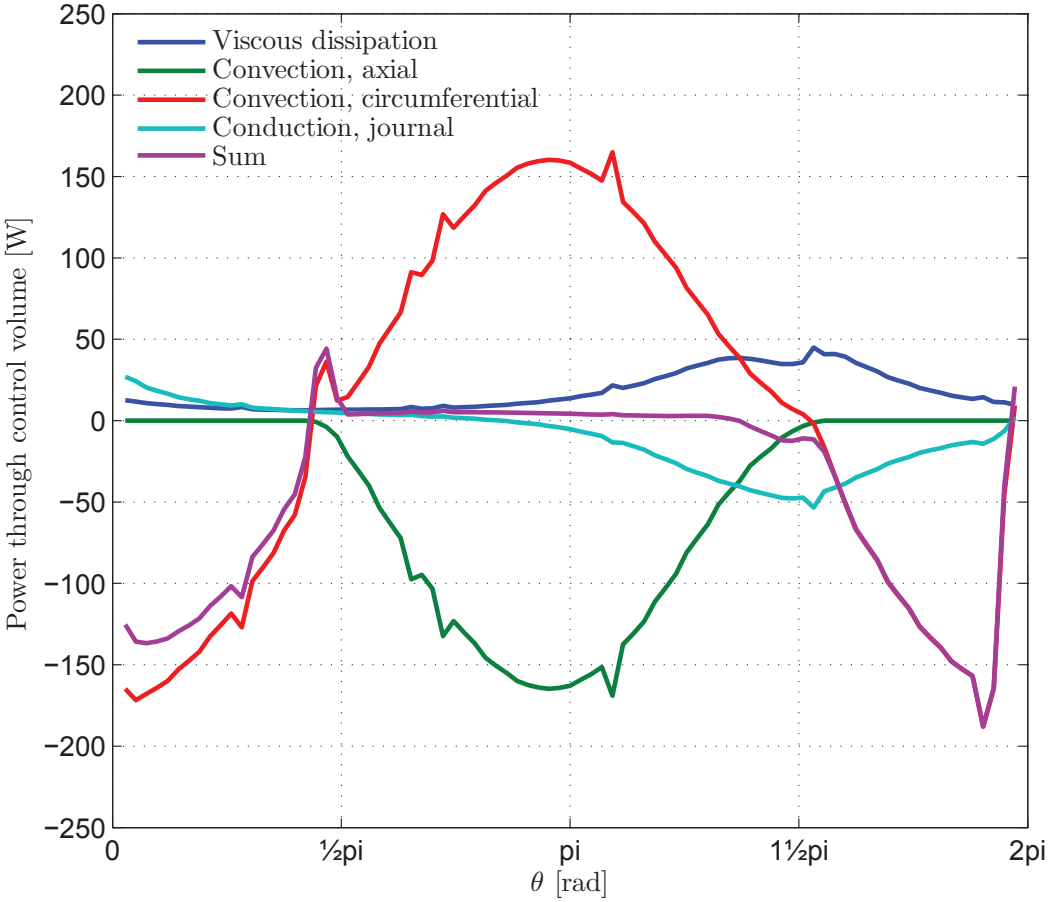

Figure 7.12: Energy balance break down.

7.6.2 Conduction using heat transfer coefficients

The same bearing configuration is used to analyze the response of the model using temperature difference and heat transfer coefficients to predict heat conduction through the journal.

Figure 7.13 shows the pressure distribution reaching a maximum pressure of 11.3 MPa giving a load carrying capacity of 16.6 kN, somewhat lower compared to the previous model.

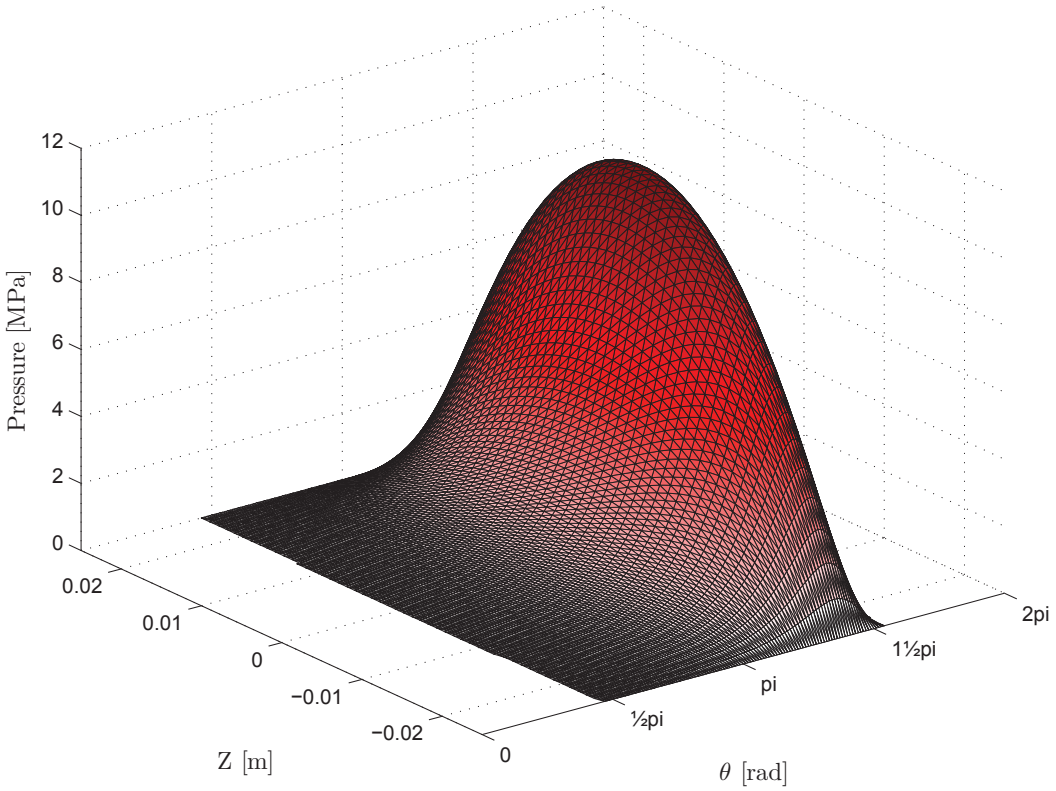

Figure 7.13: Pressure distribution. No mesh shown for cavitated nodes.

Figure 7.14 shows the local lubricant temperature with a maximum value of 82.4 °C. This is much higher compared to the previous model and is due to less cooling through the journal. The axial lubricant temperature gradient is almost zero and can, for this model and bearing parameters, be neglected if one wishes to simplify the model.

The lower heat transfer through the journal induces a correspondingly lower temperature rise to 57.3 °C compared to the 59.8 °C of the previous model. This gives a journal temperature difference of 2.3 and 4.8 °C of respectively.

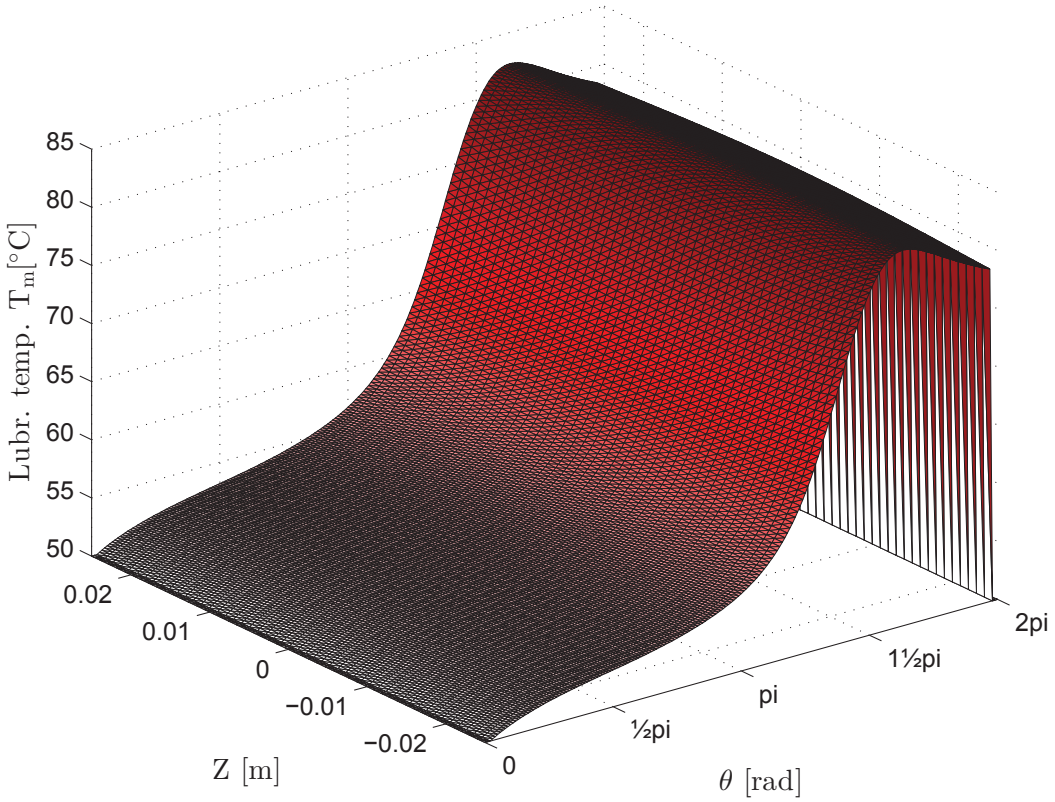

Figure 7.14: Local lubricant temperature

Figure 7.15 and 7.16 shows the journal conduction and viscous dissipation respectively. Qualitatively they have the same tendencies as for the previous model, except the conduction sees very little variation in axial direction due to the low axial lubricant and journal temperature gradients.

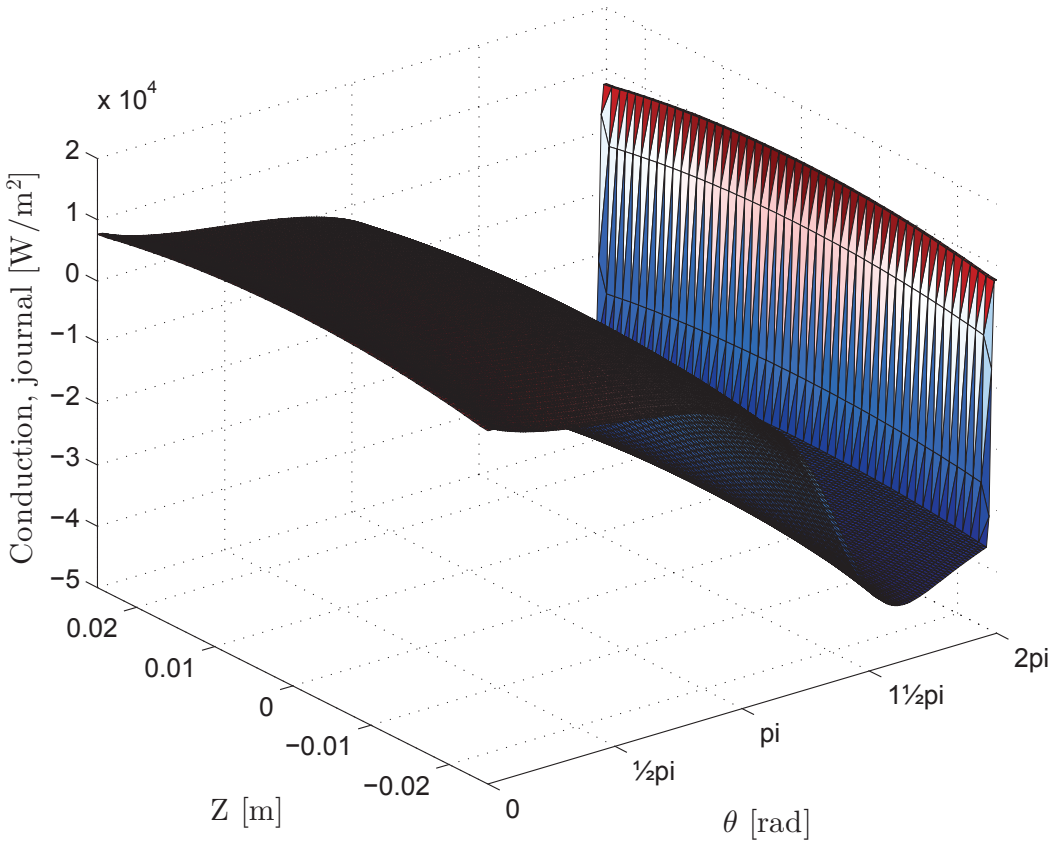

Figure 7.15: Local conduction through journal. Negative values (blue) imply cooling of the lubricant.

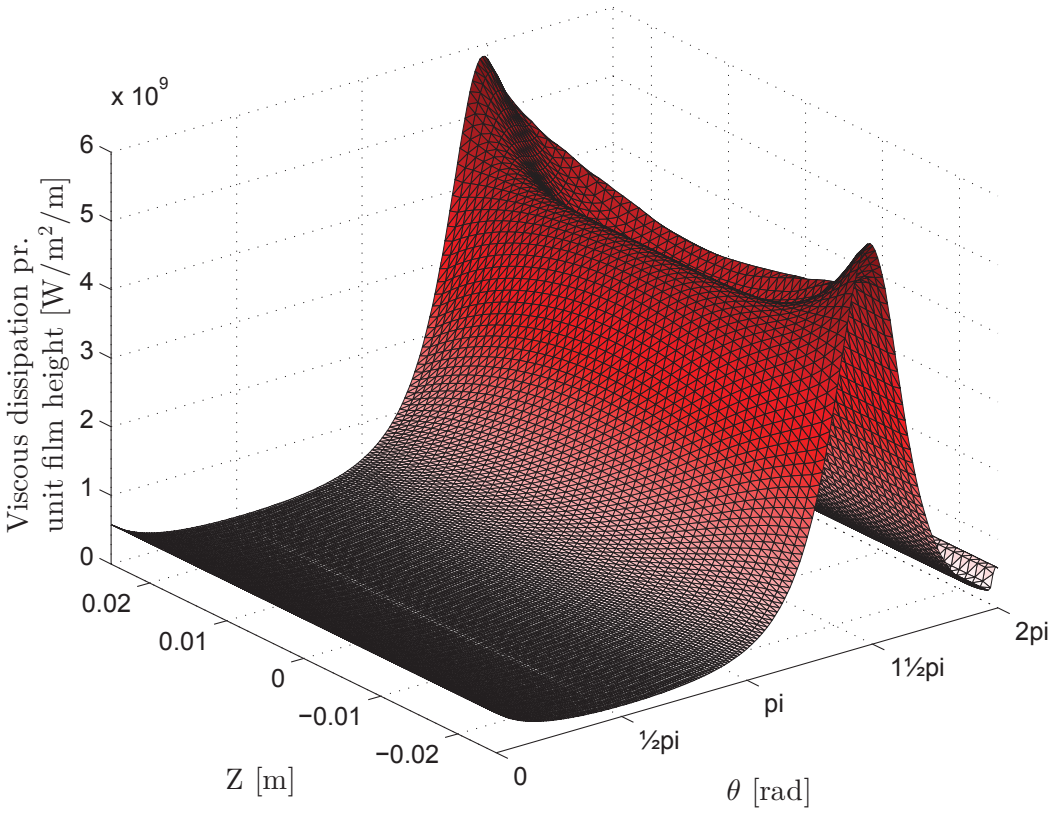

Figure 7.16: Local viscous dissipation per unit film height.

The mass- and energy-balance analysis shown in figure 7.17 is almost identical to the previous one with an error in mass-balance of 0-0.3 % and 1-3 % in energy-balance when only considering the region with pressure build-up (again showing a higher error in energy-balance, up to 19%, at the very last part with high pressure gradients).

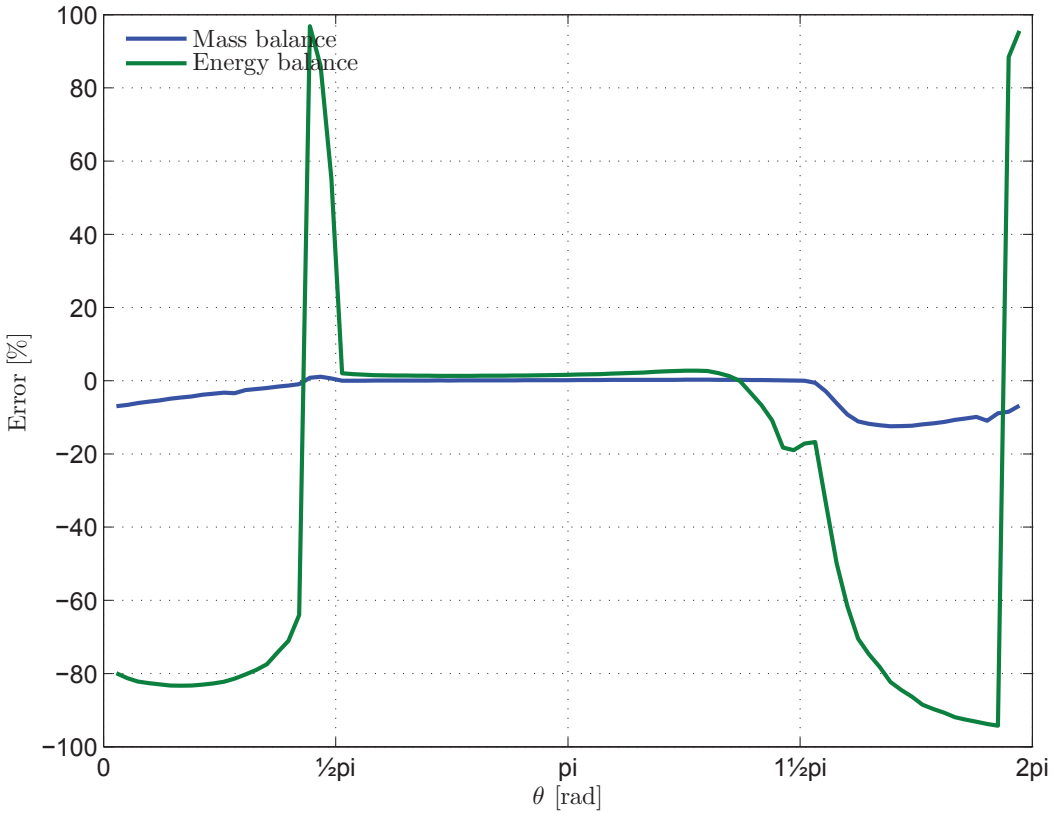

Figure 7.17: Mass and energy balance check.

Figure 7.18 shows the individual contributers of energy transfer and again positive is defined as energy into the lubricant.

For this model, with the given parameters, the majority of the viscous dissipation is carried away through convection. Not by conduction, as for the model using temperature gradient shown in figure 7.12.

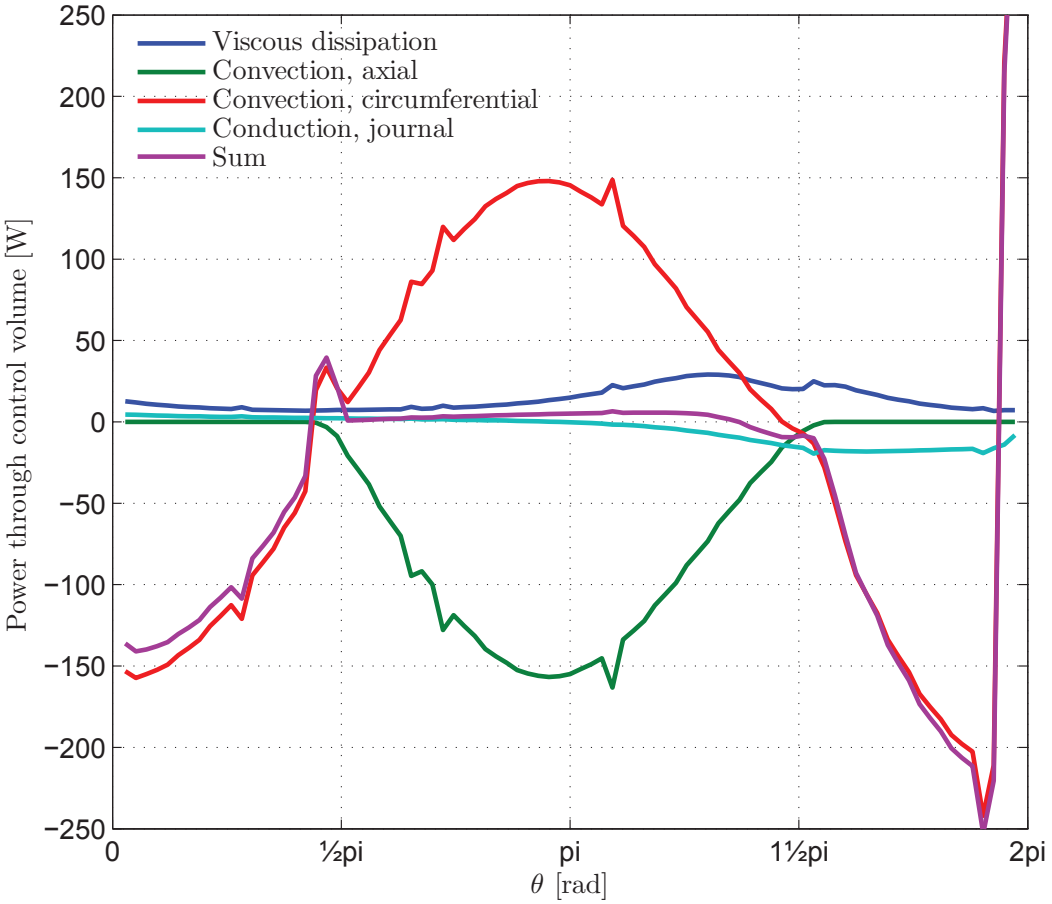

Figure 7.18: Energy balance break down.

Chapter 8

5 DOF bearing model

The bearing model described until now only allows forces and journal movements in $\bar{x}$- and $\bar{y}$-direction, e.g. 2 degrees of freedom (DOF). If accurate prediction of bearing performance is required for a full bearing system the model must be extended to 5 DOF for loads and movements.

For bearing systems where the axial and radial bearings are coupled, maybe indirectly through the elasticity of the supporting structure, it is advantageously to solve the two, or more, bearing systems simultaneously and thus avoid the iteration process that would elsewise be required to achieve a converged solution for elasticity and oil film forces.

A literature study on simulations of 5 DOF bearing systems only reveal the work of Kim et al. [72][73]. They analyze the spindle bearing of a computer harddisk drive with respect to stability and especially the influence of the angular position of the journal on stability. The stability is investigated using an analytical approach together with the dynamic coefficients of the bearing system.

No work has been found studying coupled bearing systems supporting 5 DOF and also considering the structural elasticity as presented in this work.

Equation (8.1) shows the equation of motion describing how the external forces W and moments G are counterbalanced by oil film forces and inertia forces. Again accelerations are assumed negligible and hence the inertia forces can be neglected. The mass matrix $\mathbf{M}$ is consequently removed. χ represents linear position coordinate whereas and ψ represents angular position. Subscripts refer to the axis of translation or rotation (see figure 5.1(a) page 28 for coordinate systems).

$$\begin{aligned}
&\left\{\begin{array}{c} W_{\bar{x}} \\ W_{\bar{y}} \\ W_{\bar{z}} \\ G_{\bar{x}} \\ G_{\bar{y}} \end{array}\right\} + \left\{\begin{array}{c} F_{\bar{x}} \\ F_{\bar{y}} \\ F_{\bar{z}} \\ M_{\bar{x}} \\ M_{\bar{y}} \end{array}\right\} = \left\{\begin{array}{c} 0 \\ 0 \\ 0 \\ 0 \\ 0 \end{array}\right\} \\
&\qquad = \left\{\begin{array}{c} W_{\bar{x}} \\ W_{\bar{y}} \\ W_{\bar{z}} \\ G_{\bar{x}} \\ G_{\bar{y}} \end{array}\right\} + \mathbf{K}\left\{\begin{array}{c} \chi_{\bar{x}} \\ \chi_{\bar{y}} \\ \chi_{\bar{z}} \\ \psi_{\bar{x}} \\ \psi_{\bar{y}} \end{array}\right\} + \mathbf{D}\left\{\begin{array}{c} \dot{\chi}_{\bar{x}} \\ \dot{\chi}_{\bar{y}} \\ \dot{\chi}_{\bar{z}} \\ \dot{\psi}_{\bar{x}} \\ \dot{\psi}_{\bar{y}} \end{array}\right\} + \mathbf{M}\left\{\begin{array}{c} \ddot{\chi}_{\bar{x}} \\ \ddot{\chi}_{\bar{y}} \\ \ddot{\chi}_{\bar{z}} \\ \ddot{\psi}_{\bar{x}} \\ \ddot{\psi}_{\bar{y}} \end{array}\right\}
\end{aligned} \tag{8.1}$$

The extension from 2 to 5 DOF is facilitated through 2 major changes:

- in addition to the radial bearing model for oil film forces and elasticity, using a cylindrical coordinate system, an axial bearing model is added using a polar coordinate system. These models are then solved simultaneously.
- angular and axial DOF are added to motion and load equations obtaining 5 DOF.

The element equations for the fluid forces and dynamic coefficients, for the 5 DOF system, will be derived in the following sections for the cylindrical and polar coordinate systems. The approach is similar to the one described in sections 5.2 and 5.3.

The thermal model will not be implemented for the 5 DOF model, thus the model will be elastohydrodynamic (EHD).

8.1 Cylindrical representation

Let us recall Reynolds equation in cylindrical coordinates:

$$\frac{1}{R}\frac{\partial}{\partial\theta}\left(\frac{h^3}{\mu R}\frac{\partial p}{\partial\theta}\right) + \frac{\partial}{\partial z}\left(\frac{h^3}{\mu}\frac{\partial p}{\partial z}\right) = 6\omega\frac{\partial h}{\partial\theta} + 12\frac{\partial h}{\partial t} \tag{8.2}$$

Using Lund's principle of perturbation Reynolds equation and the film thickness expression are perturbed with respect to the 5 DOF. A Taylor expansion is used and terms of orders 2 and higher are neglected since perturbations can be assumed to be small. The notation $\partial p/\partial i = p_i$ is used for the differentiations of p with respect to perturbation dimension i.

$$\begin{aligned}
p =& p_0 + \Delta\chi_{\bar{x}}p_{\chi_{\bar{x}}} + \Delta\dot{\chi}_{\bar{x}}p_{\dot{\chi}_{\bar{x}}} + \Delta\chi_{\bar{y}}p_{\chi_{\bar{y}}} + \Delta\dot{\chi}_{\bar{y}}p_{\dot{\chi}_{\bar{y}}} + \Delta\chi_{\bar{z}}p_{\chi_{\bar{z}}} + \Delta\dot{\chi}_{\bar{z}}p_{\dot{\chi}_{\bar{z}}} \\
&+ \Delta\psi_{\bar{x}}p_{\psi_{\bar{x}}} + \Delta\dot{\psi}_{\bar{x}}p_{\dot{\psi}_{\bar{x}}} + \Delta\psi_{\bar{y}}p_{\psi_{\bar{y}}} + \Delta\dot{\psi}_{\bar{y}}p_{\dot{\psi}_{\bar{y}}}
\end{aligned} \tag{8.3}$$

To facilitate projections a unit vector n normal to the bearing surface, pointing from stator towards rotor, is introduced:

$$n\left(\theta\right) = \left\{ \begin{array}{c} n_{\bar{x}} \\ n_{\bar{y}} \\ n_{\bar{z}} \end{array} \right\} = \pm \left\{ \begin{array}{c} \cos\left(\theta\right) \\ \sin\left(\theta\right) \\ 0 \end{array} \right\} \tag{8.4}$$

The perturbations are also introduced in the film thickness and squeeze term equations (8.5) and (8.6):

$$h = h_0 + \Delta\chi_{\bar{x}} n_{\bar{x}} + \Delta\chi_{\bar{y}} n_{\bar{y}} - \Delta\psi_{\bar{x}} \bar{z} n_{\bar{y}} + \Delta\psi_{\bar{y}} \bar{z} n_{\bar{x}} \tag{8.5}$$

$$\frac{\partial h}{\partial t} = \frac{\partial h_0}{\partial t} + \Delta\dot{\chi}_{\bar{x}} n_{\bar{x}} + \Delta\dot{\chi}_{\bar{y}} n_{\bar{y}} - \Delta\dot{\psi}_{\bar{x}} \bar{z} n_{\bar{y}} + \Delta\dot{\psi}_{\bar{y}} \bar{z} n_{\bar{x}} \tag{8.6}$$

From (8.5) and (8.6) it is seen that perturbations in $\bar{z}$-direction has no influence on the film thickness or squeeze term and hence the corresponding terms can be canceled from (8.3).

Equations (8.3) to (8.6) are inserted into (8.2) and separated with respect to perturbations and only keeping the first order perturbation terms.

$$\frac{1}{R}\frac{\partial}{\partial\theta}\left(\frac{h_0^3}{\mu R}\frac{\partial p_i}{\partial\theta}\right) + \frac{\partial}{\partial z}\left(\frac{h_0^3}{\mu}\frac{\partial p_i}{\partial z}\right) =$$

$$\begin{cases} +6\omega\frac{\partial h_0}{\partial\theta} + 12\frac{\partial h_0}{\partial t} & , p_i = p_0 \\ -\frac{1}{R}\frac{\partial}{\partial\theta}\left(\frac{3h_0^2 n_{\bar{x}}}{\mu R}\frac{\partial p_0}{\partial\theta}\right) - \frac{\partial}{\partial z}\left(\frac{3h_0^2 n_{\bar{x}}}{\mu}\frac{\partial p_0}{\partial z}\right) + 6\omega\frac{\partial n_{\bar{x}}}{\partial\theta} & , p_i = p_{\chi_{\bar{x}}} \\ -\frac{1}{R}\frac{\partial}{\partial\theta}\left(\frac{3h_0^2 n_{\bar{y}}}{\mu R}\frac{\partial p_0}{\partial\theta}\right) - \frac{\partial}{\partial z}\left(\frac{3h_0^2 n_{\bar{y}}}{\mu}\frac{\partial p_0}{\partial z}\right) + 6\omega\frac{\partial n_{\bar{y}}}{\partial\theta} & , p_i = p_{\chi_{\bar{y}}} \\ +\frac{1}{R}\frac{\partial}{\partial\theta}\left(\frac{3h_0^2 \bar{z} n_{\bar{y}}}{\mu R}\frac{\partial p_0}{\partial\theta}\right) + \frac{\partial}{\partial z}\left(\frac{3h_0^2 \bar{z} n_{\bar{y}}}{\mu}\frac{\partial p_0}{\partial z}\right) + 6\omega\bar{z}\frac{\partial n_{\bar{y}}}{\partial\theta} & , p_i = p_{\psi_{\bar{x}}} \\ -\frac{1}{R}\frac{\partial}{\partial\theta}\left(\frac{3h_0^2 \bar{z} n_{\bar{x}}}{\mu R}\frac{\partial p_0}{\partial\theta}\right) - \frac{\partial}{\partial z}\left(\frac{3h_0^2 \bar{z} n_{\bar{x}}}{\mu}\frac{\partial p_0}{\partial z}\right) + 6\omega\bar{z}\frac{\partial n_{\bar{x}}}{\partial\theta} & , p_i = p_{\psi_{\bar{y}}} \\ +12 n_{\bar{x}} & , p_i = p_{\dot{\chi}_{\bar{x}}} \\ +12 n_{\bar{y}} & , p_i = p_{\dot{\chi}_{\bar{y}}} \\ -12\bar{z} n_{\bar{y}} & , p_i = p_{\dot{\psi}_{\bar{x}}} \\ +12\bar{z} n_{\bar{x}} & , p_i = p_{\dot{\psi}_{\bar{y}}} \end{cases} \tag{8.7}$$

Equation (8.7) is used to solve for the pressure p_0 and its derivatives with respect to the perturbation dimensions. The derivatives are then integrated and the stiffness and damping matrix of (8.1) can be established. The perturbations in $\bar{z}$-dimension has no influence on the pressure and therefore the corresponding coefficients are zero

(third columns in (8.8) and (8.9)). Since the pressure always acts on the cylindrical surface it cannot give a reaction in $\bar{z}$-dimension, and hence the third rows are also zero.

$$\mathbf{K}_{Cylindrical} = \begin{bmatrix} k_{F_{\bar{x}}\chi_{\bar{x}}} & k_{F_{\bar{x}}\chi_{\bar{y}}} & 0 & k_{F_{\bar{x}}\psi_{\bar{x}}} & k_{F_{\bar{x}}\psi_{\bar{y}}} \\ k_{F_{\bar{y}}\chi_{\bar{x}}} & k_{F_{\bar{y}}\chi_{\bar{y}}} & 0 & k_{F_{\bar{y}}\psi_{\bar{x}}} & k_{F_{\bar{y}}\psi_{\bar{y}}} \\ 0 & 0 & 0 & 0 & 0 \\ k_{M_{\bar{x}}\chi_{\bar{x}}} & k_{M_{\bar{x}}\chi_{\bar{y}}} & 0 & k_{M_{\bar{x}}\psi_{\bar{x}}} & k_{M_{\bar{x}}\psi_{\bar{y}}} \\ k_{M_{\bar{y}}\chi_{\bar{x}}} & k_{M_{\bar{y}}\chi_{\bar{y}}} & 0 & k_{M_{\bar{y}}\psi_{\bar{x}}} & k_{M_{\bar{y}}\psi_{\bar{y}}} \end{bmatrix} \tag{8.8}$$

$$\mathbf{D}_{Cylindrical} = \begin{bmatrix} d_{F_{\bar{x}}\chi_{\bar{x}}} & d_{F_{\bar{x}}\chi_{\bar{y}}} & 0 & d_{F_{\bar{x}}\psi_{\bar{x}}} & d_{F_{\bar{x}}\psi_{\bar{y}}} \\ d_{F_{\bar{y}}\chi_{\bar{x}}} & d_{F_{\bar{y}}\chi_{\bar{y}}} & 0 & d_{F_{\bar{y}}\psi_{\bar{x}}} & d_{F_{\bar{y}}\psi_{\bar{y}}} \\ 0 & 0 & 0 & 0 & 0 \\ d_{M_{\bar{x}}\chi_{\bar{x}}} & d_{M_{\bar{x}}\chi_{\bar{y}}} & 0 & d_{M_{\bar{x}}\psi_{\bar{x}}} & d_{M_{\bar{x}}\psi_{\bar{y}}} \\ d_{M_{\bar{y}}\chi_{\bar{x}}} & d_{M_{\bar{y}}\chi_{\bar{y}}} & 0 & d_{M_{\bar{y}}\psi_{\bar{x}}} & d_{M_{\bar{y}}\psi_{\bar{y}}} \end{bmatrix} \tag{8.9}$$

8.1.1 Finite element formulation

Similar to the approach in section 5.3 the variational principle is used for deriving the element equations: The functionals corresponding to (8.7) and satisfying the Euler-Lagrange equation (5.30) are found and inserted into (5.31). The interpolation functions are then introduced giving the element equations shown in (8.10) to (8.20). The interpolation functions and element coefficients are identical to the ones used for the 2 DOF model (5.34) to (5.41). Finally the complete set of finite element equations can be assembled and solved using boundary conditions as described in chapter 5.6 *Boundary conditions and cavitation*.

$$\underset{3\times3}{\left[\mathbf{H}_{i_{jk}}\right]} \underset{3\times1}{\left\{p_{i_j}\right\}} = \underset{3\times1}{\left\{V_{i_j}\right\}} \tag{8.10}$$

where j is the node number and

$$\begin{aligned} &i = 0, \chi_{\bar{x}}, \chi_{\bar{y}}, \psi_{\bar{x}}, \psi_{\bar{y}}, \dot{\chi}_{\bar{x}}, \dot{\chi}_{\bar{y}}, \dot{\psi}_{\bar{x}}, \dot{\psi}_{\bar{y}} \\ &j = 1, 2, 3 \\ &k = 1, 2, 3 \end{aligned}$$

$$\left[\mathbf{H}_{i_{jk}}\right] = \int_{\Omega} \left[\frac{h_0^3}{4\mu A^2}\left(b_j b_k + c_j c_k\right)\right] d\Omega \tag{8.11}$$

$$\left\{V_{0_j}\right\} = \int_{\Omega} \left\{\frac{3Rb_j}{A}\omega h_0 - 12N_j\frac{\partial h_0}{\partial t}\right\} d\Omega \tag{8.12}$$

$$\left\{V_{\chi_{\bar{x}j}}\right\} = \int_{\Omega} \left\{ -\left(\frac{3h_0^2 n_{\bar{x}}}{\mu R^2} \sum_{m=1}^{3} \left(p_{0_m} \frac{R}{2A} b_m \right) - 6\omega n_{\bar{x}} \right) \frac{R}{2A} b_j \right. \\ \left. -\frac{3h_0^2 n_{\bar{x}}}{\mu} \sum_{m=1}^{3} \left(p_{0_m} \frac{1}{2A} c_m \right) \frac{1}{2A} c_j \right\} d\Omega \tag{8.13}$$

$$\left\{V_{\chi_{\bar{y}j}}\right\} = \int_{\Omega} \left\{ -\left(\frac{3h_0^2 n_{\bar{y}}}{\mu R^2} \sum_{m=1}^{3} \left(p_{0_m} \frac{R}{2A} b_m \right) - 6\omega n_{\bar{y}} \right) \frac{R}{2A} b_j \right. \\ \left. -\frac{3h_0^2 n_{\bar{y}}}{\mu} \sum_{m=1}^{3} \left(p_{0_m} \frac{1}{2A} c_m \right) \frac{1}{2A} c_j \right\} d\Omega \tag{8.14}$$

$$\left\{V_{\psi_{\bar{x}j}}\right\} = \int_{\Omega} \left\{ +\left(\frac{3h_0^2 \bar{z} n_{\bar{y}}}{\mu R^2} \sum_{m=1}^{3} \left(p_{0_m} \frac{R}{2A} b_m \right) - 6\omega \bar{z} n_{\bar{y}} \right) \frac{R}{2A} b_j \right. \\ \left. +\frac{3h_0^2 \bar{z} n_{\bar{y}}}{\mu} \sum_{m=1}^{3} \left(p_{0_m} \frac{1}{2A} c_m \right) \frac{1}{2A} c_j \right\} d\Omega \tag{8.15}$$

$$\left\{V_{\psi_{\bar{y}j}}\right\} = \int_{\Omega} \left\{ -\left(\frac{3h_0^2 \bar{z} n_{\bar{x}}}{\mu R^2} \sum_{m=1}^{3} \left(p_{0_m} \frac{R}{2A} b_m \right) - 6\omega \bar{z} n_{\bar{x}} \right) \frac{R}{2A} b_j \right. \\ \left. -\frac{3h_0^2 \bar{z} n_{\bar{x}}}{\mu} \sum_{m=1}^{3} \left(p_{0_m} \frac{1}{2A} c_m \right) \frac{1}{2A} c_j \right\} d\Omega \tag{8.16}$$

$$\left\{V_{\dot{\chi}_{\bar{x}j}}\right\} = \int_{\Omega} \left\{ -12 n_{\bar{x}} \frac{R}{2A} b_j \right\} d\Omega \tag{8.17}$$

$$\left\{V_{\dot{\chi}_{\bar{y}j}}\right\} = \int_{\Omega} \left\{ -12 n_{\bar{y}} \frac{R}{2A} b_j \right\} d\Omega \tag{8.18}$$

$$\left\{V_{\dot{\psi}_{\bar{x}j}}\right\} = \int_{\Omega} \left\{ +12 \bar{z} n_{\bar{x}} \frac{R}{2A} b_j \right\} d\Omega \tag{8.19}$$

$$\left\{V_{\dot{\psi}_{\bar{y}j}}\right\} = \int_{\Omega} \left\{ -12 \bar{z} n_{\bar{y}} \frac{R}{2A} b_j \right\} d\Omega \tag{8.20}$$

8.2 Polar representation

Reynolds equation in polar coordinates (8.21) is used to describe the thrust bearings using the same approach as for the cylindrical representation.

$$\frac{1}{R}\frac{\partial}{\partial\theta}\left(\frac{h^3}{\mu R}\frac{\partial p}{\partial\theta}\right)+\frac{\partial}{\partial R}\left(\frac{h^3}{\mu}\frac{\partial p}{\partial R}\right)=6\omega\frac{\partial h}{\partial\theta}+12\frac{\partial h}{\partial t} \tag{8.21}$$

Again Lund's principle of perturbation is introduced giving equation (8.22).

$$\begin{aligned} p =& p_0+\Delta\chi_{\bar{x}}p_{\chi_{\bar{x}}}+\Delta\dot{\chi}_{\bar{x}}p_{\dot{\chi}_{\bar{x}}}+\Delta\chi_{\bar{y}}p_{\chi_{\bar{y}}}+\Delta\dot{\chi}_{\bar{y}}p_{\dot{\chi}_{\bar{y}}}+\Delta\chi_{\bar{z}}p_{\chi_{\bar{z}}}+\Delta\dot{\chi}_{\bar{z}}p_{\dot{\chi}_{\bar{z}}} \\ &+\Delta\psi_{\bar{x}}p_{\psi_{\bar{x}}}+\Delta\dot{\psi}_{\bar{x}}p_{\dot{\psi}_{\bar{x}}}+\Delta\psi_{\bar{y}}p_{\psi_{\bar{y}}}+\Delta\dot{\psi}_{\bar{y}}p_{\dot{\psi}_{\bar{y}}} \end{aligned} \tag{8.22}$$

Using a normal vector (8.23) the film thickness and squeeze term is expressed using the perturbations as shown in (8.24) and (8.25), respectivly.

$$n=\left\{\begin{array}{c} n_{\bar{x}} \\ n_{\bar{y}} \\ n_{\bar{z}} \end{array}\right\}=\pm\left\{\begin{array}{c} 0 \\ 0 \\ 1 \end{array}\right\} \tag{8.23}$$

$$h=h_0+\Delta\chi_{\bar{z}}n_{\bar{z}}+\Delta\psi_{\bar{x}}n_{\bar{z}}\sin(\theta)\,R-\Delta\psi_{\bar{y}}n_{\bar{z}}\cos(\theta)\,R \tag{8.24}$$

$$\frac{\partial h}{\partial t}=\frac{\partial h_0}{\partial t}+\Delta\dot{\chi}_{\bar{z}}n_{\bar{z}}+\Delta\dot{\psi}_{\bar{x}}n_{\bar{z}}\sin(\theta)\,R-\Delta\dot{\psi}_{\bar{y}}n_{\bar{z}}\cos(\theta)\,R \tag{8.25}$$

From (8.24) and (8.25) it is seen that the perturbations $\chi_{\bar{x}}$ and $\chi_{\bar{y}}$ has no influence on the film thickness or squeeze term and hence the corresponding terms can be canceled from (8.22).

Equations (8.22) to (8.25) are inserted into (8.21) and separated with respect to perturbations and only keeping the first order perturbation terms giving (8.26).

$$\begin{aligned} &\frac{1}{R}\frac{\partial}{\partial\theta}\left(\frac{h^3}{\mu R}\frac{\partial p_i}{\partial\theta}\right)+\frac{\partial}{\partial R}\left(\frac{h^3}{\mu}\frac{\partial p_i}{\partial R}\right)= \\ &\begin{cases} 6\omega\frac{\partial h}{\partial\theta}+12\frac{\partial h}{\partial t} & ,\, p_i=p_0 \\ -\frac{1}{R}\frac{\partial}{\partial\theta}\left(\frac{3h_0^2n_{\bar{z}}}{\mu R}\frac{\partial p_0}{\partial\theta}\right)-\frac{\partial}{\partial R}\left(\frac{3h_0^2n_{\bar{z}}}{\mu}\frac{\partial p_0}{\partial R}\right) & ,\, p_i=p_{\chi_{\bar{z}}} \\ -\frac{1}{R}\frac{\partial}{\partial\theta}\left(\frac{3h_0^2n_{\bar{z}}\sin(\theta)R}{\mu R}\frac{\partial p_0}{\partial\theta}\right)-\frac{\partial}{\partial R}\left(\frac{3h_0^2n_{\bar{z}}\sin(\theta)R}{\mu}\frac{\partial p_0}{\partial R}\right)+6\omega n_{\bar{z}}\cos(\theta)\,R & ,\, p_i=p_{\psi_{\bar{x}}} \\ +\frac{1}{R}\frac{\partial}{\partial\theta}\left(\frac{3h_0^2n_{\bar{z}}\cos(\theta)R}{\mu R}\frac{\partial p_0}{\partial\theta}\right)+\frac{\partial}{\partial R}\left(\frac{3h_0^2n_{\bar{z}}\cos(\theta)R}{\mu}\frac{\partial p_0}{\partial R}\right)+6\omega n_{\bar{z}}\sin(\theta)\,R & ,\, p_i=p_{\psi_{\bar{y}}} \\ +12n_{\bar{z}} & ,\, p_i=p_{\dot{\chi}_{\bar{z}}} \\ +12n_{\bar{z}}\sin(\theta)\,R & ,\, p_i=p_{\dot{\psi}_{\bar{x}}} \\ -12n_{\bar{z}}\cos(\theta)\,R & ,\, p_i=p_{\dot{\psi}_{\bar{y}}} \end{cases} \end{aligned} \tag{8.26}$$

Equation (8.26) is used to solve for the pressure p_0 and its derivatives with respect to the perturbation dimensions. The derivatives are then integrated and the stiffness and damping matrix of (8.1) can be established. The perturbations $\chi_{\bar{x}}$ and $\chi_{\bar{y}}$ has no influence on the pressure and therefore the corresponding coefficients are zero (first and second columns in (8.27) and (8.28)). Since the pressure always acts on the thrust surfaces it cannot give a reaction in $\chi_{\bar{x}}$ or $\chi_{\bar{y}}$, and hence the first and second rows are also zero.

$$\mathbf{K}_{Polar} = \begin{bmatrix} 0 & 0 & 0 & 0 & 0 \\ 0 & 0 & 0 & 0 & 0 \\ 0 & 0 & k_{F_{\bar{z}}\chi_{\bar{z}}} & k_{F_{\bar{z}}\psi_{\bar{x}}} & k_{F_{\bar{z}}\psi_{\bar{y}}} \\ 0 & 0 & k_{M_{\bar{x}}\chi_{\bar{x}}} & k_{M_{\bar{x}}\psi_{\bar{x}}} & k_{M_{\bar{x}}\psi_{\bar{y}}} \\ 0 & 0 & k_{M_{\bar{y}}\chi_{\bar{x}}} & k_{M_{\bar{y}}\psi_{\bar{x}}} & k_{M_{\bar{y}}\psi_{\bar{y}}} \end{bmatrix} \tag{8.27}$$

$$\mathbf{D}_{Polar} = \begin{bmatrix} 0 & 0 & 0 & 0 & 0 \\ 0 & 0 & 0 & 0 & 0 \\ 0 & 0 & d_{F_{\bar{z}}\chi_{\bar{z}}} & d_{F_{\bar{z}}\psi_{\bar{x}}} & d_{F_{\bar{z}}\psi_{\bar{y}}} \\ 0 & 0 & d_{M_{\bar{x}}\chi_{\bar{x}}} & d_{M_{\bar{x}}\psi_{\bar{x}}} & d_{M_{\bar{x}}\psi_{\bar{y}}} \\ 0 & 0 & d_{M_{\bar{y}}\chi_{\bar{x}}} & d_{M_{\bar{y}}\psi_{\bar{x}}} & d_{M_{\bar{y}}\psi_{\bar{y}}} \end{bmatrix} \tag{8.28}$$

8.2.1 Finite element formulation

The interpolation functions for the polar representation are presented in equations (8.29) to (8.32).

$$N_j = \frac{1}{2A}\left(a_j + b_j R_c \theta + c_j R\right) \tag{8.29}$$

$$\begin{array}{lll} a_1 = R_c\left(\theta_2 R_3 - \theta_3 R_2\right) & b_1 = R_2 - R_3 & c_1 = R_c\left(\theta_3 - \theta_2\right) \\ a_2 = R_c\left(\theta_3 R_1 - \theta_1 R_3\right) & b_2 = R_3 - R_1 & c_2 = R_c\left(\theta_1 - \theta_3\right) \\ a_3 = R_c\left(\theta_1 R_2 - \theta_2 R_1\right) & b_3 = R_1 - R_2 & c_3 = R_c\left(\theta_2 - \theta_1\right) \end{array} \tag{8.30}$$

$$A = \frac{R_c}{2}\begin{vmatrix} 1 & \theta_1 & R_1 \\ 1 & \theta_2 & R_2 \\ 1 & \theta_3 & R_3 \end{vmatrix} \tag{8.31}$$

$$R_c = R\left(N_1 = N_2 = N_3 = \frac{1}{3}\right) \tag{8.32}$$

The calculation of the area using equation (8.31) introduces a small error since the centroid value R_c of the radius R is used for all three nodes. The error is small due the the small difference between the node values and the centroid value. This approach is however necessary in order to satisfy the requirements for the interpolation functions, where the sum must be one and the individual function values equal to one or zero at the boundaries.

Alternatively the elements of the polar coordinate system can be transfered into a Cartesian coordinate system. This can be accomplished using the same interpolation functions, which are isoparametric, so they can be used to interpolate both the geometry and the field variables. This approach requires two velocity terms which again adds to the complexity of the model.

Again, the variational principle described in section 5.3 is used for deriving the element equations:

$$\underset{3\times3}{\left[\mathbf{H}_{i_{jk}}\right]}\underset{3\times1}{\left\{p_{i_j}\right\}} = \underset{3\times1}{\left\{V_{i_j}\right\}} \tag{8.33}$$

where

$$\begin{aligned} &i = 0, \chi_{\bar{x}}, \chi_{\bar{y}}, \psi_{\bar{x}}, \psi_{\bar{y}}, \dot{\chi}_{\bar{x}}, \dot{\chi}_{\bar{y}}, \dot{\psi}_{\bar{x}}, \dot{\psi}_{\bar{y}} \\ &j = 1, 2, 3 \\ &k = 1, 2, 3 \end{aligned}$$

$$\left[\mathbf{H}_{i_{jk}}\right] = \int_{\Omega}\left[\frac{h_0^3}{4\mu A^2}\left(b_j b_k + c_j c_k\right)\right]d\Omega \tag{8.34}$$

$$\left\{V_{0_j}\right\} = \int_{\Omega}\left\{\frac{3Rb_j}{A}\omega h_0 - 12N_j\frac{\partial h_0}{\partial t}\right\}d\Omega \tag{8.35}$$

$$\begin{aligned}\left\{V_{\chi_{\bar{z}_j}}\right\} = \int_{\Omega}\Bigg\{&-\left(\frac{3h_0^2 n_{\bar{z}}}{\mu R^2}\sum_{m=1}^{3}\left(p_{0_m}\frac{R}{2A}b_m\right)\right)\frac{R}{2A}b_j \\ &-\frac{3h_0^2 n_{\bar{z}}}{\mu}\sum_{m=1}^{3}\left(p_{0_m}\frac{1}{2A}c_m\right)\frac{1}{2A}c_j\Bigg\}d\Omega\end{aligned} \tag{8.36}$$

$$\begin{aligned}\left\{V_{\psi_{\bar{x}_j}}\right\} = \int_{\Omega}\Bigg\{&-\left(\frac{3h_0^2\sin(\theta)\, n_{\bar{z}}}{\mu R}\sum_{m=1}^{3}\left(p_{0_m}\frac{R}{2A}b_m\right) - 6\omega R\sin(\theta)\, n_{\bar{z}}\right)\frac{R}{2A}b_j \\ &-\frac{3h_0^2 R\sin(\theta)\, n_{\bar{z}}}{\mu}\sum_{m=1}^{3}\left(p_{0_m}\frac{1}{2A}c_m\right)\frac{1}{2A}c_j\Bigg\}d\Omega\end{aligned} \tag{8.37}$$

$$\begin{aligned}\left\{V_{\psi_{\bar{y}_j}}\right\} = \int_{\Omega}\Bigg\{&+\left(\frac{3h_0^2\cos(\theta)\, n_{\bar{z}}}{\mu R}\sum_{m=1}^{3}\left(p_{0_m}\frac{R}{2A}b_m\right) - 6\omega R\cos(\theta)\, n_{\bar{z}}\right)\frac{R}{2A}b_j \\ &+\frac{3h_0^2 R\cos(\theta)\, n_{\bar{z}}}{\mu}\sum_{m=1}^{3}\left(p_{0_m}\frac{1}{2A}c_m\right)\frac{1}{2A}c_j\Bigg\}d\Omega\end{aligned} \tag{8.38}$$

$$\left\{V_{\dot{\chi}_{\bar{z}j}}\right\} = \int_{\Omega} \left\{-12 n_{\bar{z}} \frac{R}{2A} b_j\right\} d\Omega \tag{8.39}$$

$$\left\{V_{\dot{\psi}_{\bar{x}j}}\right\} = \int_{\Omega} \left\{-12 R \sin(\theta)\, n_{\bar{z}} \frac{R}{2A} b_j\right\} d\Omega \tag{8.40}$$

$$\left\{V_{\dot{\psi}_{\bar{y}j}}\right\} = \int_{\Omega} \left\{+12 R \cos(\theta)\, n_{\bar{z}} \frac{R}{2A} b_j\right\} d\Omega \tag{8.41}$$

8.3 Combining the cylindrical and polar equations

The finite element equations for the cylindrical and the polar representations are setup for all the respective elements and assembled into one system of equations to allow the solution to be found simultaneously. This is done for the pressure and also its derivatives with respect to the 2×5 perturbations so the dynamic coefficients can be established.

The equations required to find the fluidity matrices $\mathbf{H}$, for the cylindrical and polar representation respectively, are identical except for the interpolation functions and the corresponding element coefficients. This is also the case for the Jacobian matrices $\mathbf{J}$, which are used as a part of the Newton-Raphson scheme to couple elasticity and hydrodynamic forces.

Using a set of index vectors, used to differentiate between the cylindrical and polar elements and their corresponding equations, it is possible to set-up an efficient procedure that assembles the finite element equations vectorized using the technical computing software *Matlab*. Hereby it is possible to solve for the pressure and dynamic coefficients in a very efficient manner.

Chapter 9

The use of dynamic coefficients

In this work the dynamic coefficients obtained from perturbation of Reynolds equation, as described in section 5.2, are used for two purposes:

- finding the equilibrium position of the rotor that corresponds to the imposed external load
- integration in time domain in order to find the response to dynamic loads

The numerical procedures for these are described in the two following sections.

9.1 Solving for equilibrium position

When Reynolds equation is used directly, the rotor position (χ, ψ) and velocity $(\dot{\chi}, \dot{\psi})$ are defined giving the lubricant film response, which can then be integrated giving the oil film forces (F, M). However, often the external loads (W, G) are given and the rotor position which returns force equilibrium is desired.

Usually the solution of interest is that of steady state. Therefore the velocity components are set to zero, although this is not a requirement.

In order to find the equilibrium position for a given external load, a guess on rotor position is made and the corresponding film forces are found so the equation of force equilibrium (9.1) can be established.

$$\left\{ \begin{array}{c} \Delta F \\ \Delta M \end{array} \right\} = \left\{ \begin{array}{c} W \\ G \end{array} \right\} + \left\{ \begin{array}{c} F \\ M \end{array} \right\} \tag{9.1}$$

The stiffness coefficients are then used to calculate a correction, as shown in (9.2).

$$\left\{ \begin{array}{c} \Delta\chi \\ \Delta\psi \end{array} \right\} = \mathbf{K}^{-1} \left\{ \begin{array}{c} \Delta F \\ \Delta M \end{array} \right\} \tag{9.2}$$

Finally the position at the i-th iteration can be calculated using (9.3), if necessary using a coefficient of under-relaxation β.

$$\left\{ \begin{array}{c} \chi \\ \psi \end{array} \right\}_i = \left\{ \begin{array}{c} \chi \\ \psi \end{array} \right\}_{i-1} - \beta \left\{ \begin{array}{c} \Delta\chi \\ \Delta\psi \end{array} \right\} \tag{9.3}$$

For checking convergence of the iteration process (9.4) is used. Using the preceding LHS-values of (9.4) the coefficient of under-relaxation can be adjusted to achieve a faster rate of convergence.

$$\frac{\left\| \left\{ \begin{array}{c} \Delta F \\ \Delta M \end{array} \right\} \right\|}{\left\| \left\{ \begin{array}{c} W \\ G \end{array} \right\} \right\|} < 10^{-3} \tag{9.4}$$

9.2 Integration in time domain

When searching for the response of a hydrodynamic bearing subjected to dynamic loads one faces an initial value problem. This induces that the initial rotor position and velocity must be defined after which the response can be found.

At a given point in time, the equation of force equilibrium (9.1) is used to find the force unbalance and together with the damping coefficients a correction for the velocity is calculated using (9.5). Thus, the force unbalance results in a velocity change.

$$\left\{ \begin{array}{c} \Delta\dot{\chi} \\ \Delta\dot{\psi} \end{array} \right\} = \mathbf{D}^{-1} \left\{ \begin{array}{c} \Delta F \\ \Delta M \end{array} \right\} \tag{9.5}$$

Using equation (9.6) the correction is used to define a new guess for a rotor velocity, for which the oil film forces will counterbalance the external forces. This iterative procedure, using (9.1), (9.5) and (9.6), is repeated until the convergence criteria of (9.4) is satisfied.

$$\left\{ \begin{array}{c} \dot{\chi} \\ \dot{\psi} \end{array} \right\}_i = \left\{ \begin{array}{c} \dot{\chi} \\ \dot{\psi} \end{array} \right\}_{i-1} - \beta \left\{ \begin{array}{c} \Delta\dot{\chi} \\ \Delta\dot{\psi} \end{array} \right\} \tag{9.6}$$

When convergence is achieved, the rotor velocity is used to step forward in time. Equation (9.7) shows the most basic method of numerical integration, also called the *Euler method*.

$$\left\{ \begin{array}{c} \chi \\ \psi \end{array} \right\}_{t=t_1+\Delta t} = \left\{ \begin{array}{c} \chi \\ \psi \end{array} \right\}_{t=t_1} + \left\{ \begin{array}{c} \Delta\dot{\chi} \\ \Delta\dot{\psi} \end{array} \right\} \Delta t \tag{9.7}$$

The Euler method is a method of first order, meaning that the local error pr. time step is proportional to the square of the step size (Δt^{1+1}).

For this work the Bogacki-Shampine method is implemented. The method is adaptive and of third order, meaning that the local error is proportional to Δt^{3+1}.

Furthermore it possesses the first-same-as-last property, commonly denoted *FSAL*, and therefore only requires three evaluations even though it consists of four stages, as shown in the Butcher tableau of (9.8).

$$\begin{array}{c|cccc} 0 & & & & \\ 1/2 & 1/2 & & & \\ 3/4 & 0 & 3/4 & & \\ 1 & 2/9 & 1/3 & 4/9 & \\ \hline & 2/9 & 1/3 & 4/9 & \\ & 7/24 & 1/4 & 1/3 & 1/8 \end{array} \tag{9.8}$$

Using the Butcher tableau a time step n is calculated according to the procedure of equation (9.9), here performing time integration for the function $y\,(t)$.

$$\begin{aligned} k_1 &= \dot{y}\,(t_n, y_n) \\ k_2 &= \dot{y}\,(t_n + 1/2\Delta t, y_n + 1/2\Delta t k_1) \\ k_3 &= \dot{y}\,(t_n + 3/4\Delta t, y_n + 3/4\Delta t k_2) \\ y_{n+1} &= y_n + 2/9\Delta t k_1 + 1/3\Delta t k_2 + 4/9\Delta t k_3 \\ k_4 &= \dot{y}\,(t_n + \Delta t, y_{n+1}) \\ \tilde{y}_{n+1} &= y_n + 7/24\Delta t k_1 + 1/4\Delta t k_2 + 1/3\Delta t k_3 + 1/8\Delta t k_4 \end{aligned} \tag{9.9}$$

$\tilde{y}_{n+1}$ is the third order approximation to the exact solution whereas y_{n+1} is of second order. The difference of these two can be used to estimate the local error and followingly adapt the step size in order to achieve a rapid solution while staying within an acceptable margin of error e_{acc}. Equation (9.10) shows how the step size is adapted according to the local error estimate. β is an under-relaxation factor used to ensure that the acceptable error is not exceeded. For this work $\beta = 0.8$ and e_{acc} is set to the least of 0.5 μm or 1/50'th of the minimum film thickness.

$$\Delta t_{n+1} = \beta \Delta t_n \left(\frac{e_{acc}}{|\tilde{y}_{n+1} - y_{n+1}|} \right)^{\frac{1}{3+1}} \tag{9.10}$$

If $|\tilde{y}_{n+1} - y_{n+1}| > e_{acc}$ the solution must be discarded and recalculated using a smaller step size. This is of course undesirable, since it is computationally heavy. Therefore β is introduced.

The FSAL property of the Bogacki-Shampine method is achieved since the value of k_4 of step n equals k_1 of step $n+1$ and thus only three evaluations are required per time step.

Chapter 10

Verification

The bearing system shown in figure 10.1 is used to verify critical parts of the bearing model. The bearing system consists of a partial journal bearing supporting a long slender shaft.

Structurally the lower surface of the bearing house and the far end of the shaft is locked in all its DOF allowing the shaft to deform as a cantilever beam. Bearing dimensions are given in table 10.1.

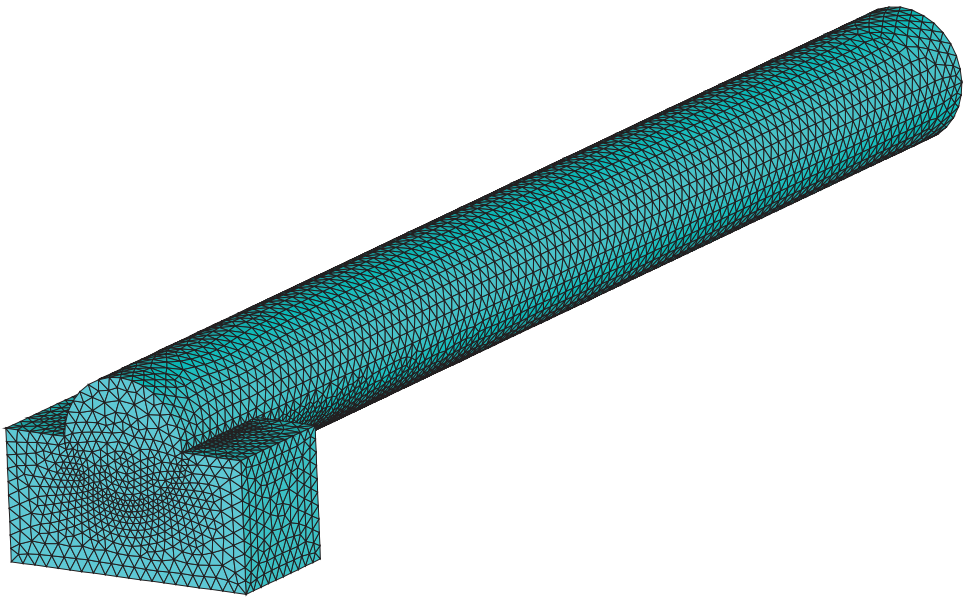

Figure 10.1: Partial journal bearing used for verification.

Figure 10.2 shows a magnification of the bearing end with the shaft in its deformed state. The bearing surface is represented by 731 nodes forming 1356 elements.

The bearing elasticity is only included in the verification of the pressure compliance matrix in section 10.4. For the remaining analyses, the bearing is considered infinitely stiff.

Bearing radius	R	2.5	mm
Bearing length	L	5	mm
Shaft length, from fixed end to center of bearing	L_{Rod}	50	mm
Bearing circumferential extent		180	°
Modulus of elasticity	E	200	GPa

Table 10.1: Bearing geometry

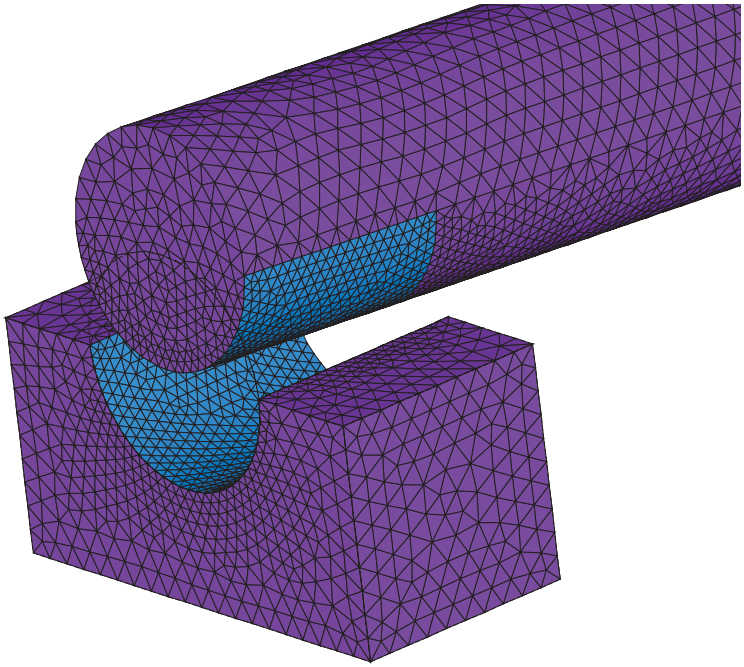

Figure 10.2: Magnification of partial bearing with shaft shown in its deformed state and also highlighting the bearing area used for the elastohydrodynamic model.

10.1 Comparison with analytical solution for the infinitely wide bearing

The numerical solution of Reynolds equation is compared with the infinite-width solution of Reynolds equation shown in equation 10.1 [74]. For the corresponding coordinate system, please see [74].

In order to obtain an infinitely wide journal bearing, the length of the bearing shown in figure 10.1 is multiplied by 10 giving it a length of 50 mm. Hence the diameter-to-length ratio is 0.1 and the circumferential pressure gradient will dominate Reynolds equation. This allows the numerical solution to be compared with the infinite-width solution of equation 10.1.

$$p(\theta) = -6\mu\left(\frac{R}{c_r}\right)^2 \left(\dot{\varepsilon}\cos\theta + \frac{2}{2+\varepsilon^2}\varepsilon\left(\dot{\phi} - \frac{\omega}{2}\right)\sin\theta\right) \cdot \left(\frac{1}{1+\varepsilon\cos\theta} + \frac{1}{(1+\varepsilon\cos\theta)^2}\right) \tag{10.1}$$

Radial clearance	C_r	20	μm
Journal position in x	χ_x	10	μm
Journal position in y	χ_y	0	μm
Journal velocity in x	$\dot{\chi}_x$	0	mm/s
Journal velocity in y	$\dot{\chi}_y$	-1	mm/s
Rotational speed	ω	100	rad/s
Viscosity	μ	0.0185	Pas

Table 10.2: Operational parameters used for verification.

The operational parameters of table 10.2 are selected in order that the Poiseuille and Couette terms of the flow equations are in the same order of magnitude.

The numerical and analytical solution for the infinitely wide journal bearing are shown in figure 10.3. It is seen that there is good correlation between the two solutions over the complete bearing area except at the edges ($z = \pm L/2$), where the axial pressure gradients cannot be assumed insignificant. The maximum pressure of the analytical solution is 1.36 ‰ higher than the corresponding result using the numerical solution.

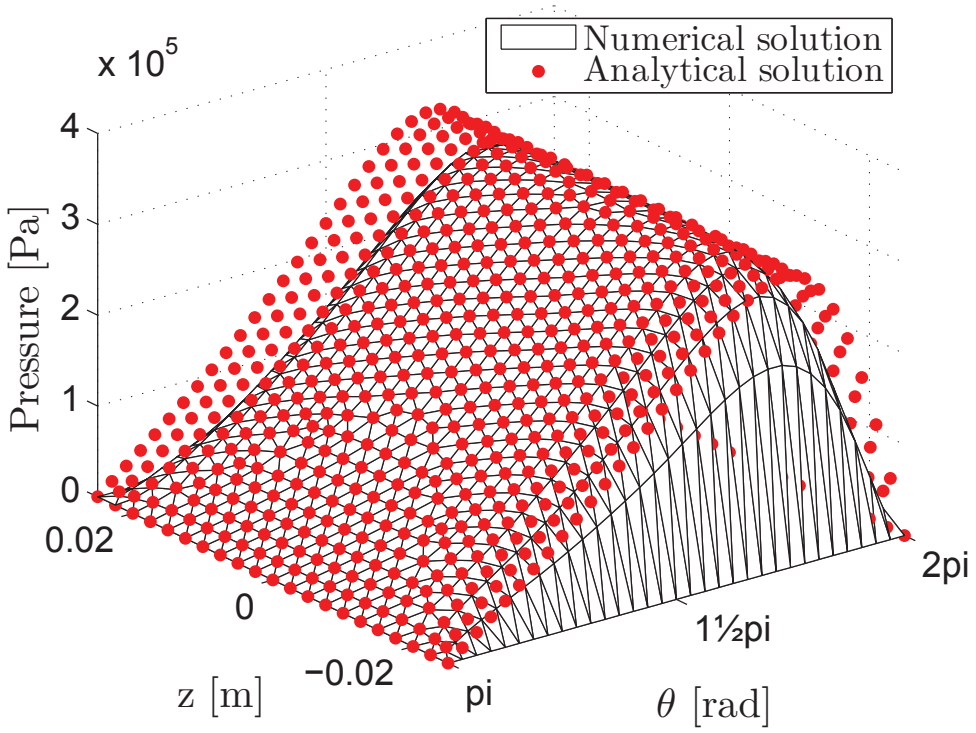

Figure 10.3: Numerical and analytical solution for long bearing

10.2 Comparison with analytical short width journal bearing theory

In this section the numerical solution of Reynolds equation is compared with the short-width solution of Reynolds equation, also known as the Ocvirk solution, shown in equation 10.2 [74]. In order to obtain a short-width bearing, the length of the bearing shown in figure 10.1 is multiplied by 0.1 giving it a length of 0.5 mm. Hence the diameter-to-length ratio is 10 and the axial pressure gradient will dominate Reynolds equation. This allows the numerical solution to be compared with the short-width solution shown in equation 10.2.

$$p(\theta, z) = -6\mu \left(\frac{R}{c_r}\right)^2 \left(\frac{L}{2R}\right)^2 \left(1 - \left(\frac{2z}{L}\right)^2\right) \cdot \frac{\dot{\varepsilon}\cos\theta + \varepsilon\left(\dot{\phi} - \frac{\omega}{2}\right)\sin\theta}{(1 + \varepsilon\cos\theta)^3} \tag{10.2}$$

Again the operational parameters listed in table 10.2 are used for the verification.

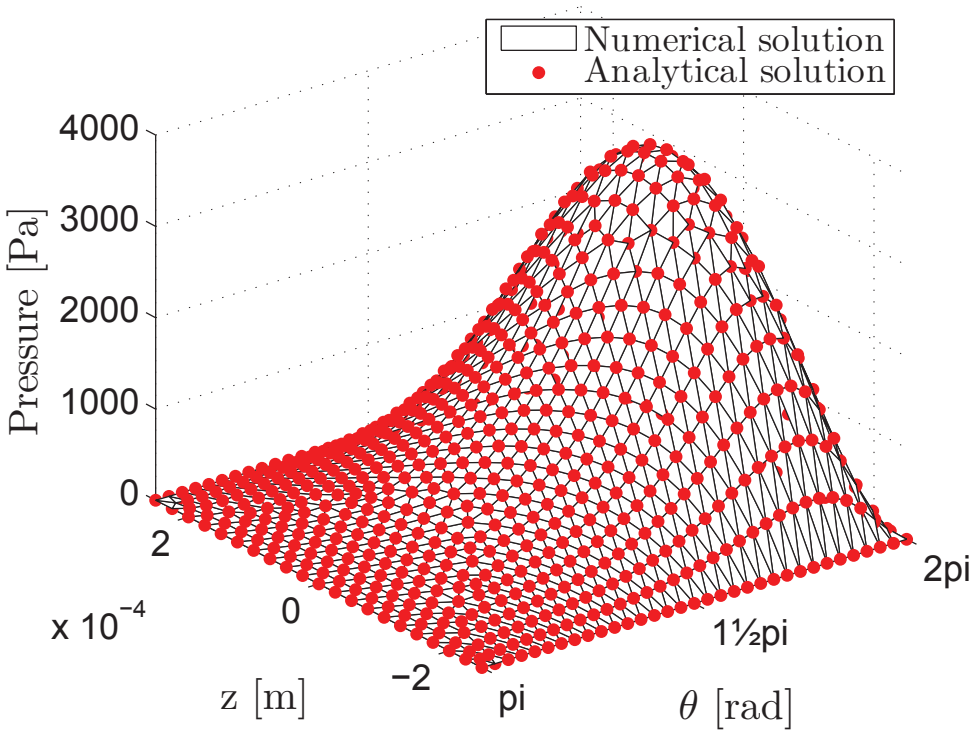

Figure 10.4: Numerical and analytical solution for short bearing

The numerical and analytical solution for the short bearing are shown in figure 10.4. It is seen that there is good correlation between the two solutions over the complete bearing area. The maximum pressure of the analytical solution is 2.16 % higher than the corresponding result using the numerical solution.

10.3 Verification of flow calculations

10.3.1 Poiseuille term

In order to verify the implementation of the Poiseuille terms belonging to the flow equations (5.12) and (5.13) the parameters of tables 10.1 and 10.2 are used with the

following exception: $\chi_x = 0$, $\chi_y = -10\mu m$, $\dot{\chi}_x = 0$, $\dot{\chi}_y = -1\frac{mm}{s}$ and $\omega = 0$. These parameters result in the pressure profile shown in figure 10.5.

Since the rotational speed is zero, there is only Poiseuille driven flow and thus only these parts of the flow equations are verified. Using the numerical model, the flow is predicted to $24.1\frac{mm^3}{s}$.

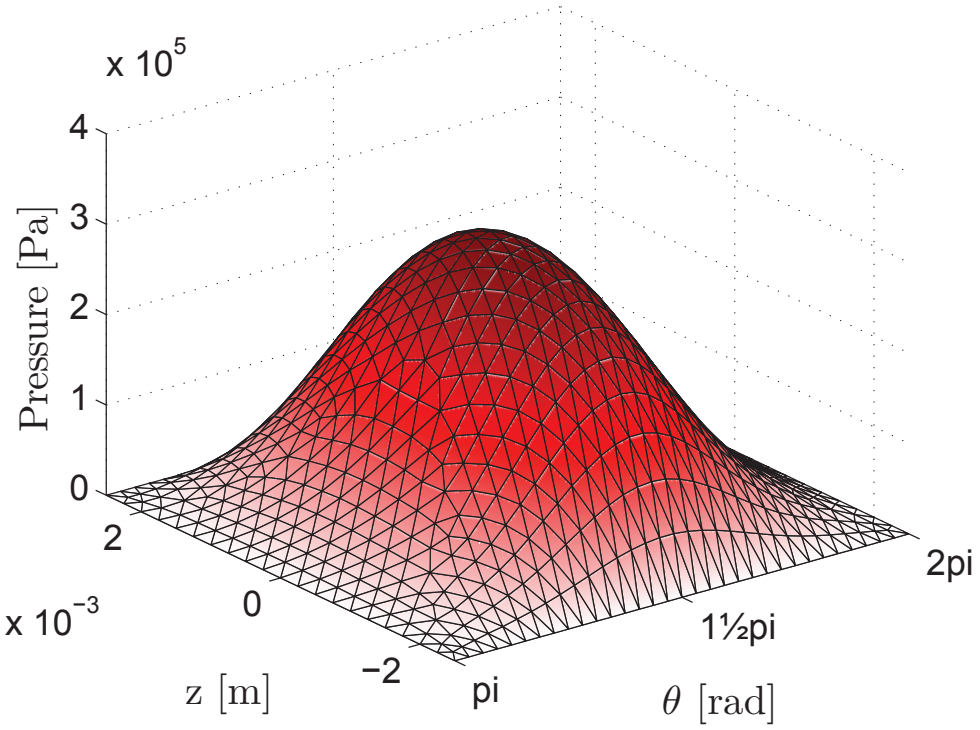

Figure 10.5: Numerical solution used for flow calculation and verification of its Poiseuille term.

The numerical result can be compared to the journal travel velocity times the projected area perpendicular to the journal's travel direction. Using this approach one obtains the result shown in equation (10.3).

$$\begin{aligned} Q =& |2RL\dot{\chi}_y| \\ =& 2 \cdot 2.5mm \cdot 5mm \cdot 1\frac{mm}{s} \\ =& 25.0\frac{mm^3}{s} \end{aligned} \tag{10.3}$$

The numerical model underestimates the flow with 3.68 % compared to the simple analytical approach.

10.3.2 Couette term

The implementation of the Couette term of the flow equation (5.12) is verified using the pressure distribution found using the parameters of tables 10.1 and 10.2 except the journal velocity is set to zero: $\dot{\chi}_y = 0$.

Using these parameters the journal center travel velocity is zero and thus there must be flow balance of lubricant in and out of the bearing when considering both the Poiseuille and Couette terms.

From the flow components of table 10.3 it is seen that there is an error in flow of 2.91 % when Couette flow into the bearing is defined as 100 %.

Flow component	Flow mm^3/s	Percentage of positive Couette
Poiseuille	- 11.9	63.7 %
Couette, negative part	- 6.26	33.4 %
Couette, positive part	18.7	100 %
Error	0.544	2.91 %

Table 10.3: Flow components in and out of bearing lubricant volume. Positive is defined as into the bearing volume.

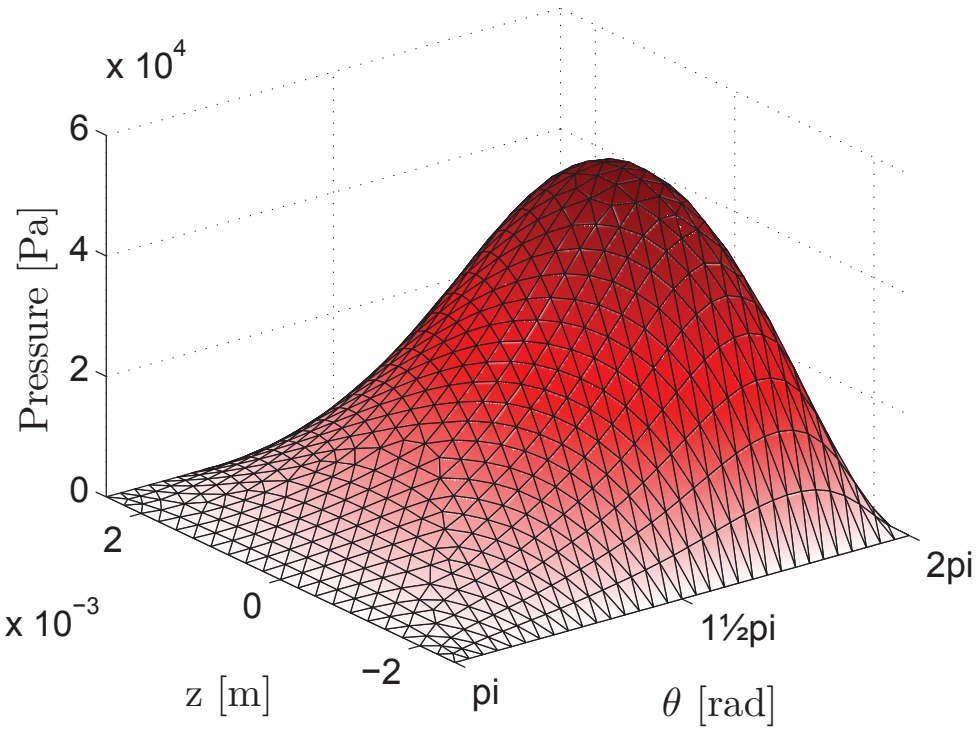

Figure 10.6: Numerical solution used for flow calculation and verification of its Couette term.

10.4 Verification of pressure compliance matrix

In order to verify the pressure compliance matrix **L** of equation (6.4) page 43 a pressure of 10 MPa is applied to the bearing surface of the model shown in figure 10.1 giving the deformation shown in 10.2. Using the pressure compliance matrix the deformation at the midsection of the bearing is found to be 1.70 mm when only considering the elasticity of the long slender beam.

For verification this result is compared with elementary beam theory. The deformation at the end of a cantilever beam with a force at the free end is found using equation (10.4) [75]. The resulting force F on the rod is replaced with the pressure times projected area giving a force of 250 N.

$$\begin{aligned} d =& \frac{FL_{Rod}^3}{3EI} = \frac{2RLpL_{Rod}^3}{3E\frac{\pi R^4}{4}} \\ =& \frac{2 \cdot 2.5mm \cdot 5mm \cdot 10\frac{N}{mm^2} \cdot (50mm)^3}{3 \cdot 200{\cdot}10^3 \frac{N}{mm^2} \frac{\pi(2.5mm)^4}{4}} \\ =& 1.70mm \end{aligned} \tag{10.4}$$

Using the same geometry and material parameters the deformation is found to be identical to the result using the pressure compliance matrix: 1.70 mm. From this it is concluded that the pressure compliance matrix is implemented correct.

This furthermore entails that the force stiffness matrix **K** is condensed correctly from 3 DoF (x,y,x) to 1 DoF (film thickness direction). The correctness of the integration matrix **A**, which is used to transform to pressure compliance matrix, is also verified during this procedure.

Chapter 11

Analysis of 5 DOF bearing

In this chapter the response of a bearing supporting 5 degrees of freedom is analyzed. Firstly, an analysis on system-level is performed examining the bearing's overall steady-state response when exposed to a range of combined radial and moment loads. Secondly, the most severe load-case is picked out for further analysis looking into the individual pad behavior.

11.1 Bearing geometry

The bearing geometry is shown in figure 11.1 with main dimensions. Further geometrical and operational parameters are given in table 11.1.

The generated mesh for establishing the super element representing rotor- and stator-flexibility is shown in figure 11.2, displaying the rotor and stator individually in (a) and (b) respectively. The surfaces which are used to constrain the structural model are pointed out in figure 11.1.

Figure 11.2(c) shows an enlargement of the mesh on the pad surfaces which are also used for the oil film model. Furthermore the radial flexure support is visible between the two thrust pads.

Care is taken to obtain a mesh-density on the pad surfaces for the oil film model that will allow for good oil film results without being too computational demanding. Furthermore an extra fine mesh is employed for the flexure supports since the response of these are of vital importance for the simulation output.

Table 11.2 shows the amount of nodes and elements used for the oil film and structural models. As indicated by the table, 7,440 nodes are used for the oil film model. This induces a super element of size $3 \cdot 7,440 \times 3 \cdot 7,440$ for both rotor and stator since the structural model has 3 DOF whereas the oil film model only has 1. This gives a total number of coefficients of $1.0 \cdot 10^9$ requiring 8 GB of memory to store.

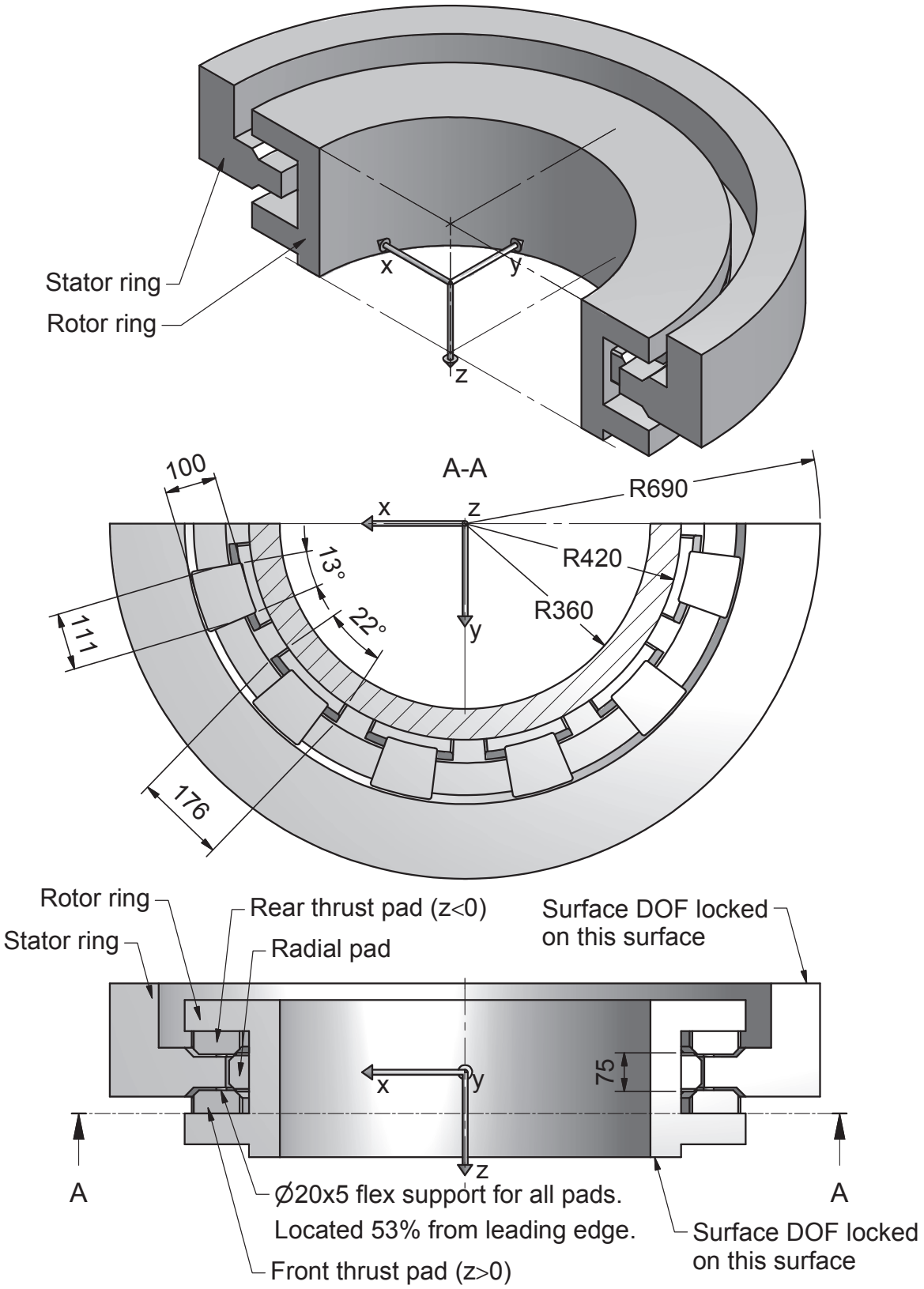

Figure 11.1: Bearing with main dimensions, terminology and coordinate system. Note that only half the bearing is shown.

Axial clearance	c_a	75	μm
Radial clearance	c_r	75	μm
Journal radius	R_J	420	mm
Radial pad radius	R_p	421.075	mm
Leading edge chamfer dimensions	-	5 x $5{\cdot}10^{-3}$	mm
Flexure support diameter	-	20	mm
Flexure support hight	-	5	mm
Flexure support location from leading edge	-	53	%
Lubricant viscosity grade	-	320	ISO VG
Lubricant temperature	T	50	°C
Lubricant viscosity	μ	0.1716	Pas
Lubricant density	ρ	854	kg/m^3
Lubricant specific heat capacity	c_p	2000	J/kg/°C
Rotational velocity	ω	30	rpm
External force in x-direction	$W_{\bar{x}}$	0	kN
External force in y-direction	$W_{\bar{y}}$	-0.1 to -300	kN
External force in z-direction	$W_{\bar{z}}$	0	kN
External moment about x-axis	$G_{\bar{x}}$	-0.1 to -500	kNm
External moment about y-axis	$G_{\bar{y}}$	0	kNm
Modulus of elasticity	E	200	GPa
Poisson's ratio	ν	0.3	-

Table 11.1: Bearing parameters and operating conditions

	Rotor flexibility	Stator flexibility	Oil film
Nodes	299,983	870,696	7,440
Elements	234,228	638,469	12,768

Table 11.2: Number of nodes and elements used for the models

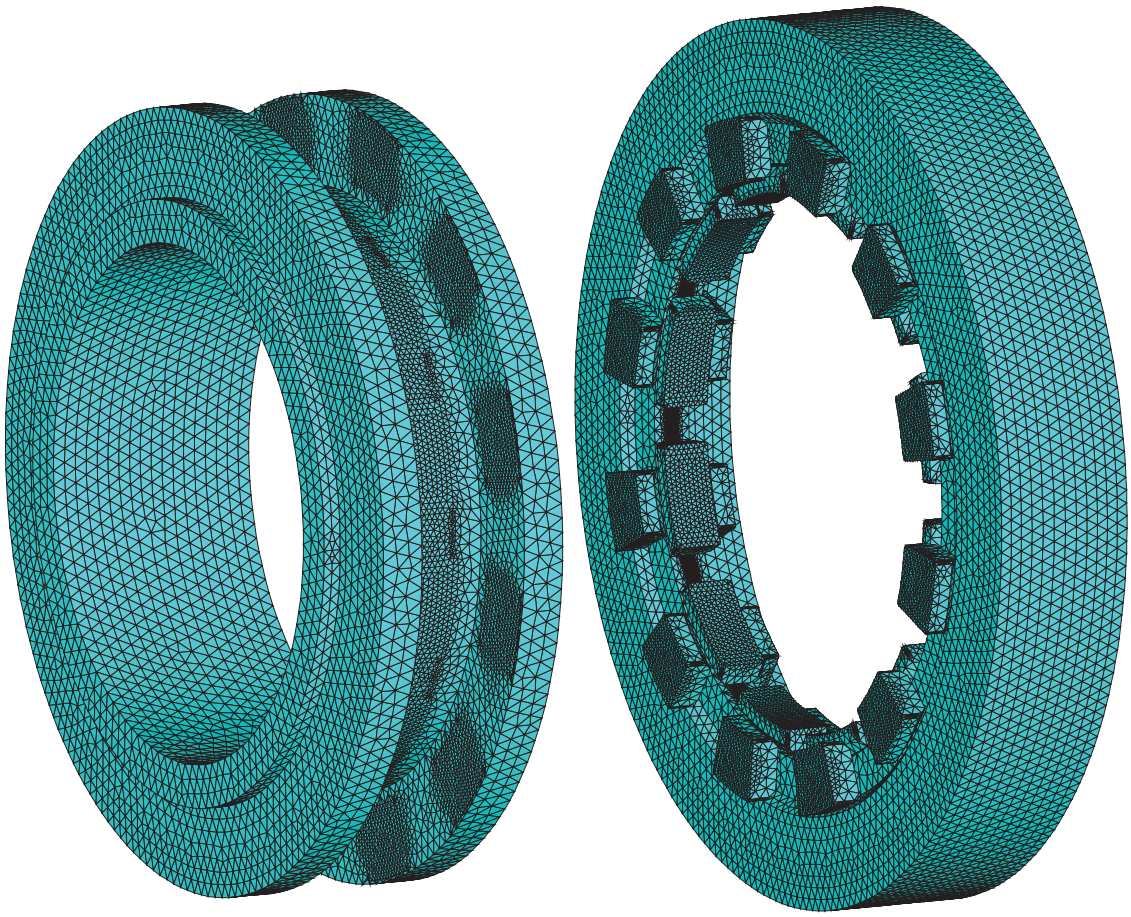

(a) Rotor

(b) Stator

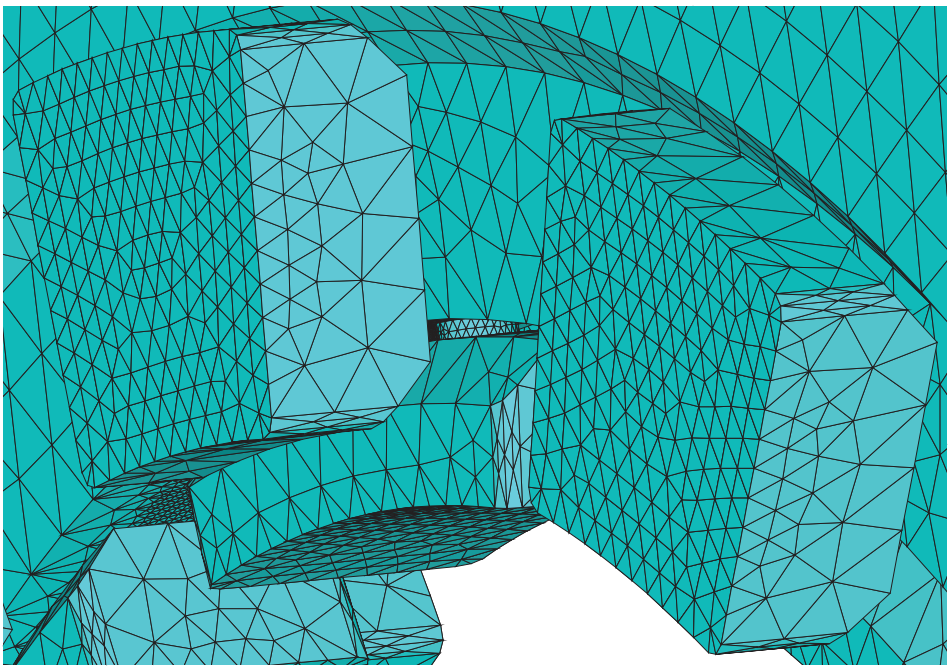

(c) Zoom on pads. The radial pad flex support is visible between the thrust pads

Figure 11.2: Meshed bearing

11.2 Bearing response to radial loads and bending moments

Firstly, the system response of the bearing is analyzed in section 11.2.1 after which section 11.2.2 is devoted to showing the rotor position in the stator as a function of the bearing load.

Since the external loads $W\&G$ are negative, the bearing reactions $F\&M$ are plotted on the axes.

11.2.1 Oil film response on system level

Figure 11.3 shows the global minimum oil film thickness in the bearing as function of bearing reaction forces. In the unloaded part of the figure, $F_{\bar{y}}$=0.1 kN and $M_{\bar{x}}$=0.1 kNm, the film thickness is close to that of the radial and thrust clearances (67 μm vs. 75 μm).

The 90 ° bends of the isolines reveal that the response of the radial and axial pads are not coupled strongly. One half of any of the isolines is governed by the radial pads whereas the other half is governed by the thrust pads, with the transition lying at the 90 ° bend, where both the radial and thrust pad systems display identical minimum film thicknesses.

This non-coupled nature shows on all system level figures. Even though the pad response shows little signs of coupling when looking at the tribological parameters, the axial and radial bearing elastic responses are still indirectly coupled by the supporting structure.

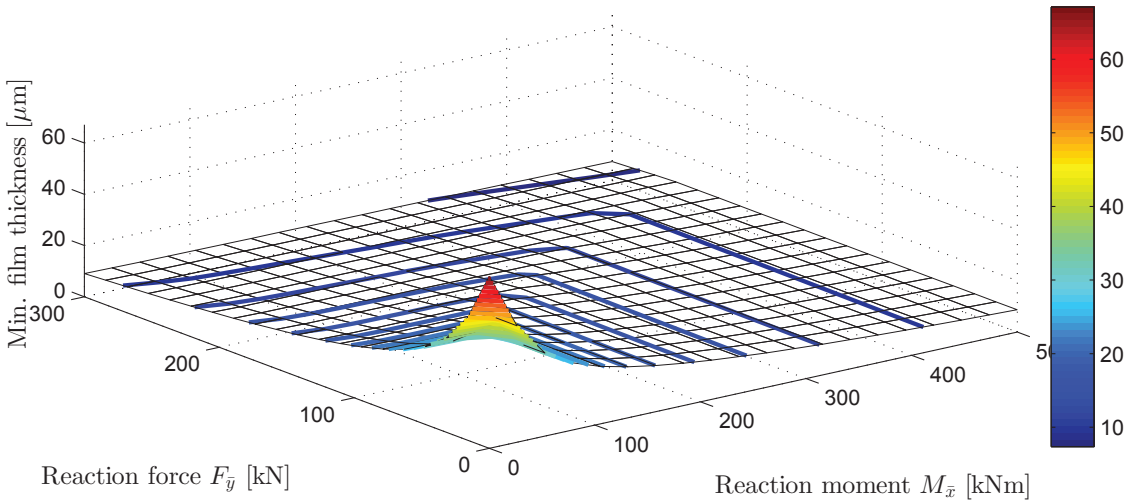

Figure 11.3: Minimum oil film thickness in bearing as function of bearing load. Isoline difference: 2 μm

Figure 11.4 shows the global maximum pressure in the bearing. Again we see the 90 ° bends of the isolines. The isoline-bends for the pressure plot are not located at the same loads as for the minimum film thickness isoline-bends. This induces that for some loads, the minimum film thickness occurs in the radial pads whereas at the same load, the maximum pressure is on the thrust pads.

The correlation between external load and maximum pressure is very linear telling two things:

- the flexure supports work as intended, allowing the pads to adjust according to operating conditions
- the deformations are not excessive, giving unfavorably pressure distributions. This could be the case if, for example, the pad bodies where too flexible

However, if thermohydrodynamic modeling is included, this linear correlation will cease to exist due to the strong temperature dependence on viscosity.

The maximum pressure of 36 MPa is in a range where care must be taken with respect to material fatigue properties, if many load cycles of this magnitude are expected.

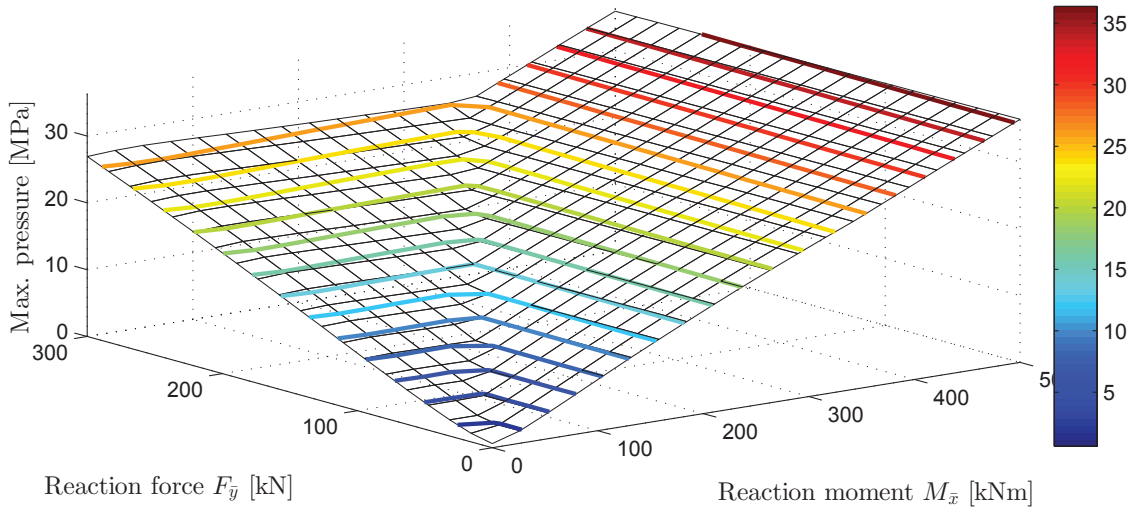

Figure 11.4: Maximum pressure as function of bearing load. Isoline difference: 2 MPa

Figure 11.5 shows the maximum deformation in the bearing including the rigid body motion that the pads undergo when the flexure supports deform. Again we see a clear division between radial and thrust pads and also a very linear correlation between deformation and external load.

Figure 11.6 shows the total viscous dissipation in the bearing. This parameter fits very well with a plane for the entire load spectrum and does not exhibit the division into radial and thrust regimes as seen previously.

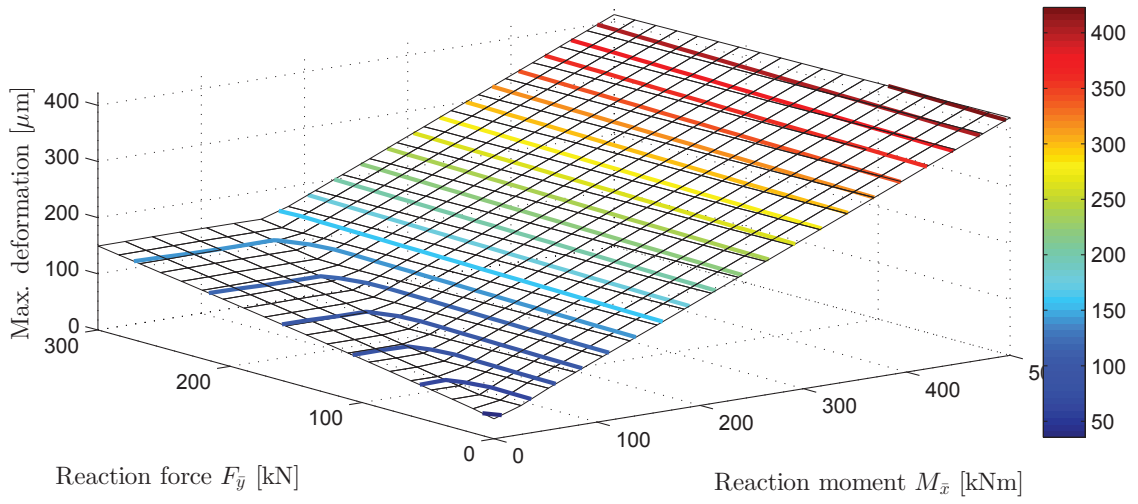

Figure 11.5: Maximum deformation, incl. rigid body motion of pads, as function of bearing load. Isoline difference: 20 μm

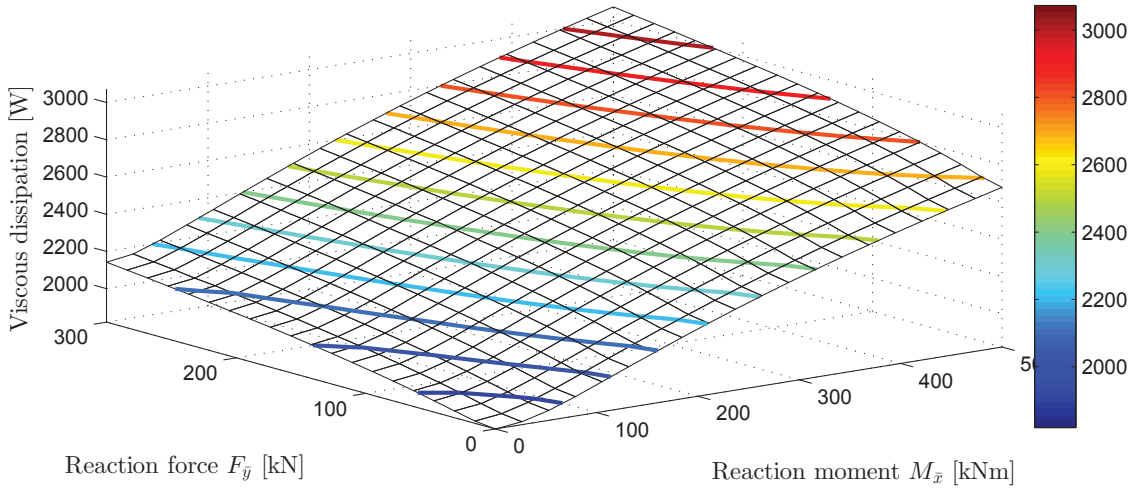

Figure 11.6: Total viscous dissipation as function of bearing load. Isoline difference: 100 W

In order to calculate the coefficient of friction for the bearing equation (11.1) is established and used for generating figure 11.7 which shows the COF as function of external load. Values as low as $1.6{\cdot}10^{-3}$ are obtained for the highest load case.

$$COF = \frac{P/\omega}{|M_x| + |F_y R|} \tag{11.1}$$

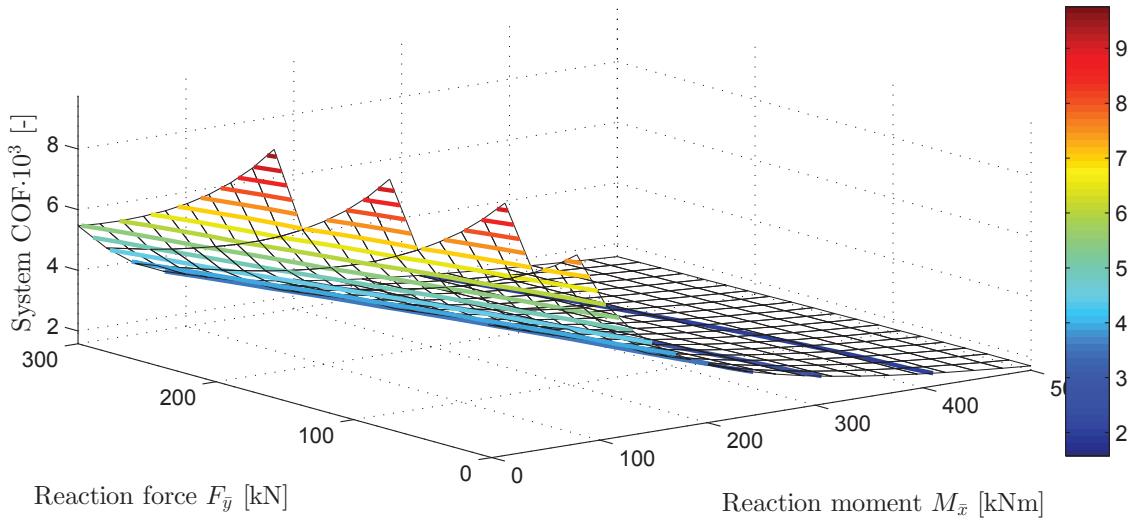

Figure 11.7: Coefficient of friction as function of bearing load. Values above $10{\cdot}10^{-3}$ are clipped. Isoline difference: 0.5

11.2.2 Rotor position in stator

In this section the bearing rotor position in the stator is shown as function of the bearing load in figures 11.8 to 11.12.

The figures show that the bearing displays very little cross-coupling between the 5 DOF. Only χ_y (figure 11.9) and ψ_x (figure 11.11), which are directly related to the imposed loads $F_{\bar{y}}$ and $M_{\bar{x}}$, show large variations across the load spectrum.

Again, the variations are close to linear except for the small changes the cross-coupled reactions for χ_x (figure 11.8), χ_z (figure 11.10) and ψ_y (figure 11.12).

The unsymmetrical translation χ_z (figure 11.10), i.e. translation in axial direction, is due to the unsymmetrical boundary conditions for the stiffness model where only one side has its DOF locked (if neccesary, see figure 11.1 page 106 for illustration).

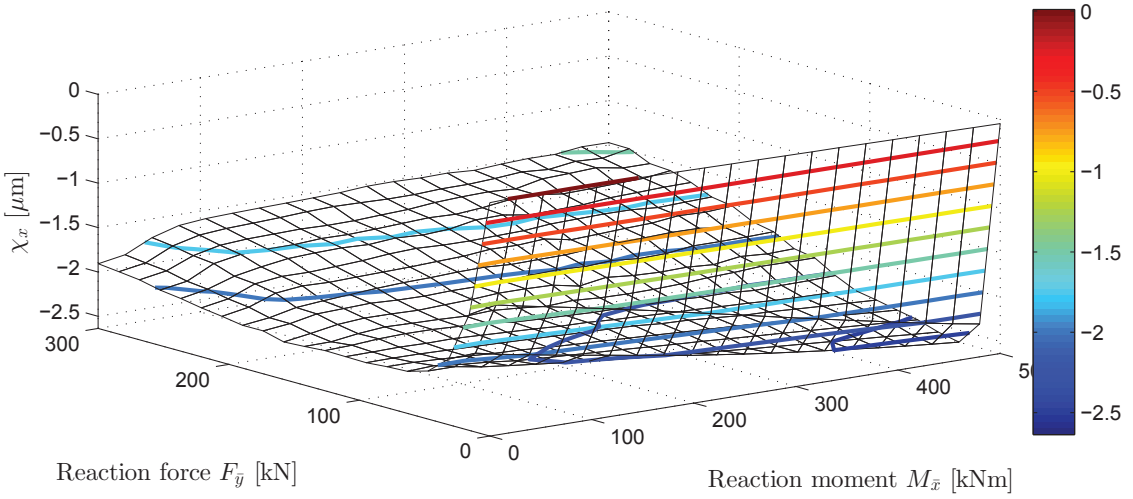

Figure 11.8: Rotor position χ_x as function of bearing load. Isoline difference: 0.25 μm

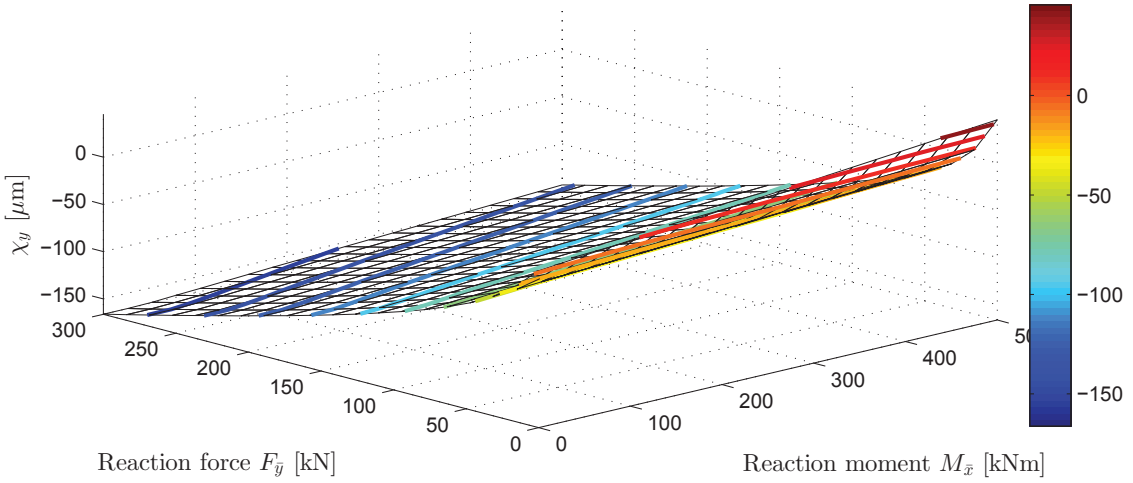

Figure 11.9: Rotor position χ_y as function of bearing load. Isoline difference: 15 μm

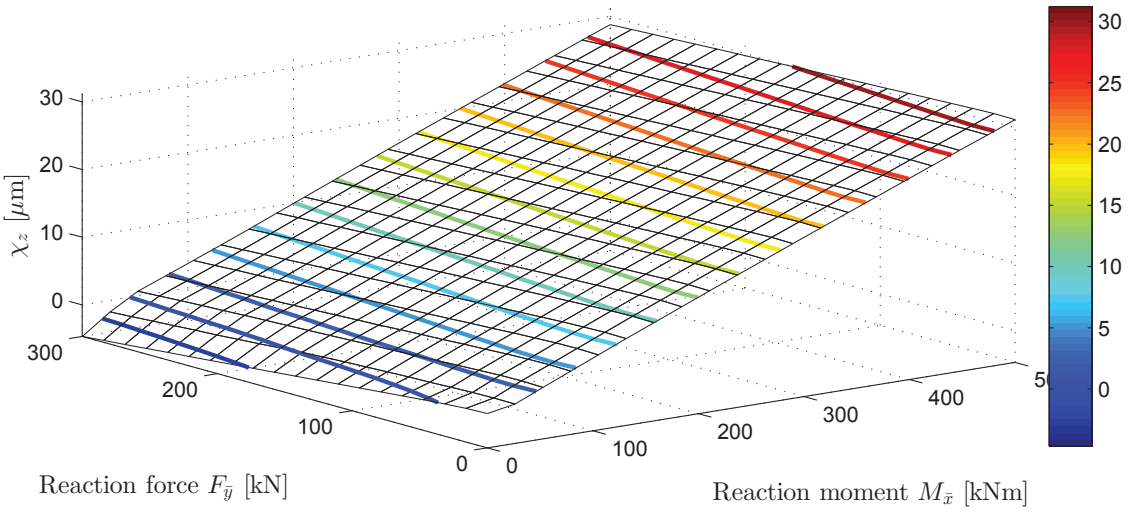

Figure 11.10: Rotor position χ_z as function of bearing load. Isoline difference: 2.5 μm

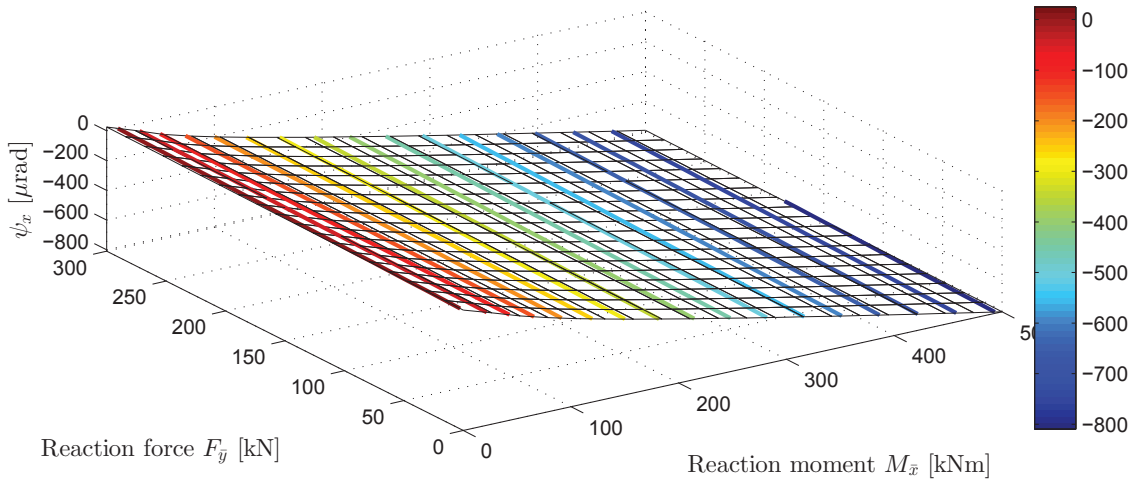

Figure 11.11: Rotor angular position ψ_x as function of bearing load. Isoline difference: 50 μrad

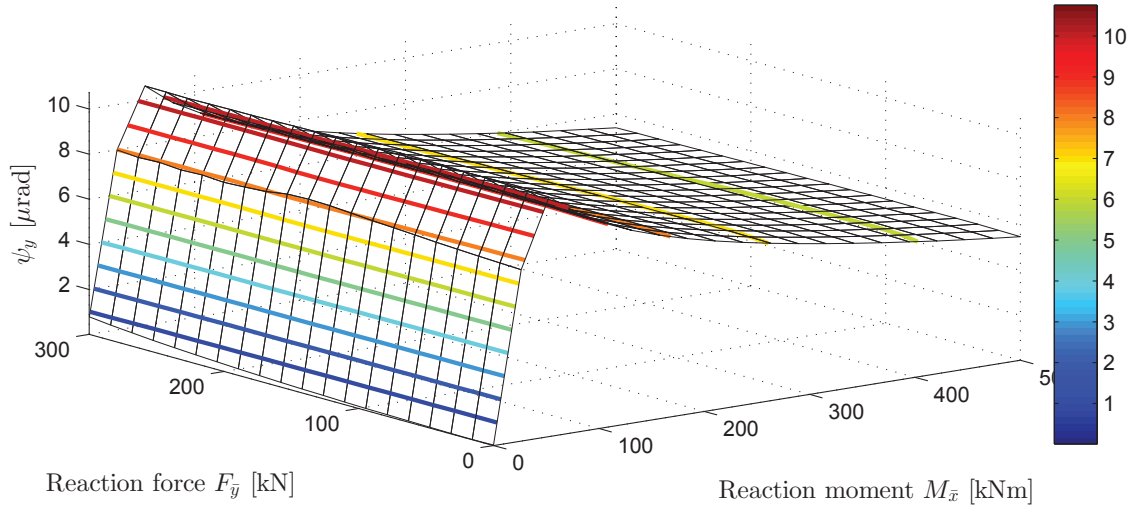

Figure 11.12: Rotor angular position ψ_y as function of bearing load. Isoline difference: 1 μrad

11.3 Analysis of single load case

This section is devoted to the steady state analysis of the most severe load case from the previous study, i.e. a radial force in y-direction $W_{\bar{y}}$ = -300 kN in combination with a bending moment around the x-axis $G_{\bar{x}}$ = -500 kNm.

First the system response is studied looking at the response of all 3×12 pads and finally a single thrust and a single radial pad is chosen further analysis.

11.3.1 System response

Pressure and film thickness profiles

In this section the pressure and film thickness profiles are shown for all pads in the bearing. Emphasis is on the qualitative characteristics whereas a more quantitative approach is used in the next section.

Figure 11.13 shows the pressure distribution for all pads in the bearing with a maximum value of 36 MPa. It is clearly seen that the pressure build-up corresponds to the external load comprised of a radial force in combination with a bending moment.

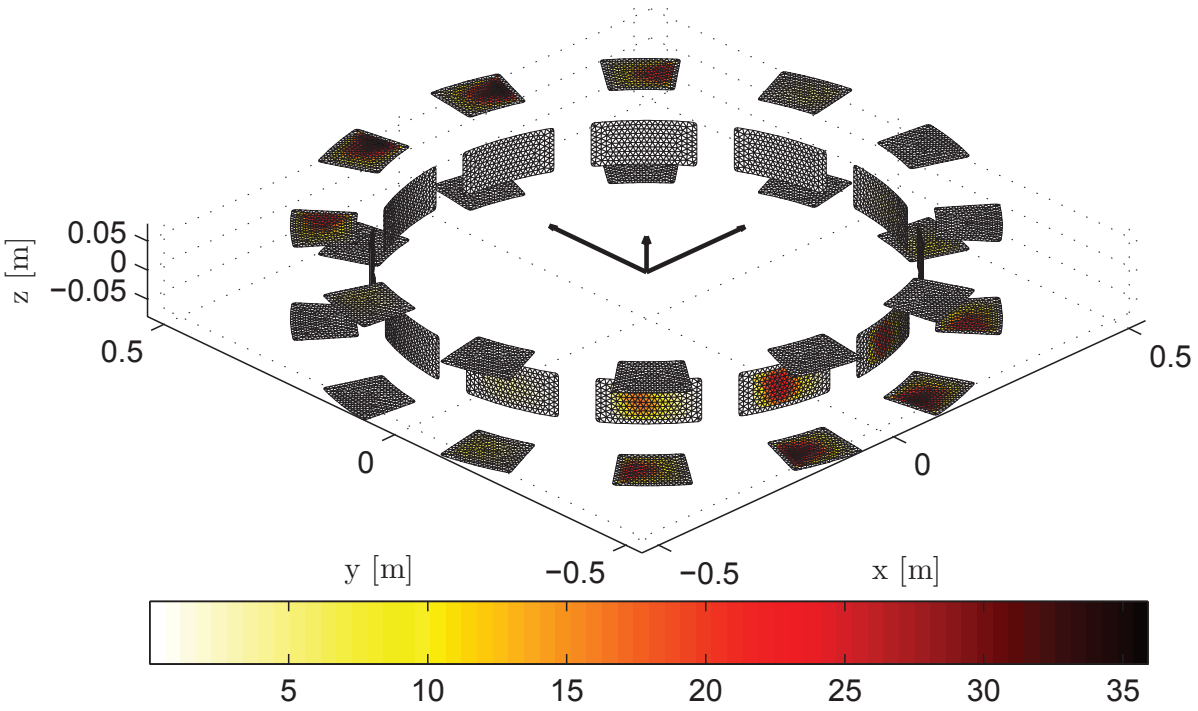

Figure 11.13: Oil film pressure [MPa]

Figure 11.14 shows the film thickness for the thrust pads. Is is seen how the rings and pads have deformed in the loaded sections and thereby allowing more pads to build up a pressure in the lubricant due to the low film thickness. This is also seen for the radial pads in figure 11.15.

Usually for a conventional pivoted tilting pad bearing, the unloaded pads will also build up and oil film pressure, although often negligible. This is not always the case for the flexure supported pads because it takes a minimum force to facilitate the flexing and achieve a converging lubricant film geometry allowing the pressure to build up hydrodynamically.

Interestingly the the maximum film thickness for the thrust pads is 510 μm (for the rear thrust pads) and when adding the film thickness of the corresponding pad sitting on the front row (10 μm) it gives a total axial clearance of 520 μm. The total axial clearance in the bearing's undeformed state is 2×75 μm. Thus the flexibility is responsible for up to 147 % extra axial clearance in the bearing. Radially the flexibility adds 100 % extra clearance at the given load.

The original clearance of 75 μm in radial and axial direction in the undeformed state seems small, but these values are justified because of the significant elastic deformation of pads and supporting structure.

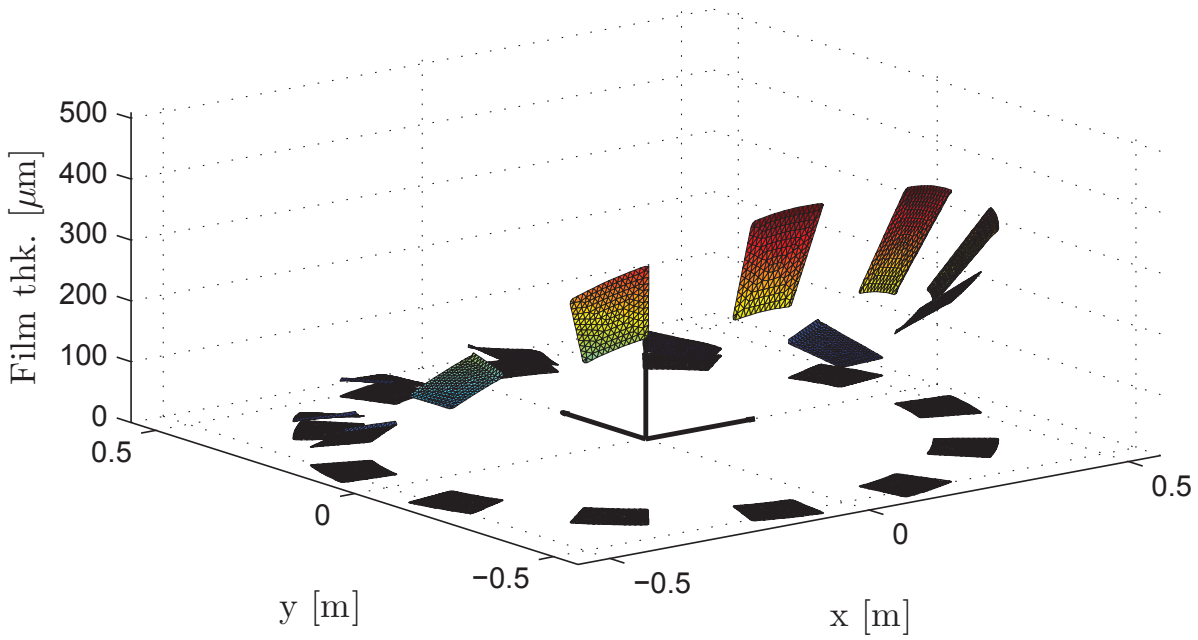

(a) Rear thrust pads

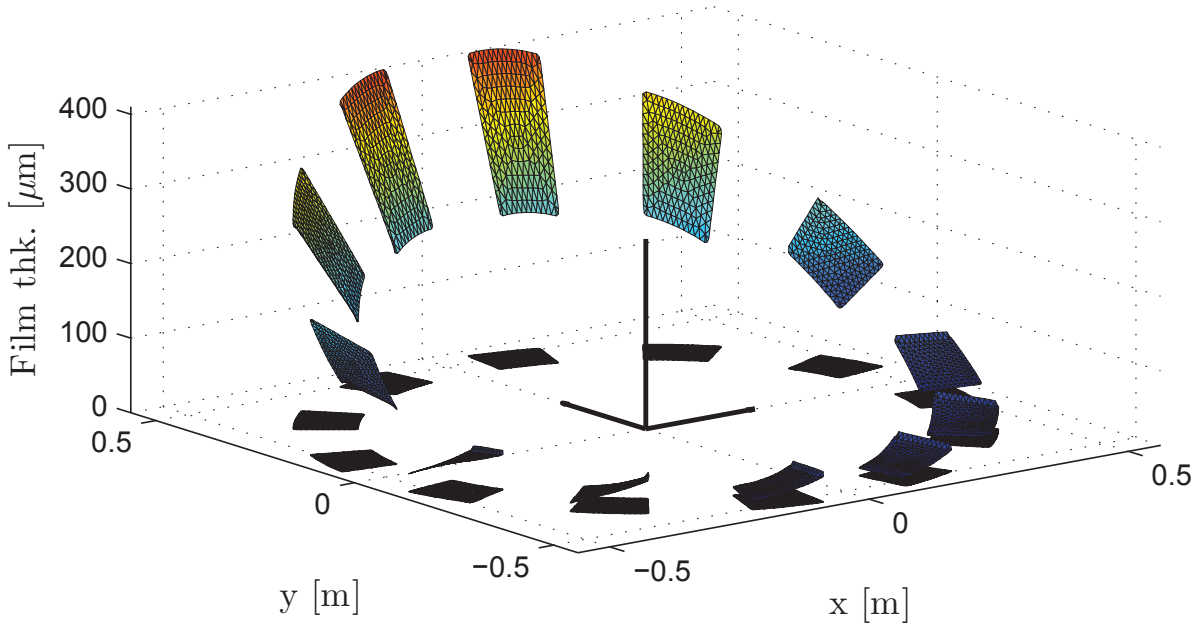

(b) Front thrust pads

Figure 11.14: Oil film thickness for thrust pads

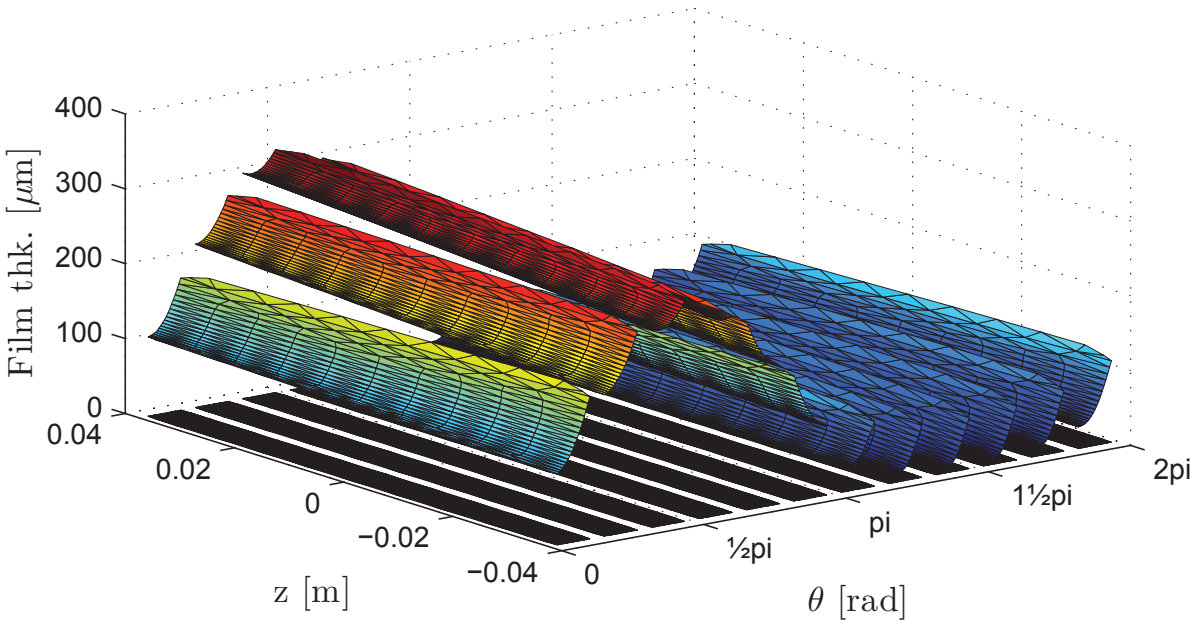

Figure 11.15: Oil film thickness for radial pads

Individual pad operational parameters

In this section the bearing performance is analyzed through figures 11.16 to 11.18. Each dot on the curves represents a discrete location, namely the combined pad parameter at that given location, and thus the lines connecting the dots do not represent a continuous function. They merely connect the dots to allow for easier interpretation.

The resulting forces on the pads, corresponding to the pressures from figure 11.13, are shown in figure 11.16(a).

For an infinitely stiff bearing the front thrust pads would show exactly the same force distribution as the rear thrust pads. Due to the non-symmetric deformation there is a small difference as seen in figure 11.16(a): the front row pads have a narrower distribution and thus also higher peak values.

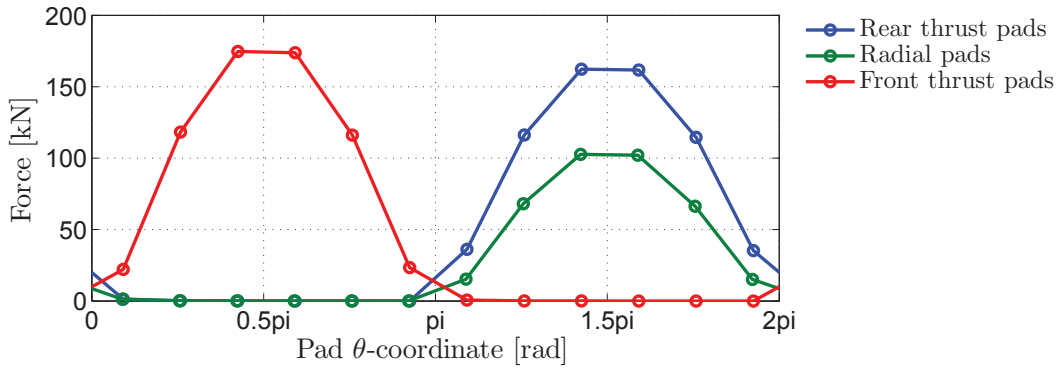

(a) Resulting force

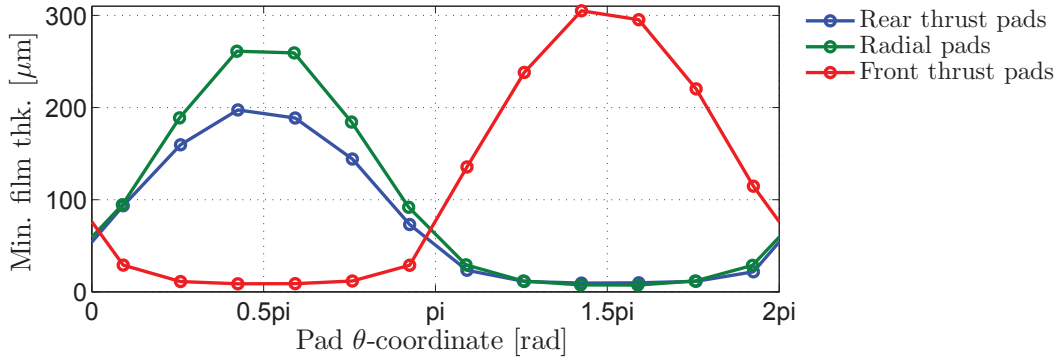

(b) Minimum film thickness

Figure 11.16: Pad parameters for the individual pads

Figure 11.16(b) shows the minimum film thicknesses for the individual pads with minimum values of 8.8 and 7.4 μm for the thrust and radial pads respectively.

Figure 11.17(a) shows the viscous dissipation for the individual pads. The total loss is 3,072 W of which the 18 unloaded pads account for 352 W, i.e. a parasitic loss of 11 %.

Figure 11.17(b) shows the lubricant flow for the individual pads. The combined flow for all pads is 24 l/min of which the 18 loaded pads account for just 4.0 l/min. Since the unloaded pads do not carry any load, it is not strictly necessary to supply the full amount of oil to these pads (assuming a spray bar or leading edge groove lubrication system is used, where the lubrication of each individual pad is specified).

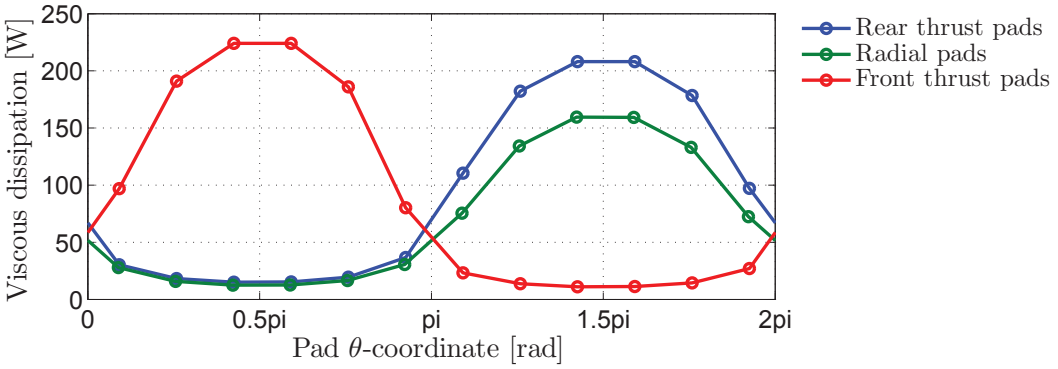

(a) Viscous dissipation

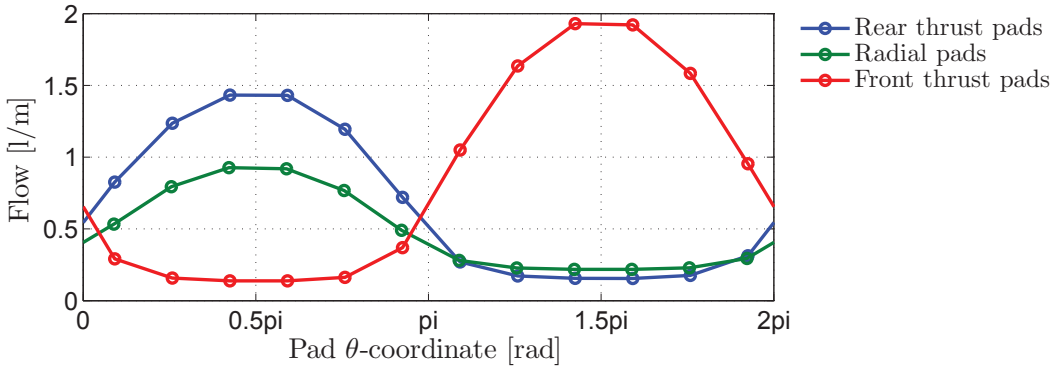

(b) Lubricant flow rate

Figure 11.17: Pad parameters for the individual pads

When lubricant properties, flow rate and viscous dissipation are known, the corresponding temperature rise can be calculated assuming adiabatic boundary conditions using equation (11.2). The equation is only valid for steady state conditions, where the viscous loss and lubricant flow rate can be considered constant over time. If this is not the case, the lubricant volume within the lubricant zone must also be considered, since it acts as a heat sink.

$$\Delta T = \frac{P}{q c_p \rho} \tag{11.2}$$

The temperature rise, assuming adiabatic boundaries, is shown in figure 11.18. A temperature rise of 57 °C is found for the hardest loaded pads. This shows that the iso-viscous model cannot be expected to return reliable results even though the inlet

temperature of 50 °C is set somewhat high. Preferably the model should be extended to include the thermohydrodynamic-model proposed in section 7.

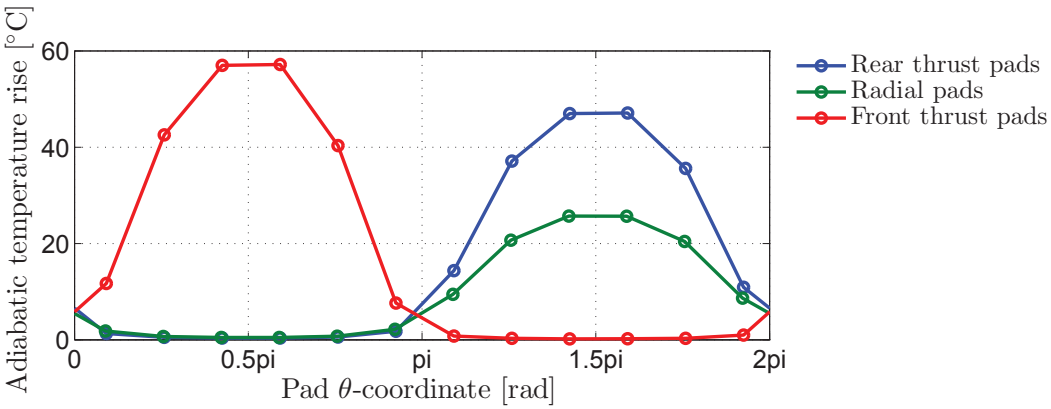

Figure 11.18: Lubricant temperature rise for the individual pads assuming adiabatic boundaries

11.3.2 Elastic behavior of thrust pad

In this section the elastic behavior of the hardest loaded rear thrust pad carrying 162 kN is analyzed. Since the film thickness and pressure profile is closely connected to the deformation, these parameters are shown in figure 11.19.

Figure 11.19(a) shows the film thickness and interestingly the location of the flexure support can be seen as a small curvature. The pressure profile of figure 11.19(b) shows very high gradients at the trailing edge of the pad. This could lead to an error in the calculated lubricant flow rate at this boundary, since this calculation is based directly in the pressure gradients at the edges. The load carrying capacity, derived from the pressure distribution, is not expected to be influenced in a significant extent.

Figure 11.20(a) shows the combined deformation of the rotor and stator (incl. the pad) projected into the film thickness direction. Values up to 413 μm is observed.

In order to see how the pad itself deforms, excluding rigid body motions and contributions from the supporting structure, a plane is fitted through the deformation plot from figure 11.20(a) using the method of least-mean-squares. This plane is then subtracted from the deformation values giving the values shown in figure 11.20(b). It must be noted that the deformation still includes local contributions from both rotor and stator. Positive deformation values induce larger film thickness due to deformation.

Again the curvature arising from the extra stiffness just over the flexure support is clearly visible. It is also seen that the pad deformation is not only due to bending, since the deformation has a local maximum at the same location as the maximum pressure and not at the edges. The bending is deemed to be on a moderate level

and from this, and also the film thickness plot of figure 11.19(a), it is concluded that the bad body is sufficiently stiff. This is also backed up by the linear nature seen on figure 11.4, which displays the maximum pressure as function of bearing load.

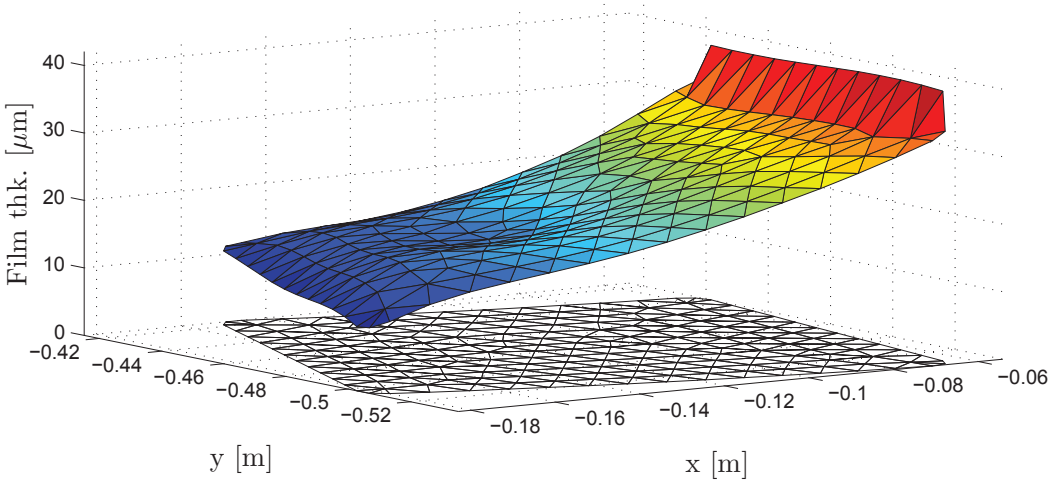

(a) Film thickness

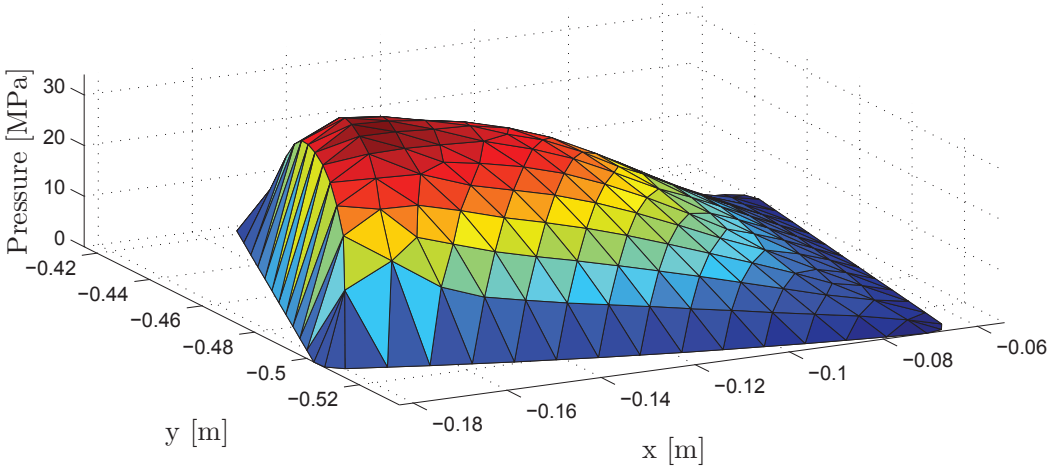

(b) Pressure

Figure 11.19: Hardest loaded rear thrust pad response

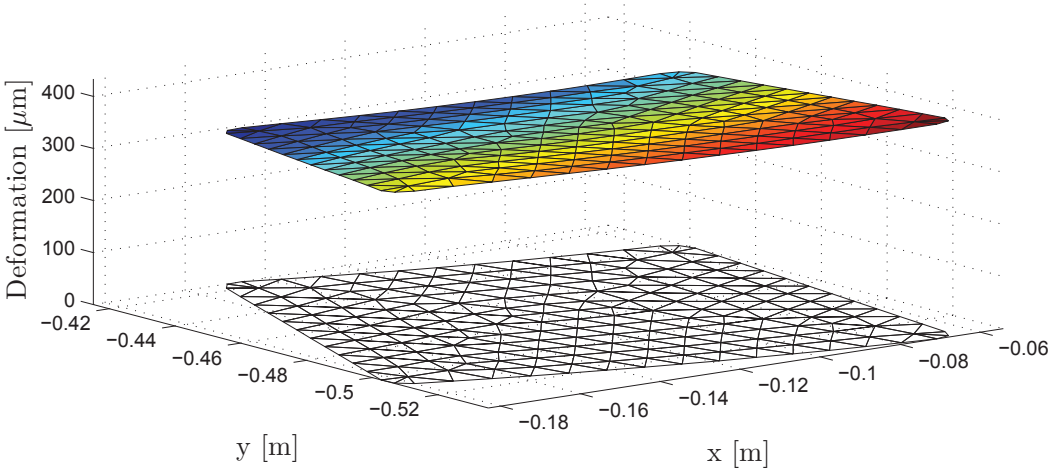

(a) Deformation

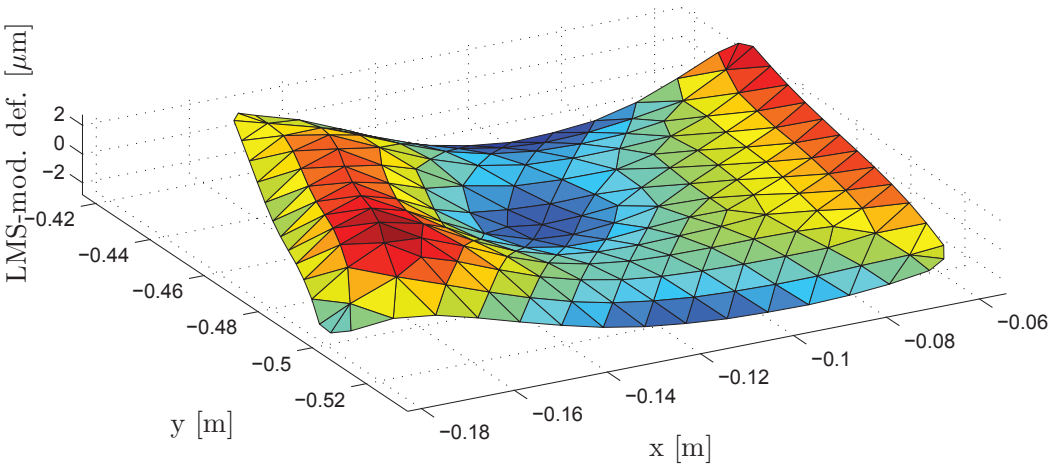

(b) Deformation modified with least-mean-squares plane

Figure 11.20: Hardest loaded rear thrust pad response

11.3.3 Elastic behavior of radial pad

As for the thrust pad, the hardest loaded radial pad is examined. Figure 11.21 shows the film thickness and corresponding pressure distribution. Cavitation is observed at the trailing edge of the pad.

The film thickness has a saddle shape which is somewhat contra-intuitive since one may expect that the bending would contribute most significantly. However, the local compression is biggest giving large deformations corresponding to the pressure profile. This is probably due to the low width of the radial pad (75 mm) compared to the diameter of the flex support (20 mm). This only leaves 27.5 mm overhang on each side of the flexure support.

At the applied load the angular position of the rotor ψ_x is -794 μrad c.f. figure 11.11. This corresponds to a difference in film thickness of 60 μm over the 75 mm width of the radial pad. However, as seen on figure 11.21(a) there is no sign of edge loading indicating that the flexure support works as intended.

The flex support location is not clearly visible on the deformation plot (figure 11.22(b)), as for the thrust pad. It is possibly due to the narrower pad and lower pressure levels.

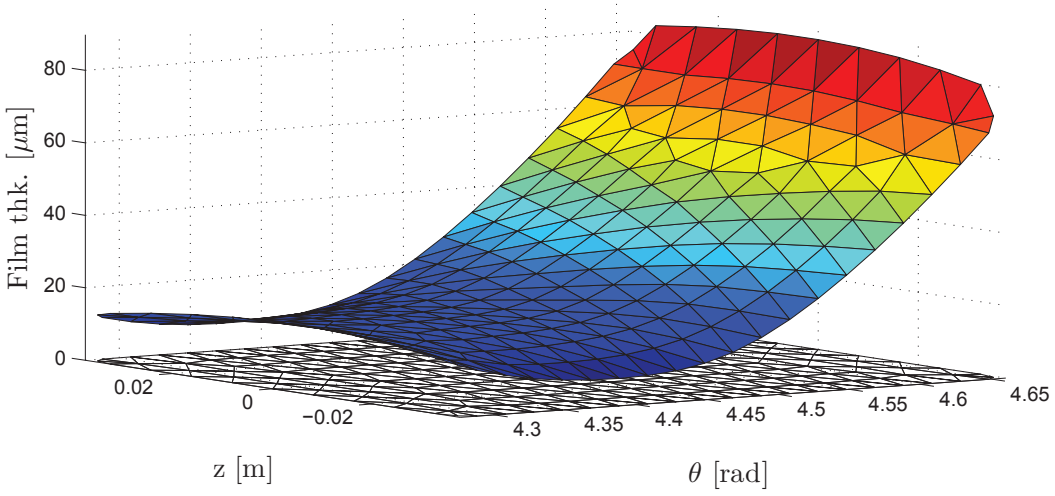

(a) Film thickness

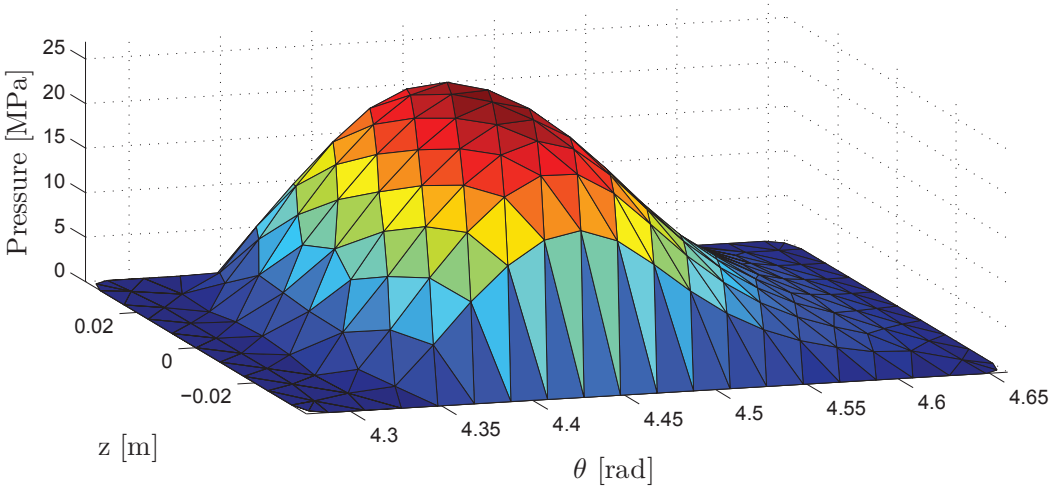

(b) Pressure

Figure 11.21: Hardest loaded radial pad response

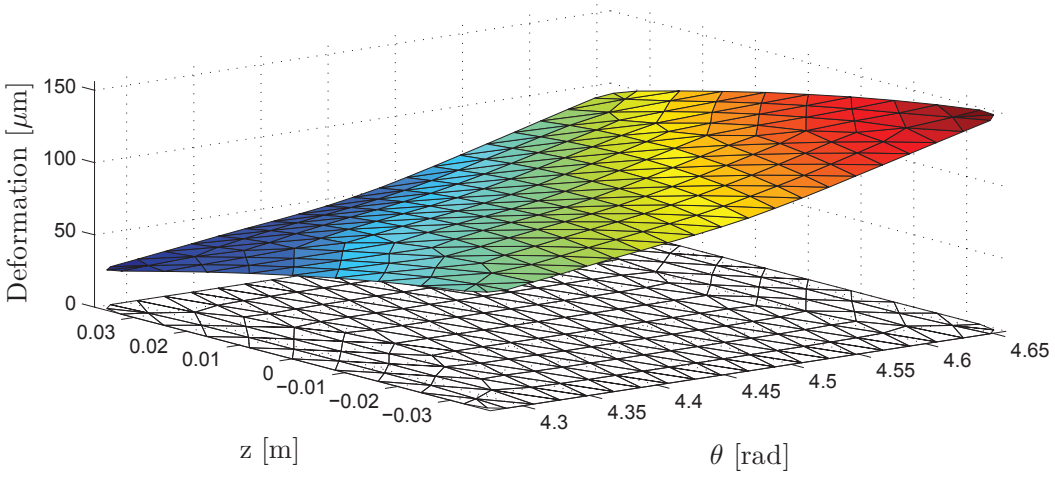

(a) Deformation

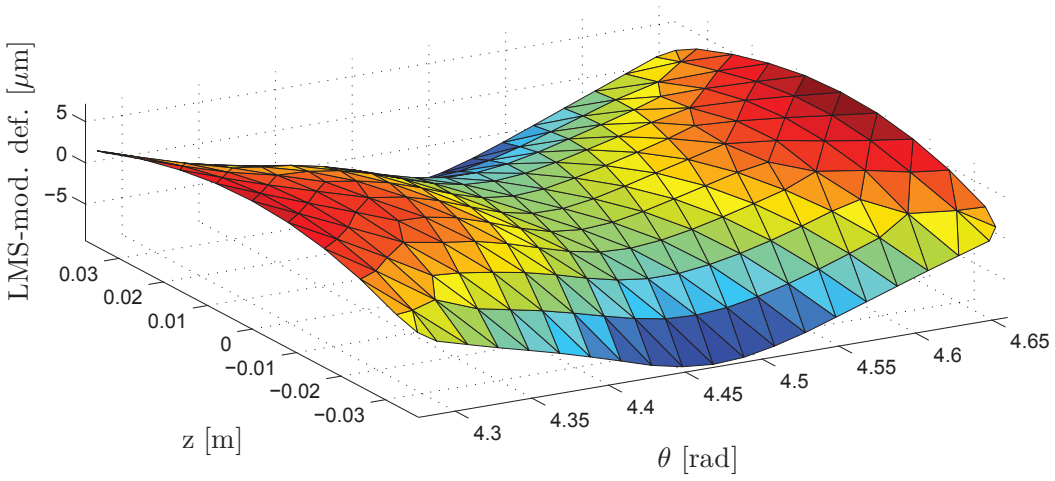

(b) Deformation modified with least-mean-squares plane

Figure 11.22: Hardest loaded radial pad response

Chapter 12

Conclusion

The present thesis deals with numerical modeling of hydrodynamic bearings focusing on the operational conditions of modern wind turbines. The unique operational conditions for these are discussed as well as general design limits for hydrodynamic bearings.

Elaborate work is done on developing numerical models capable of predicting the behavior of hydrodynamic bearings under the conditions that apply for wind turbines.

The variational principle is applied to Reynolds equation, using the classical assumptions, in order to establish the finite element equations that allow for calculation of the oil film forces and cavitated regions. A model for the angular equilibrium position of tilting pads is established and implemented. Lund's perturbation method is applied in order to efficiently and accurately determine the dynamic coefficients of the bearings.

The fluid film pressure model is coupled with an elastic deformation model for the bearing solids giving an elastohydrodynamic model. Two different modeling approaches are investigated. The first model includes the local deformation of the liner using a column model and can thus be used to study the effect of compliant liners. The second, and much more comprehensive, model includes the full structure of a bearing using state of the art industrial software to set up the matrix correlating force and displacement. This model is then coupled with the film force model using the Newton-Raphson iterative method. The, in this respect, essential Jacobian matrix is derived using the Galerkin principle.

In order to study the heat transfer in the hydrodynamic bearings the energy equation is solved using the finite difference method. Four different energy models are presented of which two include heat conduction through the journal. One model is based on the radial temperature gradient whereas the other uses heat transfer coefficients to calculate the radial heat transfer. Furthermore a new model is presented for the journal heat transfer, which enables calculation of the axial temperature variation in the journal without extensive numerical efforts.

Finally the EHD model is extended into 5 DOF allowing for accurate simulations of complex bearing systems. The presented approach, where the polar and cylindrical

representation of Reynolds equation is solved simultaneously and coupled with elasticity, is not seen before in the literature and therefore considered to be groundbreaking within this field.

Furthermore a wear model, which omits the need of determining the contact forces, is proposed and implemented.

A significant part of the present thesis is devoted to flexure bearings and through several studies the flexure mechanism is proven to work well and new ways of taking advantage of bearing flexibility are presented.

In the following sections the individual achievements of this work are presented. Four of the studies are published as journal papers.

Application of a new wear model

The aim of this work is to develop a wear model which can be used for wear estimation at thin lubricant films and at the same time be applicable for conventional EHD solvers without requiring extensive modifications.

A model, where the wear is based on the local film thickness, is presented and applied for a misaligned journal bearing. The predicted wear rate and pattern is compared quantitatively with experimental findings and good correlation is found.

The advantage using this model is that there is no need for estimation of contact pressure, which most wear models are based upon together with wear coefficients. Instead, the proposed model directly links film thickness with wear rate and thus indirectly includes the contact pressure and other influencing parameters in the experimentally obtained wear coefficients.

The wear model requires wear coefficients that correlate the wear rate with film thickness. These must be obtained through experimental work. However, it is difficult to measure the film thickness in the zone of mixed lubrication, especially if one sliding part comprises a compliant polymer.

Discontinuity effects in dynamically loaded tilting pad journal bearings

Based on the HD model two discontinuity effects that can occur in dynamically loaded tilting pad journal bearings are revealed and it is shown how the tilting pads in a radial tilting pad bearing display two distinct equilibrium positions, of which only one is stable.

The first discontinuity effect is related to a pressure build-up discontinuity and its fundamental cause is the fact that the squeeze term can vary significantly along the circumferential pad extent. Thus the squeeze term can cause cavitation at one end of the pad while increasing pressure at the other end.

The other discontinuity effect is caused by contact between tilting pad and journal and once this is included in the numerical model the discontinuity disappears. Thus it is not a real physical phenomenon.

In order for the first discontinuity to appear two conditions are required:

- the squeeze term must dominate the right-hand side of Reynolds equation. This requires slow rotation in combination with large dynamic loads.
- the pad circumferential extent must be large, so that the influence from the shaft center velocity on the squeeze term is different from leading edge to trailing edge of the pad.

Compliant liners and their influence on dynamically loaded hydrodynamic journal bearings

The influence of the liner stiffness on the dynamic response of a highly dynamically loaded journal bearing is evaluated by varying the stiffness and comparing the response using a soft EHD model. The hydrodynamic performance is evaluated on the parameters that are traditionally used to evaluate hydrodynamic bearing designs: dynamic response, maximum pressure, minimum film thickness, wear, power loss and temperature response.

The primary findings are that the maximum pressures are reduced significantly and this comes at the expense of slightly higher eccentricity ratios during operation.

The influence of the geometrical design parameters and compliant liners on a radial flexure pad

A hydrodynamic journal bearing utilizing flexure pads with a compliant liner is studied and its performance is evaluated through a parametric study using the EHD model. The main geometrical dimensions are varied and the effect on pad performance is analyzed.

This has put more knowledge into the design and function of flexure pads. Guidelines are given to the design of the flexure pads, including the polymer liner.

It is found that the use of flexure pads is an attractive alternative to pivoted pads. Pivot contact-related failure modes are eliminated and load capacity is not restricted by the force that can be transferred through the pivot contact. When combined with a polymer liner, the pad performance is enhanced further, especially when operating at thin lubricant films.

Improvement of journal bearings operating at heavy misalignment using flexure design and compliant liners

Misalignment is the root cause of many journal bearing failures and therefore a flexure journal bearing design is proposed that improves the operational behavior of a journal bearing operating at heavy misalignment. The design does not add extra components or systems that require fine machining and can thus be categorized as inexpensive. The design does however require extra space for the flexure web that may be difficult to combine with some bearing applications.

Using the TEHD model it is shown that the proposed flexure journal bearing design effectively increases bearing performance when operating at high misalignments. The performance at low or no misalignment is not affected.

Based on the predicted minimum film thicknesses the proposed flexure journal bearing can operate at 3 times the misalignment compared to the stiff bearings. The studied bearing has a width to diameter ratio of only 0.5 and the effects are expected to be even more pronounced for bearings with higher ratios since these are more sensitive to misalignment.

Furthermore the influence of a compliant bearing liner is investigated and a remarkable increase in hydrodynamic performance is found when applied to the stiff bearing, interestingly also at low or no misalignment. The positive influence is however not seen on flexure bearings. The polymer liner does, however, still give the increased performance at boundary or mixed lubrication, giving better wear properties and lower friction. This comes with the side-effect of increased thermal insulation.

It is also shown that the traditional assumption of infinitely stiff journal and bearing is not valid since a high deformation, several times the minimum film thickness, is observed for the bearing configuration using a solid steel housing.

Analysis of a novel compact moment-carrying hydrodynamic bearing supporting 5 DOF

A novel moment-carrying hydrodynamic bearing supporting 5 DOF is presented and its hydrodynamic performance is studied using the EHD model.

The bearing performance is studied for a combination of radial forces and bending moments. When studying the global behavior of the bearing system, i.e. maximum and minimum values for parameters such as pressure and lubricant film thickness, the radial and axial pads are found not to couple strongly. That is, for a region of the applied loads, the hydrodynamic parameter is governed primarily by the radial load *or* the bending moment.

A linear relationship is found between radial force and maximum pressure and also between bending moment and maximum pressure. For the bearing configuration investigated it is demonstrated that the pad deformations are not excessive giving unfavorable pressure distributions. It is furthermore found that the flexure supports work as intended allowing the pads to adjust according to the external loads.

This linear relationship can only be observed because the thermoelastohydrodynamic model is not yet implemented for the 5 DOF bearing model. The effect of the heat transfer and thermo-viscous effects will influence the results in a very nonlinear manner, especially for the highest loads, where a temperature rise of 57 °C is found assuming adiabatic boundary conditions.

As expected for a tilting pad bearing only little cross coupling is found between the 5 DOF.

When studying a single load case the seemingly rigid bearing structure is found to deform to a high degree, compared to the bearing clearance. The clearance is

found to increase with 147 % axially and 100 % radially. This inevitably results in correspondingly high rotor eccentricities in the stator, it does however also lead to a high degree of load equalization between neighboring pads.

Recommendations for further work

In order for the presented 5 DOF bearing model to accurately describe the full operational envelope of a hydrodynamic bearing, the thermoelastohydrodynamic model must be expanded to cover 5 DOF.

Additionally it is recommended to extend the lubrication regime, at which the multiphysics bearing model is valid, into the mixed lubrication regime. This includes the effects at very thin films, where surface roughness affects the pressure build-up as well as the influence on friction from asperity contacts.

Appendix A

Journal paper: Discontinuity effects in dynamically loaded tilting pad journal bearings

Accepted for publication in Journal of Engineering Tribology [8].

Discontinuity effects in dynamically loaded tilting pad journal bearings

K Thomsen[1]*, **P Klit**[1], and **A Vølund**[2]
[1]Department of Mechanical Engineering, Technical University of Denmark, Lyngby, Copenhagen, Denmark
[2]MAN B&W, Copenhagen, Denmark

The manuscript was received on 11 August 2010 and was accepted after revision for publication on 16 February 2011.

DOI: 10.1177/1350650111403037

Abstract: This article describes two discontinuity effects that can occur when modelling radial tilting pad bearings subjected to high dynamic loads. The first effect to be treated is a pressure build-up discontinuity effect. The second effect is a contact-related discontinuity that disappears when a contact force is included in the theoretical model. Methods for avoiding the pressure build-up discontinuity effect are proposed.

Keywords: radial tilting pad journal bearing, discontinuity, instability, flutter, dynamic loads

1 INTRODUCTION

Flexible rotors operating at high rotational speeds are often supported in tilting pad journal bearings.

Radial tilting pad bearings are usually chosen for this type of machinery due to their stabilizing effect compared to other bearing types with fixed pads. The tilting pads ensure that the cross-coupling coefficients in the stiffness and damping matrices of the bearing are small compared to the diagonal coefficients. For applications where high shaft misalignments are unavoidable, radial tilting pad bearings can also be the preferred choice over plain journal bearings due to low sensitivity to this issue.

Desbordes *et al.* [**1**] studied the influence of pad deformations in a tilting pad journal bearing under dynamic loading. For normal operating conditions with a static load and a small mass unbalance, the flexibility of the pads hardly modifies the shaft orbit. Under severe operating conditions with large mass unbalance, the pad deformations do not affect the shape of the shaft centre trajectory, but increase the amplitude of the orbit significantly. The pad deformations furthermore increase the maximum pressure and decrease the minimum film thickness.

Haugaard and Santos [**2**] studied the stability properties of actively lubricated tilting pad journal bearings. It is shown that active hybrid lubrication can act to widen the range of operation conditions for which the bearing is stable, but it can also narrow it. Furthermore, it is shown that assuming the bearing pads to be rigid can produce a substantial error. A rigid pad model will overestimate the stable range of the bearing.

Abu-Mahfouz and Adams [**3**] has studied two mechanisms producing subharmonic and chaotic motions different from the classical oil whirl in a radial tilting pad bearing. The first one is that of a centrally loaded pad with mass unbalance. The second mechanism represents a concentric rotor acted upon by centring springs and large mass unbalance. It is demonstrated that geometric preloading stabilizes the rotor in both cases.

This study studies two specific discontinuity phenomena in radial tilting pad bearings. Other studies have shown other phenomena also leading to pad instabilities, also referred to as pad flutter.

Gardner [**4**] studied instabilities of unloaded radial pads and found that insufficient oil flow leading to starved conditions can cause pad instabilities.

Corresponding author: Department of Mechanical Engineering, Technical University of Denmark, Lyngby, Copenhagen, Denmark. email: kimth@mek.dtu.dk

Seongheon *et al.* [**5**] studied instabilities caused by self-excited vibrations and suggests a new pad geometry with a wedge-shaped groove in order to reduce risk of pad fluttering due to self-excited vibrations from high-speed machinery.

Hargreaves and Fillon [**6**] studied fluttering and spragging and describes how an instability at one pad can cause the neighbouring pads to reach instabilities when the journal changes position due to the decreased pressure at some pads.

Implementation of a time integration procedure for a slow rotating radial tilting pad bearing subjected to large dynamic loads showed problems with discontinuity phenomena in pad load-carrying capability. The instability phenomena are investigated by examining a bearing system consisting of only one pad. The pad has a circumferential extent of 70° and the pivot is located 60 per cent from leading edge and at 225° in the bearing, as shown on Fig. 1. This bearing configuration is obviously not of practical use, but it is advantageous in order to show how a particular pad performs when it is a part of, for example, a three- or four-pad bearing.

The rotational speed is 20 r/min and with a journal radius of 0.6 m, the surface sliding speed is 1.3 m/s. This is clearly in the low end of the operational envelope for hydrodynamic bearings in general. The low rotational speed requires a high-viscosity oil and an ISO VG 320 oil is used for this analysis.

The response of the pad, shown in Fig. 1, when subjected to high dynamic loads is studied by fixing the shaft centre position (C) together with all the operating parameters except for the shaft centre velocity ($\dot{C}$) whose X- and Y-components are varied.

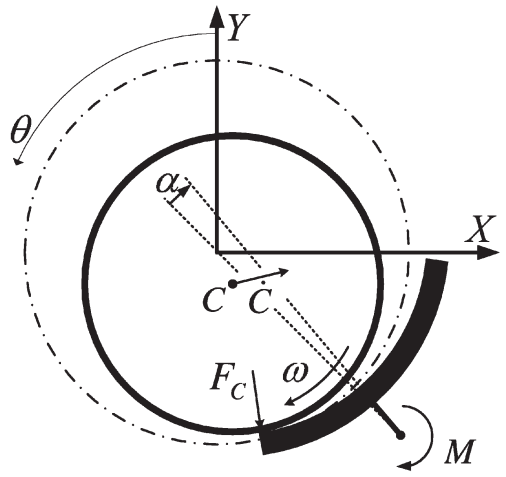

Fig. 1 Bearing system for modelling

2 THEORY AND MODELLING

2.1 Reynolds equation

A finite element method model with three-node triangular elements is used for solving Reynolds equation (1) and thus finding the pressure distribution. The thermoviscous effect is handled through an effective viscosity, corresponding to the average temperature giving energy balance assuming that 15 per cent of the frictional heat is conducted though pad and shaft. The remaining 85 per cent ($\beta = 0.85$) is transported with the lubricant flow. The average temperature and corresponding viscosity are calculated using equations (2) to (7)

$$\frac{1}{R}\frac{\partial}{\partial\theta}\left[\frac{h^3}{\mu R}\frac{\partial p}{\partial\theta}\right]+\frac{\partial}{\partial Z}\left[\frac{h^3}{\mu}\frac{\partial p}{\partial Z}\right]=6\omega\frac{\partial h}{\partial\theta}+12\frac{\partial h}{\partial t} \tag{1}$$

The frictional power generated in the lubricant is calculated from equations (2) and (3)

$$P=\omega R F_{\mathrm{S}} \tag{2}$$

$$F_{\mathrm{S}}=\int\left(\frac{h}{2R}\frac{\partial p}{\partial\theta}+\frac{\mu\omega R}{h}\right)\mathrm{d}A \tag{3}$$

Lubricant flow into the bearing is calculated according to equation (4)

$$Q=\int\left(\frac{h^3}{12\mu R}\frac{\partial p}{\partial\theta}+\frac{h\omega R}{2}\right)\mathrm{d}L \tag{4}$$

Generated power transported through convection

$$P_{\mathrm{conv}}=\rho c_{\mathrm{p}} Q\Delta T \tag{5}$$

Generated power transported through convection and conduction

$$P=P_{\mathrm{conv}}+P_{\mathrm{cond}}=P_{\mathrm{conv}}+P_{\mathrm{conv}}\left(\frac{1}{\beta}-1\right)=\frac{P_{\mathrm{conv}}}{\beta} \tag{6}$$

The Walther and McCoull equation [**7**] is used to describe the temperature–viscosity relationship

$$\log\log(\nu+a)=b-n\log T \tag{7}$$

Results from time integration show that the influence of the tilting angular velocity ($\dot{\alpha}$) of the pad on the squeeze term can be of the same order of magnitude as the influence from the shaft centre velocity ($\dot{C}$) at the leading and trailing edges of the pad. In order to exclude time history dependency, the pad angular velocity is set to zero ($\dot{\alpha}=0$) for the studies in this article.

2.2 Cavitation and boundary conditions

An iterative procedure is used to find the cavitated region. In each iteration, the system of equations is solved to find p. Nodes with negative pressures are identified and a pressure value of 0 is enforced on the regions with the lowest pressure. This procedure is repeated until no nodes exhibit negative pressures.

This algorithm ensures neither Reynolds boundary condition where $\partial p/\partial\theta = 0$ at the onset of cavitation nor mass conservation. Kumar and Booker [**8**] suggest a cavitation algorithm which ensures mass conservation. This algorithm is not implemented in this study.

The general boundary condition for the nodes located at the edges of the pad is a pressure of 0, and thus the ambient pressure must be added to all nodes if absolute pressure is required.

2.3 Pad angular equilibrium

Several forces act on the tilting pad and these forces must counterbalance each other, giving moment equilibrium. The forces originate from contact force $\boldsymbol{F}_{\mathrm{C}}$, oil pressure forces $\boldsymbol{F}_{\mathrm{P}}$, and oil shear forces on the pad surface $\boldsymbol{F}_{\mathrm{S}}$. The balance of moment $\boldsymbol{M}$ on the pad around the pivot centre is calculated by summing the contribution from all elements n. $\boldsymbol{S}$ is the distance vector from element centre to pad pivot centre

$$\boldsymbol{M} = -\sum_{e=1}^{n} [(\boldsymbol{F}_{\mathrm{P\_}e} + \boldsymbol{F}_{\mathrm{S\_}e}) \times \boldsymbol{S}_{\_e}] - \boldsymbol{F}_{\mathrm{C}} \times \boldsymbol{S}_{\mathrm{C}} \tag{8}$$

The elements of equation (8) are shown in Fig. 2. The pivot of the bearing is assumed frictionless and hence it has no influence on the pad angular equilibrium position. In practice, the pivot will always cause a resistance towards motion and this will require $|\boldsymbol{M}| > \boldsymbol{M}_{\mathrm{Resistance}}$ in order for the pad to adjust position according to the external loads.

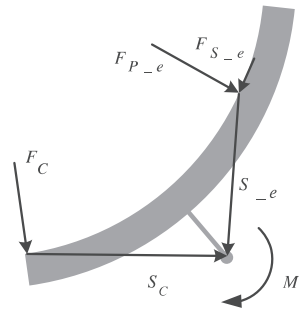

Fig. 2 Calculation of moment contribution from element

A typical relationship between $\boldsymbol{M}$ and pivot tilting angle α is shown in Fig. 3. For all operating conditions, $\boldsymbol{M} = 0$. $\boldsymbol{M} \neq 0$ exists only mathematically and is encountered in the seeking of the parameters giving $\boldsymbol{M} = 0$.

A combination of the bisection method and the secant method is used to create a robust algorithm to find the α-values corresponding to $\boldsymbol{M} = 0$.

If the minimum oil film thickness $h_{\min}$ reaches 0 in the seeking of moment equilibrium while $\boldsymbol{M} > 0$, a contact force at the trailing edge is introduced to give moment equilibrium.

The value of $\boldsymbol{M}$, when $h_{\min} = 0$, is used to calculate the contact force $\boldsymbol{F}_{\mathrm{C}}$ that gives moment equilibrium.

Usually, it is not possible to include contact forces when solving Reynolds equation. In this case, the trailing edge, where the contact occurs, is cavitated because the magnitude of the negative squeeze term in Reynolds equation is higher than the Couette term and therefore gives cavitation at the contact region.

This is also influenced by the simplification $\dot{\alpha} = 0$ which is debatably when there is contact at the trailing edge of the pad.

The model could include the moment from the friction force coming from the contact between pad and shaft. This contribution to the moment balance will only affect the magnitude of the contact force and not change the oil film forces. Therefore, the contribution is judged to be of minor importance.

2.4 Verification of the mathematical model

The solution of Reynolds equation and the method employed for finding the pad angular equilibrium and integration in time domain are verified by modelling the three-pad journal bearing presented in reference [**1**] and comparing the dynamic response for

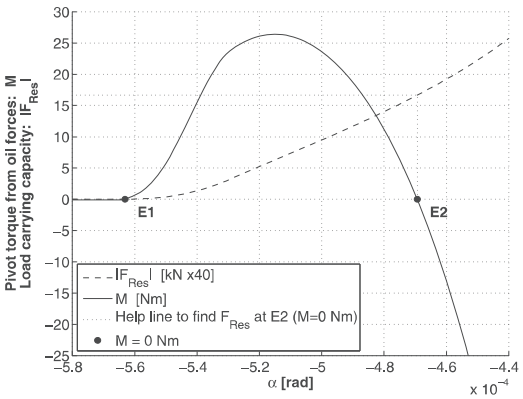

Fig. 3 $M(\alpha)$ and $\boldsymbol{F}_{\mathrm{Res}}(\alpha)$ curves for point E in Fig. 4

operation at a light and a severe mass unbalance situation.

The bearing consists of three pads located at 0°, 130°, and 230° when measuring from 12'clock and counter clockwise. The pad circumferential extents are 60°, 80°, and 80°, respectively. Bearing radius is 60 mm and the rotational speed is 3000 r/min. The static load on the bearing is 30 kN and the rotational mass 1000 kg exerting an unbalance load at eccentricities (e) of 100 and 506 μm. The complete description of the bearing is found in reference [**1**].

The model developed for the simulations in this study only accepts pads of equal size and therefore all pads are modelled using a circumferential extent of 80°. This deviation only affects the part of the shaft centre trajectory where the small pad builds up a significant oil pressure and therefore the results can still be used for verification purpose.

The found shaft centre trajectories shown in Fig. 4 are consistent with the findings of reference [**1**] although there is a little divergence for the highly unbalanced load case at the upper part of the curve. At this section of the curve, it is visible that the upper pad is 33 per cent bigger and therefore has a higher load capacity giving a lower eccentricity ratio when compared to the results from reference [**1**].

The method employed for handling cavitation is verified by disabling the pad rotational degree of freedom in the model and modelling the connecting rod big end bearing of the Hornsby 6VEBX Mk III four-stroke diesel engine. The dynamic response of the bearing is calculated and compared to the findings of McIvor and Fenner [**9**]. The result is shown in Fig. 4 and it is consistent with the findings of reference [**9**].

3 RESULTS AND DISCUSSION

With the purpose of studying the operation of tilting pad bearings subjected to dynamic loads, the bearing configuration shown in Fig. 1 is examined.

The shaft centre velocity will change as a function of the magnitude and dynamics of the external load as well as the bearing properties. In order to examine the discontinuities of the pad load-carrying capacity $\boldsymbol{F}_{\mathrm{Res}}$, the shaft centre velocity is varied while keeping all other parameters constant. Hereby, the effect of shaft centre velocity on pad performance is examined.

If one wishes to do the reverse calculation and determine the shaft centre velocity from a specific external load, the damping coefficients can be calculated and used as described by, respectively, Klit and Lund [**10**] and Vølund and Klit [**11**].

3.1 Results from varying shaft centre velocity

Figure 5 shows the result from varying the shaft centre X- and Y-velocity components. The vertical axis shows the resulting force from the pad to the shaft.

For locations with $\boldsymbol{F}_{\mathrm{Res}} = 0$, there is no value for α giving moment equilibrium and thus the pad has no load-carrying capacity. The discontinuities discussed in this article are shown with the lines I and II. The lines I and II do not meet.

3.2 Pad load-carrying discontinuity

Line I on Fig. 5 represents a pad load discontinuity line. When it is crossed, the load-carrying capacity of the pad drops to zero.

In order to investigate this phenomena, the correlation between the pivot tilting angle α, the pivot

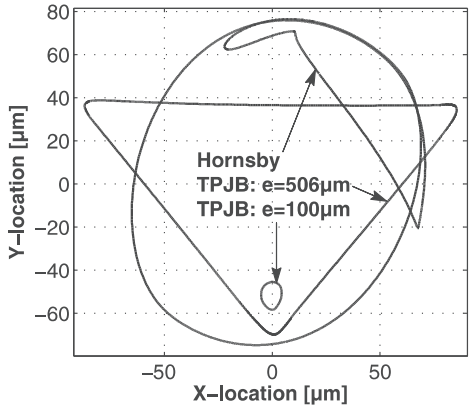

Fig. 4 Calculated shaft orbits for validation of mathematical model

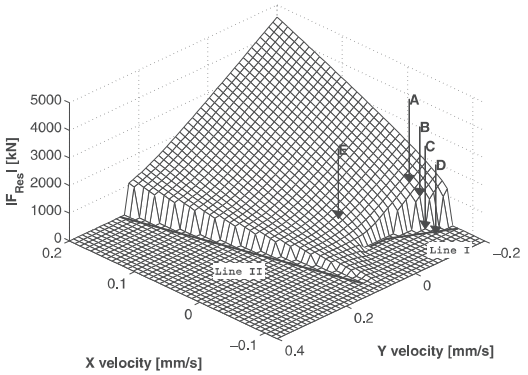

Fig. 5 Pad load-carrying capacity at different shaft centre velocities

moment $\boldsymbol{M}$, and the load-carrying capacity $\boldsymbol{F}_{\mathrm{Res}}$ is examined.

Five data points from Fig. 5 are used in this analysis: A, B, C, D, and E. The data point E corresponds to the static situation where the X- and Y-components of the shaft centre velocity are zero. The correlation between the three parameters α, $\boldsymbol{M}$, and $\boldsymbol{F}_{\mathrm{Res}}$ at point E is shown in Fig. 3.

From Fig. 3, it is seen that there are two equilibrium conditions ($\boldsymbol{M}=0$) where the moment contribution from the oil pressure exactly counterbalances the moment contribution from the shear of the oil. There is no contact force at E1 and E2 and therefore $\boldsymbol{F}_{\mathrm{C}} = 0$ in equation (8). $\boldsymbol{M} < 0$ in Fig. 3 imposes $\dot{\alpha} < 0$ and correspondingly $\boldsymbol{M} > 0$ imposes $\dot{\alpha} > 0$. Therefore, the solution at E2 is the only stable solution since a small perturbation at E1 will destabilize the equilibrium and the pivot tilting angle will move away from E1. If $\dot{\alpha} > 0$, the pivot tilting angle will move towards E2. If $\dot{\alpha} < 0$ from point E1, the leading edge of the pad will make contact with the journal. If one or more pads operate in the region of E1, there is risk of pad flutter and spragging, as described by Hargreaves and Fillon [**6**].

The moment curves for the points A to D in Fig. 5 are shown in Fig. 6. Note that the letters A to D on Fig. 6 do not represent a *point* of interest. The letters in Fig. 6 tell the names of the lines that correspond to the points of the same names in Figs 5 and 7.

It is seen that A + B and C + D are located on either side of the discontinuity line I and thus moment equilibrium positions only exist for A and B.

The moment curves for points A and B both have two equilibrium positions of which only one is stable. Each moment curve for data points lying exactly on the discontinuity line (line I, Fig. 5) will have coinciding α-values for $\boldsymbol{M}=0$ and $\partial \boldsymbol{M}/\partial\alpha = 0$ and thus only have one equilibrium position. This position is stable.

When the shaft centre velocity components for this point on the discontinuity line is changed towards the zero-load capacity side of the discontinuity line, the load-carrying capacity of the pad will drop instantly from ~800 kN to 0 kN, and $\dot{\alpha} < 0$ since $\boldsymbol{M} < 0$.* The minimum film thickness at line I in Fig. 5 is >0 and therefore $\boldsymbol{F}_{\mathrm{C}} = 0$ in equation (8).

Depending on the full bearing configuration, primarily the location and number of other pads, the shaft will accelerate towards the pad that has just crossed the discontinuity line and therefore loose its load-carrying capability. When accelerating towards the pad, the shaft centre velocity components will change, and the discontinuity line will be crossed again and thus the pad regains a pressure build-up.

*800 kN = 20 × 40 kN, c.f. interpolation in Fig. 6.

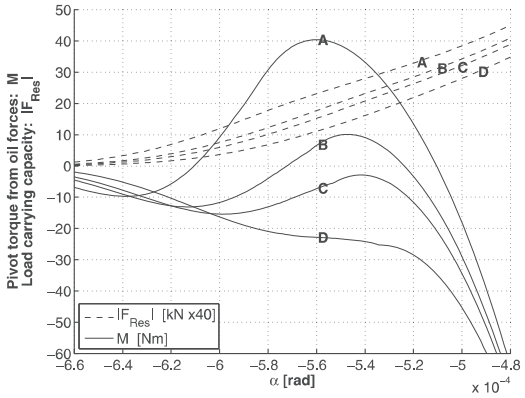

Fig. 6 $M(\alpha)$ and $\boldsymbol{F}_{\mathrm{Res}}(\alpha)$ curves for point A, B, C, and D in Fig. 4

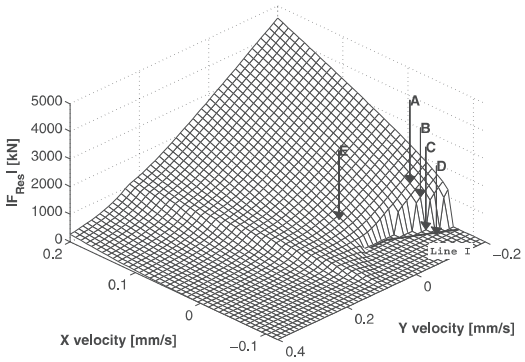

Fig. 7 Pad load capacity at different shaft centre velocities when the contact force is included

The fundamental cause of the discontinuity is cavitation and the fact that the shaft centre velocity causes a squeeze term of the pad that is varying along the circumferential extent of the pad.

If pressures below zero were allowed in the model or the circumferential extent of the pad was small, the pad load-carrying discontinuity would not occur. Therefore, the load-carrying discontinuity is not observed in a tilting pad thrust bearing.

The location of the discontinuity line I in Fig. 5 can be moved or even eliminated by changing the design of the tilting pad or adding features to the pads.

1. Decreasing the circumferential extent of the pad will decrease the variation in the squeeze term pressure effect along the pad and hence move the discontinuity line further away from normal operation conditions.

2. Preloading the pad with a positive moment will move the moment lines up (Fig. 6) and thus move the discontinuity line further away from normal operation conditions. The preloading could be introduced by means of a spring, a rubber-mounted pivot, or even a flexible steel support for the pad. These changes require careful design; otherwise, the pad performance could be reduced and give rise to other contact problems because the ability of the pad to rotate freely according to the load is reduced.
3. Introducing a leading edge groove with pressurized oil supply for the pad will give a positive moment contribution and move the discontinuity line further away from normal operation conditions. The level of oil pressure will determine the effect of the oil groove.

3.3 Trailing edge contact with journal

At line II in Fig. 5, there is contact between the journal and the trailing edge of the pad. $\boldsymbol{M} > 0$ for the α-value where contact occurs. $\boldsymbol{M} > 0$ induces $\dot{\alpha} > 0$ but motion is blocked due to the contact and therefore a contact force is required to give moment equilibrium. When the contact force is included in the model, the discontinuity line II in Fig. 5 disappears, as shown in Fig. 7.

From Fig. 7, it can be seen that the slopes $\partial \boldsymbol{F}_{\mathrm{Res}}/\partial \dot{X}$ and $\partial \boldsymbol{F}_{\mathrm{Res}}/\partial \dot{Y}$ increase when contact between pad and journal is present. The reason is that the pad cannot rotate freely and therefore not position itself at the desired operation pivot tilting angle. Figure 8 shows the magnitude of the contact force.

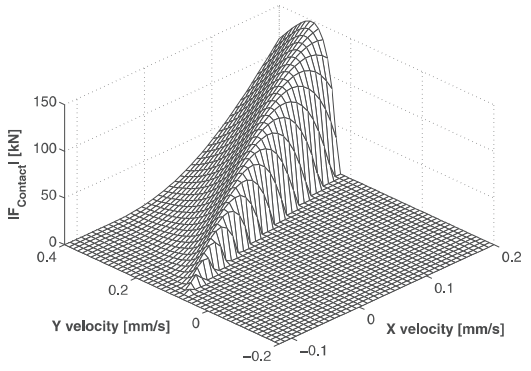

Fig. 8 Magnitude of the contact force at trailing edge. The figure is rotated −90° about the Z-axis compared to Figs 5 and 7

4 CONCLUSION

The results presented demonstrate that there is a possibility of having contact at the trailing edge of the pad and having load-carrying discontinuity effects when the squeeze term dominates Reynolds equation.

Two conditions are required for the load discontinuity phenomena to occur.

1. The squeeze term must dominate the right-hand side of Reynolds equation. This requires slow rotation in combination with large dynamic loads.
2. The pad circumferential extent must be large, so that the squeeze term influence from the shaft centre velocity is different from leading edge to trailing edge of the pad.

ACKNOWLEDGEMENT

The financial support of the Danish Agency for Science, Technology and Innovation is gratefully acknowledged.

REFERENCES

1 **Desbordes, H., Fillon, M., Chan Hew Wai, C.,** and **Frene, J.** Dynamic analysis of tilting-pad journal bearing — influence of pad deformations. *J. Tribol.*, 1994, **116**, 621–627.
2 **Haugaard, A.** and **Santos, I. F.** Stability of multi orifice active tilting-pad journal bearings. *Tribol. Int.*, 2010, **43**, 1742–1750.
3 **Abu-Mahfouz, I.** and **Adams, M. L.** Numerical study of some nonlinear dynamics of a rotor supported on a three-pad tilting pad journal bearing (TPJB). *J. Vib. Acoust.*, 2005, **127**, 262–272.
4 **Gardner, W. W.** An experimental study of thrust pad flutter. *J. Tribol.*, 1998, **120**(3), 577–582.
5 **Seongheon, Y., Chaesil, K.,** and **Wonchang, L.** Prevention of fluttering fatigue damage in a tilting pad journal bearing. *Tribol. Int.*, 2009, **42**(6), 816–822.
6 **Hargreaves, D. J.** and **Fillon, M.** Analysis of a tilting pad journal bearing to avoid pad fluttering. *Tribol. Int.*, 2007, **40**(4), 607–612.
7 **Seeton, C. J.** Viscosity–temperature correlation for liquids. *Tribol. Lett.*, 2006, **22**(1), 67–78.
8 **Kumar, A.** and **Booker, J. F.** A finite element cavitation algorithm. *J. Tribol.*, 1991, **113**(2), 276–286.
9 **McIvor, J. D. C.** and **Fenner, D. N.** Finite element analysis of dynamically loaded flexible journal bearings: a fast Newton-Baphson method. *J. Tribol.*, 1989, **111**(4), 597–604.
10 **Klit, P.** and **Lund, J. W.** Calculation of the dynamic coefficients of a journal bearing using a variational approach. *J. Tribol.*, 1985, **108**, 421–425.

11 **Vølund, A.** and **Klit, P.** Shaft center orbit in dynamically loaded radial bearings. In Proceedings of the 10th Nordic Symposium on *Tribology*, Nordtrib, 13–17 June 2002.

APPENDIX

Notation

a	coefficient for Walther and McCoull function (m^2/s)
A	area (m^2)
b	coefficient for Walther and McCoull function $\log\log(m^2/s)$
c_p	heat capacity of lubricant (J/kg/K)
C	journal centre X- and Y-coordinates (m)
e	eccentricity of mass (m)
$\boldsymbol{F}_C$	force from contact (N)
$\boldsymbol{F}_P$	force from lubricant pressure (N)
$\boldsymbol{F}_{Res}$	resulting force (N)
$\boldsymbol{F}_S$	force from lubricant shear (N)
h	film thickness (m)
L	bearing dimension in axial direction (m)
$\boldsymbol{M}$	moment on tilting pad (Nm)
n	coefficient for Walther and McCoull function $\log\log(m^2/s)/\log(K)$
p	lubricant pressure (Pa)
P	power (J/s)
Q	lubricant flow (m^3/s)
R	journal radius (m)
$\boldsymbol{S}$	distance vector (m)
t	time (s)
T	lubricant temperature (K)
X	Cartesian coordinate (m)
Y	Cartesian coordinate (m)
Z	Cartesian coordinate (m)
α	pad pivot tilting angle (rad)
β	fraction of heat transported trough convection (–)
θ	polar coordinate (rad)
μ	absolute viscosity of lubricant (Pa s)
ν	kinematic viscosity of lubricant (m^2/s)
ρ	density (kg/m^3)
ω	rotational speed (rad/s)

Appendix B

Journal paper: A study on compliant layers and its influence on dynamic response of a hydrodynamic journal bearing

Accepted for publication in Journal of Tribology International [20].

Tribology International 44 (2011) 1872–1877

Contents lists available at ScienceDirect

Tribology International

journal homepage: www.elsevier.com/locate/triboint

A study on compliant layers and its influence on dynamic response of a hydrodynamic journal bearing

Kim Thomsen *, Peder Klit [1]

Department of Mechanical Engineering, Technical University of Denmark, Nils Koppels Alle, Building 404, 2800 Kgs. Lyngby, Denmark

ARTICLE INFO

Article history:
Received 23 March 2011
Received in revised form
25 July 2011
Accepted 28 July 2011
Available online 4 August 2011

Keywords:
Journal bearing
Elastohydrodynamic
Dynamically loaded
Polymer

ABSTRACT

For some hydrodynamic bearing applications polymer-lined bearings are chosen over traditional metal alloy bearings due to their better wear and friction properties when operating at very thin films, e.g. in the mixed lubrication region. The introduction of a compliant layer also affects the dynamic behavior of the bearing. The influence of the liner stiffness on the dynamic response of a highly dynamically loaded journal bearing is evaluated by varying the stiffness and comparing the response. The configurations with different liner stiffnesses are evaluated on the parameters that are traditionally used to evaluate hydrodynamic bearing designs: dynamic response, maximum pressure, minimum film thickness, wear, power loss and temperature response. The primary findings are that the maximum pressures are reduced significantly and this comes at the expense of slightly higher eccentricity ratios during operation.

1. Introduction

Recently many authors have worked with polymer-lined hydrodynamic bearings [1–4] and [5]. Most work is done with respect to wear, operating at static loads and stability criteria for a statically loaded bearing.

In [2] Glavatskih and Fillon compare theoretical findings with experimental results for PTFE-faced thrust pads. The maximum pressure is found to decrease when increasing the PTFE liner thickness. The minimum film thickness also decreases at the leading and trailing edge because the deformation of the compliant PTFE layer gives a concave geometry. Furthermore it is found that the insulating properties of the polymer layer affects the thermal response of the thrust pad significantly giving higher lubricant temperatures.

In [3] Mahieux compares thrust bearings lined with babbitt, PTFE and PFA experimentally. The test results show that the PTFE-lined thrust pad has a higher maximum pressure than the babbitt-lined thrust pad. This finding is in contrast with the common finding from other theoretical and experimental studies. Another interesting finding in this study is that the PTFE- and PFA-lined thrust pads show significantly different hydrodynamic behavior even though their material properties are very similar. There is no explanation for this observation.

McCarthy and Glavatskih [4] study the friction and wear resistance of pure PTFE and PTFE-composites during the start-up phase of a journal bearing. It is found that the composites perform significantly better than both the pure PTFE and babbitt. Babbitt showed almost twice the coefficient of friction compared to the composites.

Simmons et al. [5] analyse the use of large thrust pads with PTFE lining for hydropower plants and describe the learnings from up-rating the thrust bearing in a hydropower plant. The existing babbitt-faced pads were replaced with PTFE-faced pads and it was concluded that the high-pressure lubricant-injection systems were used to enable safe start-up and shut-down can be dispensed with. The PTFE pads can operate under harder conditions allowing the bearings to be designed smaller and thus more energy efficient or with similar size as a babbitted bearing but with higher safety margin.

PTFE and PEEK composites are popular choices for bearing applications. The polymer composition and fillers have major influence on its mechanical and tribological properties and this may be used to engineer the best compromise among the required material properties. For example a major disadvantage of using pure PTFE is creep. PTFE will creep even at low temperatures and it is therefore not suitable for highly loaded applications in its pure form. Therefore PTFE is often reinforced with glass- or carbon-fibers.

The polymer technology has been implemented for diverse bearing applications. Examples from the industry are water hydraulic pumps, thrust bearings for hydropower plants and propulsion shaft

Abbreviation: EHD, elastohydrodynamic; FEM, finite element method; PEEK, polyether ether ketone; PFA, perfluoroalkoxy; PTFE, polytetrafluoroethylene; TEHD, thermoelastohydrodynamic.

* Corresponding author. Tel.: +45 30 37 69 90; fax: +45 99992222.
E-mail addresses: kimth@mek.dtu.dk (K.R. Thomsen), klit@mek.dtu.dk (P. Klit).
[1] Tel.: +45 45256267; fax: +45 45931577.

0301-679X/$ - see front matter © 2011 Elsevier Ltd. All rights reserved.
doi:10.1016/j.triboint.2011.07.011

Nomenclature

α	relaxation factor (–)
c_p	lubricant-specific heat capacity (J/kg/°C)
c_r	radial clearance of bearing (m)
d	liner deformation (m)
E	modulus of elasticity (N/m^2)
θ	angular coordinate (rad)
h	film thickness (m)
h_0	film thickness of undeformed bearing (m)
i	node number (–)
I	functional (J/s)
L	compliance (m/Pa)
μ	lubricant viscosity (Pas)
v	Poisson's ratio (–)
N	interpolation function (–)
p	pressure (Pa)
P	power loss (J/s)
Q	lubricant flow (m^3/s)
ρ	lubricant density (kg/m^3)
R	radius (m)
t	compliant liner thickness (m)
t	time (s)
T	temperature (°C)
it v	sliding speed (m/s)
x	journal center position in x-direction (m)
$\dot{x}$	Journal center velocity in x-direction (m/s)
y	journal center position in y-direction (m)
$\dot{y}$	journal center velocity in y-direction (m/s)
z	linear coordinate (m)
ω	rotational speed (rad/s)

and stern tube bearings used in marine applications. Cases from the industry show that it is possible to up-rate existing machinery when replacing the existing metal alloy faced bearings with polymer liners. The uprating can either be used to decrease the bearing size and thereby reduce loss or to simply use the same bearings to carry a higher load and hereby increase the load density of the machinery. The upscaling is possible because the polymer bearings are less sensible to imperfections in the bearing surface geometry. This is particularly interesting for large radial bearings.

When using polymer-lined bearings it is furthermore possible to design hydrodynamic bearing systems, which would traditionally need jack-up systems, without jack-up. This is because of the polymers' low brake away friction and good wear properties when operating in the mixed lubrication region. The better operational characteristics at thin films make it possible to use alternative lubricants, in some cases even water, or to use thinner oil in order to reduce power loss.

In this work the response from a highly dynamically loaded journal bearing is investigated and a traditional bearing with a stiff metal alloy liner is compared to bearings with compliant polymer liners.

The bearing geometry and loads from the connecting rod big end bearing of the Hornsby 6VEB-X Mk III 4 stroke diesel engine have been selected as a basis for this work due to its very dynamic load cycle and because it has been studied by many authors previously.

The influence of the bearing structure elasticity for this bearing is investigated in [6] and it is found that the elasticity has a significant impact on the journal center orbit and thus cannot be neglected. The focus of this work is to study the effect of implementing a compliant liner in a dynamically loaded journal bearing. Therefore the elasticity of the surrounding structure is not of direct interest for this work and has not been implemented. Description of the Hornsby loads and bearing dimensions can be found in [6].

2. Model used for simulation

2.1. Reynolds equation

A three-node triangular FEM model is used for solving Reynolds equation in its cylindrical form (1) and thus finding the pressure distribution. The coordinate system is presented in Fig. 1:

$$\frac{1}{R}\frac{\partial}{\partial\theta}\left[\frac{h^3}{\mu R}\frac{\partial p}{\partial\theta}\right]+\frac{\partial}{\partial z}\left[\frac{h^3}{\mu}\frac{\partial p}{\partial z}\right]=6\omega\frac{\partial h}{\partial\theta}+12\frac{\partial h}{\partial t} \tag{1}$$

The finite element formulation shown in Eq. (2) is derived using the variational approach [7].

$$\frac{\partial I}{\partial p_i}=\int_A\left(\frac{h^3}{\mu}\left[\frac{1}{R^2}\frac{\partial N_i}{\partial\theta}\sum\frac{\partial N_j}{\partial\theta}p_j+\frac{\partial N_i}{\partial z}\sum\frac{\partial N_j}{\partial z}p_j\right]-[6\omega h_0+12\dot{x}\sin\theta-12\dot{y}\cos\theta]\frac{\partial N_i}{\partial\theta}\right)dA \tag{2}$$

2.2. Thermal response

A constant viscosity is applied and the equivalent temperature rise is used for evaluating the thermal response of the bearing:

$$\Delta T=\frac{P}{Q\rho c_p} \tag{3}$$

The equation describes a stationary state and only includes the mass flow, not the total mass of the lubricant which represents a big heat sink. Therefore the equations can only be used to give a picture of the instantaneous ratio between lubricant flow and viscous power loss.

2.3. Cavitation

Cavitation is handled through an algorithm where consecutive iterations solve for the pressure p using (1). Nodes which fulfill the cavitation requirement, $p<0$, are identified and a fraction of the nodes, counting from the trailing edge of the cavitated region,

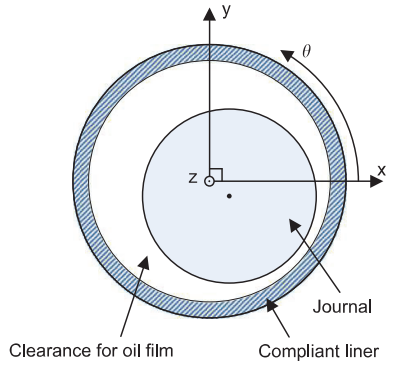

Fig. 1. Journal bearing components and stationary coordinate system.

are selected and the pressure is set to zero at these nodes and next iteration is initiated. Time history is not included in the cavitation algorithm and thus it is assumed that there is always oil to fill the clearance. This algorithm does neither ensure Reynolds boundary condition $dp/d\theta = 0$ at the onset of cavitation nor it ensure mass conservation.

2.4. Compliant liner

The connection rod housing and journal are treated as infinitely stiff and thus only the compliant liner will deform. The film thickness of the undeformed bearing is a function of the radial clearance c_r and the journal position defined by x and y as expressed in Eq. (4):

$$h_0 = c_r - x\cos(\theta) - y\sin(\theta) \tag{4}$$

The film thickness h_0 is modified with the deformation of the liner $[L]\{p\}$:

$$\{h\} = \{h_0\} + [L]\{p\} \tag{5}$$

The compliance matrix $[L]$ of the polymer layer is modeled with the Winkler/Column model [8], which is also used by other authors for modeling compliant layers [2]:

$$L_{i,i} = \frac{(1+\nu)(1-2\nu)}{1-\nu}\frac{t_i}{E} \tag{6}$$

The model assumes that the liner thickness, t, is much smaller than the other dimensions. There is no cross-coupling of deformation and pressure and thus $[L]$ only contains non-zero coefficients in the diagonal. If the material thickness t and material properties are homogeneous across the surface the diagonal coefficients are all identical.

For this work a PEEK composite is used, having a modulus of elasticity of $E = 6$ GPa and a Poisson's ratio of $\nu = 0.4$. The material properties of polymers can be highly dependent on temperature. For this particular application the high-pressure zone moves around along the bearing circumference due to the highly dynamic load and preventing local hot spots in the polymer.

2.5. Coupling of elasticity and oil film forces

A direct method was used to implement the compliance of the liner using strong under-relaxation. The strong under-relaxation is required because there is a very non-linear coupling between the oil film forces and the liner compliance. Convergence can be difficult to achieve because only the liner deformation is considered and furthermore the column model is used. This approach gives no direct coupling of deformation between neighboring nodes and high-pressure gradients are prone to cause convergence problems. A fine mesh in high-pressure regions reduces instabilities in the iteration procedure. The deformation of neighboring nodes is only coupled indirectly through Reynolds equation.

Eqs. (7) and (8) show the iterative method of under relaxation. α is the under relaxation factor and d_k is the deformation at the kth iteration:

$$d_k = \alpha L p_k + (1-\alpha) d_{k-1} \tag{7}$$

$$h_k = h_0 + d_k \tag{8}$$

Typical α-values for the results presented in this work are 10^{-1}–10^{-3} depending on the eccentricity ratio. Using these under relaxation factors convergence is achieved within 280–14,000 iterations. When selecting the relaxation factor it is important that the deformation may never be overestimated since this will lead to diverging results due to the very non-linear behavior of Reynold's equation.

2.6. Integration in time domain

A first-order perturbation is used to derive the damping coefficients for the bearing as described in [9]. The coefficients are then used for calculating the shaft orbit employing an implicit time integration procedure with variable step size and error control. The variable step size and error control are implemented through an embedded Runge–Kutta pair. The use of the damping coefficients is an alternative method to the traditional Mobility Method, developed by Booker in 1965 [10].

3. Results

Three different bearing configurations of the Hornsby connecting rod bearing are used for the analysis in this work: a traditional setup with a metal alloy bearing liner, which is considered as stiff, and two setups with 1 and 2 mm thick polymer liners. The dynamic responses for these bearings are then calculated and compared.

For each bearing the load cycle is repeated several times until two successive load cycles give identical shaft orbits. The orbits are shown in Fig. 2.

The responses of the three bearings are evaluated based on the design parameters that are traditionally used to evaluate a given design of a hydrodynamic bearing: dynamic response, maximum pressure, minimum film thickness, wear, power loss and temperature response.

3.1. Dynamic response

Evaluated from the dynamic response of the shaft, the stiff liner performs slightly better than the compliant ones because the eccentricity ratio (Fig. 3) is smaller at almost the complete cycle. Only at $t = 0.085$ and 0.13 s (the points are marked on the figure) the stiff liner has a higher eccentricity ratio, but the ratio is in the range of $e = 0.75$ and therefore not critical with respect to potential bearing damage because the lubricant film thickness is high. From this follows that the shaft center velocity is generally higher for the configurations with a compliant layer. This is because the total traveled distance during a complete shaft orbit is higher.

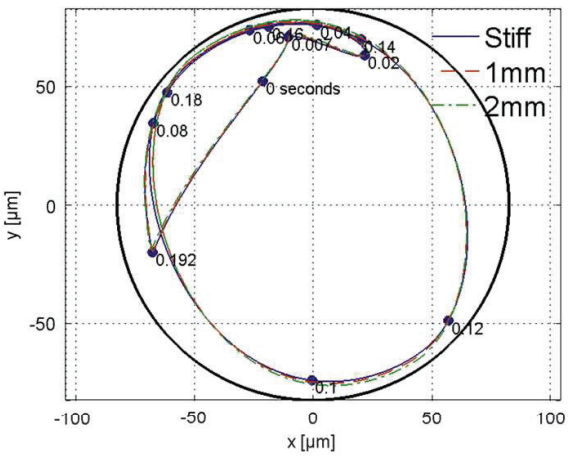

Fig. 2. Journal orbit for a complete combustion cycle giving two journal rotations. The black circle represents a journal eccentricity of 1.

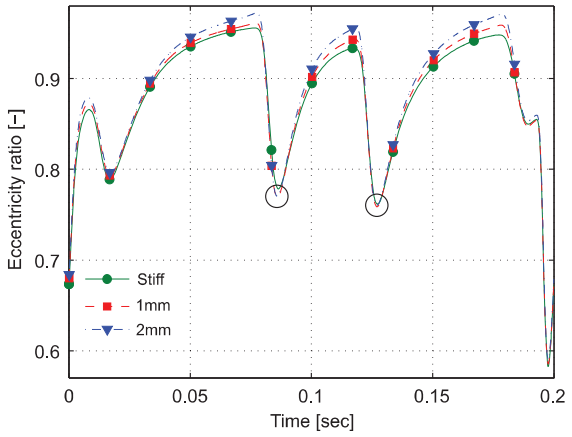

Fig. 3. Eccentricity ratio during the complete combustion cycle.

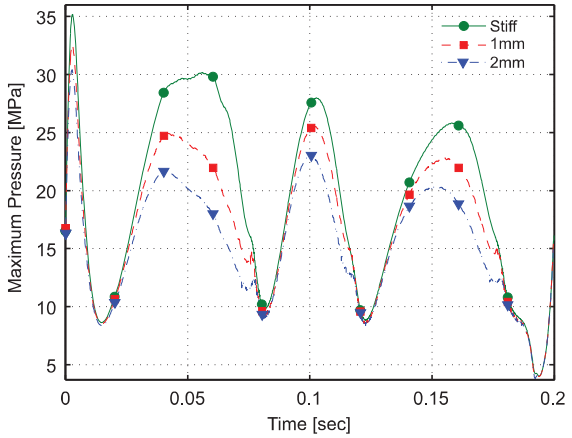

Fig. 4. Maximum pressure during the complete combustion cycle.

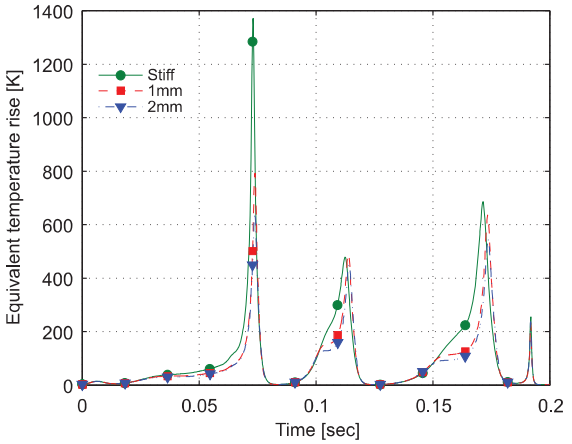

Fig. 5. Equivalent temperature rise during the complete combustion cycle.

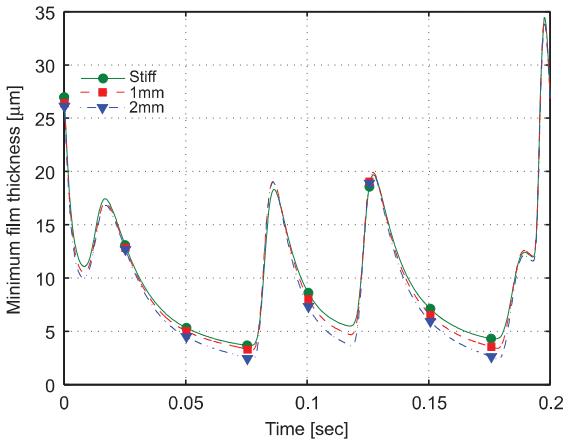

Fig. 6. Global minimum film thickness during the complete combustion cycle.

3.2. *Pressure*

From Fig. 4 it is seen that the maximum pressure in the bearing drastically decreases with the compliance of the bearing liner and hence a thick polymer is desirable. The positive effect of the compliant layer will increase if the bearing is edge-loaded, for example due to shaft misalignment or bending. Some ripples can bee seen on the pressure curves. These originate from using a fixed and relatively coarse mesh. Every time the cavitated zone expands or shrinks the maximum pressure jumps a little because the non-cavitated area is not a continuous function of time. The axial and circumferential pressure profiles at $t=0.073$ s are shown in Figs. 9 and 10. The two vertical lines in the figures show the circumferential and axial locations of the section views respectively.

3.3. *Minimum film thickness and wear*

Generally the minimum film thickness at the bearing edges is always lower for the bearing configurations with a compliant bearing liner. This is shown in Fig. 6 and can be explained by the overall lower stiffness and damping coefficients for bearings with compliant liners. The lower dynamic coefficients cause the bearings to operate at higher eccentricity ratios. At the edge of the bearing there is no pressure buildup and hence no deformation of the polymer. The combination of these circumstances entails that the polymer bearings will almost always have a lower film thicknesses.

This general characteristic for polymer bearings is only valid for journal bearings which are rigidly supported under the entire bearing surface. A tilting pad bearing which is only supported in the middle of the pad will not necessarily have the minimum film thickness at the edge due to deformation and thermal crowning. In fact the deformation of the polymer counteracts the deformation and crowning of the entire pad and can give a better overall geometry for pressure build-up.

When looking at the film thickness at the bearing centerline (Fig. 7) it is seen that compliant liners generally increase the minimum film thicknesses except at every local minimum of the curve where the bearings with compliant liners have smaller film thicknesses for a short duration of time. This is because the influence of the squeeze term in Reynold's equation is higher than the wedge term (the Couette term) and when the journal has reached its maximum eccentricity ratio and starts to move back toward the bearing center, the area of the bearing with minimum film thickness will cavitate.

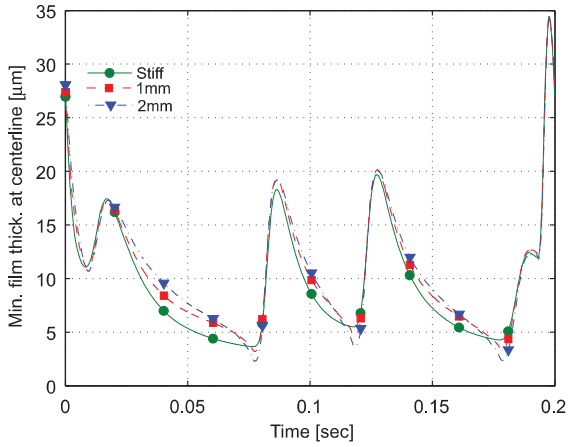

Fig. 7. Minimum film thickness at center line during the complete combustion cycle.

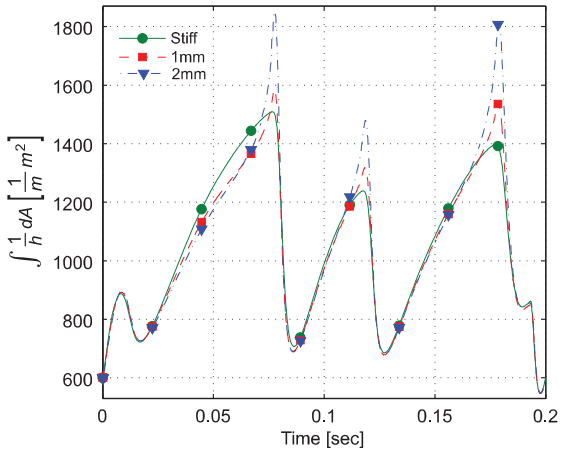

Fig. 8. Wear measure $\int(1/h)\,dA$ during the complete combustion cycle.

Table 1
Wear measure: $\iint(1/h)\,dA\,dt$.

Lining characteristics	Wear measure (ms)
Stiff	210
1 mm	207
2 mm	211

In [11] it is reported that the wear rate can be modeled with good approximation as a function of film thickness only. This method is applied to evaluate the wear at every time step of the bearings by plotting $1/h$ integrated over the bearing surface as shown in Fig. 8. The curves are then integrated over the complete cycle of 0.2 s and the results are shown in Table 1.

Table 1 shows almost identical values for the wear measure indicating that the overall film thickness throughout the complete cycle is the same for the three configurations. The wear during operation at full hydrodynamic lubrication is expected to be insignificant compared to the wear occurring at start-up and shutdown and thus the transient start-up and shutdown phases are also important for this comparison.

The above comparison is based on film thickness only and can naturally only be used as a guideline. Generally the wear properties of polymer bearings are much better than metal alloy bearings. This is shown experimentally by McCarthy and Glavatskih [4]. They compare the wear of a white metal alloy bearing with the wear of a similar PTFE-lined bearing and show that there can be a difference of up to 800% in wear rate in favor of the PTFE-lined bearing. When this factor is included in the comparison it is evident that the wear properties of the dynamically loaded compliant polymer bearings are much better than that of the stiff metal alloy bearings.

3.4. Power loss

The power loss is integrated over the complete cycle for the three configurations giving the total energy loss. The results are shown in Table 2 and it is clear that there are only marginal differences.

3.5. Temperature response

The equivalent temperature rise is calculated according to Eq. (3) and the result is shown in Fig. 5. The mean values are shown in Table 3.

It is clear that a more compliant bearing liner gives a smaller equivalent temperature rise for the bearing. The difference in temperature rise cannot be explained by overall difference in flow rate, since the flow rate integrated over time is almost identical.

The big difference in equivalent temperature rise is caused by the very low flow rate at the three temperature peaks in Fig. 5. At these locations the flow for the compliant bearings is up to 220% higher. The higher flow rate is a little counterintuitive because, at these peaks, the minimum film thickness at the edges of the compliant bearings is smaller when compared to the stiff bearing. The smaller film thickness is more than counterbalanced by a higher pressure gradient at the edges and a bigger pressure area in circumferential direction. A more compliant liner will give a flatter pressure profile at the bearing center and a higher gradient at the edges. An example of this is shown in Figs. 9 and 10 where the axial and circumferential pressure profiles at $t=0.073$ s are shown.

The method of the equivalent temperature rise is based on the instantaneous power loss and volume flow and does not consider the heat sink composed by the lubricant volume. The heat sink will dampen the peaks on Fig. 5 but the figure is still believed to

Table 2
Energy loss: $\int P\,dt$.

Lining characteristics	Energy loss (J)
Stiff	127
1 mm	126
2 mm	128

Table 3
Mean equivalent temperature rise.

Lining characteristics	Eq. temperature rise (° C)
Stiff	103
1 mm	80.0
2 mm	72.9

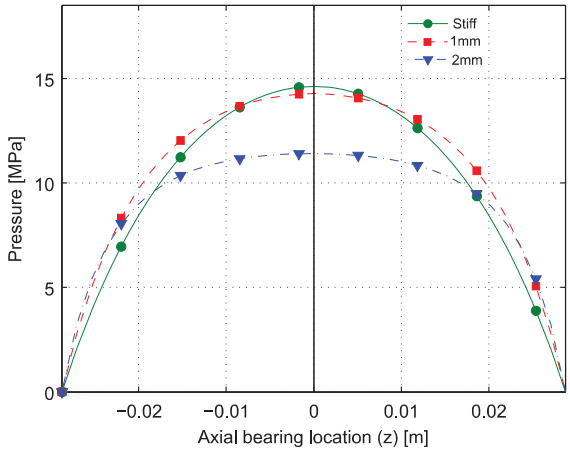

Fig. 9. Axial pressure profile at $t=0.073$ s.

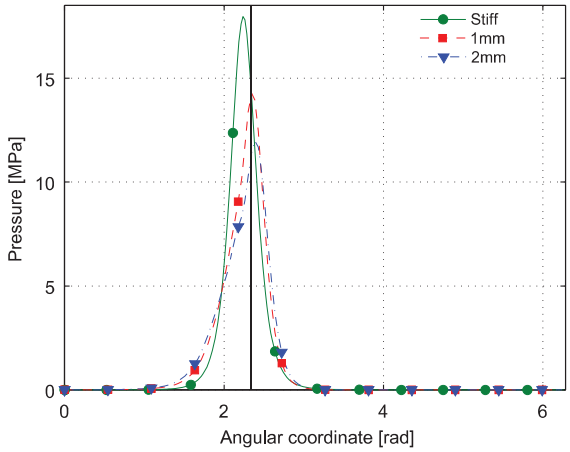

Fig. 10. Circumferential pressure profile through center of bearing at $t=0.073$ s.

show if there is an adequate ratio between power loss and flow rate. Furthermore the method is based on an adiabatic model concerning heat exchange with the bearing and sleeve and therefore conservative in the case of a metal alloy bearing liner, since this surface will conduct some of the friction power away from the oil and therefore a smaller flow is required to keep the oil at the same temperature compared to the compliant bearing configurations.

From Fig. 5 it is seen that there is a significant power dissipation compared to the lubricant flow, so it is important to study the local thermal response in order to achieve results which resemble actual conditions.

Based on the thermal properties most general purpose bearings will benefit from a thin or no polymer layer due to high conductivity resulting in better cooling of the oil. Some applications will benefit from a thick polymer liner. Examples of this are machinery where the bearing housing is warmer than the oil and thus a low conductivity is preferable. Another application is a tilting pad bearing where thermal crowning can be reduced significantly by insulating the pad from the oil and thus reducing the pad temperature difference.

4. Concluding comments

It is shown that highly dynamic loaded hydrodynamic journal bearings can benefit from a compliant liner because peak pressures are reduced significantly. This comes at the expense of a slightly higher eccentricity ratio and consequently a smaller film thickness at the edges of the bearing. The equivalent temperature rise indicates that the bearing with a compliant liner will perform better. A more detailed model, which includes conductivity and transient thermo-viscous effects, must be established before making any definite conclusions on this. If the right material is chosen for the compliant liner, it can have much better wear properties and also better friction properties. This means less friction and wear when operating in the mixed lubrication regime.

Apart from the dynamic response one must also consider the operational boundaries for the materials when comparing traditional metal alloys with polymer bearings. In [1,4] and [5] several important material parameters are discussed: wear rate, corrosion resistance, temperature range, brake away friction, friction coefficient at mixed and boundary lubrication, *pv* value range, creep and pressure ranges.

Acknowledgments

The financial support of the Danish Agency for Science, Technology and Innovation is gratefully acknowledged.

References

[1] Glavatskih S, Fillon M. Unique performance aspects of PTFE lined thrust bearings. Hydro Review Worldwide 2005;13(6):32–7.
[2] Glavatskih S, Fillon M. TEHD analysis of thrust bearings with PTFE-faced pads. Journal of Tribology 2006;128(1):49–58.
[3] Mahieux C. Experimental characterization of the influence of coating materials on the hydrodynamic behavior of thrust bearings: a comparison of babbitt, ptfe, and pfa. Journal of Tribology 2005;127(3):568–74.
[4] McCarthy D, Glavatskih S. Assessment of polymer composites for hydrodynamic journal-bearing applications. Lubrication Science 2008;21(8):331–41.
[5] Simmons J, Knox R, Moss W. The development of ptfe-faced hydrodynamic thrust bearing for hydrogenerator application in the united kingdom. Journal of Engineering Tribology 1998;212(Part J):345–52.
[6] McIvor J, Fenner D. Finite element analysis of dynamically loaded flexible journal bearings. Journal of Tribology 1989;111(4):597–604.
[7] Huebner K, Dewhirst D, Smith D, Byron T. The Finite Element Method for Engineers. John Wiley & Sons; 2001. ISBN-13 978-0-471-37078-9.
[8] Rades M. Dynamic analysis of an inertial foundation model. International Journal of Solids and Structures 1972;8(12):1353–72.
[9] Klit P, Lund J. Calculation of the dynamic coefficients of a journal bearing using a variational approach. Journal of Tribology 1985;108(3):421–4.
[10] Booker J. Dynamically loaded journal bearings: mobility method of solution. Journal of Basic Engineering 1965;187(3):537–46.
[11] Thomsen K, Klit P. Application of a new wear model in hydrodynamic metal-polymer bearings, in: 9th EDF/Pprime (LMS) Poitiers Workshop: Futuroscope, October 2010.

Appendix C

Journal paper: Geometrical design parameters for journal bearings with flexure pads and compliant liners

Accepted for publication in Journal of Engineering Tribology [14].

Original Article

Institution of MECHANICAL ENGINEERS

Journal of ENGINEERING TRIBOLOGY

Proc IMechE Part J:
J Engineering Tribology
226(4) 274–283

DOI: 10.1177/1350650111431525
pij.sagepub.com

SAGE

Geometrical design parameters for journal bearings with flexure pads and compliant liners

Kim Thomsen and Peder Klit

Abstract

A hydrodynamic journal bearing utilizing flexure pads with a compliant liner is studied and its performance enhanced through a parametric study. The main geometrical dimensions are varied and the affect on pad performance is analyzed. This will put more knowledge into the design and function of flexure pads. Guidelines are given to the design of the pads and are also covering the polymer liner. It is found that the use of flexure pads is an attractive alternative to pivoted pads. Pivot contact-related failure modes are eliminated and load capacity is not restricted by the force that can be transferred through the pivot contact. When combined with a polymer liner, the pad performance is enhanced further, especially when operating at thin lubricant films.

Keywords

Flexure pad, elastohydrodynamic, misaligned, polymer

Date received: 9 June 2011; accepted: 3 November 2011

Introduction

Since Michell's discovery of the tilting pad bearing it has been widely adopted for both thrust and radial bearing applications. The pivoted pad bearing allows the angular position of the pad to adjust according to the operating condition. Ideally, the pivot insures that the pad operates with constant ratio between oil film thickness at leading and trailing edges of the pad.[1] Thereby, the pivoted pad operates better over a much broader range of operation conditions compared to a fixed geometry pad like the tapered thrust pad with a flat land.

Other positive effects of the pivoted pads are their stabilizing effects due to low cross-coupling coefficients for radial bearings. For applications where high shaft or runner misalignments are unavoidable, tilting pads can also be the preferred choice over fixed geometry pads due to low sensitivity to this issue.

One drawback of the pivoted pad is however, that the contact point in the pivot joint is highly loaded and adds contact-related failure modes to the bearing. Examples of failure modes are fretting, fatigue damage, and plastic deformation. Ettles[2] and Kepple et al.[3] describe examples of fatigue and fretting. Unless advanced designs are used, the contact point restricts the pivoted pad to smaller sizes because of the limited force that can be transferred through this contact mechanism. The pivot mechanism also introduces additional flexibility in the bearing system decreasing the overall bearing stiffness and damping and thereby increasing journal vibration.[4] Nicholas[5] studies pivot designs for heavily loaded radial tilting pad bearings and gives good design guidelines on various pivot mechanisms and also considerations for the moment required to overcome the frictional resistance in the pivot. Examples of pivot mechanisms loaded to failure are also shown.

An alternative to the pivoted pad bearing is the flexure pad bearing. It utilizes a solid attachment between the pad body and the bearing housing. The angular adjustment of the pad body then relies on the deformation of the supporting structure of the pad, from hereon called the 'column'. Since there is no relative motion

Department of Mechanical Engineering, Technical University of Denmark, Denmark

Corresponding author:
Kim Thomsen, Department of Mechanical Engineering, Technical University of Denmark, Nils Koppels Alle, Building 404, 2800 Kgs. Lyngby, Denmark.
Email: kimth@mek.dtu.dk

between parts, there is no wear on the components. Furthermore, the solid connection between pad body and bearing housing gives a robust load transfer compared to the pivoted pad. The flexure pads combine the simplicity and sturdiness of the fixed geometry pad with the adaptable nature of the pivoted pad. For some applications, the flexure pad can combine the best from fixed geometry and tilting pad bearings.

Kepple et al.[3] describe the improvement when going from a traditional journal bearing to a tilting pad bearing and further improvements when applying a flexure pad bearing. Walton and Andrés[6] study a four-pad flexure bearing subjected to various operating conditions experimentally and compare measurements with theoretical results. They find that the particular bearing geometry predictably and reliably operates for all subjected conditions. Andrés and Santiago[7] experimentally study the dynamic response of a flexure pad bearing. They find that the cross-coupling stiffness and damping coefficients are small and that the bearing's response to imbalance loads is good with stable performance in the entire range of operating conditions.

Using a flexure design can eliminate the pivot point contact failure modes from a pad design. The pad performance at thin films can also be improved. This is done by changing the liner material from babbitt to a polymer composite. Local pressures up to 35 MPa are common for bearings in large combustion engines using babbitted liners and typical industry design guidelines state around 4 MPa as maximum specific pressure for babbitted bearings. Ettles[2] reports specific loads up to 5.5 MPa and down to 3.3 MPa for large thrust bearings. Nicholas[5] reports a load of 3.5 MPa for heavy loaded radial tilting pad bearings.

When using polymer lined pads, the specific pressure can be increased and thereby increase the potential load density of the bearing. Specific loads of up to 11 MPa are reported as safe operational loads for large thrust bearings in hydro power plants.[8] Simmons et al.[9] describe the learning from up-rating a thrust bearing in a hydropower plant by replacing the existing babbitt-faced pads with polytetra-fluoro-ethylene (PTFE)-faced pads. They concluded that the high-pressure lubricant-injection systems, used to enable safe start-up and shut-down, can be dispensed with. Ettles et al.[10] directly compare the performance of PTFE-faced pads with babbitted ones. Their most significant findings are as follows.

1. No difference in dissipated power and no significant difference in measured lubricant temperature.
2. Reduced thermal crowning for PTFE-faced pads.
3. Oil jack-up systems for separating the bearing surfaces at start-up can be dispensed with in some cases if PTFE-faced pads are used. However, it is system dependent.
4. The PTFE-faced pads are less sensitive to manufacturing tolerances because the compliant polymer will adjust by elastic deformation and creep.

McCarthy and Glavatskih[11] study the friction and wear resistance of pure PTFE and PTFE composites during the start-up phase of a journal bearing. They found that the composites perform significantly better than both the pure PTFE and babbitt. Babbitt showed almost twice the coefficient of friction compared to the composites. Glavatskih and Fillon[12] compare theoretical findings with experimental results for PTFE-faced thrust pads. The maximum pressure is found to decrease when the PTFE liner thickness is increased. The minimum film thickness also decreases at the leading and trailing edges because the deformation of the compliant PTFE layer gives a concave geometry. Furthermore, they found that the insulating properties of the polymer layer affect the thermal response of the thrust pad significantly giving higher lubricant temperatures.

Flexure pad study

In this study, polymer-lined radial flexure pads operating at steady-state conditions are studied and the influence from varying geometrical parameters is investigated. Finally, the performance of the pad is tested at increasing misalignment. The study demonstrates the flexure pad performance as a function of its geometrical parameters and thus acts as a guide to future studies on flexure pads. Figure 1 shows the pad and the symbols representing dimensions. The column location, *Cl*, is given from center of column in percentage from the leading edge. Figure 2 shows the pad in its deformed state.

The pad is loaded by a radial force of 50 kN and the specific load is set to 5 MPa giving a pad area of 0.01 m^2. A low sliding speed of 1 m/s is used together with a high-viscosity ISO VG 320 oil running at a constant temperature of 50°C. These operational conditions are held constant throughout the analysis and

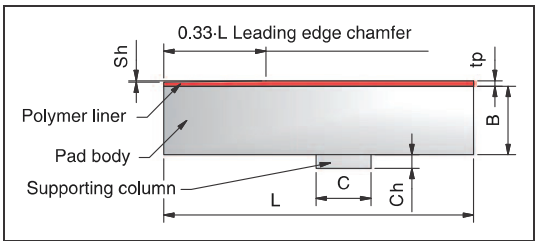

Figure 1. Flexure pad geometry.

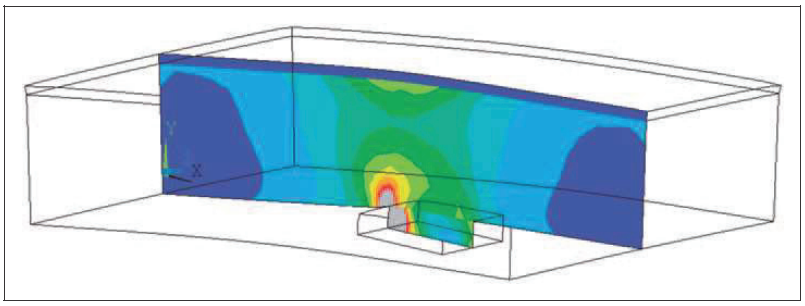

Figure 2. The flexure pad in its deformed state showing Von Mises stress contours in the mid section.

Table 1. Initial geometry of pad.

Geometrical parameter	Initial value
Pad length, *L*	100 mm
Pad width, *W*	100 mm
Pad body thickness, *B*	20 mm
Column cross-section, *CxC*	$30 \times 30\ \text{mm}^2$
Column height, *Ch*	5 mm
Column position from leading edge, *Cl*	60 %
Shoulder height, *Sh*	10 μm

Table 2. Material data.

	Body and column	Liner
Material	Steel	Polymer liner
E	200 GPa	6 GPa
ν	0.3	0.4

only the geometrical parameters are varied. This approach is followed in order to keep the number of variables on a moderate level, but it does, however, also limit the generality of the work. Liner thicknesses of 0, 1, 2, 4 and 8 mm are used for each parameter investigation; the thickness of 0 mm represents a traditional pad lined with a stiff material like babbitt. Table 1 shows the initial dimensions of the pad.

A chamfer at the leading edge is introduced in order to insure a converging wedge that will give a hydrodynamic pressure build-up. Chamfer dimensions are *Sh* times $0.33L$. The chamfer may not extend over 50% of the pad, or at least not past the column location, in order to maintain a converging wedge at the leading edge when the pad rests on the flat land of the pad at standstill. Table 2 shows the material data.

The radial flexure pad is unwrapped when the parametric model is created. This corresponds to a radial pad supporting a journal with a large radius compared to the pad circumferential extent and consequently the curvature can be neglected. This is done in order to reduce the problem and not get into topics concerning load direction and multi-pad related issues like load-on-pad or load-between-pad.

Model used for simulation

Reynolds equation

A three-node triangular FEM model is used for solving Reynolds equation (1) and thus finding the pressure distribution. Isothermal conditions are assumed and it is believed that the results are still valid because the pad size is moderate and the sliding speed low. Therefore, the resulting thermal variation across the pad is deemed to be accordingly small. However, it is acknowledged that the thermal response of hydrodynamic bearings is often of high importance

$$\frac{1}{R}\frac{\partial}{\partial\theta}\left[\frac{h^3}{\mu R}\frac{\partial p}{\partial\theta}\right]+\frac{\partial}{\partial z}\left[\frac{h^3}{\mu}\frac{\partial p}{\partial z}\right]=6\omega\frac{\partial h}{\partial\theta}+12\frac{\partial h}{\partial t} \tag{1}$$

The element equations corresponding to (1) are derived using the variational approach[13] and shown in equations (2) to (4). Three-node triangular elements are used giving linear interpolation functions. The coefficients b and c are constants of the element and are deduced from its geometry

$$\underset{3x3}{[\mathbf{H}_{jk}]}\ \underset{3x1}{\{p_j\}}=\underset{3x1}{\{V_j\}} \tag{2}$$

$$[\mathbf{H}_{jk}]=\int_\Omega\left[\frac{h^3}{4\mu A^2}\left(b_jb_k+c_jc_k\right)\right]\mathrm{d}\Omega \tag{3}$$

$$\{V_j\}=\int_\Omega\left\{\frac{3Rb_j}{A}(\omega h-2\dot{x}\sin(\theta)+2\dot{y}\cos(\theta))\right\}\mathrm{d}\Omega \tag{4}$$

Equation (2) is setup for all elements and assembled into a set of equations combining all nodes which can

then be used to solve for the pressure p. The pressure is set to 0 for all boundary nodes. For a thorough derivation of the element equations, see Booker's and Huebner's work.[13,14]

Cavitation is handled through an algorithm where consecutive iterations solve for the pressure. Nodes which fulfill the cavitation requirement, $p < 0$, are identified and a fraction of the nodes, counting from the trailing edge of the cavitated region, is selected and the pressure is set to zero at these nodes and next iteration is initiated. The procedure is repeated until no nodes fulfill the cavitation requirement. Mass conservation is fulfilled because no pressure buildup exists after the potential cavitated region.

Elasticity

An industrial state-of-the-art structural finite element program, in this case Ansys, is used to generate a parametric model of the flexure pad. A link is created so that Ansys can be called from the developed simulation tool in order to export the stiffness matrix. Since the fluid film forces are only acting on the pad surface it is advantageous to condense the stiffness matrix into a super element before exporting it. The method of exporting and reading the stiffness matrix $\mathbf{K}$ is verified by modeling geometries than can be compared to analytical results using elementary beam theory. The force stiffness matrix $\mathbf{K}$ is converted to pressure compliance matrix $\mathbf{L}$ using the integration matrix $\mathbf{A}$ as shown in equation (5)

$$\begin{aligned}[\mathbf{K}]\{d\} = \{F\} \Leftrightarrow \{d\} &= [\mathbf{K}]^{-1}\{F\} \\ &= [\mathbf{K}]^{-1}[\mathbf{A}]\{p\} = [\mathbf{L}]\{p\}\end{aligned} \tag{5}$$

The Ansys model utilizes from 260,000 to 1,800,000 elements of which 1400–5700 are on the bearing surface. The mesh from the bearing surface nodes are then used to calculate the oil film forces using equations (2) to (4). All nodes at the bottom surface of the column in Figure 2 are locked in all its degrees of freedom giving a rigidly supported column.

Coupling of oil film forces and elasticity

Reynolds equation is coupled with pad elasticity using the Newton–Raphson method. Using a Taylor expansion around the solution $f(p)$ with respect to p and neglecting derivatives of orders higher than one gives equation (6)

$$\Delta p \frac{\partial f(p)}{\partial p} = f(p + \Delta p) - f(p) \tag{6}$$

The functionals $f(p)$ and $f(p+\Delta p)$ are the usual Reynolds equation (1) where the latter is perturbed with respect to the pressure. The two functionals are expanded and simplified to equation (7). The derivation of (7) and also the element equations will not be shown here, as this will be too lengthy; h_0 is the oil film thickness for the flexure pad in its undeformed state

$$\begin{aligned}\Delta p \frac{\partial f(p)}{\partial p} = &\frac{1}{R}\frac{\partial}{\partial \theta}\left(\frac{3h^2 L\Delta p}{\mu R}\frac{\partial p}{\partial \theta}\right) + \frac{\partial}{\partial z}\left(\frac{3h^2 L\Delta p}{\mu}\frac{\partial p}{\partial z}\right) \\ &+ \frac{1}{R}\frac{\partial}{\partial \theta}\left(\frac{h^3}{\mu R}\frac{\partial \Delta p}{\partial \theta}\right) + \frac{\partial}{\partial z}\left(\frac{h^3}{\mu}\frac{\partial \Delta p}{\partial z}\right) \\ &- 6\omega\frac{\partial L\Delta p}{\partial \theta} - 12\frac{\partial L\Delta p}{\partial t},\ h = h_0 + Lp\end{aligned} \tag{7}$$

Equation (7) is expressed in finite element formulation and used to solve for Δp using equation (8). S is the residual of the assembled version of equation (2) after the right hand side is moved to the left hand side

$$\left[\frac{\partial f(p)}{\partial p}\right]\{\Delta p\} = \{S\} = [\mathbf{H}]\{p\} - \{V\} \tag{8}$$

The final solution for the state of deformation d and the corresponding pressure p is found by solving equation (8) multiple times through an iterative procedure until the convergence criterion stated in (9) is fulfilled

$$\frac{|\Delta p|}{|p|} < 10^{-4} \tag{9}$$

For a thorough derivation of the Newton–Raphson method applied for EHD-problems see McIvor's work[15] on this topic.

Results

Variation of body thickness

Figures 3 and 4 show the variation of pad performance as a function of the pad body thickness. The performance is measured on the four parameters:

(a) maximum oil film pressure;
(b) minimum oil film thickness;
(c) viscous power loss;
(d) lubricant flow.

From Figure 3, it is clear that in general, the pad body must be as stiff as possible in order to give low peak pressure and high minimum lubricant film thickness. However, it is interesting that for every thickness of the compliant layer, there is an optimum pad body thickness that produces the largest minimum film thickness. In Figure 3, it is clearly visible for the 8 mm configuration, that the minimum film thickness drops

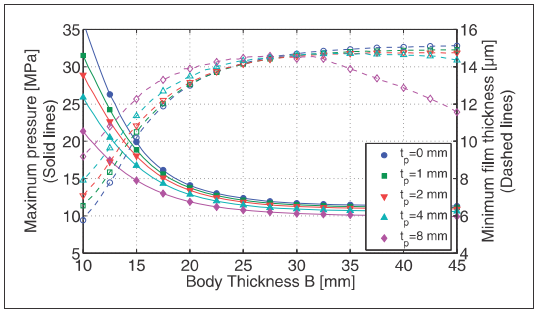

Figure 3. Pressure and film thickness with variation of body thickness for various liner thicknesses t_p.

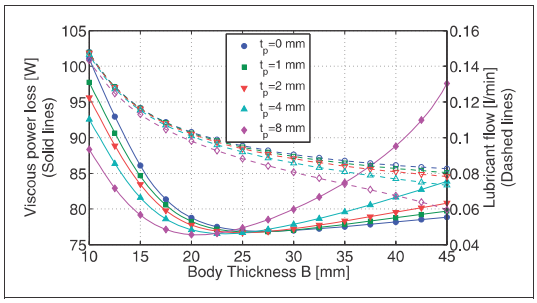

Figure 4. Power loss and lubricant flow with variation of body thickness for various liner thicknesses t_p.

rapidly at body thicknesses above 32 mm. The optimum pad body thickness can also be identified for the 4 mm polymer liner configuration. For the 1 and 2 mm configuration, the optimum pad body thickness is outside the studied interval of 10–45 mm.

The optimum pad body thickness exists because the deformation of the pad body gives a convex contribution, i.e. it increases the radius of curvature, giving lower film thickness at the center of the pad. In contrast, the deformation of the compliant liner gives a concave contribution, i.e. it reduces the radius of curvature, giving lower film thickness at the edges of the pad.

Two extreme configurations using 10 and 45 mm body thicknesses are shown in Figures 5 and 6. From these, it is clear that neither of the configurations are desirable. The pad with 10 mm body thickness excessively deforms and the pressure buildup zone is limited to the center of the pad giving very high pressure levels of up to 21.4 MPa. The 45 mm pad virtually sees no body deformation and only the liner deforms. This gives the lowest film thicknesses at the edges of the pad, where the pressures are correspondingly low.

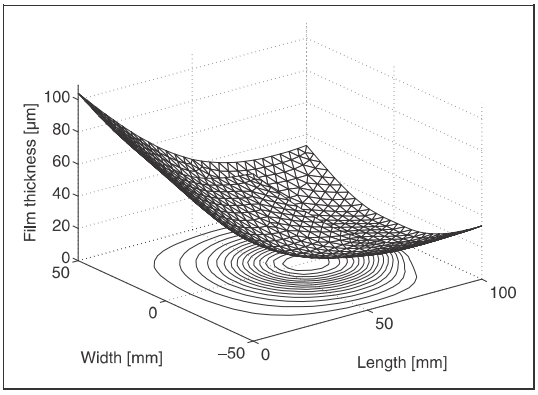

Figure 5. Pressure and film thickness profiles for pad with 8 mm liner (t_p) and 10 mm body thickness (B) corresponding to Figures 3 and 4. Maximum pressure, 21.4 MPa; minimum film thickness; 9.2 μm.

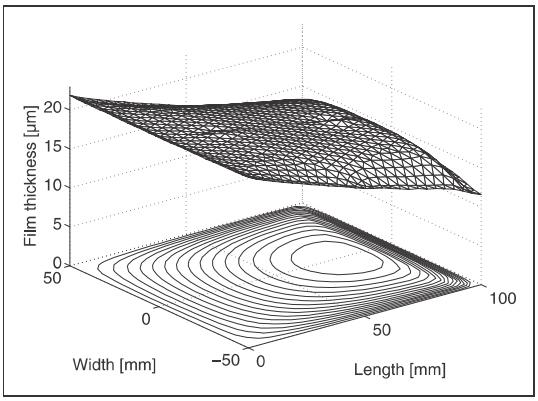

Figure 6. Pressure and film thickness profiles for pad with 8 mm liner (t_p) and 45 mm body thickness (B) corresponding to Figures 3 and 4. Maximum pressure, 10.0 MPa; minimum film thickness, 11.6 μm.

The compliant liner insures a wide pressure buildup zone with a peak pressure of 10.0 MPa.

The deformations of the pad body and the compliant liner counterbalance each other and for any given load an optimum exists. This is not the case for full journal bearings where the bearing deformation is ignored or at least does not give a convex contribution to the overall geometry.

From Figure 4, it can be seen that for all five configurations there is an optimum body thickness with respect to viscous power loss. The optimum body thickness is in the range 20–30 mm depending on the thickness of the compliant layer. A body thickness of 25 mm

is used for the following parameter analysis in this study.

Variation of shoulder height

Figure 7 shows the variation of pad performance as a function of the leading edge chamfer dimension represented by the parameter shoulder height. From Figure 7, it is clear that pad performance is almost constant even though the shoulder height is varied from 0 to 20 μm. The small variation in pressure and minimum film thickness indicates that the column is able to deform and adapt according to the external load. From this, it can be concluded that the flexure support works as intended and that the primary function of the shoulder height is to insure a converging wedge geometry at startup. The wedge insures that the pad will build up a hydrodynamic pressure when starting up from standstill. When the bearing is up and running, the interaction between pressure and elasticity insures a good film geometry.

Variation of column location

Figures 8 and 9 show the variation of pad performance as a function of the column location measured from the leading edge. The highest minimum lubricant film thickness is observed for column locations of 54–58% from the leading edge depending on liner thickness. For all liner thicknesses the lowest peak pressure is observed at a column location of 58%. Heinrichson[16] reports 57% as optimum location with respect to minimum peak pressure using a TEHD model for simulation.

In Figure 9, it can be seen that the power loss is lowest at a column location of 80% independent of liner thickness. It is also noted that the lubricant flow dramatically increases when moving the column location away from the leading edge. From evaluation of these two parameters, it is evident that a column location as far back as possible will give the lowest lubricant temperature. However, this will come at the expense of lower film thickness and higher peak pressures. Glavatskih[17] discusses various studies using TEHD models and notes that 65% is reported as optimum column location with respect to minimum peak pressure and temperature.

The low sliding speed of the application studied in this study will only lead to limited viscous dissipation and consequently the pad can be optimized with respect to film thickness and pressure. A column location of 58% is chosen for the remaining parameter studies.

Variation of column stiffness

Figures 10 and 11 show the variation of pad performance as a function of the column stiffness. The column stiffness is represented by the column cross-section dimensions. The cross-section is kept square and thus width and length are equal but only the width is displayed at the abscissa of Figures 10 and 11. From Figure 10, it can be seen that there is an optimum column width with respect to film thickness of

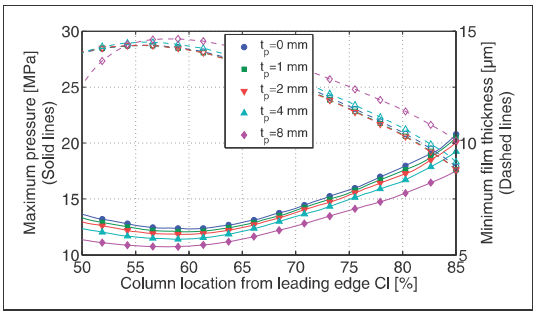

Figure 8. Pressure and film thickness with variation of column location for various liner thicknesses t_p.

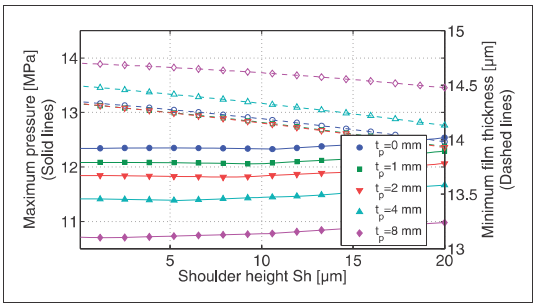

Figure 7. Pressure and film thickness with variation of shoulder height for various liner thicknesses t_p.

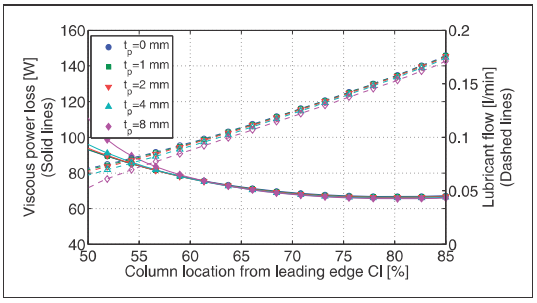

Figure 9. Power loss and lubricant flow with variation of column location for various liner thicknesses t_p.

approximately 35 mm for the 1, 2 and 4 mm lined pads. Lubricant peak pressure drops with increasing column width and this is somewhat counter intuitive since the flexure mechanism is stiffer and thus less able to adjust its angular position according to the applied load. However, the size of the column cross-section also affects the stiffness of the pad body and thus a bigger cross-sectional area causes the body deformation to decrease and thereby giving a flatter pressure profile with reduced peak pressure.

Figure 11 shows the performance parameters used to evaluate the thermal response of the pad. From a thermal point of view, it is clear that the column width must be as small as possible since this minimizes viscous power loss and also maximizes lubricant flow. The more flexible column width of 20 mm is chosen for the remaining parameter studies. A further advantage of this is that the pad will have a lower sensitivity to misalignment and resulting edge loading. The selected column dimension leads to Von Mises stresses in the range of 400 MPa and thus no plastic deformation is expected.

Variation of pad length and width

Figures 12 and 13 show the variation of pad performance as a function of pad length-to-width ratio. The pad area is kept constant and thus the specific load is also constant at 5 MPa. From Figure 12, it is seen that a pad length-to-width ratio a little larger than 1.0 gives the lowest peak pressures, whereas a ratio of 1.3 to 1.4 gives the highest minimum lubricant film thickness depending on liner thickness.

From Figure 13, it is observed that the lowest power loss occurs at a pad length-to-width ratio from 0.95 to 1.3 depending on liner thickness. For the pad configurations with liner thicknesses of 0–4 mm, the pad length-to-width ratio has almost no influence on flow rate. This is interesting because intuitively one could deduce that a low ratio, and hence a wide pad, would give a higher flow rate. However, the influence from the wider pad is counterbalanced by a steeper pressure gradient at the leading edge of the pad which reduces the lubricant flow into the pad.

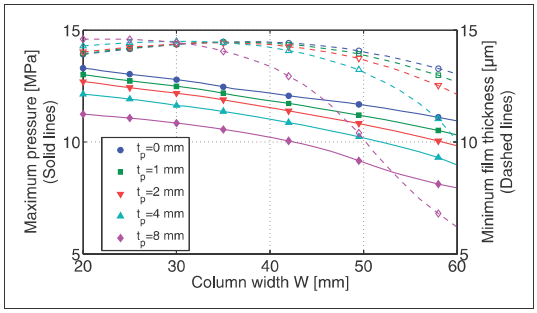

Figure 10. Pressure and film thickness with variation of column stiffness, represented by column width, for various liner thicknesses t_p.

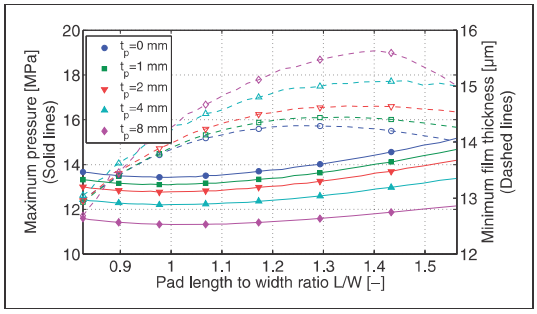

Figure 12. Pressure and film thickness with variation of pad length-to-width ratio for various liner thicknesses t_p.

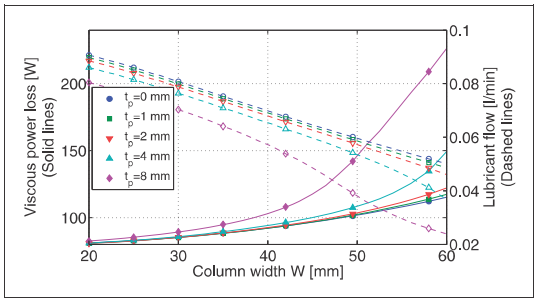

Figure 11. Power loss and lubricant flow with variation of column stiffness, represented by column width, for various liner thicknesses t_p.

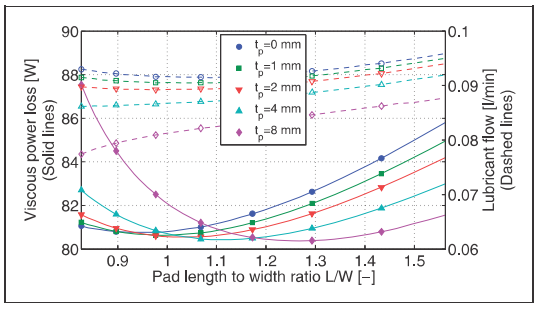

Figure 13. Power loss and lubricant flow with variation of pad length-to-width ratio for various liner thicknesses t_p.

A pad length-to-width ratio of 1.28 is chosen for the remaining parameter studies in this article giving a pad size of 113 × 88.5 mm (length × width).

Pad performance at misalignment

One of the primary functions of the pivot mechanism in a pivoted pad bearing is to allow the pad body to adjust itself according to the external load and also to misalignment. In order to assess how well the flexure pad studied in this study performs when misaligned the misalignment is varied from 0 to 100 μm. The misalignment is defined as the difference in film thickness at one side of the pad compared to the other side when the pad is in its unloaded state. The results are shown in Figure 14. From this figure, it is seen that the lubricant film thickness at no misalignment is about 15 μm and thus 100 μm is a significant misalignment considering that the pad is only 88.5 mm wide. The misalignment has limited influence on the lubricant peak pressure, whereas the minimum lubricant film thickness is affected to a higher degree. The minimum film thickness is above 11 μm for all liner configurations and the bearing is therefore considered to safely operate without any contact or wear. Misalignment only affects power loss moderately and has almost no influence on the flow rate.

Figure 15 shows the pressure and film thickness profiles for a pad with 8 mm liner (t_p) operating at 100 μm misalignment corresponding to Figure 14. The contour lines represent the pressure distribution with a maximum of 12.1 MPa. Even though the pad is operating at very high misalignment the peak pressure is only moved slightly away from the pad center line. The minimum film thickness is located at the trailing edge of the pad, where the film thickness varies from 11.1 to 23.1 μm from one side to the other. The difference of 12 μm is very moderate when compared to the misalignment of 100 μm.

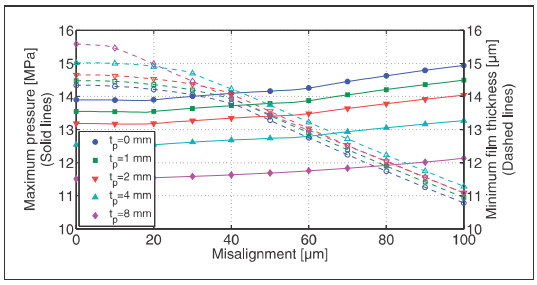

Figure 14. Pressure and film thickness with variation of misalignment for various liner thicknesses t_p.

Conclusion

A hydrodynamic radial flexure pad with a compliant liner has been studied and the effect of varying its geometrical design parameters has been analyzed. Throughout the study, the pad design has undergone one iteration loop of optimization. The learnings are summarized below.

1. Body stiffness is crucial for pad performance. An optimum stiffness exists and it is a compromise between high lubricant film thickness and low peak pressure versus thermal response.
2. The column stiffness plays an important role for the ability of the pad to adjust itself according to different loading conditions and misalignment. The support must be as flexible as possible while still being able to carry the external load. This makes the design of the flexure mechanism a structural problem rather than a tribological.
3. The dimensions of the leading edge chamfer are not important for the flexure pad. The function of the chamfer is to initiate a hydrodynamic pressure build-up and once the lubricant pressure is established, the pad and column elasticity will insure a good pad geometry for pressure build-up.
4. The column location is a compromise between lubricant film thickness and pressure versus thermal response and thus the position must be adapted to the specific machine the bearing is intended for. A column position between 55% and 65% is a good choice.
5. The length-to-width ratio of the flexure pad must be in the range from 1.0 to 1.3 for good pad performance.

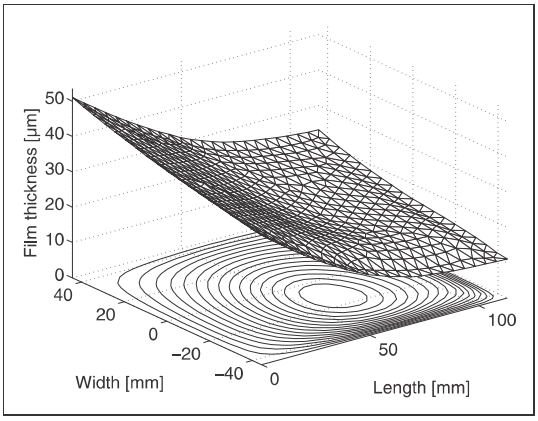

Figure 15. Pressure and film thickness profiles for pad with 8 mm liner (t_p) operating at 100 μm misalignment corresponding to Figure 14. Maximum pressure, 12.1 MPa; minimum film thickness, 11.1 μm.

The compliant polymer liner gives distinct advantages for the flexure pad if it operates at thin films or has many starts and stops and thus frequently operates in the mixed lubrication regime. The compliant liner also influences the operation at full hydrodynamic lubrication.

1. The polymer liner clearly reduces peak pressures giving a flatter pressure profile. Increased compliance reduces peak pressures.
2. The concave deformation contribution of the polymer liner reduces the lubricant flow into the pad because the film thickness is reduced at the edges of the pad.
3. There is no clear trend in the polymer liner effect on either power loss or lubricant film thickness. For any operation condition, an optimum polymer thickness exists that will maximize lubricant film thickness.
4. Very compliant liners must be avoided. If liner deformation is excessive, its concave contribution will exceed the convex contribution from the pad body and thus pad performance decreases drastically. Thicknesses of 2 mm are generally performing well.

A topic not covered in this study is the low thermal conductivity of the polymers. This reduces thermal crowning but on the other hand also leads to reduced cooling of the lubricant. For applications with high sliding speeds and accordingly high viscous dissipation, a TEHD model is recommended.

Flexure pads can replace pivoted pads and thus eliminate the pivot contact related failure modes and also increase load capacity because the allowable load on a pivot contact is limited. The allowable load capacity can be increased further by adding a polymer liner of 1–4 mm thickness; this will also increase performance at low lubricant film thicknesses.

If the flexure support is combined with polymer liners it is possible to design very robust pads that can operate at higher specific loads than common babbitted tilting pad bearings. This comes at an expense of a slight reduction in performance at high misalignments.

Funding

This work was supported by The Danish Agency for Science, Technology and Innovation [grant no. 08-041149].

Acknowledgment

The financial support of the Danish Agency for Science, Technology and Innovation is gratefully acknowledged.

References

1. Stachowiak G and Batchelor A. *Engineering lubrication*, 3rd ed. Amsterdam: Elsevier Inc., 2005.
2. Ettles C. Size effects in tilting pad thrust bearings. *Wear* 1980; 59: 231–245.
3. Kepple W, Read D, Zeidan F, Paraskevakos C and Dawson M. Experience in the use of flexure pivot tilt pad bearings in boiler feedwater pumps. In: *Proceedings of the 15th international pump users symposium*. Houston, TX, USA, March 1998, vol.1509, pp.77–83.
4. Nicholas J and Barret L. The effect of bearing support flexibility on critical speed prediction. *ASLE Trans* 1986; 29: 329–338.
5. Nicholas J. Tilting pad journal bearing pivot design for high load applications. In: *Proceedings of the 24th turbomachinery symposium*, College Station, TX, USA, May 2005, pp. 33–47. College Station, TX: Texas A&M University.
6. Walton N and San Andrés L. Measurements of static loading versus eccentricity in a flexure-pivot tilting pad journal bearing. *J Tribol* 1997; 119: 297–304.
7. San Andrés L and De Santiago O. Imbalance response of a rotor supported on flexure pivot tilting pad journal bearings in series with integral squeeze film dampers. *J Eng Gas Turbines Power* 2003; 125: 1026–1032.
8. Glavatskih S. Evaluating thermal performance of a *ptfe*-faced tilting pad thrust bearing. *J Tribol* 2003; 125: 319–324.
9. Simmons J, Knox R and Moss W. The development of PTFE-faced hydrodynamic thrust bearing for hydrogenerator application in the united kingdom. *Proc IMechE Part J: J Engineering Tribology* 1998; 212: 345–352.
10. Ettles C, Knox R, Ferguson J and Horner D. Test results for *ptfe*-faced thrust pads, with direct comparison against babbitt-faced pads and correlation with analysis. *J Tribol* 2003; 125: 814–823.
11. McCarthy D and Glavatskih S. Assessment of polymer composites for hydrodynamic journal-bearing applications. *Lubr Sci* 2008; 21(8): 331–341.
12. Glavatskih S and Fillon M. TEHD analysis of thrust bearings with PTFE-faced pads. *J Tribol* 2006; 128: 49–58.
13. Huebner K, Dewhirst D, Smith D and Byron T. *The finite element method for engineers*. West Sussex: John Wiley & Sons, 2001.
14. Booker JF and Huebner KH. Application of finite element methods to lubrication: an engineering approach. *Trans ASME, J Lubric Technol* 1972; 94(4): 313–323.
15. McIvor J. *The analysis of dynamically loaded flexible journal bearings using higher-order finite elements*. PhD Dissertation, University of London, UK, 1988.
16. Heinrichson N. *On the design of tilting-pad thrust bearings*. PhD Dissertation. Denmark: Technical University of Denmark, 2006.
17. Glavatskih S. Tilting pad thrust bearings. In: *Proceedings of the 29th Leeds-Lyon symposium on tribology*, Bodington Hall, Leeds, 3–6 September 2002, pp. 379–390. Leeds, UK: Elsevier.

Appendix

Notation

A	element area (m^2)
$\mathbf{A}$	integration matrix (m^2)
b	element coefficient (m)
B	pad body thickness (m)
c	element coefficient (m)
C	column width and length (m)
Ch	column height (m)
Cl	column center location from leading edge (%)
d	deformation vector (m)
E	modulus of elasticity (N/m^2)
f	functional (m^3/s)
F	force (N)
h	pad film thickness (m)
h_0	pad film thickness in the undeformed state (m)
$\mathbf{H}$	fluidity matrix ($m^3/(Pas)$)
$\mathbf{K}$	force stiffness matrix (N/m)
L	pad length (m)
$\mathbf{L}$	pressure compliance matrix (m/Pa)
p	pressure (Pa)
R	radius (m)
S	residual (m^3/s)
Sh	shoulder height (m)
t	time (s)
t_p	liner thickness (m)
V	fluidity vector (m^3/s)
W	pad width (m)
x, y, z	linear coordinates (m)
$\dot{x}$	journal speed in x-direction (m/s)
$\dot{y}$	journal speed in y-direction (m/s)
θ	angular coordinate (rad)
μ	lubricant viscosity (Pas)
ν	Poisson's ratio (–)
ω	rotational speed (rad/s)
Ω	area (m^2)

Appendix D

Journal paper: Improvement of journal bearing operation at heavy misalignment using bearing flexibility and compliant liners

Accepted for publication in Journal of Engineering Tribology [15].

Original Article

Institution of MECHANICAL ENGINEERS
Journal of ENGINEERING TRIBOLOGY

Proc IMechE Part J:
J Engineering Tribology
226(8) 651–660

DOI: 10.1177/1350650112439372
pij.sagepub.com
SAGE

Improvement of journal bearing operation at heavy misalignment using bearing flexibility and compliant liners

Kim Thomsen and Peder Klit

Abstract

A flexure journal bearing design is proposed that will improve operational behaviour of a journal bearing at pronounced misalignment. Using a thermoelastohydrodynamic model, it is shown that the proposed flexure journal bearing has vastly increased the hydrodynamic performance compared to the stiff bearing when misaligned. The hydrodynamic performance is evaluated on lubricant film thickness, pressure and temperature. Furthermore, the influence of a compliant bearing liner is investigated and it is found that it increases the hydrodynamic performance when applied to a stiff bearing, whereas the liner has practically no influence on the flexure journal bearing's performance.

Keywords

Flexure bearing, thermoelastohydrodynamic, misalignment, polymer liner

Date received: 24 October 2011; accepted: 27 January 2012

Introduction

Misalignment is the root cause of many journal bearing failures. It is, however, difficult to avoid misalignment since many factors add to it. These are improper assembly, elastic and thermal distortions of the shaft and bearing housing, and also manufacturing tolerances. Therefore, it is important to consider misalignment when designing journal bearings. A traditional solution for misalignment is to include a spherical seat in the housing and thereby allow the bearing to rotate and align to the journal at the assembly. This will, however, only apply a static correction and not permit any dynamic misalignment. Another design approach is to add a well-defined crowning for the bearing liner. This approach can be problematic since the required liner modification is smaller than 0.5 times the minimum lubricant film thickness and therefore difficult to manufacture.

The aim of this study is to show that bearing flexibility can be used to effectively improve a bearing's ability to operate under heavy misalignment. It is accomplished by decreasing the angular stiffness of the bearing and at the same time maintaining a high radial stiffness. This allows the bearing to maintain a high performance at low or no misalignment and also to deform when subjected to misalignment. Thereby, the lubricant film thickness is increased at the highly loaded areas that could otherwise make contact and lead to failure.

In this study, the term *flexure bearing* is used for bearings for which important parts of their tribological characteristics are achieved through structural flexibility.

In this study, it is shown that by using a flexure bearing design, it is possible to design an inexpensive, simple and robust bearing that can operate at high misalignment without suffering from edge loading and potential bearing damage. Furthermore, it is also studied if a compliant liner will improve the tolerance towards misalignment when combined with a flexure bearing and also on a traditional stiff bearing.

Department of Mechanical Engineering, Technical University of Denmark, Denmark

Corresponding author:
Kim Thomsen, Department of Mechanical Engineering, Technical University of Denmark, Nils Koppels Alle, Building 404, DK-2800 Kgs, Lyngby, Denmark.
Email: kimth@mek.dtu.dk

Bouyer, Fillon and Pierre have done an extensive work[1–4] on the effects of misalignment on the operational behaviour of traditional journal bearings. They observe the most significant reduction in bearing performance at low rotational speed and as expected, the pressure peak moves away from the centre plane and towards the edge of the bearing when subjected to misalignment. They propose two optimized bearing geometries and show that they can improve performance considerably when operating with misalignment. However, they do not take elasticity into account.

Nikolakopoulos et al.[5] show a novel application of bearing optimization using Pareto analysis together with an elastohydrodynamic (EHD) model. They optimize the geometry of a misaligned journal bearing through variation of the traditional bearing parameters. It is also shown that a misaligned bearing can benefit from a limited amount of wear.

Mihailidis et al.[6] study the influence of bushing geometry on the performance of a misaligned hydrodynamic journal bearing and find that parabolic and crowned liner modifications perform well.

A flexure bearing is designed to take advantage of its structural flexibility in order to adapt its geometry to various operating conditions. The bearings are known as alternatives to pivoted bearings, for both radial and thrust bearings.

Walton and San Andrés[7] study a four-pad flexure bearing subjected to various operating conditions experimentally and compare measurements with theoretical results. They find that the particular bearing geometry operates predictably and reliably for all subjected conditions. San Andrés and de Santiago[8] study the dynamic response of a flexure pad bearing experimentally. They find that bearing response to unbalance loads is good and has a stable performance in the entire range of operating conditions.

Thomsen and Klit[9] study a radial flexure pad bearing operating under misaligned conditions and it is found that the use of flexure pads is an attractive alternative to pivoted pads. Pivot contact related failure modes are eliminated and load capacity is not restricted by the force that can be transferred through the pivot contact. It is furthermore found that if the flexure support is combined with a polymer liner, it is possible to design a very robust pad that can operate at higher specific loads than common babbitted tilting pad bearings.

The study of compliant liners has seen increasing interest in the recent years. Due to the polymer liners' low break away friction and good wear properties, the liners have very good operational characteristics at thin films. The compliant nature of the polymer bearings mean that they are less sensible to imperfections in the bearing surface geometry. This is particularly interesting for large bearings. The polymers do, however, also give the design engineers new challenges in the form of creep, the Achilles' heel of polymers when applied to bearing applications. In order to decrease the creep to an acceptable level, the polymers are often reinforced with glass or carbon fibres. The low thermal conductivity of polymers must also be taken into account when introducing polymer liners in hydrodynamic bearings, as it will reduce the heat flux between bearing and lubricant.

Simmons et al.[10] analyse the use of large thrust pads with polytetrafluoroethylene (PTFE) liners for hydropower plants and describe the learning from uprating the thrust bearing in a hydropower plant. The existing babbitt-faced pads were replaced with PTFE-faced pads and it was concluded that the high-pressure lubricant-injection systems used to enable safe start-up and shut-down could be dispensed with. The PTFE pads can operate under harder conditions, allowing the bearings to be designed smaller and thus more energy efficient or with similar size as a babbitted bearing but with a higher safety margin.

Thomsen and Klit[11] study the compliant liners and their influence on the dynamic response of a dynamically loaded journal bearing. The primary findings are that the maximum pressures are reduced significantly at the expense of slightly higher eccentricity ratio during operation.

As stated earlier, the aim of this study is to show that bearing flexibility can be used for bearings operating at heavy misalignment advantageously. A traditional two-lobe journal bearing with circular bore operating at steady-state conditions is used for the analysis. A stiff bearing and a flexure bearing geometry will be studied and compared. In addition to this, the effects of compliant liners are studied by including variants with and without compliant bearing lining. Thus, four bearings are studied in total:

- a traditional stiff bearing;
- a traditional stiff bearing with compliant polymer liner;
- a flexure bearing; and
- a flexure bearing with compliant polymer liner.

Figure 1 shows the geometry of the flexure journal bearing with a compliant liner. The low rotational stiffness of the flexure web allows the flexure tube, and thus the bearing, to rotate and adjust according to journal misalignment.

The compliant liner is 2-mm thick. For the bearings without a compliant liner, the steel bodies are moved 2 mm towards the bearing centre line and thereby the overall stiffness of the bearings is influenced minimally when removing the compliant liners. The two stiff

bearings are modelled using the same figure, except that the web of 15 mm is extended to the full width of 150 mm. The journal is assumed infinitely stiff. Remaining bearing data and operating conditions are given in Table 1. The same operating conditions are used throughout the analysis.

The full flexibility of the bearing is included in the elastic model, and thus, there is an exhaustive number of geometrical parameters to investigate when optimize the geometry for the given load. For this study, the thickness of the flexure web and flexure tube, 15 mm and 35 mm, respectively, was chosen after trying several configurations. This particular combination returns good bearing response, although not fully optimized, for the given operating conditions.

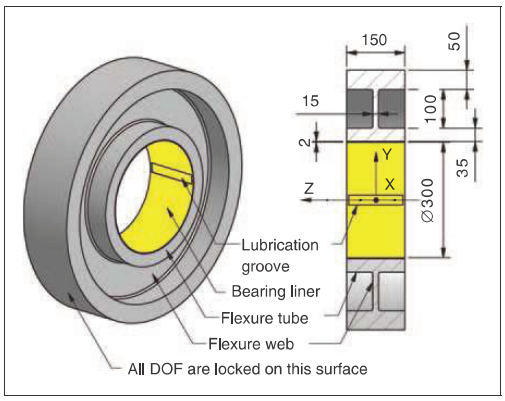

Figure 1. Flexure journal bearing geometry and system coordinates.
DOFs: degrees of freedom.

Table 1. Bearing data and operating conditions.

Parameter	Value
Bearing diameter	300 mm
Bearing width, L	150 mm
Radial clearance	150 μm
Circumferential extension of oil inlet groove	10°
Number of oil inlets	2
Bearing load in y-direction	−225 kN
Specific pressure	5 MPa
Rotational speed, ω	1500 r/min
Lubricant viscosity grade	ISO VG 32
Lubricant density, ρ	854 kg/m^3
Lubricant specific heat capacity, c_p	2000 J/kg/K
Oil inlet temperature	40 °C
Journal temperature at bearing edges	40 °C
Polymer liner: modulus of elasticity	6 GPa
Polymer liner: Poisson's ratio	0.4
Steel: modulus of elasticity	200 GPa
Steel: Poisson's ratio	0.3
Journal thermal conductivity, k_j	40 W/m/K
Heat transfer coefficient: journal/oil α_j	2000 W/m^2/K

Governing equations and model set-up

A thermoelastohydrodynamic model has been developed for this study on flexure bearings. A brief description of the simulation model and its sub-models is given in the following sections.

The hydrodynamic part of the model is verified using the bearing geometry and loads from the connecting rod big end bearing of the Hornsby 6VEB-X Mk III 4 stroke diesel engine[12] giving identical results as other studies. The elasticity part is verified by comparison with elastic structures where the deformation can be compared with elementary beam theory. The thermal part is difficult to compare directly with other studies since, in this article, one surface is treated as adiabatic and heat transfer through the other surface is calculated using a heat transfer coefficient. Furthermore, the journal temperature varies axially in this study. The approach has, however, been widely used and accepted as a simplified method for thermoelastohydrodynamic modelling.

Reynolds equation

A three-node triangular fine element method (FEM) model is used for solving the steady-state form of Reynolds equation (1) and thus finding the pressure distribution

$$\frac{1}{R}\frac{\partial}{\partial\theta}\left[\frac{h^3}{\mu R}\frac{\partial p}{\partial\theta}\right]+\frac{\partial}{\partial z}\left[\frac{h^3}{\mu}\frac{\partial p}{\partial z}\right]=6\omega\frac{\partial h}{\partial\theta} \tag{1}$$

The element equations corresponding to equation (1) are derived using the variational approach[13] and shown in equations (2) to (4). Three-node triangular elements are used, giving linear interpolation functions. The coefficients b and c are constants of the element and are deduced from its geometry

$$\underset{3\times3}{\left[\mathbf{H}_{jk}\right]}\underset{3\times1}{\left\{p_j\right\}}=\underset{3\times1}{\left\{V_j\right\}} \tag{2}$$

$$\left[\mathbf{H}_{jk}\right]=\int_\Omega\left(\frac{h^3}{4\mu A^2}\left(b_jb_k+c_jc_k\right)\right)\mathrm{d}\Omega \tag{3}$$

$$\left\{V_j\right\}=\int_\Omega\left(\frac{3Rb_j}{A}\omega h\right)\mathrm{d}\Omega \tag{4}$$

Equation (2) is a set-up for all elements and assembled into a set of equations, combining all nodes which can then be used to solve for the pressure p.

The pressure is set to zero for all nodes located on the bearing edges and in the lubrication grooves.

Cavitation is handled through an algorithm where consecutive iterations are solved for the pressure. Nodes which fulfil the cavitation requirement, $p<0$, are identified and a fraction of the nodes, counting from the trailing edge of the cavitated region, is selected and the pressure is set to zero at these nodes and next iteration is initiated. The procedure is repeated until no nodes fulfil the cavitation requirement.

Elasticity

An industrial state-of-the-art structural finite element program, in this case Ansys,[14] is used to create the bearing models in order obtain the corresponding stiffness matrices. Since the fluid film forces are acting only on the liner surface, it is advantageous to condense the stiffness matrices into super elements before exporting them. The method of exporting and reading the stiffness matrix $\mathbf{K}$ is verified by modelling geometries that can be compared to analytical results using elementary beam theory. The force stiffness matrix $\mathbf{K}$ is converted to pressure compliance matrix $\mathbf{L}$ using the integration matrix $\mathbf{A}$, as shown in equation (5)

$$[\mathbf{K}]\{d\} = \{F\} \Leftrightarrow \{d\} = [\mathbf{K}]^{-1}\{F\} = [\mathbf{K}]^{-1}[\mathbf{A}]\{p\} = [\mathbf{L}]\{p\} \tag{5}$$

The super elements utilize 5500 elements. The meshes from the super elements are also used for the oil film model using equations (2) to (4). For the structural model, all nodes at the outer surface of the bearing in Figure 1 are locked in all its degrees of freedom.

Coupling of oil film forces and elasticity

Reynolds equation is coupled with bearing elasticity using the Newton–Raphson method. A Taylor expansion around the solution $f(p)$ with respect to p and neglecting derivatives of orders higher than one gives equation (6)

$$\Delta p \frac{\partial f(p)}{\partial p} = f(p+\Delta p) - f(p) \tag{6}$$

The functionals $f(p)$ (7) and $f(p+\Delta p)$ (8) are the usual Reynolds equation (1) where the latter is perturbed with respect to the pressure. The two functionals are expanded and simplified to equation (9) using (6). The term h_0 is the oil film thickness for the flexure bearing in its undeformed state

$$f(p) = \frac{1}{R}\frac{\partial}{\partial\theta}\left(\frac{h^3}{\mu R}\frac{\partial p}{\partial\theta}\right) + \frac{\partial}{\partial z}\left(\frac{h^3}{\mu}\frac{\partial p}{\partial z}\right) - 6\omega\frac{\partial h}{\partial\theta} \tag{7}$$

where $h = h_0 + Lp$

$$f(p+\Delta p) = \frac{1}{R}\frac{\partial}{\partial\theta}\left(\frac{h^3}{\mu R}\frac{\partial(p+\Delta p)}{\partial\theta}\right) + \frac{\partial}{\partial z}\left(\frac{h^3}{\mu}\frac{\partial(p+\Delta p)}{\partial z}\right) - 6\omega\frac{\partial h}{\partial\theta} \tag{8}$$

where $h = h_0 + L(p+\Delta p)$

When h^3 from equation (8) is expanded, the terms including $L\Delta p$ in powers of two or higher are neglected

$$\Delta p\frac{\partial f(p)}{\partial p} = \frac{1}{R}\frac{\partial}{\partial\theta}\left(\frac{3h^2L\Delta p}{\mu R}\frac{\partial p}{\partial\theta}\right) + \frac{\partial}{\partial z}\left(\frac{3h^2L\Delta p}{\mu}\frac{\partial p}{\partial z}\right) + \frac{1}{R}\frac{\partial}{\partial\theta}\left(\frac{h^3}{\mu R}\frac{\partial\Delta p}{\partial\theta}\right) + \frac{\partial}{\partial z}\left(\frac{h^3}{\mu}\frac{\partial\Delta p}{\partial z}\right) - 6\omega\frac{\partial L\Delta p}{\partial\theta} \tag{9}$$

where $h = h_0 + Lp$

Equation (9) is then put into finite element formulation, using the Galerkin principle, giving the left-hand side (LHS) of equation (10), which is then used to solve for Δp where S is the residual of the assembled version of equation (2) after the right-hand side (RHS) is moved to the LHS

$$\left[\frac{\partial f(p)}{\partial p}\right]\{\Delta p\} = \{S\} = [\mathbf{H}]\{p\} - \{V\} \tag{10}$$

The final solution for the state of deformation d and the corresponding pressure p is found by solving equation (10) multiple times until the residual S vanishes.

For a thorough derivation of the Newton–Raphson method applied for EHD problems, see McIvor's[15] work on this topic.

Energy equation

The energy equation (11) is solved using a two-dimensional model. The local temperature T_m represents the mean temperature over the film thickness direction. The lubricant temperature is specified at the lubricant supply grooves and full lubricant exchange is assumed

$$\rho c_p\left(\frac{1}{R}\frac{\partial T_m}{\partial\theta}q'_\theta + \frac{\partial T_m}{\partial z}q'_z\right) = \alpha_J(T_J - T_m) + \frac{\mu_m\omega^2R^2}{h} + \frac{h^3}{12\mu_m}\left(\frac{1}{R^2}\left(\frac{\partial p}{\partial\theta}\right)^2 + \left(\frac{\partial p}{\partial z}\right)^2\right) \tag{11}$$

The conductive term only includes conduction through the journal; this is a good boundary condition when the bearing is covered with a highly thermally insulating polymer liner. It does, however, give an underestimation of the heat conduction from the lubricant when the model is used for the metal lined bearings, because the heat transport through the liner is neglected. The approach is chosen in order to be able to compare the four bearing configurations without complicating the evaluation of the results.

The conduction is calculated using the heat transfer coefficient α_J together with the temperature difference between journal and lubricant: $T_J - T_m$.

The journal temperature profile in the axial direction $T_J(z)$ is determined assuming that the journal temperature is constant at any radial cross-section ($z = z_{cs}$). Thereby, the power conduction through a section of the journal can be calculated using equation (12). The journal temperature is then defined at the bearing edges only ($z = \pm\frac{L}{2}$)

$$P_{J_{z=z_{cs}}} = A_J k_J \frac{\partial T_J}{\partial z}_{z=z_{cs}} \tag{12}$$

For simplicity, the conduction from lubricant to journal is assumed to be symmetric about the midsection of the bearing ($z = 0$). When this assumption is combined with the conductive term of equation (11), the power through any cross section can also be expressed as equation (13)

$$P_{J_{z=\pm z_{cs}}} = R \int_{-z_{cs}}^{+z_{cs}} \int_{-\pi}^{+\pi} \frac{\alpha_J (T_J - T_m)}{2} \mathrm{d}\theta \mathrm{d}z \tag{13}$$

Equations (12) and (13) can then be combined into equation (14), expressing the journal temperature gradient at any cross-section of the journal

$$\frac{\partial T_J}{\partial z}_{z=\pm z_{cs}} = \frac{R \int_{-z_{cs}}^{+z_{cs}} \int_{-\pi}^{+\pi} \alpha_J (T_J - T_m) \mathrm{d}\theta \mathrm{d}z}{2 A_J k_J} \tag{14}$$

The axial temperature profile of the journal $T_J(z)$ can then be found by solving the boundary value problem described by the differential equation (14) knowing the temperature at $z = \pm\frac{L}{2}$.

The energy equation is solved using the finite difference method. For this purpose, the results from the arbitrary mesh layout of the FEM is interpolated onto the equidistant finite different mesh.

Finally, the Walther and McCoull[16] expression is used to describe the temperature and viscosity correlation.

Results

Variation of misalignment

A load of −225 kN, corresponding to a specific pressure of 5 MPa, is applied to the bearings in the Y-direction (see Figure 1 for coordinate system), while increasing the angular misalignment from 0 to 1 mrad around the X-axis. This corresponds to a difference of 150 μm film thickness from one bearing side to the other, the same as the radial clearance. Nikolakopoulos et al.[5] states that a misalignment of up to 0.3 mrad is generally accepted in most industrial and marine applications. Figure 2 shows the flexure bearing geometry operating at maximum misalignment in its deformed state. It is seen how the flexible web allows the flexure tube to rotate and adapt to the journal misalignment and thereby increase the film thickness at the hardest loaded area of the bearing. The tube also deforms and bends just over the bearing centre, where the tube is supported by the web. The bending of the tube is undesirable as it creates a pressure peak if the bending is too high. In this case, the tube wall thickness of 35 mm ensures that the amount of bending

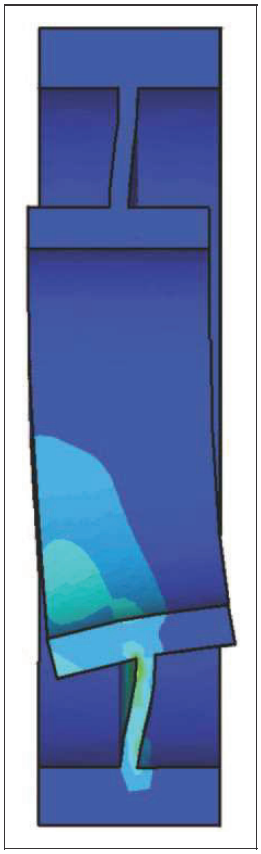

Figure 2. Ansys model showing deformed state of flexure bearing at maximum misalignment. The colour grades represent von Mises reference stress; maximum is 128 MPa.

is limited. The colour grades represent the von Mises stress levels in the bearing, and a maximum stress of 128 MPa is observed. The maximum stress is found at the interface web-to-tube, where no fillets are used in the structural model. Thus, the stress levels can be expected to decrease when introducing these.

Figure 3 shows the minimum film thickness for the four bearing configurations at increasing misalignment. It is seen that the two stiff bearings reach a minimum film thickness of 0.3 and 1.4 μm already at 0.44 mrad, whereas the two flexure bearings maintain a thickness of 14 μm at this amount of misalignment. The flexure configurations maintain a film thickness of more than 3 μm up to the maximum misalignment of 1 mrad. The gradients of the two flexure bearing curves change from almost horizontal to decreasing at 0.09 mrad misalignment. At this point, the location of the minimum film thickness changes from the midsection of the bearing to the edge.

For the stiff bearing, it is seen that the compliant liner increases the minimum film thickness over the entire range of misalignment with a relative high quantity. The reason for this improvement is that the cavitated area is reduced when using the compliant liner and thus the load-carrying area of the bearing is increased. In the case of the flexure bearing, there is no significant difference when using a compliant liner.

A topic not covered by this study is the wear and friction properties of the compliant polymer liner during mixed lubrication, which is generally better for polymers. McCarthy and Glavatskih[17] has shown this by comparing polyether ether ketone and babbitt experimentally. Therefore, the bearings with a compliant liner can be operated safely at lower film thicknesses compared to bearings using babbitt liners.

Figure 4 shows the maximum lubricant pressure for the four bearing configurations at increasing misalignment. As expected, the two stiff configurations show rapidly increasing pressures, whereas the two flexure bearings display a very light increase in maximum pressure over the entire range of misalignment. Again, the compliant liner gives remarkably increased performance for the stiff bearing, whereas the performance change is only moderate for the flexure bearing.

Figure 5 shows the maximum lubricant temperature at increasing misalignment. Again, the two stiff configurations display a fast increase to very high values and it is seen that the compliant liner increases bearing performance for the stiff bearing. The flexure bearings display a slowly increasing maximum temperature with misalignment, and there is virtually no difference between the bearings with noncompliant and compliant liner. The model predicts a peak temperature for the stiff bearing of 500 °C and a minimum film thickness of 0.3 μm. The simulation model cannot predict reliable results in these ranges since new physical phenomena will show in the form of gas release and asperity contact.

Figure 6 shows the journal eccentricity as a function of misalignment and it is obvious that even though the flexure web is designed to maintain a high radial stiffness, the bearing still suffers from lower stiffness coefficients. It is, however, very counterintuitive that the stiff bearing has a lower stiffness than the corresponding bearing with compliant liner. From this, and also Figure 3, it is evident that the compliant liner improves the hydrodynamic effects and thereby increases the film thickness and correspondingly also increases the bearing stiffness coefficients. The opposite is true for the

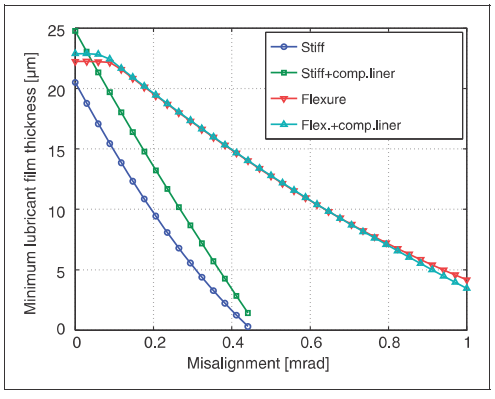

Figure 3. Minimum lubricant film thickness as a function of journal misalignment.

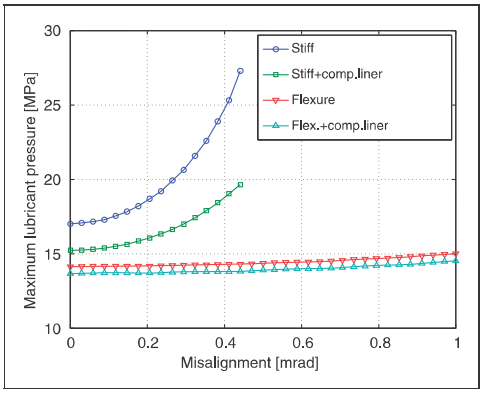

Figure 4. Maximum lubricant pressure as a function of journal misalignment.

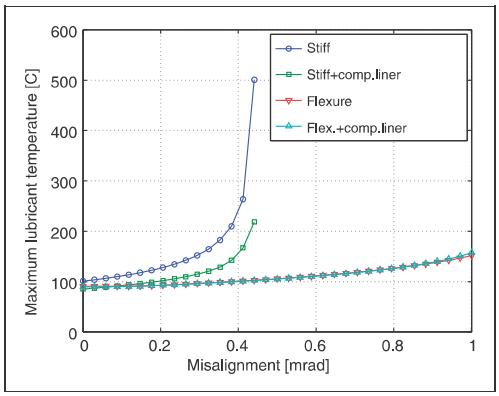

Figure 5. Maximum lubricant temperature as a function of journal misalignment.

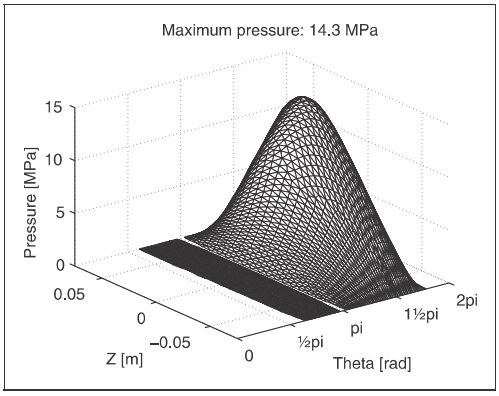

Figure 7. Pressure profile for flexure bearing with 225 kN load and 0.44 mrad misalignment.

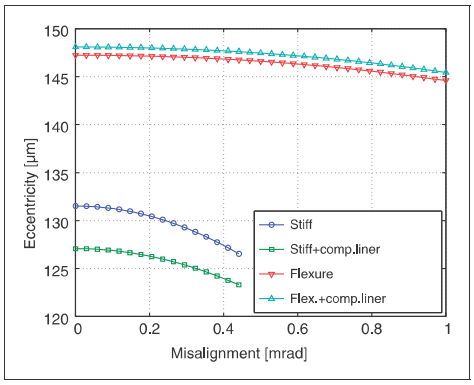

Figure 6. Journal eccentricity as a function of journal misalignment.

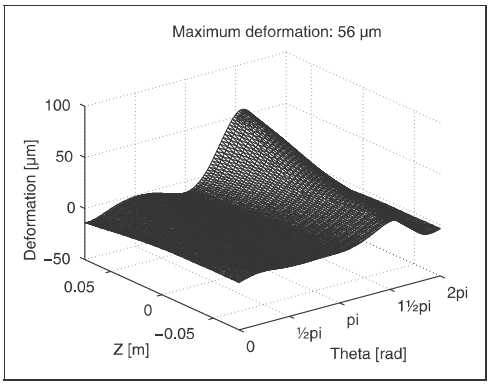

Figure 8. Liner deformation of flexure bearing with 225 kN load and 0.44 mrad misalignment.

flexure bearing where the eccentricity increases slightly with the compliant liner.

Full bearing liner plots

Figures 7 to 13 show bearing data for the applied load and misalignment corresponding to the point on Figures 3 to 6 that can be read at 0.44 mrad, i.e. the last points for the stiff bearings.

Figure 7 shows the pressure profile for the flexure bearing. It is seen that the pressure peak is still very close to the bearing centre and that the profile is comparable to the usual profile from a bearing operating at no misalignment. The mesh is not shown at the cavitated areas.

Figure 8 shows the deformation corresponding to the pressure shown in Figure 7. As expected, the bearing has a very high deformation at the area at which the journal tries to make contact due to the misalignment. It is also interesting to see that the deformation is negative in some areas. From this, it can be concluded that the bearing ovalizes under the misaligned bearing load.

Figure 9 shows the lubricant temperature over the flexure bearing liner surface. As expected, the maximum temperature is at the bearing edge, at the same location as the minimum film thickness.

Axial liner plots

Figure 10 shows the axial pressure profiles for the four bearing configurations. The stiff bearing has very high pressure levels and gradients at the bearing edge, same

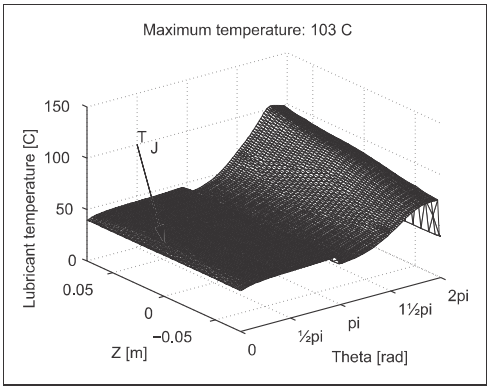

Figure 9. Lubricant mean temperature T_m for flexure bearing with 225 kN load and 0.44 mrad misalignment. Axial journal temperature T_J profile is also shown. $T_{J_{max}} = 50.3\,^{\circ}\mathrm{C}$.

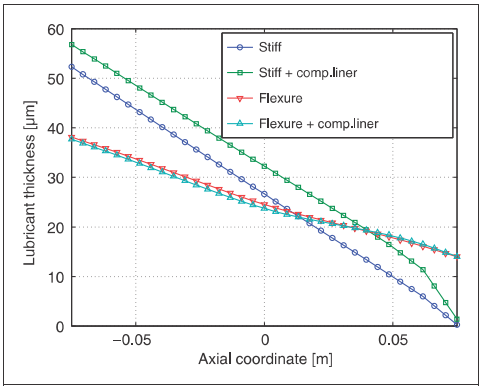

Figure 11. Axial film thickness profiles for bearings with 225 kN load and 0.44 mrad misalignment at circumferential location with minimum film thickness.

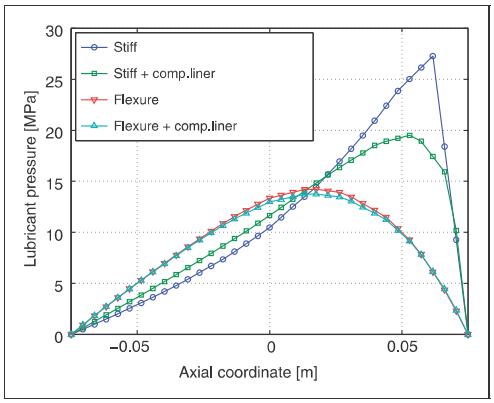

Figure 10. Axial pressure profiles for bearings with 225 kN load and 0.44 mrad misalignment at circumferential location with maximum pressure.

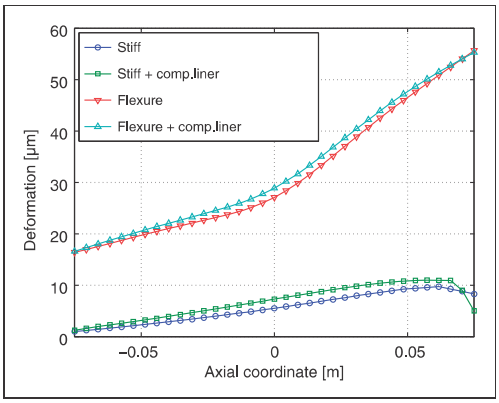

Figure 12. Axial liner deformation profiles for bearings with 225 kN load and 0.44 mrad misalignment at circumferential location with maximum deformation.

tendency as shown in numerous studies. The compliant liner decreases the pressure level significantly for the stiff bearing, but there is no significant change for the flexure bearing. It is seen that the pressure profiles for the flexure bearings are close to the typical pressure profile of a nonmisaligned bearing.

Figure 11 shows the axial film thickness profiles. The stiff bearing shows an almost linear film thickness variation, whereas the stiff bearing with a compliant liner has a higher gradient close to the bearing edge. This is due to the direct correlation between local pressure and local deformation due to the compliant liner. As in Figure 2, it is seen that the flexure tube of the flexure bearing bends at the centre where it is supported by the flexure web. Again, it seen that the compliant liner only influences the stiff bearing.

Figure 12 shows the bearing deformations. The deformation profiles explain why the flexure bearings exhibit lower bearing stiffness coefficients and therefore operate at higher eccentricity ratios, as shown in Figure 6. Again, the flexure tube bending is evident with the gradient change at the middle of the bearing. The results also show that even if the stiff bearing is modelled using a solid steel ring, it still has a significant deformation. Many bearing studies assume the bearing to be infinitely stiff. Figure 12 shows that this assumption does not hold true.

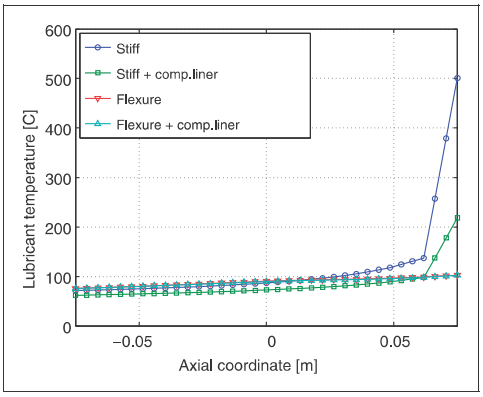

Figure 13. Axial temperature T_m profiles for bearings with 225 kN load and 0.44 mrad misalignment at circumferential location with maximum temperature.

Figure 13 shows the axial temperature profiles. The stiff bearing leaps out with extremely high temperatures. This can be explained by the high-pressure gradients shown in Figure 10 in combination with the low film thickness of Figure 11. The stiff bearing with a compliant liner also shows a high-pressure peak at the bearing edge, it is, however, not as pronounced as for the stiff bearing. This can be explained by the increased film thickness that induces a higher lubricant flow in the hardest loaded area. The flexure bearings show only a moderate temperature increases over the axial length, as also shown in Figure 9.

Conclusion

Using a thermoelastohydrodynamic model, it is shown that the proposed flexure journal bearing design can effectively increase bearing performance when operating at high misalignments. This is achieved without reducing performance at low or no misalignment and also without adding extra components or systems that require fine machining. The proposed flexure design does, however, require extra space for the flexure web that may be difficult to combine with some bearing applications.

Based on the predicted minimum film thicknesses, the proposed flexure journal bearing can operate at three times the misalignment compared to the stiff bearings. This analysis was performed for a short journal bearing with a width- to diameter-ratio of 0.5. The effects will be even more pronounced for bearings with higher ratios since these are more sensitive to misalignment.

The flexure tube must be as stiff as possible in order to give a wide pressure distribution in axial direction, whereas the flexure web must be compliant to allow for angular deformation when operating at misalignment. The lower thickness limit of the flexure web is determined from the structural strength as well as the radial stiffness of the flexure web.

The compliant liner shows a remarkable increase in the hydrodynamic performance when applied to the stiff bearing, also at low or no misalignment. The positive influence is, however, not seen on flexure bearings. The polymer liner does, however, still give the increased performance at boundary or mixed lubrication, giving better wear properties and lower friction. This comes with the side-effect of increased thermal insulation.

Funding

This work was supported by The Danish Agency for Science, Technology and Innovation (grant no. 08-041149).

Acknowledgements

The authors gratefully acknowledge the financial support provided by the Danish Agency for Science, Technology and Innovation.

References

1. Bouyer J and Fillon M. Improvement of the thd performance of a misaligned plain journal bearing. *J Tribol* 2003; 125: 334–342.
2. Bouyer J and Fillon M. An experimental analysis of misalignment effects on hydrodynamic plain journal bearing performances. *J Tribol* 2002; 124: 313–319.
3. Bouyer J, Fillon M and Pierre I. Thermohydrodynamic behaviour of misaligned plain journal beaings: theoretical and experimental approaches. *Tribol Trans* 2003; 47: 594–604.
4. Fillon M. On the thermal effects in hydrodynmaic journal bearings. *Int J Appl Mech Eng* 2005; 3: 441–450.
5. Nikolakopoulos P, Papadopoulos C and Kaiktsis L. Elastohydrodynamic analysis and pareto optimization of intact, worn and misaligned journal bearings. *Meccanica* 2011; 46: 577–588.
6. Mihailidis A, Bakolas V, Panagiotidis K, et al. Influence of the bushing geometry on the thermohydrodynamic performance of a misaligned journal bearing. *Proc IMechE Part J: J Engineering Tribology* 2010; 224: 37–53.
7. Walton N and San Andrés L. Measurements of static loading versus eccentricity in a flexure-pivot tilting pad journal bearing. *J Tribol* 1997; 119: 297–304.
8. San Andrés L and de Santiago O. Imbalance response of a rotor supported on flexure pivot tilting pad journal bearings in series with integral squeeze film dampers. *J Eng Gas Turbines Power* 2003; 125: 1026–1032.
9. Thomsen K and Klit P. Geometrical design parameters for journal bearings with flexure pads. *Proc IMechE Part J: J Engineering Tribology*. Epub ahead of print, DOI: 10.1177/1350650111431525.

10. Simmons J, Knox R and Moss W. The development of PTFE-faced hydrodynamic thrust bearing for hydrogenerator application in the united kingdom. *Proc IMechE Part J: J Engineering Tribology* 1998; 212: 345–352.
11. Thomsen K and Klit P. A study on compliant layers and its influence on dynamic response of a hydrodynamic journal bearing. *Tribol Int* 2011; 44: 1872–1877.
12. McIvor J and Fenner D. Finite element analysis of dynamically loaded flexible journal bearings. *J Tribol* 1989; 111: 597–604.
13. Huebner K, Dewhirst D, Smith D, et al. *The finite element method for engineers*. New York: John Wiley & Sons, 2001.
14. Ansys. Version 12.1, http://www.ansys.com (2009, accessed 1 September 2011).
15. McIvor J. *The analysis of dynamically loaded flexible journal bearings using higher-order finite elements*. PhD dissertation. University of London, London, 1988.
16. Seeton J. Viscosity-temperature correlation for liquids. *Tribol Lett* 2006; 22: 67–78.
17. McCarthy D and Glavatskih S. Assessment of polymer composites for hydrodynamic journal-bearing applications. *Lubr Sci* 2009; 21(8): 331–341.

Appendix

Notation

A	element area (m^2)
A_J	journal cross-sectional area (m^2)
$\mathbf{A}$	integration matrix (m^2)
b, c	element coefficients (m)
c_p	specific heat capacity of lubricant (J/kg/K)
d	deformation vector (m)
E	modulus of elasticity (N/m^2)
f	functional (m^3/s)
F	force (N)
h	pad film thickness (m)
h_0	pad film thickness in the undeformed state (m)
$\mathbf{H}$	fluidity matrix ($m^3/(Pa\,s)$)
k_J	journal thermal conductivity (W/m/K)
$\mathbf{K}$	force stiffness matrix (N/m)
L	journal width (m)
$\mathbf{L}$	pressure compliance matrix (m/Pa)
p	pressure (Pa)
P	power (J/s)
q	lubricant flow (m^3/s)
R	radius (m)
S	residual (m^3/s)
T_J	journal temperature (C)
T_m	lubricant mean temperature (C)
V	fluidity vector (m^3/s)
x, y, z	linear coordinates (m)
α_J	heat transfer coefficient between interface: journal/oil ($W/m^2/K$)
θ	angular coordinate (rad)
μ	lubricant viscosity (Pa s)
μ_m	mean lubricant viscosity (Pa s)
ν	Poisson's ratio (−)
ρ	lubricant density (kg/m^3)
ω	rotational speed (rad/s)
Ω	area (m^2)

Appendix E

Workshop presentation: Application of a new wear model in hydrodynamic metal-polymer bearings

Presented at 9th EDF/Pprime (LMS) Poitiers Workshop:
Improvement of Bearing Performance and Evaluation of Adverse Conditions [38].

Application of a new wear model in hydrodynamic metal-polymer bearings
Proposition et application d'un modèle d'usure dans les paliers métal-polymères

Thomsen K. and Klit P.

Technical University of Denmark, Anker Engelundsvej 1 101A, DK-2800 Kgs. Lyngby, Denmark.

Keywords: Wear estimation, metal-polymer, hydrodynamic, bearing.
Mots clés: Estimation de l'usure, métal-polymère, hydrodynamique, palier.

Heavily loaded bearings and bearings subjected to intermittent operation will often operate in the mixed film lubrication regime resulting in wear of the bearing surfaces. In the design procedure it is useful to have an effective tool to estimate the wear in order to avoid over- and under dimensioning.
A model for estimating wear in metal-polymer bearings (Soft EHL) is proposed. The wear is assumed to be a function of the film thickness only. As opposed to models which rely on calculation of contact forces the proposed wear model is relatively simple to introduce to an existing soft EHL simulation program and does not require additional computational capacity.
The method is implemented and the estimated wear pattern and wear rate is compared qualitatively with experimental findings. The results are discussed as well as test procedures for finding the required wear coefficients.
A weakness of the presented wear model is that it is complicated to find the wear coefficients, mainly because film thickness measurements in metal-polymer bearings are complicated to perform.

Les paliers fortement chargés ou fonctionnant par intermittence opèrent souvent en régime de lubrification mixte ce qui entraîne l'usure des surfaces constituant le palier. Lors de la conception, il est utile de disposer d'un outil d'estimation de l'usure afin de ne pas sur ou sous dimensionner le composant.
Un modèle pour estimer l'usure de paliers en métal-polymères (élastohydrodynamique) est proposé. L'usure est considérée comme une fonction unique de l'épaisseur de film. Contrairement aux modèles qui basent leur calcul sur les forces de contact, le modèle proposé est suffisamment simple pour être implémenté dans un code de calcul élastohydrodynamique et ne requiert aucune puissance de calcul supplémentaire.
La méthode est présentée et les résultats de profils d'usure ainsi que de taux d'usure sont comparés à des résultats expérimentaux. Les résultats ainsi que la méthode pour trouver les coefficients d'usure nécessaire aux calculs sont ensuite discutés. Une faiblesse du modèle présenté est qu'il est compliqué de trouver les coefficients d'usure, principalement en raison de la difficulté à obtenir des mesures d'épaisseur de film dans des paliers metal-polymères.

1 Alternative wear models

The wear in metal-polymer bearings can be characterized by three mechanisms: adhesive, abrasive and fatigue wear. If the metallic part is smooth the wear is mainly adhesive. A run-in process is normally seen where a thin layer of the polymer is transferred to the metallic part. After this run-in the wear rate decreases and stabilizes. For rough surfaces the abrasive wear mechanism will normally be dominant. Fatigue wear may be found for hard polymers. In the present case soft polymers are investigated so that the wear mainly will be due to adhesive and abrasive mechanisms.

Traditionally wear estimation relies on the calculation of contact pressure using for example stochastic, deterministic or micro-macro models and then applying a wear model. A popular choice for this is Archards wear law [9]+[10].

If the focus of interest is wear simulation these methods are relative complex to introduce, and they still rely on experimental results in order to calculate the wear. The aim of this work is to propose a model where the contact pressure is not needed in order to perform the wear calculation. Instead experimental work is carried out in order to define the wear as a function of film thickness. This approach eliminates the requirement of knowing the contact pressure.

1.1 Wear as function of film thickness

The wear rate W is assumed to be a function of the local film thickness h at a given surface roughness R_q of the metal part of the compliant bearing.
Figure 1 shows different correlations between film thickness and wear rate for a specified surface roughness. The axes values have been normalized with the factors K_A and $K_B R_q$.

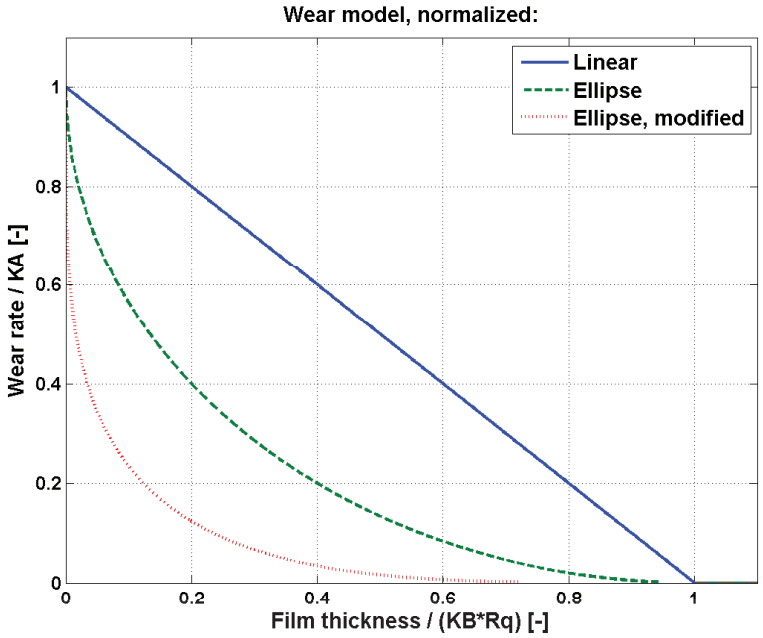

Figure 1: Three different wear models

The equations for the three models in figure 1 are listed in eq. 1 to 3.

Linear:

$$W_{Linear} = \frac{K_A V}{K_B R_q}\left(K_B R_q - h\right),\ h < K_B R_q \tag{1}$$

Ellipse:

$$W_{Ellipse} = K_A V\left[1-\left(1-\frac{\left(h-K_B R_q\right)^2}{\left(K_B R_q\right)^2}\right)^{\frac{1}{2}}\right],\ h < K_B R_q \tag{2}$$

Modified ellipse:

$$W_{Modified\ ellipse} = K_A V\left[1-\left(1-\frac{\left(h-K_B R_q\right)^4}{\left(K_B R_q\right)^4}\right)^{\frac{1}{4}}\right],\ h < K_B R_q \tag{3}$$

The wear rate at 0 film thickness is determined by the coefficient K_A and the sliding speed V.
The onset of wear is determined by the coefficient $K_B R_q$.

For this work K_A is set to the wear rate at dry lubrication using coefficients from [3]. This is very conservative but the aim of this work is not to give accurate results but rather to discuss the proposed wear model.

According to experimental findings from [4] the presence of oil in a sliding bearing with no pressure build-up, and hence zero film thickness, can reduce the wear rate with a factor of 14 to 400 depending on the polymer type and the specific energy of adhesion at the interface.

K_B is defined as the factor Lambda [11] at the onset of wear:

$$K_B = \lambda_{onset} = \frac{h_{onset}}{\sqrt{R_{q\ steel}^2 + R_{q\ polymer}^2}} \tag{4}$$

The polymer is very compliant compared to the steel counter surface and all wear is expected to happen on the polymer part. Therefore R_q of the polymer is set to 0 giving:

$$K_B = \frac{h_{onset}}{R_{q\ steel}} \tag{5}$$

The wear model assumes no particles in the lubricant and could be extended with a similar curve giving the wear rate due to particles in the lubricant. $K_{A\ particle}$ could then be dependent on particle size and particle concentration. $K_{B\ particle}$ could be a function of particle size and film thickness.

1.2 Implementation and comparison with experimental data

The soft EHL model is created using Reynolds equation together with the Winkler/Column model as used in [8] for modelling a metal-polymer bearing.

When a bearing is subjected to wear it will operate with very thin film thicknesses in the wearing zones. Therefore one could also consider including the surface roughness effect on pressure build-up in this zone. The average flow model could be used for this purpose as described by [5]+[6].

[7] analyses the effect of roughness on bearing performance in a metal-metal bearing using a deterministic EHL model. It is concluded that including the roughness increases the minimum film thickness with 8% in the example with transversal roughness and less with longitudinal roughness. When the surfaces are assumed rigid the effect is an increase of 30%.
Therefore the effect in a compliant bearing with longitudinal roughness on the metal surface will be <<8% and implementing the surface roughness effect on pressure build-up is assumed to be non-critical for wear simulation in the soft EHL model.

Test bearing parameters:

Bearing diameter:	100mm
Bearing length:	70mm
Radial clearance:	130µm
Nominal speed:	1960 rpm
Load:	32kN (Specific pressure: 4.6MP)
Oil viscosity:	ISO VG 32 at 50 degr. C
Angular misalignment:	$0.92 \cdot 10^{-3}$ rad

The angular misalignment corresponds to a film thickness difference over the entire bearing length of 65µm (50% of the radial clearance).

$K_B R_q$ is set to $6 \cdot 10^{-6}$ m.

The high misalignment gives a maximum pressure of 39MPa (8.5x specific pressure) at the most heavily loaded region of the bearing at the start of the simulation.

Results for linear and elliptic wear model:
The wear simulation is initialized with steady state conditions and the results are shown below together with scaled experimental data from [12].

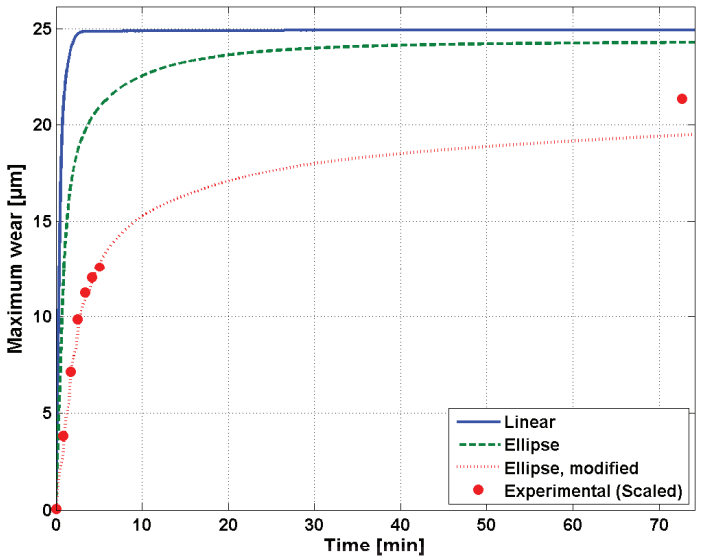

Figure 2: Simulation results

The experimental data from [12] are scaled in X- and Y-direction to fit with the simulations using the modified elliptic wear law since these show the best correlation.

The experimental data was acquired using a metal-metal bearing with similar dimensions and applying 2160 start/stop cycles while measuring the wear.

This is somewhat different from the simulations where the speed is kept constant and one bearing part is compliant. Therefore no conclusions can be made on these comparisons other than discussing the versatility of the proposed model.

From the figure it is seen that the linear model, as expected, reaches a zero wear rate situation sooner than the elliptic. The final wear picture, when zero wear rate is reached, is determined by K_B. The time to reach this condition is determined by KA together with the curvature from K_A to $K_B R_q$. As a result the different models will always converge when identical K_B values are used.

1.3 Qualitatively comparisons with test results

Comparison of wear curves:
When comparing the linear and elliptic wear models from figure 2 with the experimental data it is seen that the modified elliptic model fits well with the *scaled* experimental data, although it is not a perfect fit. When this fit is obtained, it is only a matter of using the correct coefficients in order to make the simulations fit with the *unscaled* experimental data.

Comparison of final wear picture:
Figure 3 shows the wear picture after 75 minutes using the modified elliptic wear model. The maximum wear is not in the same direction as the external load. This is in accordance with the fact that the shaft centre steady state position follows the locus curve. The same trend is observed in the experimental results from [12] measuring the wear during slow and constant rotational speed.

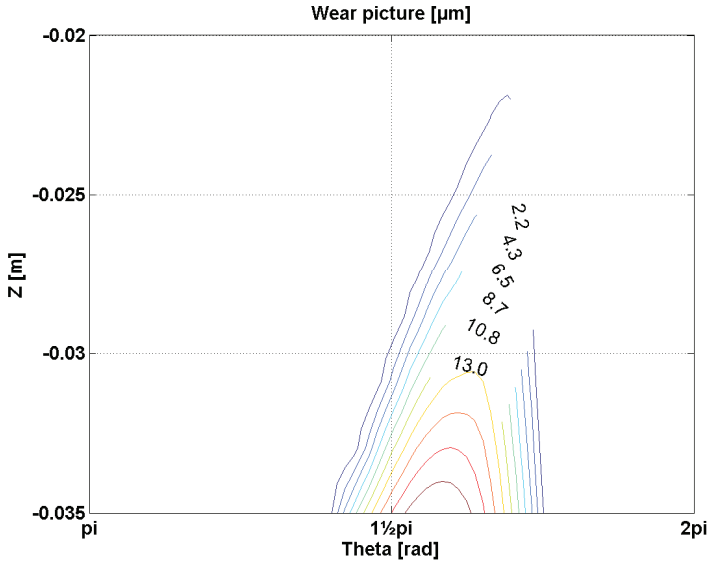

Figure 3: Wear picture at 75 minutes using the modified ellipse wear model.
The figure is zoomed at the worn area (showing 10% of the bearing area).

1.4 Test procedures for finding wear coefficients for polymer-metal bearing

It is important to perform the testing under operational conditions similar to the ones which will be found in the real bearing. This minimizes the risk of having other failure mechanisms or influence from parameters that are not integrated in the wear model.
An example is the temperature of the counter surface. A polymer like HDPE (high molecular density poly-ethylene) has excellent wear properties at temperatures under 50℃ but above this temperature the wear rate increases radically [1].

Some parameters of importance are surface roughness, surface hardness, temperature and specific energy of adhesion at the interface [3]+[10].

Samyn and Schoukens [2] conclude that small-scale test rigs, like cylinder-on-plate, cannot be used to generate wear coefficients for use in normal sized bearings because the coefficients strongly depend on the sample geometry. Larger-scale test rigs are required and consequently they use a flat-on-flat with a contact area of 150x150mm^2 for this.

Proposed test procedure for finding K_A:
The coefficient K_A determines the wear rate at 0 film thickness. A block-on-plate or alternatively a pin-on-disc test rig with constant load can be used to find the value for K_A. The parallel surfaces between the polymer block and the metal plate will ensure zero pressure build-up and keep lubricant film thickness to a minimum.
K_A is determined from measuring the wear as a function of sliding distance.
The polymer layer thickness should be kept small in order to avoid deformation and resulting converging film thickness geometry which will result in a lubricant pressure build-up.

This procedure is somewhat problematic because it is a different lubrication mode than expected in a hydrodynamic bearing. The test results are likely to be pressure (load) dependent as opposed to a hydrodynamic bearing where the primary factor for wear rate is film thickness which then among others depends on pressure.
An alternative procedure is to find intermediate points between K_A and $K_B R_q$ and use these points to generate the wear curve without knowing the value at zero film thickness.

Test procedure for finding K_B:
The coefficient K_B determines the onset of wear together with R_q. The above mentioned block-on-plate test rig can be used to find K_B. Instead of constant load the block position is fixed with a slight preload on the plate. The polymer block will deform correspondingly and this deformation d must be measured. The plate is then rotated until a zero wear rate condition is reached on the block.

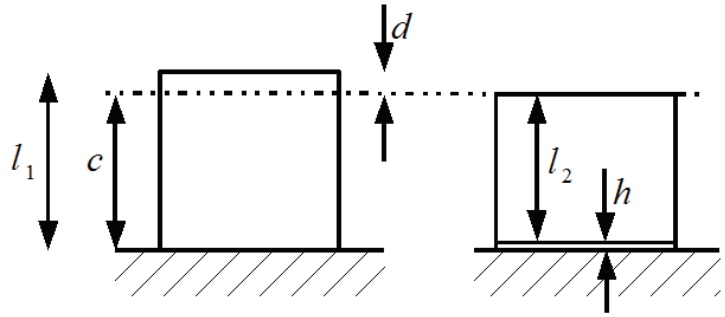

Figure 4: Distance measurements for finding K_B

The length c is constant throughout the test because of the fixed position. This gives the following relationship between the lengths:

$$c = l_1 - d = l_2 + h \Leftrightarrow h = l_1 - l_2 - d \tag{6}$$

K_B can then be calculated using eq. 5:

$$KB = \frac{h_{onset}}{R_{q\,steel}} = \frac{l_1 - l_2 - d}{R_{q\,steel}} \tag{7}$$

This procedure requires perfect alignment of the plate in order to avoid any wobbling during the rotation cycle.
The method also assumes no deformation of the polymer block at the zero wear rate condition. The wear can create a situation where some parts of the interface are able to build up a pressure. To minimize this effect it is advantageous to machine grooves in the block that will degrade the ability to

build up a pressure and hence ensure no deformation due to a pressure build-up in the lubricant. The grooves will furthermore ensure an even lubricant distribution in the bearing interface.

The general accepted λ value for the transition between mixed and full hydrodynamic lubrication is in the range 3 to 6 and therefore this is also the expected value for K_B

Test procedure for finding the curvature of the wear model:
When the coefficients K_A and K_B are known the curvature can be determined by comparing simulations with data from experiments in the same manner as shown in fig. 2.

1.5 Conclusion

It is demonstrated that the proposed wear model can give useful results and is relatively simple to implement, although more work is required in order to verify the wear model and preferably in a broad range of operating conditions. The weakness of the presented wear model is that it is difficult to find the wear coefficients, mainly because film thickness measurements in metal-polymer bearings are complicated to perform.

At present time no work has been done on the experimental part with respect to finding wear coefficients or verification of the wear model. These tasks are required before using the model for any kind of design work.

2 References

[1] VDI 2541: Gleitlager aus thermoplastischen Kunstoffen. October 1975

[2] P.Samyn, G. Schoukens (2008) Experimental extrapolation model for friction and wear of polymers on different testing scales. International Journal of Mechanical Sciences 50 p. 1390–1403.

[3] N.Viswanath, D.G. Bellow (1995) Development of an equation for the wear of polymers. Elsevier, Wear.

[4] Z.Rymuza (1990) Predicting wear in miniature steel-polymer journal bearings. Elsever, Wear.

[5] N.Patir, H.S.Cheng (1978) An average flow model for determining effects of three-dimensioned roughness on partial hydrodynamic lubrication. Transactions of ASME vol. 100. p. 12-17.

[6] N.Patir, H.S.Cheng (1979) Application of average flow model to lubrication between rough sliding surfaces. Transactions of ASME vol. 101. p. 220-230.

[7] M.B.Dobrica, M.Fillon, P. Maspeyrot (2006) Mixed Elastohydrodynamic Lubrication in a Partial Journal Bearing - Comparison Between Deterministic and Stochastic Models. Transactions of ASME vol. 128. p. 778-788.

[8] S.B.Glavatskih, M.Fillon (2006) TEHD analysis of thrust bearings with PTFE-faced pads. Journal of Tribology, Vol. 128, p. 49-58.

[9] Q.J.Wang (2004) Contact, mixed lubrication, and failure of engineering surfaces and design of journal bearing systems. EDF-LMS Futuroscope, 7 October 2004.

[10] D.Zhu (2007) Simulation of sliding wear in mixed lubrication. Transactions of ASME, Vol. 129, p. 544-552.

[11] B.J.Hamrock (2004) Fundamentals of fluid film lubrication. ISBN 0-8247-5371-2

[12] J. Bouyer, M.Fillon, I Pierre-Danos (2006) Experimental Characterization of Wear and its Influence on the Behavior of a Two- lobe Hydrodynamic Journal Bearing. 5th EDF & LMS Poitiers Workshop.

Bibliography

[1] A. Leopard, "Tilting pad bearings - limits of safe operation," *Lubrication Engineering*, vol. 32, no. 12, pp. 637–644, 1976.

[2] B. Jacobson, "Nano-meter film rheology and asperity lubrication," *Journal of Tribology*, vol. 124, no. 3, pp. 595–599, 2002.

[3] T. Someya, *Journal-Bearing Databook*. Springer-Verlag, 1989. ISBN-13: 978-3540170747.

[4] G. Stachowiak and A. Batchelor, *Engineering Tribology, 3rd. ed.* Elsevier Inc., 2005.

[5] S. Glavatskih, "Tilting pad thrust bearings," *Tribology series: Proceedings of the 29th Leeds-Lyon Symposium on Tribology*, no. 41, 2002. ISBN 0-444-51243-8.

[6] J. Nicholas and K. Wygant, "Tilting pad journal bearing design for high load applications," *Proceedings of the 24th Turbomachinery Symposium*, vol. May, pp. 33–47, 2005.

[7] S. Kim and K. Kim, "Influence of pad pivot friction on tilting pad journal bearing," *Tribology International*, vol. 41, pp. 694–703, 2008.

[8] K. Thomsen, P. Klit, and A. Volund, "Discontinuity effects in dynamically loaded tilting pad journal bearings," *Engineering Tribology*, vol. 225, no. 7, pp. 663–669, 2011.

[9] D. Hargreaves and M. Fillon, "Analysis of a tilting pad journal bearing to avoid pad fluttering," *Tribology International*, vol. 40, no. 4, pp. 607–612, 2006.

[10] W. Gardner, "An experimental study of thrust pad flutter," *Journal of tribology-transactions of the ASME*, vol. 120, no. 3, pp. 577–582, 1998.

[11] M. L. Adams and S. Payandeh, "Self-excited vibration of statically unloaded pads in tilting-pad journal bearings," *Journal of Lubrication Technology*, vol. 105, no. 7, pp. 377–384, 1983.

[12] C. Ettles, "Size effects in tilting pad thrust bearings," *Wear*, vol. 59, no. 1, pp. 231–245, 1980.

[13] N. Heinrichson, *On the Design of Tilting-Pad Thrust Bearings*. Ph.D. dissertation, Technical University of Denmark, 2006.

[14] K. Thomsen and P. Klit, "Geometrical design parameters for journal bearings with flexure pads and compliant liners," *Engineering Tribology*, vol. 226, no. 4, pp. 274–283, 2012.

[15] K. Thomsen and P. Klit, "Improvement of journal bearing operation at heavy misalignment using bearing flexibility and compliant liners," *Engineering Tribology*, vol. 226, no. 8, pp. 651–660, 2012.

[16] J. Simmons, R. Knox, and W. Moss, "The development of PTFE-faced hydrodynamic thrust bearing for hydrogenerator application in the United Kingdom," *Journal of Engineering Tribology*, vol. 212, no. Part J, pp. 345–352, 1998.

[17] J. Nicholas, "Tilting pad journal bearing pivot design for high load applications," in *Proceedings of the 24th Turbomachinery Symposium*, May 2005.

[18] S. Glavatskih, "Evaluating thermal performance of a ptfe-faced tilting pad thrust bearing," *Journal of Tribology*, vol. 125, pp. 319–324, 2003.

[19] B. Bhushan, "Adhesion and stiction: Mechanisms, measurement techniques, and methods for reduction," *Journal of Vacuum Science & Technology*, vol. 21, no. 6, pp. 2262–2296, 2003.

[20] K. Thomsen and P. Klit, "A study on compliant layers and its influence on dynamic response of a hydrodynamic journal bearing," *Tribology International*, vol. 44, no. 12, pp. 1872–1877, 2011.

[21] B. Hamrock, S. Schmid, and B. Jacobsen, *Fundamentals of fluid film lubrication, 2nd ed.* Marcel Dekker Inc., 2004.

[22] P. Cann, E. Ioannides, B. Jacobson, and A. Lubrecht, "The lambda ratio - a critical reexamination," *Wear*, vol. 175, no. 1-2, pp. 177–188, 1994.

[23] X. Lu and M. Khonsari, "On the lift-off speed in journal bearings," *Tribology and lubrication technology*, vol. 62, no. 3, pp. 40–46, 2006.

[24] E. Booser, F. Ryan, and C. Linkinhoker, "Maximum temperature for hydrodynamic bearings under steady load," *Lubrication Engineering*, vol. 26, no. July, pp. 225–232, 1970.

[25] P. Piotr, *Simulation of transient states in large hydrodynamic thrust bearings*. Ph.D. dissertation, Gdansk University of Technology, 2010.

[26] J. Neale, *The Tribology Handbook, 2nd edition.* Butterworth Heinemann, 1996. ISBN-13: 978-0-7506-1198-5.

[27] D. Garner, "The use of design procedures for plain bearings," *Conference sponsored by the Industrial Unit of Tribology. University of Leeds*, September 1980.

[28] D. McCarthy and S. Glavatskih, "Assessment of polymer composites for hydrodynamic journal-bearing applications," *Lubrication Science*, vol. 21, no. 8, pp. 331–341, 2008.

[29] A. Birkett and J. Lancaster, "Counterface effects on the wear of a composite dry-bearing liner," *Proc. JSLE Int. Tribology Conference*, pp. 465–470, 8-10 July 1985.

[30] T. Barrett, G. Stachowiak, and A. Batchelor, "Effect of roughness and sliding speed on the wear and friction of ultra-high molecular weight polyethylene," *Wear*, vol. 153, no. 2, pp. 331–350, 1992.

[31] J. Archard, "Single contacts and multiple encounters," *Journal of Applied Physics*, vol. 32, no. 8, pp. 1420–1425, 1961.

[32] N. Patir and H. Cheng, "Average flow model for determining effects of three-dimensional roughness on partial hydrodynamic lubrication.," *Journal of Lubrication Technology*, vol. 100, no. 1, pp. 12–17, 1978.

[33] N. Patir and H. Cheng, "Application of average flow model to lubrication between rough sliding surfaces," *Journal of Lubrication Technology*, vol. 101, no. 2, pp. 220–230, 1979.

[34] M. Dobrica, M. Fillon, and P. Maspeyrot, "Mixed elastohydrodynamic lubrication in a partial journal bearing - comparison between deterministic and stochastic models," *Journal of Tribology*, vol. 128, no. 4, pp. 778–788, 2006.

[35] J. Greenwood and J. Tripp, "The contact of two nominally flat rough surfaces," *Proc. Instn. Mech. Engrs.*, vol. 185, no. 48, pp. 625–633, 1970-1971.

[36] Y. Hu and D. Zhu, "A full numerical solution to the mixed lubrication in point contacts," *Journal of Tribology*, vol. 122, no. 1, pp. 1–9, 2000.

[37] D. Zhu, A. Martini, W. Hu, B. Lisowsky, and Q. Wang, "Simulation of sliding ear in mixed lubrication," *Journal of tribology*, vol. 129, no. 3, pp. 544–552, 2007.

[38] K. Thomsen and P. Klit, "Application of a new wear model in hydrodynamic metal-polymer bearings," *9th EDF/Pprime (LMS) Poitiers Workshop*, 2010.

[39] A. Szeri, *Tribology: Friction, Lubrication and Wear.* McGraw Hill Higher Education, 1980. ISBN-13: 978-0070626638.

[40] D. Dowson and C. March, "A thermohydrodynamic analysis of journal bearings," *Proceedings of the Institution of Mechanical Engineers*, vol. 181, no. 15, pp. 117–126, 1966.

[41] P. Klit and J. Lund, "Calculation of the dynamic coefficients of a journal bearing using a variational approach," *Journal of Tribology*, vol. 108, no. 3, pp. 421–424, 1985.

[42] Z. Qui and A. Tieu, "The effect of perturbation amplitudes on eight force coefficients of journal bearings," *Tribology Transactions*, vol. 39, no. 2, pp. 469–475, 1996.

[43] E. Kuznetsov and S. Glavatskih, "Stability analysis of a compliant lemon bore journal bearing," in *Proceedings of the 9th biennial conference on engineering systems design and analysis - 2008*, vol. 3, pp. 561–568, 2009.

[44] Booker and Huebner, "Application of finite element methods to lubrication: An engineering approach," *Transactions of the ASME, Journal of Lubrication Technology*, vol. 94, no. 4, pp. 313–323, 1972.

[45] K. Huebner, D. Dewhirst, D. Smith, and T. Byron, *The Finite Element Method for Engineers*. John Wiley & Sons, 2001. ISBN-13 978-0-471-37078-9.

[46] J. Seeton, "Viscosity-temperature correlation for liquids," *Tribology letters*, vol. 22, pp. 67–78, 2006.

[47] S. B. Glavatskih, M. Fillon, and R. Larsson, "The significance of oil thermal properties on the performance of a tilting-pad thrust bearing," *Journal of Tribology*, vol. 124, no. 2, pp. 377–385, 2002.

[48] C. Barus, "Isothermals, isotopics, and isometrics relative to viscosity," *American journal of science*, vol. 45, pp. 87–96, 1893.

[49] C. Roelands, *Correlational aspects of the viscosity-temperature-pressure relationship of lubricating oils*. Ph.D. dissertation, Technische Hogeschool Delft, The Netherlands, 1966.

[50] J. Booker and A. Kumar, "A finite element cavitation algorithm," *Journal of Tribology*, vol. 113, no. 2, pp. 276–286, 1991.

[51] T. Garnier, D. Bonneau, and C. Grente, "Three-dimensional EHD behaviour of the engine block /camshaft assembly for a four cylinder inline automotive engine," *Journal of Tribology*, vol. 121, no. 4, pp. 721–730, 1999.

[52] H. Desbordes, M. Fillon, J. Frene, and C. C. H. Wai, "The effects of three-dimensional pad deformations on tilting-pad journal bearings under dynamic loading," *Journal of Tribology*, vol. 117, no. 3, pp. 379–384, 1995.

[53] J. McIvor, *The analysis of dynamically loaded flexible journal bearings using higher-order finite elements*. Ph.D. dissertation, University of London, 1988.

[54] J. McIvor and D. Fenner, "Finite element analysis of dynamically loaded flexible journal bearings: A fast newton-raphson method," *Journal of Tribology*, vol. 111, no. 4, pp. 597–604, 1989.

[55] S. Glavatskih and M. Fillon, "TEHD analysis of thrust bearings with PTFE-faced pads," *Journal of Tribology*, vol. 128, no. 1, pp. 49–58, 2006.

[56] R. van Ostayen and A. van Beek, "Thermal modelling of the lemon-bore hydrodynamic bearing," *Tribology International*, vol. 42, no. 1, pp. 23–32, 2009.

[57] D. Dowson, J. Hudson, H. B., and C. March, "An experimental investigation of the thermal equilibrium of steadily loaded journal bearings," *Proceedings of the Institution of Mechanical Engineers*, vol. 181, no. 15, pp. 70–80, 1966.

[58] P. Klit, *En analyse af varmebalancen for et glideleje*. Ph.D. dissertation, Technical University of Denmark, 1980.

[59] H. Heshmat and O. Pinkus, "Mixing inlet temperatures in hydrodynamic bearings," *Journal of Tribology*, vol. 108, no. 2, pp. 231–248, 1986.

[60] C. Ettles, "Hot oil carry-over in thrust bearings," *Proceedings of the Institution of Mechanical Engineers*, vol. 184, no. 75-81, p. 12, 1969.

[61] L. Roy, "Thermo-hydrodynamic performance of grooved oil journal bearing," *Tribology International*, vol. 42, no. 8, pp. 1187–1198, 2009.

[62] P. Monmousseau, M. Fillon, and J. Frene, "Transient thermoelastohydrodynamic study of tilting-pad journal bearings - comparison between experimental data and theoretical results," *Journal of Tribology*, vol. 119, no. 3, pp. 401–407, 1997.

[63] P. Monmousseau, M. Fillon, and J. Frene, "Transient thermoelastohydrodynamic study of tilting-pad journal bearings under dynamic loading," *Journal of Engineering for Gas Turbines and Power*, vol. 120, no. 2, pp. 405–409, 1998.

[64] B. Kucinschi, M. Fillon, J. Frene, and M. Pascovici, "A transient thermoelastohydrodynamic study of steadily loaded plain journal bearings using finite element method analysis," *Journal of Tribology*, vol. 122, no. 1, pp. 219–226, 2000.

[65] Y. Cengel and R. Turner, *Fundamentals of Thermal-fluid Sciences*. McGraw Hill Higher Education, 2007. ISBN-13 978-0-07-332748-8.

[66] L. Jiji, *Heat Convection*. Springer Berlin Heidelberg New York, 2006. ISBN-13 978-3-540-30692-4.

[67] B. H.D. and K. Stephan, *Heat and Mass Transfer*. Springer Berlin Heidelberg New York, 2006. ISBN-13 978-3-540-29526-6.

[68] T. Almqvist, S. B. Glavatskih, and R. Larsson, "THD analysis of tilting pad thrust bearings. comparison between theory and experiments," *Journal of Tribology*, vol. 122, no. 2, pp. 412–417, 2000.

[69] J. Kim, A. Palazzaolo, and R. Gadangi, "TEHD analysis for tilting-pad journal bearings using upwind finite element method," *Tribology Transactions*, vol. 4, no. 37, pp. 771–783, 1994.

[70] I. Christie, D. F. Griffith, A. R. Mitchell, and O. C. Zienkiewicz, "Finite element methods for second order differential equations with significant first derivatives," *International Journal of Numerical Methods in Engineering*, vol. 10, no. 6, pp. 1389–1396, 1976.

[71] J. C. Heinrich, P. S. Huyakorn, O. C. Zienkiewicz, and A. R. Mitchell, "An upwind finite element scheme for two-dimensional convective transport equation," *International Journal of Numerical Methods in Engineering*, vol. 11, no. 1, pp. 131–143, 1977.

[72] H. Kim, G. Jang, and S. Lee, "Complete determination of the dynamic coefficients of coupled journal and thrust bearings considering five degrees of freedom for a general rotor-bearing system," *Microsystem Technologies*, vol. 17, no. 5, pp. 749–759, 2011.

[73] M. Kim, G. Jang, and H. Kim, "Stability analysis of a disk-spindle system supported by coupled journal and thrust bearings considering five degrees of freedom," *Tribology International*, vol. 43, no. 8, pp. 1479–1490, 2010.

[74] J. Booker, "Dynamically loaded journal bearings: Mobility method of solution," *Journal of basic engineering*, vol. 187, no. 3, pp. 537–546, 1965.

[75] J. Gere and S. Timoshenko, *Mechanics of Materials, 4th Edition*. Pws Pub. Co., 1997. ISBN-13 978-0-534-93429-3.

DTU Mechanical Engineering
Section of Solid Mechanics
Technical University of Denmark

Nils Koppels Allé, Bld. 404
DK- 2800 Kgs. Lyngby
Denmark
Phone (+45) 4525 4250
Fax (+45) 4593 1475
www.mek.dtu.dk
ISBN: 978-87-90416-84-3

DCAMM
Danish Center for Applied Mathematics and Mechanics

Nils Koppels Allé, Bld. 404
DK-2800 Kgs. Lyngby
Denmark
Phone (+45) 4525 4250
Fax (+45) 4593 1475
www.dcamm.dk
ISSN: 0903-1685